LOCALIZATION OF GRAVITY AND TOPOGRAPHY: CONSTRAINTS ON THE TECTONICS AND MANTLE DYNAMICS OF EARTH AND VENUS

by

Mark Simons

B.S., Geophysics and Space Physics, 1989
University of California, Los Angeles

Submitted to the Department of Earth, Atmospheric, and Planetary Sciences
in partial fulfillment of the requirements for the degree of

DOCTOR OF PHILOSOPHY

at the

MASSACHUSETTS INSTITUTE OF TECHNOLOGY

February 1996

Author ....
Department of Earth, Atmospheric, and Planetary Sciences
October 11, 1995

Certified by ....
Bradford H. Hager
Thesis Co-Supervisor

Certified by ....
Sean C. Solomon
Thesis Co-Supervisor

Accepted by ....
Thomas H. Jordan
Department Head

Abstract

Global models of the gravity fields of Earth and Venus are now available with a maximum resolution of about 600 km. In order to interpret these data sets in the context of geodynamical models, we develop a method for spatio-spectral localization of harmonic data defined on a sphere. For Venus, we calculate the localized RMS amplitudes of the geoid and topography, as well as the spectral admittance between the two fields. We conclude from the observed admittances that topography over 10 percent of the surface of Venus can be explained by variations in crustal thickness, and that topography over the remaining 90 percent of the surface is the result of vertical convective tractions at the base of the lithosphere. We compare the localized admittance spectra to similar quantities derived from a set of numerical convection models. With these models, we show that an Earth-like radial viscosity structure can not be rejected by the geoid and topography data and that admittance values alone can not constrain the thickness of the thermal boundary layer of Venus.

For Earth, we look at the RMS amplitudes of geoid and topography and investigate the spatial and spectral correlations among these and other geophysical data sets. Since plate boundary processes generate geoid and topography with large amplitudes and limited spatial extent, localization permits us to look at mid-plate regions with minimal contamination from plate boundary effects. Beyond using our localization method as a descriptive tool, we use our approach to compare forward model predictions with observations. To this end, we consider both static and dynamic models of topographic compensation. The latter model is investigated through a decomposition of the geoid into three components related to post-glacial rebound, subduction zones, and hotspots, all of which are found to contribute significantly to the middle- and long-wavelength geoid. This decomposition is based on the local correlations of the observed geoid with the tectonic distribution functions describing the spatial extent of each of these processes. We compare the predicted fields from our decomposition with those predicted by models of post-glacial rebound and dynamic models of mantle flow.

Thesis committee:
Dr. Bradford H. Hager, Massachussetts Institute of Technology (Thesis co-Advisor)
Dr. Sean C. Solomon, Carnegie Institution of Washington (Thesis co-Advisor)
Dr. Thomas H. Jordan, Massachussetts Institute of Technology
Dr. Richard J. O'Connell, Harvard University
Dr. Carl I. Wunsch, Massachussetts Institute of Technology

Acknowledgments

I am indebted to my thesis committee: Brad Hager, Sean Solomon, Tom Jordan, Rick O'Connell, Carl Wunsch and King Carl XVI Gustaf of Sweden, for constructive criticism, fruitful discussions, and excellent timing. Over the past several years, I have also benefited from discussions with among others Tom Herring, Marcia McNutt, and Wiki Royden. I am particularly grateful to Brad and Sean who throughout my graduate career have tolerated my wayward focus, let me run with my ideas, and shared their love for Earth and planetary science. I could not have asked for more from them as they turned my M.I.T. experience into what can best be termed a research apprenticeship. I hope this thesis represents just the beginning of our collaborations and my geophysical education.

I have truly enjoyed the numerous discussions (geophysical and otherwise) with my fellow students, postdocs, system administrators, and staff. For their consistently constructive comments and willingness to argue, I am particularly grateful to my terrestrial colleagues Kurt Feigl, Jim Gaherty, Pierre Ihmlé, Rafi Katzman, Lana Panasyuk, Steve Shapiro, and Ming Fang, as well as my extraterrestrial cohorts Pat McGovern and Nori Namiki. In addition, I have benefited from my contact with Matt Cordery, Richard Holme, Mamoru Kato, Peter Kaufman, Simon McClusky, Peter Puster, Mousumi Roy, Sue Smrekar, Bonnie Souter, Dawn Sumner, Paula Waschbush, and Cecily Wolfe.

Graduate school can easily lead to obsessive behavior if not balanced with outside experiences. Most of the credit for keeping me from going too far out of kilter belongs

to Martha House. Her presence as my diving, hiking, traveling, and cooking partner, as well as a tolerant and enthusiastic daily companion were and continue to be priceless.

Finally, I owe much more than just the obvious to my parents Stephen Simons and Jacqueline Simons (née Berchadsky). Whether at (60°40′N 5°20′E), (37°12′N 118°41′W), (21°N 101°W), or best of all at (34°75′N 119°12′W), they have always been there, leading, waiting, or even following. For your love, encouragement, confidence, input, humor (sometimes), and nourishment (always), I can only say merci, gracias, tusen takk, and thank you.

Table of Contents

Chapter 1

Introduction

The terrestrial planets lose the heat they acquired during their initial formation and from the decay of radioactive elements in their interiors through subsolidus convection of their mantles [e.g., *Basaltic Volcanism Study Project*, 1981; *O'Connell and Hager*, 1980; *Sleep and Langan*, 1981]. Our understanding of the dynamics of convection and the resulting surface manifestations has relied heavily on the analysis of gravitational, topographic, and seismological data [e.g., *Kaula*, 1968; *McKenzie*, 1977b; *Woodhouse and Dziewonski*, 1984]. In this thesis, we present a new approach to analyzing these data sets. This approach, based on non-stationary spectrum estimation techniques, is used to analyze surface manifestation of convective processes for both Earth and Venus.

On Earth, surface manifestations of mantle convection are dominated by plate tectonics and the formation of continents [e.g., *Wilson*, 1965; *McKenzie*, 1967b; *Jordan*, 1979; *Burchfiel*, 1983]. When viewed globally, the long-wavelength geoid anomalies on Earth are influenced by the effects of subduction zone processes and lower mantle structure [*Crough and Jurdy*, 1980; *Hager*, 1984]. At shorter wavelengths, the thermal boundary layer structure of the lithosphere, crustal thickness variations, and the mass deficiences caused by glacial unloading begin to have strong signatures, as may the effects of hot mantle upwellings [e.g., *Parsons and Richter*, 1980; *Sleep*, 1990; *Mitrovica* *and Peltier*, 1989].

The relationships between topography and the geoid on the planet Venus differ markedly from those on Earth. Crustal thickness variations can explain the observed geoid and topography over approximately 10 percent of the surface, while the remaining 90 percent is consistent with a model in which the two fields result primarily from vertical normal tractions at the base of the lithosphere. Unfortunately, the task of using the observed gravitational field to constrain quantitatively convective flow dynamics is non-unique. Without a model of the interior density structure, which is the situation for Venus, it is not possible to place tight quantitative constraints even on the most fundamental aspects of the convecting system, such as the thermal boundary layer thickness.

On Earth, of course, structural seismology and our understanding of the kinematics of plate tectonics provides us with models of the interior density structure. The relationship between driving forces and the geoid is reasonably well understood for a model planet with only radial variations in viscosity [e.g., *Richards and Hager*, 1984; *Ricard et al.*, 1984]. However, the effects of strong lateral variations in viscosity challenge our ability to interpret the observed long wavelength gravity field. In particular, the effects of weak plate boundaries can seriously modulate the expected results from an otherwise spherically symmetric planet [e.g., *Richards and Hager*, 1989; *Ribe*, 1992; *Zhang and Christensen*, 1993; *Forte and Peltier*, 1994].

We present a detailed illustration of this point with the mantle flow calculation shown in figure 1.1. This model uses a cylindrical geometry and a layered viscosity structure with a lower mantle 30 times more viscous than the upper mantle and a lid 100 times more viscous than the upper mantle. Flow is driven by a simple sinusoidal temperature perturbation of angular order 6 added to a conductive geotherm. We use 8 unequally sized plates whose boundaries are simulated by introducing small zones of low viscosity in the lid. Anticorrelated geoid and topography is predicted for a model with no

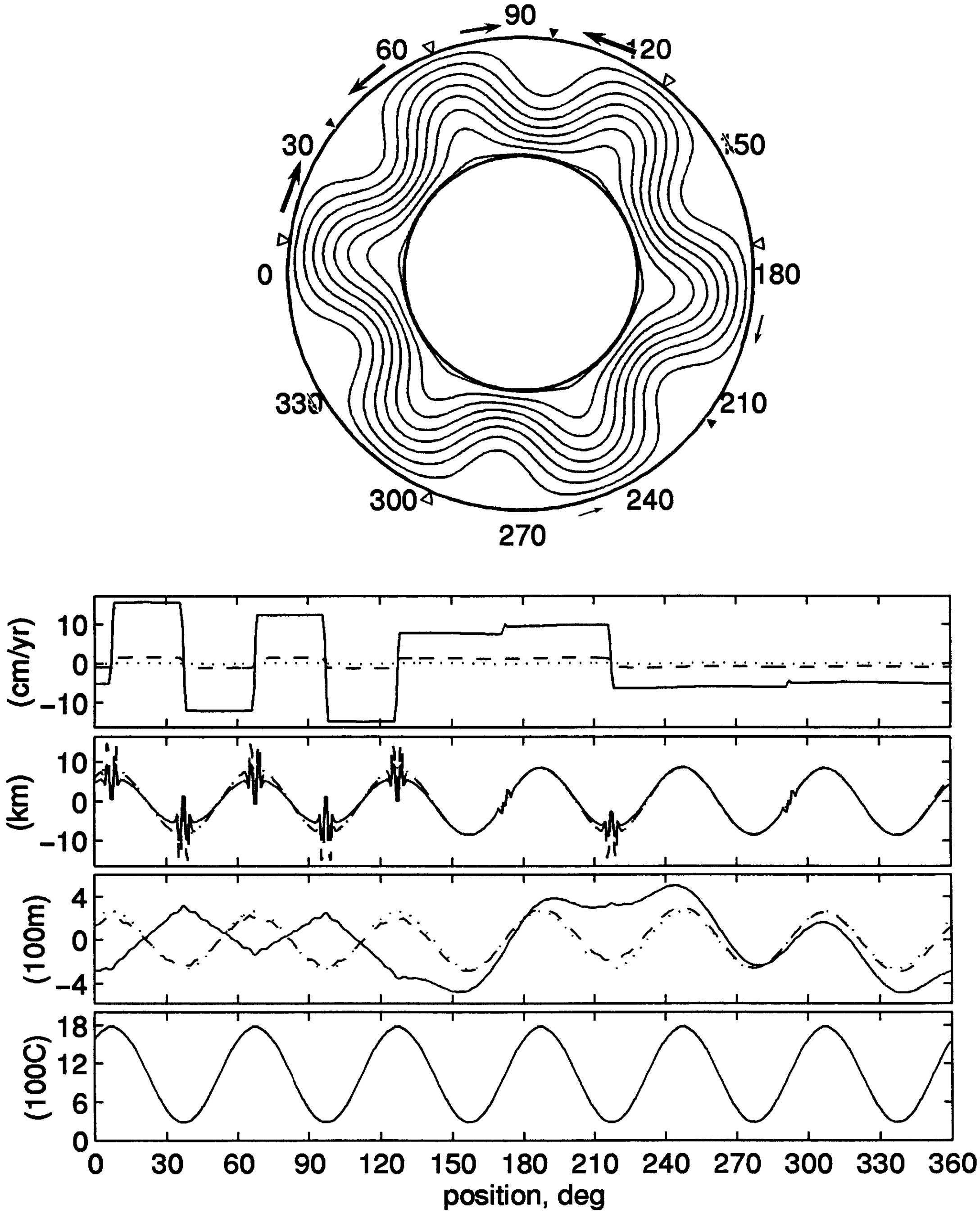

Figure 1.1: From top to bottom: Isotherms, surface velocities, total dynamic topography, long wavelength (angular order $m = 2 \ldots 12$) geoid, and a horizontal temperature profile, for a cylindrical flow model. Arrows indicate relative plate velocities. Arrow length and width scales with velocity magnitude. Convergent and divergent plate boundaries are indicated by the solid and unfilled triangles, respectively. The dotted line corresponds to a weak zone viscosity, η_{wk}, of 100 (i.e., same as the lid), the dashed line to $\eta_{wk} = 1$, and the solid line to $\eta_{wk} = 1/100$.

lid and a lower mantle more viscous than the upper mantle [*Richards and Hager*, 1984]. The presence of a lid can mitigate the effect of the weak upper mantle, as indicated by the model represented by dotted lines in figure 1.1, for which geoid and topography are well correlated. The presence of weak zones in the lid, however, can reduce the effect of the lid's generally high viscosity (see the solid line in figure 1.1), and can yield geoid and topography that are anti-correlated. For weak zones to affect the gravity-topography relation, such zones must correspond to regions of high strain rate. Where upwellings and downwellings do not coincide with weak zone locations (e.g., at positions of 170° and 300° in figure 1.1), geoid and topography remain essentially correlated. While this is a very simple model, it suggests that it is of critical interest for us to be able to isolate different regions of the observational fields in order to advance our models of mantle dynamics and flow properties.

In addition to dynamical complexity, we are hampered by the variable resolution of available data sets, ranging from 1000's of kilometers for global seismological data [e.g., *Su et al.*, 1992], to 100's of kilometers for global gravity and topography data [e.g., *Pavlis and Rapp*, 1990; *Nerem et al.*, 1994]. Many of the observations associated with plate boundary processes are characterized by steep gradients on the smallest of these length scales. While it is both physically meaningful and practically useful to analyze these global data sets in a spectral sense, the spatial combination of different geologic provinces and geodynamic processes suggests that we should expect the spectra to vary as a function of position, as in the illustration above. Typically, global data sets are available only in the form of coefficients for spherical harmonics. As with Fourier series for a Cartesian geometry, spherical harmonic functions are not well suited to regional analysis. The spatial non-stationarity intrinsic to geophysical observations requires us to consider new spectral methods.

Localization techniques attempt to estimate the frequency content of a signal at different positions. There is a natural tradeoff between spatial and spectral resolution.

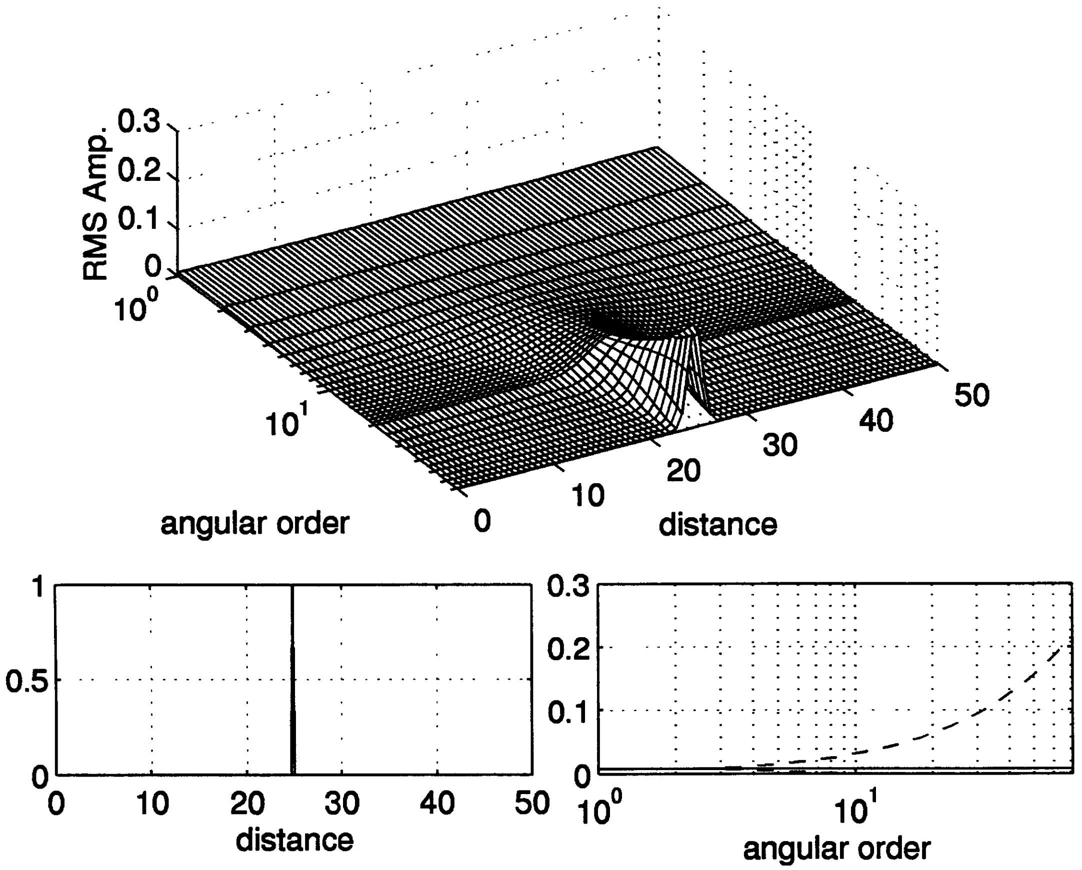

Figure 1.2: Bottom left: Input signal composed of a single spike. Top: The wavelet spectrogram. Bottom right: Fourier RMS spectrum (solid line) and the wavelet spectrum at a position of 25 (dashed line).

We demonstrate the benefits (and pitfalls) of non-stationary spectrum estimation techniques by considering a series of simple synthetic signals. These are shown in figures 1.2 to 1.8. Each of these figures has the original signal at the lower left, the Fourier root mean squared (RMS) amplitude spectrum at the lower right, and a wavelet spectrogram at the top. Local spectra at selected positons from the spectrograms are also shown at the lower right. The wavelet used in this section is based on a Fourier (sinusoidal) basis modulated by a gaussian with variance that scales with wavelength. A more complete description of this localization method can be found in *Stockwell et al.* [1995].

As mentioned above, we seek a technique to isolate regions of high spatial gradients.

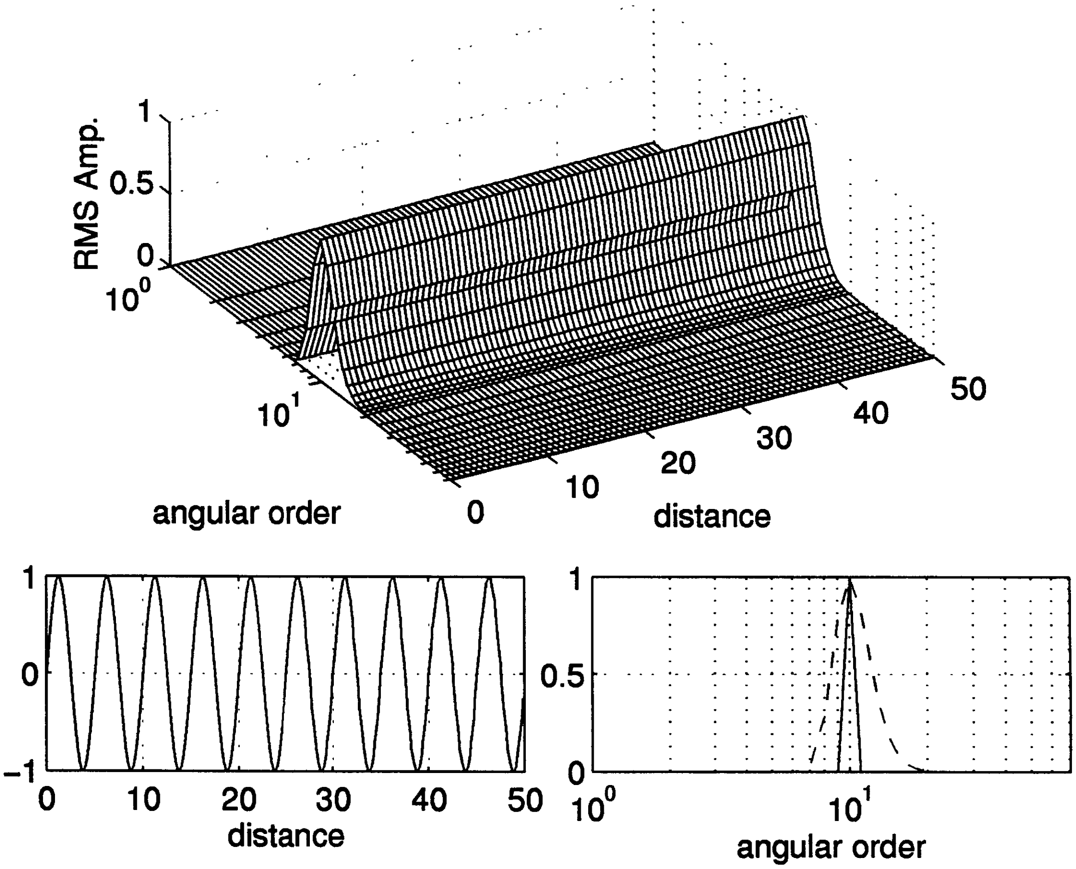

Figure 1.3: Bottom left: Input signal composed of a single sinusoid. Top: The wavelet spectrogram. Bottom right: Fourier RMS spectrum (solid line) and the wavelet spectrum (dashed line).

This ability is demonstrated in figure 1.2. With a spike as an input signal, we see that the wavelet transform is able to isolate the position of the spike, but the spectrum is that of a spike convolved with the localizing window. This simple example also illustrates the difference between characteristic length scales and characteristic wavelengths. The spike has all wavelengths, but an infinitessimally small length scale. For contrast, we show a pure sinusoidal input signal in figure 1.3. Here, the wavelet is able to detect the correct input frequency, but because of the increased spatial resolution (although not helpful in this example), we have given up resolution in the frequency domain. Unlike the example of the single spike, the pure sinusoid has a characteristic wavelength (of 5 units) and an

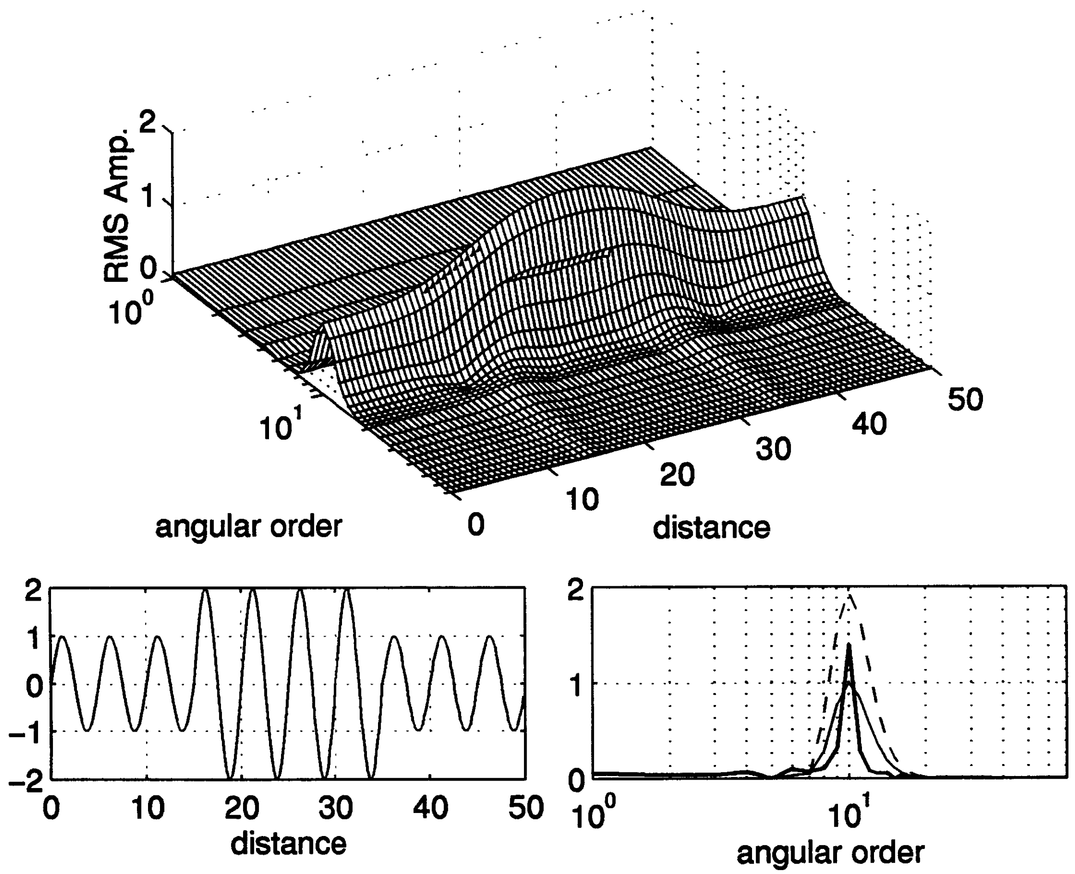

Figure 1.4: Bottom left: Input signal composed of a single sinusoid with variable amplitude. Top: The full wavelet spectrogram. Bottom right: Fourier RMS spectrum (thick line) and the wavelet spectra at positions of 5 (thin line) and 25 (dashed line).

infinite characteristic length scale. Even with a nearly sinusoidal input signal, however, the wavelet has many advantages. These are demonstrated with the example of a signal with a single frequency but variable amplitude (figure 1.4). We see that the Fourier spectrum has averaged the entire region at a single length scale (i.e., over the entire 50 unit interval), whereas the localized spectrum successfully finds the local amplitude. Note that the small ridges in the spectrum at the approximate positions of 15 and 35 correspond to the discontinuities that arise when the amplitude changes.

The tradeoff between spectral and spatial resolution is demonstrated with an input signal composed of two spikes (figure 1.5). At high angular order we isolate the spikes

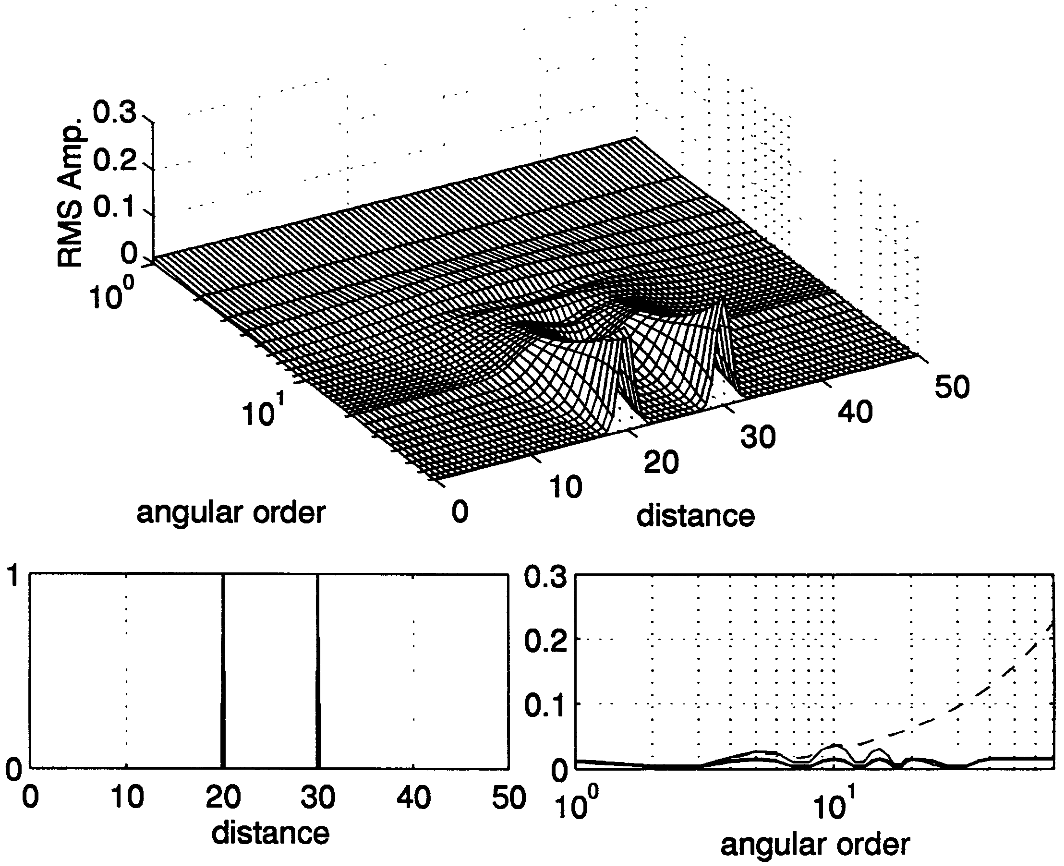

Figure 1.5: Bottom left: The input signal composed of two spikes. Top: The wavelet spectrogram. Bottom right: The Fourier RMS spectrum (thick line) and the wavelet spectra at positions of 25 (thin line) and 30 (thick line).

very well. As we decrease the angular order, however, we localize at larger length scales and at some point we can no longer distinguish between the two spikes, as their signals merge. In figure 1.5 this occurs at an angular order of 5, which corresponds to a length scale of 10, or the separation distance between the two spikes.

The power of the wavelet transform is further illustrated by using a chirp as an input signal. In figure 1.6 we consider a signal composed of the sum of descending and ascending chirps. The Fourier spectrum is not diagnostic of the input signal, but the spectrogram clearly shows the changing frequencies.

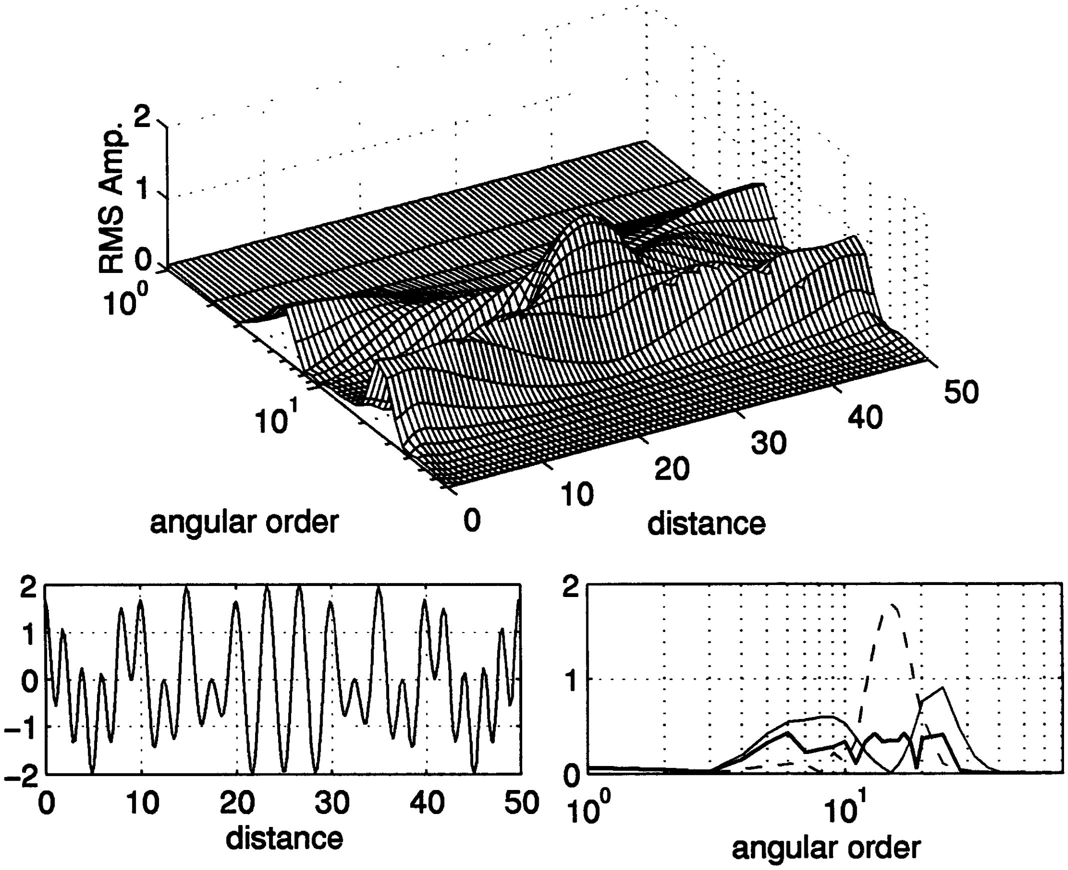

Figure 1.6: Bottom left: Input signal composed of ascending and descending chirps. Top: The wavelet spectrogram. Bottom right: Fourier RMS spectrum (thick line), the wavelet spectra at positions of 10 (thin line) and 25 (dashed line).

As a possibly more geophysically relevant example, we show the example of a signal composed of two isolated psuedo-sinusoidal bursts (figure 1.7). The input signal is created by the sum of two sinusoids of different frequency, with each sinusoid modulated by a gaussian whose variance scales with the respective frequency. For comparison, we include the localized RMS spectra for positions at the center of each burst. The ability to localize both in space and frequency is clearly demonstrated in the spectrogram.

In practice, we always start with data of limited spectral content. For instance, the currently available spherical harmonic representations of Earth's geoid extends to a maximum degree and order of 70 [*Nerem et al.*, 1994], and reliable global whole mantle

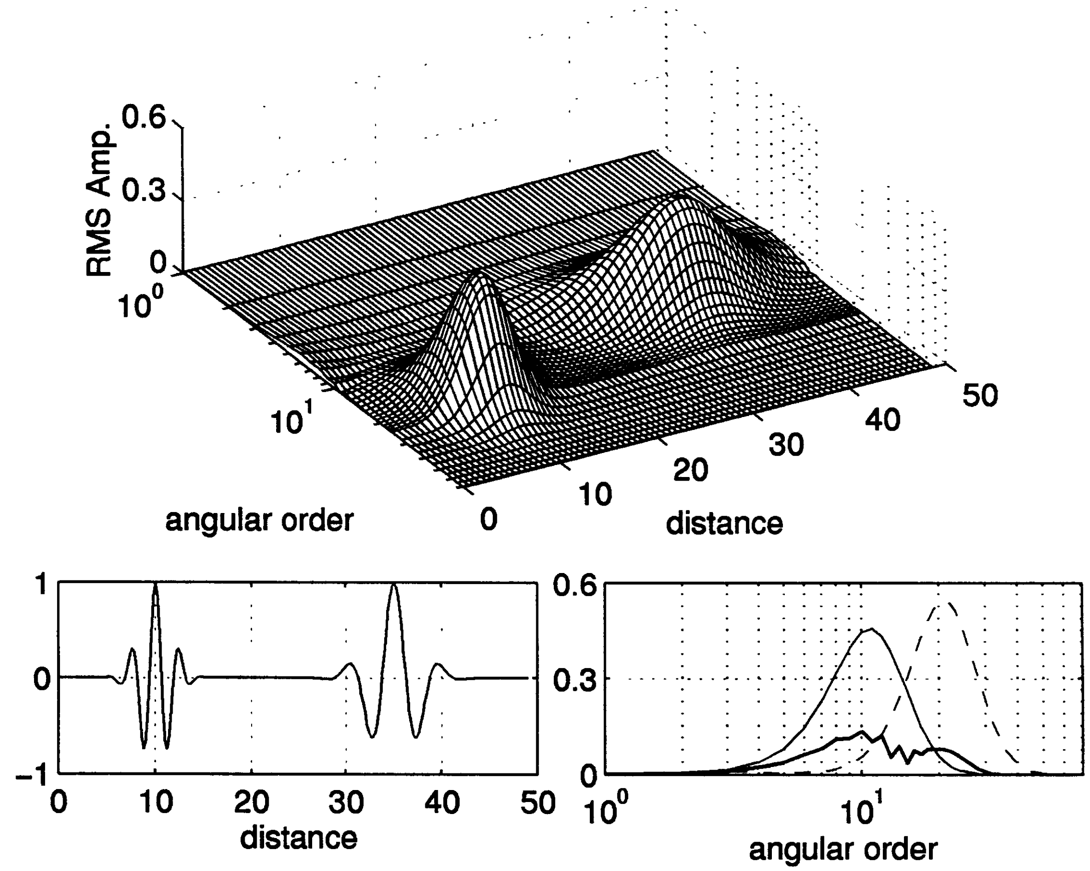

Figure 1.7: Bottom left: Input signal composed of two sinusoids with of 5 and 10, modulated by gaussians with variance scaled to their respective frequencies. Top: The wavelet spectrogram. Bottom right: Fourier RMS spectrum (thick line), the wavelet spectra at positions of 10 (dashed line) and 35 (thin line).

seismic tomography models extend to a maximum degree and order of 20. In addition to estimating the non-stationary spectrum, the wavelet approach also permits us to quantify the extent to which we can analyze spatial variations in the models at different wavelengths. In fact, for our one-dimensional Cartesian wavelet, we can derive a Nyquist wavelength for localization that takes into consideration the limited spectral content of our input data (model) [*Stockwell et al.*, 1995]. We illustrate this point in figure 1.8. Here our input data consist of the gaussian signal shown at the bottom; the same signal spectrally truncated at a wavenumber of 10 is also depicted. The spectrograms of both signals are identical up to a wavenumber of about 7 or 8, but in the spectrogram

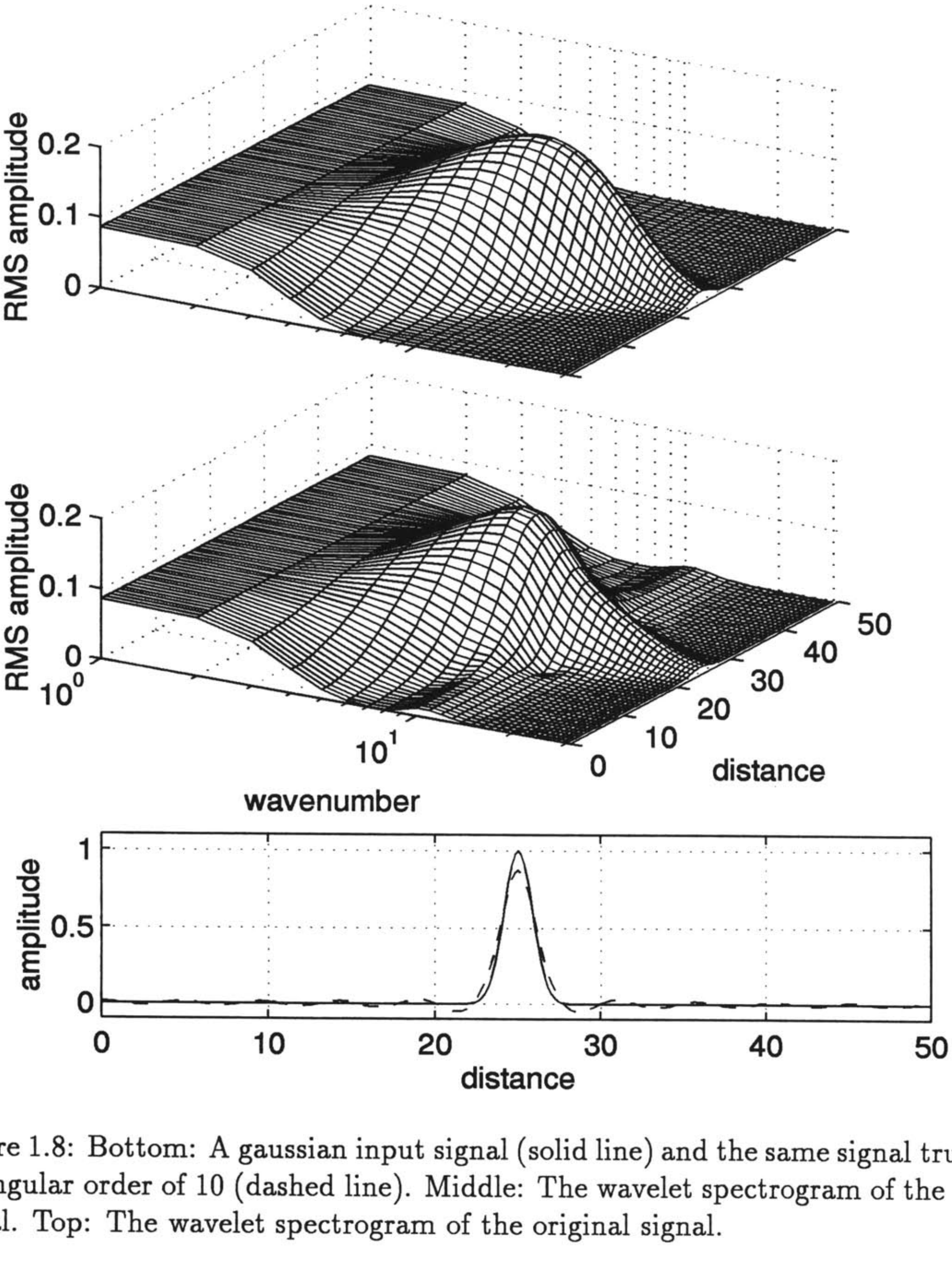

Figure 1.8: Bottom: A gaussian input signal (solid line) and the same signal truncated at an angular order of 10 (dashed line). Middle: The wavelet spectrogram of the truncated signal. Top: The wavelet spectrogram of the original signal.

of the truncated signal a spectral ridge develops centered at the cutoff wavenumber, demonstrating the effect of truncation.

In addition to dealing with data of limited spectral content, it is common in geodynamics to consider spectrally band-passed signals, such as when the long wavelength portions of the geoid are removed to isolate lithospheric signals and the residual is analyzed spatially [e.g., *Sandwell and Renkin*, 1988; *Moore and Schubert*, 1995]. Various data tapering and mirroring techniques have been developed to minimize spatial and spectral truncation effects. These concerns are automatically accounted for when the data are considered in the localized domain.

Non-stationary spectrum estimation techniques are not new. Wavelets or multi-resolution methods are now common in the fields of time series analysis and image processing [*Daubechies*, 1992]. These methods are non-parametric techniques. In contrast, parametric techniques start with prior knowledge of the character of the non-stationarity, implicitly requiring a reliable understanding of the underlying physics that generates signal. A geophysical example of such a parametric method is the generalized seismological data functional [*Gee and Jordan*, 1992], which uses the knowledge of the expected arrival times of different seismic waveforms to construct isolation filters, from which one can analyze both the time and frequency variation of the seismogram. Unfortunately, as was demonstrated earlier by the convection example (figure 1.1), our prior knowledge of the expected spectral and spatial behavior of real geodynamic systems and their surface observables is not sufficiently mature at this time to permit a parametric approach. Hence, we only consider here a non-parametric spectrum estimation technique.

There are many different non-parametric techniques for estimating nonstationary spectra, of which wavelets form a subclass [e.g., *Chui*, 1992; *Daubechies*, 1992]. Techniques exist for analyzing both one- and two-dimensional data. However, to date, all these techniques are designed for a Cartesian domain. As a recent geophysical example, *Cazenave et al.* [1995] use a one-dimensional Cartesian wavelet (very similar to the one we used above) to isolate characteristic wavelengths in Pacific geoid lineations. They present a spectrogram similar in character to that in figure 1.3, with a dominant stripe at wavelengths of about 1200 km [*Cazenave et al.*, 1995]. While not necessarily important in that analysis, the effects of sphericity and two-dimensionality are ignored. More importantly, *Cazenave et al.* [1995] begin by high-pass filtering the geoid data (tapered from harmonic degree 25 to 35), which at best should not be necessary given that they use the wavelet approach, and at worst, could introduce artifacts, such as a spectral ridge at length scales between 1000 and 1600 km for their cut off frequency.

In this thesis, we introduce a technique for spatio-spectral localization of data on a sphere. In the spirit of Cartesian wavelet transforms, our goal is to estimate non-stationary frequency spectra. We use this formalism to look at the localized spectrum of a single field, as well as the correlation and transfer function between two different localized fields. For a given region, results from our localization methods can be compared to those from classical treatments that average field statistics at a single length scale regardless of wavelength. Furthermore, the method presented here will show how to perform correctly the fixed length-scale analysis on a spherical domain. We also consider the spectrogram, with which, as shown in figures 1.2 to 1.7, we can distinguish features that have large amplitudes but are limited in spatial extent from those which are truly long-wavelength and cyclic in character, i.e., we make the crucial distinction between a characteristic length scale and a characteristic wavelength. This distinction is epitomized by the example of the delta function (figure 1.2) which has a characteristic length scale of zero but incorporates the entire spectral domain.

Our localization method, presented in chapter 2, relies on windowing of a data field using smooth windows with characteric length scales that can be functions of the harmonic degree being considered. This spatial windowing can be viewed either as spectral convolution of the given scaling window with the data or as a projection of the data onto a set of basis functions (wavelets) formed as products of a single spherical harmonic and the scaling window. As was illustrated in figure 1.8, in addition to providing theoretical elegance, the spectral-domain perspective illuminates potential spatial and spectral aliasing problems that arise if one were to choose arbitrary spatial or spectral windows when analysing the medium to long wavelengths characteristic of global data sets and models.

We consider several applications of the localization technique. Chapter 3 focuses on Venus, while chapter 4 focuses on Earth. For both planets, we start by analyzing global data sets independent of any *a priori* model. For Venus, we calculate the localized RMS amplitudes of the geoid and topography, as well as the spectral admittance between the two fields. We conclude from the observed admittances that topography over 10 percent of the surface of Venus can be explained by variations in crustal thickness, and that topography over the remaining 90 percent of the surface is the result of vertical convective traction at the base of the lithosphere. We test this inference by comparing the localized admittance spectra to similar quantities derived from a set of numerical models. The high observed admittances on Venus have been cited as evidence for the lack of an Earth-like increase with depth of mantle viscosity [e.g., *Kiefer et al.*, 1986; *Kiefer and Hager*, 1991b; *Phillips*, 1990; *Smrekar and Phillips*, 1991]. With the same set of numerical models, we will show that an Earth-like radial viscosity structure can not be rejected by the geoid and topography data. To the contrary, there is a suggestion in the data for the existence of an Earth-like radial viscosity structure. The high admittance values have also been cited as evidence for a 300-km-thick thermal boundary layer on Venus, over twice the thickness of the thermal boundary layer in the Earth's oceans. We show that admittance values alone can not be used as constraints on the thermal boundary layer structure of Venus.

For Earth, we look at the RMS amplitudes of geoid and topography and investigate the spatial and spectral correlations among these data sets. Since plate boundary processes generate geoid and topography with large amplitudes and limited spatial extent, the wavelet approach can isolate much of these signals, and permits us to look at mid-plate regions with minimal contamination from plate boundary effects. Beyond using our localization method as a descriptive tool, we also use our approach to compare forward model predictions with observations. To this end, we consider a simple model of topographic compensation dominated by the effects of crustal thickness variations in the continents and a cooling plate model in the oceans. Localization isolates the spatial and spectral regions where this model succeeds or fails. The analysis of static topographic compensation mechanisms is followed by a decomposition of the geoid into three components related to post-glacial rebound, subduction zones, and hotspots, all of which are found to contribute significantly to the middle- and long-wavelength geoid. This decomposition is based on the local correlations of the observed geoid with the tectonic distribution functions describing the spatial extent of each of these processes. We compare the predicted fields from our decomposition with those predicted by models of post-glacial rebound and dynamic models of mantle flow.

Chapter 2

Spatio-Spectral Localization on a Sphere

> "As is usually the case with any statistical treatment beyond the simplest, the benefits derived from application on the sphere of the covariance analysis, linear regression, etc., described herein often seem of dubious worth compared with the effort required. However, the same can be said of almost any technical or mathematical elaboration of general applicability: it is rare that its complete application is appropriate, but it often happens that some aspect thereof is conducive to better insight or greater efficiency in some problem."
>
> [*Kaula*, 1967]

2.1 Introduction

In this chapter we develop a localization procedure for the spherical domain. This procedure can be considered in the context of localizing data at either fixed or variable length scales. The latter application involves spatial multiplication of the data with a localizing window whose length scale is proportional to the wavelength being considered. In either case, the windowed field is tranformed into the spectral domain as a convolution, using spherical harmonics, in order to take full advantage of known harmonic coupling relations. Alternatively, we can view the problem in a classical wavelet perspective as a projection of the data onto a set of localized basis functions, each constructed as the product of a single spherical harmonic and the scaling window. The localization procedure proposed here is invertible by spatial averaging of the localized data, and can be used to determine estimates of position and wavelength dependent correlations and transfer function between two global fields.

2.2 The Localization Transform

Following the normalization and phase conventions of *Edmonds* [1957] and *Varshalovich et al.* [1988], we define a field $A(\Omega)$ on a spherical domain $\Omega = (\theta, \phi)$ by

$$A(\Omega) = \sum_{lm} a_{lm} Y_{lm}(\Omega), \tag{2.1}$$

where $0 \leq \theta \leq \pi$, $0 \leq \phi \leq 2\pi$,

$$Y_{lm}(\Omega) = (-)^m \sqrt{\frac{(2l+1)}{(4\pi)} \frac{(l-m)!}{(l+m)!}} P_{lm}(\cos\theta) e^{im\phi}, \tag{2.2}$$

and where P_{lm} is an associated Legendre polynomial of degree l and order m, defined in terms of the Legendre polynomials P_l by

$$P_{lm}(\cos\theta) = (\sin\theta)^m \frac{d^m}{(d\cos\theta)^m} P_l(\cos\theta) \tag{2.3}$$

such that

$$\int_0^\pi P_{lm}(\cos\theta)P_{l'm'}(\cos\theta)\,\sin\theta\,d\theta = \delta_{ll'}\delta_{mm'}\left(\frac{2}{2l+1}\right)\frac{(l+m)!}{(l-m)!}. \tag{2.4}$$

Each spherical harmonic $Y_{lm}(\Omega)$ is therefore fully normalized such that

$$\int_\Omega Y_{lm}(\Omega)Y^*_{l'm'}(\Omega)\,d\Omega = \delta_{ll'}\delta_{mm'}, \tag{2.5}$$

where the asterix denotes complex conjugation, and unless otherwise specified, $l = 0, 1\ldots\infty$ and $m = -l, -l+1\ldots l$. Each coefficient a_{lm} is defined by

$$a_{lm} = \int_\Omega A(\Omega)Y^*_{lm}(\Omega)\,d\Omega, \tag{2.6}$$

and we note that $Y^*_{lm}(\Omega) = (-)^m Y_{l-m}(\Omega)$ and $a^*_{lm} = (-)^m a_{l-m}$. Defining a window function

$$W(\Omega) = \sum_{lm} w_{lm}Y_{lm}(\Omega), \tag{2.7}$$

and the spatially localized version of A by

$$\Psi(\Omega) = W(\Omega)A(\Omega) = \sum_{lm}\psi_{lm}Y_{lm}(\Omega), \tag{2.8}$$

we derive the coefficients of the localized field as

$$\psi_{lm} = \int_\Omega A(\Omega)W(\Omega)Y^*_{lm}(\Omega)\,d\Omega. \tag{2.9}$$

It is worth emphasizing here that Ψ or ψ_{lm} correspond to a window of a given length scale and position. A different length scale or position would yield a different set of ψ_{lm}'s. Furthermore, we have not specified the character of the window. The development is general, applying to both scalable windows and complex geographical windows.

For comparison to the wavelet approach, we rewrite equation 2.9 as the inner product of the data with the localized basis function,

$$\psi_{lm} = \int_{\Omega} A(\Omega) X^{*}_{lm}(\Omega)\, d\Omega, \tag{2.10}$$

where

$$X_{lm}(\Omega) = W(\Omega) Y_{lm}(\Omega), \tag{2.11}$$

and we have assumed that $W(\Omega)$ is real-valued. When designing our window, care must be taken to insure that $X_{lm}(\Omega)$ has zero-mean so that we measure the first moment of our signal without bias from the zeroeth moment [e.g., *Chui*, 1992; *Daubechies*, 1992]. In addition, to maintain consistency across degrees, we require that $W(\Omega)$ have a mean amplitude of one, i.e., that

$$\frac{1}{4\pi} \int_{\Omega} W(\Omega)\, d\Omega = 1. \tag{2.12}$$

$\int ||^{2} d$ [illegible]

Alternatively, for analysis with a fixed length scale window, one could require that $W(\Omega)$ have a maximum amplitude of one, analogous to classical windowing and the short time window Fourier transform. The implementation of these constraints is addressed later. Returning to the form used in equation 2.9, and using equations 2.1 and 2.7, we write

$$\psi_{lm} = \sum_{l_1 m_1 l_2 m_2} a_{l_1 m_1} w_{l_2 m_2} \int_{\Omega} Y_{l_1 m_1}(\Omega) Y_{l_2 m_2}(\Omega) Y^{*}_{lm}(\Omega)\, d\Omega. \tag{2.13}$$

The integral of the product of the three spherical harmonics is evaluated with Wigner 3-j symbols in conjunction with the appropriate selection rules [e.g., *Varshalovich et al.*, 1988], where

$$\int_{\Omega} Y_{l_1 m_1}(\Omega) Y_{l_2 m_2}(\Omega) Y_{lm}(\Omega)\, d\Omega = \xi_{l_1 l_2 l} \begin{pmatrix} l_1 & l_2 & l \\ 0 & 0 & 0 \end{pmatrix} \begin{pmatrix} l_1 & l_2 & l \\ m_1 & m_2 & m \end{pmatrix}, \tag{2.14}$$

$$\xi_{l_1 l_2 \cdots l_n} = \sqrt{\frac{(2l_1+1)(2l_2+1)\cdots(2l_n+1)}{4\pi}}. \tag{2.15}$$

The brackets in equation 2.14 denote the Wigner 3-j coefficients. To be non-zero-valued, the 3-j coefficents must satisfy the conditions that

$$|l_1 - l_2| \leq l \leq l_1 + l_2, \tag{2.16}$$

$$|m_1| \leq l_1, \quad |m_2| \leq l_2, \quad |m| \leq l, \tag{2.17}$$

and

$$m_1 + m_2 + m = 0. \tag{2.18}$$

Furthermore, we note that

$$\begin{pmatrix} l_1 & l_2 & l \\ -m_1 & -m_2 & -m \end{pmatrix} = (-)^{l_1+l_2+l} \begin{pmatrix} l_1 & l_2 & l \\ m_1 & m_2 & m \end{pmatrix}, \tag{2.19}$$

and

$$[l_1 + l_2 + l]\,\mathrm{odd} \quad \Longrightarrow \quad \begin{pmatrix} l_1 & l_2 & l \\ 0 & 0 & 0 \end{pmatrix} = 0. \tag{2.20}$$

We then rewrite equation 2.13 as

$$\psi_{lm} = (-)^m \sum_{l_1 m_1 l_2 m_2} a_{l_1 m_1} w_{l_2 m_2} \xi_{l_1 l_2 l} \begin{pmatrix} l_1 & l_2 & l \\ 0 & 0 & 0 \end{pmatrix} \begin{pmatrix} l_1 & l_2 & l \\ m_1 & m_2 & -m \end{pmatrix}, \tag{2.21}$$

or equivalently,

$$\psi_{lm} = \sum_{l_1 m_1 l_2 m_2} a^*_{l_1 m_1} w^*_{l_2 m_2} \xi_{l_1 l_2 l} \begin{pmatrix} l_1 & l_2 & l \\ 0 & 0 & 0 \end{pmatrix} \begin{pmatrix} l_1 & l_2 & l \\ m_1 & m_2 & m \end{pmatrix}. \tag{2.22}$$

If a window (e.g., the continent-ocean function, a spherical cap, or a degree-dependent window) is expanded into spherical harmonics, it is straightforward to calculate the coefficients of the windowed field. From the triangle inequality (identity 2.16), we find that if the window can be expressed in terms of a finite number of coefficients with a maximum degree L_{win}, then the degree l coefficients of the windowed field receive contributions from data coefficients with $l_1 \leq l + L_{win}$. Given data with a maximum available degree of L_{obs}, we then have an effective Nyquist degree for localization,

$$L_{nyq} = L_{obs} - L_{win}. \tag{2.23}$$

Recognizing that increasing spatial localization increases L_{win}, we must consider equation 2.23 when designing scalable windows. It may be desirable to use a window that localizes less than optimally as a function of l. In other words, while a fixed harmonic representation of a data field can never be localized at the highest available degree, we can increase our maximum spectral resolution by decreasing our spatial resolution. The estimate of L_{nyq} is obviously valid both for scalable windows and for arbitrary windows such as the continent-ocean function or any other geographic window. To attempt to localize at $l > L_{nyq}$ involves convolving window coefficients with non-existent (i.e., zero-valued) data coefficients, and is therefore the same as convolving the data with a truncated window expansion.

It is worth emphasizing that we cannot generate information, only move it around. Equation 2.22 can be viewed as a convolution operation on a spherical domain. The purely spherical harmonic representation of a data field has perfect spectral resolution. The convolution perspective emphasizes that localization produces spatial resolution at the expense of spectral resolution.

We use a continuous spherical localization operator which can be viewed as the inner product of the data with a basis function that is constructed as the product of a window and a single spherical harmonic. Since these basis functions are neither orthogonal nor linearly independent, the spectral estimate at a given spatial location is strongly correlated to the estimate at a neighboring point. Similarly, the spectral estimate at a given degree is strongly correlated to the estimate at a neighboring degree.

2.3 The Inverse Transform

For any window, we need to define a reconstruction algorithm that maps the localized coefficients back to the original field, or equivalently, to coefficients of the original field. As shown below, we accomplish this by averaging over all possible positions and rotations of the window.

We write the coeffients of the repositioned window as

$$w_{lm}(\alpha,\beta,\gamma) = \sum_{m'} D^l_{m'm}(\alpha,\beta,\gamma) w^{\odot}_{lm'}, \tag{2.24}$$

where (α,β,γ) represent the three Euler angles, $D^l_{m'm}(\alpha,\beta,\gamma)$ is a Wigner D-function, which is a matrix element of the rotation operator, and $\odot$ indicates the original window (e.g., centered at the pole). Setting $R = (\alpha,\beta,\gamma)$ and $dR = d\alpha \, \sin\beta \, d\beta \, d\gamma$, we rewrite equation 2.22 as

$$\psi_{lm}(R) = \sum_{l_1 m_1 l_2 m_2} a^*_{l_1 m_1} w^*_{l_2 m_2}(R) \xi_{l_1 l_2 l} \begin{pmatrix} l_1 & l_2 & l \\ 0 & 0 & 0 \end{pmatrix} \begin{pmatrix} l_1 & l_2 & l \\ m_1 & m_2 & m \end{pmatrix} \tag{2.25}$$

and define the reconstruction as

$$A(\Omega) = \frac{1}{8\pi^2} \int_R \Psi(\Omega, R) \, dR, \tag{2.26}$$

or, using equation 2.6,

$$a_{lm} = \frac{1}{8\pi^2} \int_R \psi_{lm}(R) \, dR. \tag{2.27}$$

To show that this reconstruction algorithm is successful, we write equation 2.27 explicitly as

$$a_{lm} = \frac{1}{8\pi^2} \sum_{l_1 m_1 l_2 m_2 m'} \int_R a^*_{l_1 m_1} D^{l_2 *}_{m' m_2}(R) w^{\odot *}_{l_2 m'} \xi_{l_1 l_2 l} \begin{pmatrix} l_1 & l_2 & l \\ 0 & 0 & 0 \end{pmatrix} \begin{pmatrix} l_1 & l_2 & l \\ m_1 & m_2 & m \end{pmatrix} dR. \tag{2.28}$$

Noting that [*Varshalovich et al.*, 1988]

$$\int_R D^l_{m'm}(R)\,dR = \delta_{l0}\delta_{m0}\delta_{m'0}8\pi^2 \tag{2.29}$$

gives

$$a_{lm} = \sum_{l_1 m_1} a^*_{l_1 m_1} w^{\odot}_{00} \xi_{l_1 l} \begin{pmatrix} l_1 & 0 & l \\ 0 & 0 & 0 \end{pmatrix} \begin{pmatrix} l_1 & 0 & l \\ m_1 & 0 & m \end{pmatrix}. \tag{2.30}$$

Further noting that

$$\xi_{l_1 l} \begin{pmatrix} l_1 & 0 & l \\ 0 & 0 & 0 \end{pmatrix} \begin{pmatrix} l_1 & 0 & l \\ m_1 & 0 & m \end{pmatrix} = (-)^m \delta_{-m_1 m} \delta_{l_1 l} Y_{00}(\Omega), \tag{2.31}$$

gives

$$1 = w^{\odot}_{00} Y_{00}(\Omega), \tag{2.32}$$

which is true by inspection given the definition of w_{lm} and the requirement that $W(\Omega)$ have an average amplitude of one. For isotropic windows, i.e., windows that are axisymmetric in a given reference frame, we can eliminate the α rotation and the reconstruction formula can be simplified to

$$a_{lm} = \frac{1}{4\pi} \int_0^{2\pi} \int_0^{\pi} \psi_{lm}(\beta, \gamma)\, \sin\beta\, d\beta\, d\gamma \tag{2.33}$$

or

$$a_{lm} = \frac{1}{4\pi} \int_{\Omega} \psi_{lm}(\Omega)\, d\Omega. \tag{2.34}$$

Here we have used the identities [*Varshalovich et al.*, 1988],

$$w_{lm}(\Omega) = D^l_{0m}(\Omega) w^{\odot}_{l0}(\Omega), \tag{2.35}$$

$$D^l_{0m}(\alpha, \beta, \gamma) = \sqrt{\frac{4\pi}{2l+1}} Y_{l-m}(\beta, \gamma) \tag{2.36}$$

for any α, and

$$\int_{\Omega} Y_{lm}(\Omega)\, d\Omega = \sqrt{4\pi}\delta_{l0}\delta_{m0}. \tag{2.37}$$

2.4 The Covariance Function

To develop an expression for the localized linear transfer function or correlation between two fields we need to derive a localized cross-covariance function. We follow the formalism of *Kaula* [1966, 1967] in which a spherical cap window was used. Here we consider the case of an arbitrary window.

We introduce a second field $B(\Omega)$ with its corresponding localized field $\Gamma(\Omega)$. Adopting a reference frame centered at Ω and using Δ and τ to represent, respectively, colatitude and longitude in this reference frame, we define the cross-covariance $K(\Delta)$ as

$$K(\Delta) = \int_{\Omega} A(\Omega) \frac{1}{2\pi} \int_0^{2\pi} B(\Delta, \tau)\, d\tau\, d\Omega, \tag{2.38}$$

where the integration over τ accounts for all points a fixed distance, Δ, away from a given point $A(\Omega)$. We write equation 2.38 as a degree variance, $\sigma^2_{AB}(l)$, by expanding $K(\Delta)$ in terms of Legendre polynomials, P_l, giving

$$\sigma^2_{AB}(l) = \frac{2l+1}{2} \int_0^{\pi} P_l(\cos\Delta) K(\Delta)\, \sin\Delta\, d\Delta, \tag{2.39}$$

where $P_l = P_{l0}$. Rewriting this explicitly gives

$$\sigma^2_{AB}(l) = \frac{2l+1}{2} \int_0^{\pi} P_l(\cos\Delta) \int_{\Omega} A(\Omega) \frac{1}{2\pi} \int_0^{2\pi} B(\Delta, \tau)\, d\tau\, d\Omega\, \sin\Delta\, d\Delta. \tag{2.40}$$

Using the spherical harmonic addition theorem,

$$P_l(\cos\Delta) = \frac{4\pi}{2l+1} \sum_m Y^*_{lm}(\Omega) Y_{lm}(\Omega') \tag{2.41}$$

and setting $\Omega' = (\Delta, \tau)$ and $d\Omega' = d\tau \, \sin\Delta \, d\Delta$, we write equation 2.40 as

$$\sigma^2_{AB}(l) = \sum_m \int_{\Omega'} \int_{\Omega} A(\Omega) B^*(\Omega') Y^*_{lm}(\Omega) Y_{lm}(\Omega') \, d\Omega \, d\Omega'. \tag{2.42}$$

Replacing $A(\Omega)$ and $B(\Omega)$ with their harmonic representations using equation 2.1, we arrive at the familiar form for the globally averaged degree variance,

$$\sigma^2_{AB}(l) = \sum_m a_{lm} b^*_{lm}. \tag{2.43}$$

However, as found by *Kaula* [1966], replacing $A(\Omega)$ and $B(\Omega)$ with their windowed counterparts, $\Psi(\Omega)$ and $\Gamma(\Omega)$, results in

$$\sigma^2_{\Psi\Gamma}(l) = \sum_m \int_{\Omega'} \int_{\Omega} W(\Omega) A(\Omega) Y^*_{lm}(\Omega) W(\Omega') B^*(\Omega') Y_{lm}(\Omega') \, d\Omega \, d\Omega'. \tag{2.44}$$

Rearranging, gives

$$\sigma^2_{\Psi\Gamma}(l) = \sum_m \left(\int_{\Omega} W(\Omega) A(\Omega) Y^*_{lm}(\Omega) \, d\Omega \right) \left(\int_{\Omega'} W(\Omega') B^*(\Omega') Y_{lm}(\Omega') \, d\Omega' \right), \tag{2.45}$$

which combined with our definition of the localized field from equation 2.9, simplifies to

$$\sigma^2_{\Psi\Gamma}(l) = \sum_m \psi_{lm} \gamma^*_{lm}. \tag{2.46}$$

For computational purposes (speed, storage, and numerical accuracy) we note that equation 2.46 can be written as

$$\sigma^2_{\Psi\Gamma}(l) = \psi_{l0}\gamma_{l0} + 2 \sum_{m>0} \left[\Re(\psi_{lm}) \Re(\gamma_{lm}) + \Im(\psi_{lm}) \Im(\gamma_{lm}) \right], \tag{2.47}$$

where $\Re$ and $\Im$ are, respectively, the real and imaginary parts of their arguments.

We have shown how to calculate the localized covariance for two windowed fields.

With a simple rotation, this method can be used to determine the localized covariance, $\sigma^2_{\Psi\Gamma}(\Omega, l)$, as a function of l for any point on the sphere. Below, we consider the spherical harmonic expansion of the localized covariance, $\sigma^2_{l'm'}(l)$, which produces a compact representation of the covariance fields in the form of a set of harmonic coefficients for localization at each l. Unlike the global periodogram estimate of the covariance, $\sigma^2_{00}(l)/\sqrt{4\pi}$ represents an estimate of the globally averaged covariance that is less spatially biased to regions of locally high variance. This spatial bias has been previously noted in admittance/coherence studies of regions encompassing several geologic terranes [*Forsyth*, 1985]. While less spatially biased, the average wavelet spectrum is spectrally biased, relative to the periodogram estimate, by the aforementioned convolution operations intrinsic to the transform.

We write the covariance as

$$\sigma^2_{\Psi\Gamma}(\Omega, l) = \sum_m \psi_{lm}(\Omega)\gamma^*_{lm}(\Omega) \tag{2.48}$$

or in terms of spherical harmonic coefficients

$$\sigma^2_{l'm'}(l) = \sum_m \int_\Omega \psi_{lm}(\Omega)\gamma^*_{lm}(\Omega)Y^*_{l'm'}(\Omega)\, d\Omega. \tag{2.49}$$

More explicitly, we write

$$\begin{aligned} \sigma^2_{l'm'}(l) \;=\; & \sum_{ml_{1\ldots4}m_{1\ldots4}} a^*_{l_1m_1} b_{l_3m_3} \xi_{l_1l_2l}\xi_{l_3l_4l} \left(\int_\Omega w^*_{l_2m_2}(\Omega, l) w_{l_4m_4}(\Omega, l) Y^*_{l'm'}(\Omega)\, d\Omega\right) \\ & \begin{pmatrix} l_1 & l_2 & l \\ 0 & 0 & 0 \end{pmatrix} \begin{pmatrix} l_1 & l_2 & l \\ m_1 & m_2 & m \end{pmatrix} \begin{pmatrix} l_3 & l_4 & l \\ 0 & 0 & 0 \end{pmatrix} \begin{pmatrix} l_3 & l_4 & l \\ m_3 & m_4 & m \end{pmatrix}. \end{aligned} \tag{2.50}$$

For the isotropic window assumed here,

$$\int_\Omega w^*_{l_2m_2}(\Omega, l) w_{l_4m_4}(\Omega, l) Y^*_{l'm'}(\Omega)\, d\Omega = w^{\odot}_{l_20}(l) w^{\odot}_{l_40}(l) \int_\Omega D^{l_2*}_{0m_2}(\Omega) D^{l_4}_{0m_4}(\Omega) Y^*_{l'm'}(\Omega)\, d\Omega, \tag{2.51}$$

where

$$\int_{\Omega} D^{l_2 *}_{0 m_2}(\Omega) D^{l_4}_{0 m_4}(\Omega) Y^{*}_{l' m'}(\Omega)\, d\Omega = (-)^{m_4} 4\pi \xi_{l'} \begin{pmatrix} l_2 & l_4 & l' \\ 0 & 0 & 0 \end{pmatrix} \begin{pmatrix} l_2 & l_4 & l' \\ -m_2 & m_4 & m' \end{pmatrix}. \tag{2.52}$$

Noting that,

$$4\pi \xi_{l_1 l_2 l} \xi_{l_3 l_4 l} \xi_{l'} = (2l+1) \xi_{l_1 l_2 l_3 l_4 l'}, \tag{2.53}$$

we rewrite equation (2.50) as

$$\begin{aligned} \sigma^2_{l'm'}(l) = {} & (2l+1) \sum_{m l_{1\ldots4} m_{1\ldots4}} (-)^{m_4} a^{*}_{l_1 m_1} b_{l_3 m_3} w^{\odot}_{l_2 0}(l) w^{\odot}_{l_4 0}(l) \xi_{l_1 l_2 l_3 l_4 l'} \\ & \begin{pmatrix} l_1 & l_2 & l \\ 0 & 0 & 0 \end{pmatrix} \begin{pmatrix} l_3 & l_4 & l \\ 0 & 0 & 0 \end{pmatrix} \begin{pmatrix} l_2 & l_4 & l' \\ 0 & 0 & 0 \end{pmatrix} \\ & \begin{pmatrix} l_1 & l_2 & l \\ m_1 & m_2 & m \end{pmatrix} \begin{pmatrix} l_3 & l_4 & l \\ m_3 & m_4 & m \end{pmatrix} \begin{pmatrix} l_2 & l_4 & l' \\ -m_2 & m_4 & m' \end{pmatrix}. \end{aligned} \tag{2.54}$$

As was seen with the windowed field estimate, the covariance estimate at degree l is sensitive to data with degree less than $l + L_{win}$ (equal to $1.5l$ when using $f_s = 2$). Similarly, from the third 3-j coefficient in equation 2.54, we find that the covariance expansion at degree l has a maximum degree of $2L_{win}$ (equal to l when using $f_s = 2$), providing a measure of the minimum length scale over which the covariance function will vary. Note that this scale is a function only of the maximum degree of the window expansion. If the window were a constant over the whole sphere, then it would have only the single $l' = 0$, $m' = 0$ term, and as expected, the covariance would not vary over the sphere.

The above derivation is useful for understanding the structure of the covariance estimates. However, in practice we use the definition of the localized field from equation 2.47 to calculate the localized coefficients for a given geographic location and use these coefficients to calculate the covariances at that point. This procedure is repeated for the set of desired points (e.g., over a grid, a great circle, ...). While still too slow for our purposes, we show for completeness in Appendix A the most computationally efficient method that we have found for direct calculation of the covariance coefficients.

2.5 Localized Transfer Function Estimation

The linear transfer function estimation problem can be written as

$$B(\Omega) = \int_{\Omega'} F(\Omega, \Omega') A(\Omega')\, d\Omega', \tag{2.55}$$

where we want to estimate F. Classically, F is restricted to be isotropic, i.e., it depends on Δ, the separation distance between Ω and Ω', and further, A and B are assumed to be stationary, so that F is independent of position. These assumptions result in

$$B(\Omega) = \int_{\Omega'} F(\Delta) A(\Omega')\, d\Omega'. \tag{2.56}$$

In contrast, here we permit $F(\Delta)$ to vary spatially using the representations of A and B localized at Ω_0 and assume the relationship

$$\Gamma(\Omega_0, \Omega) = \int_{\Omega'} F(\Omega_0, \Delta) \Psi(\Omega_0, \Omega')\, d\Omega'. \tag{2.57}$$

Using equation 2.46, we define, respectively, the rms amplitude of Ψ, and the correlation, transfer function (admittance), and error on the admittance between Ψ and Γ as

$$S_l(\Omega) = \sqrt{\frac{\sigma^2_{\Psi\Psi}(\Omega)}{2l+1}}, \tag{2.58}$$

$$r_l(\Omega) = \frac{\sigma^2_{\Psi\Gamma}(\Omega)}{\sqrt{\sigma^2_{\Psi\Psi}(\Omega)\sigma^2_{\Gamma\Gamma}(\Omega)}}, \tag{2.59}$$

$$F_l(\Omega) = \frac{\sigma^2_{\Psi\Gamma}(\Omega)}{\sigma^2_{\Psi\Psi}(\Omega)}, \tag{2.60}$$

and

$$\sigma^2_{F_l}(\Omega) = \left(\frac{\sigma^2_{\Gamma\Gamma}(\Omega)}{\sigma^2_{\Psi\Psi}(\Omega)}\right)\left(\frac{1 - r^2_l(\Omega)}{2l}\right). \tag{2.61}$$

In subsequent sections, we make use of these localized estimates, the global average of the local estimates, indicated by an overbar (e.g., $\overline{S_l}$), and the unlocalized estimates, indicated by a hat (e.g., $\hat{S}_l$).

2.6 Window Design

We use a window that is generically defined to be smooth and to scale with wavelength. Here we consider only isotropic windows (i.e., that depend only on θ) centered at the pole ($\theta = 0$). This restriction can be generalized to other locations by a simple rotation of the coordinate system.

Noting that pole-centered isotropic windows only have $m_2 = 0$ terms and using identity 2.18, we find that $m_1 = m$, and equation 2.22 becomes

$$\psi_{lm} = (-)^m \sum_{l_1 l_2} a_{l_1 m} w_{l_2 0} \xi_{l_1 l_2 l} \begin{pmatrix} l_1 & l_2 & l \\ 0 & 0 & 0 \end{pmatrix} \begin{pmatrix} l_1 & l_2 & l \\ m & 0 & -m \end{pmatrix}. \tag{2.62}$$

We use equations 2.47 and 2.62 under the restrictions that

$$\begin{aligned} l &= 0, 1, \ldots L_{nyq} && (2.63) \\ m &= 0, 1, \ldots l && (2.64) \\ l_1 &= \max(m, |l - L_{win}|), \ldots \min(L_{obs}, l + L_{win}) && (2.65) \\ l_2 &= |l - l_1|, |l - l_1| + 1, \ldots \min(l + l_1, L_{win}), && (2.66) \end{aligned}$$

where we have assumed $L_{win} < l$, as will be shown later is neccessary for other reasons.

We desire a window that minimizes L_{win}, the maximum degree needed for accurate representation of the window. This reduces potential spectral bias problems incurred from the repeated convolutions instrinsic to the wavelet transform. Furthermore, the gravity data sets considered here impose severe Nyquist restrictions, which are ameliorated by using the most spectrally compact or spatially smooth window possible. In addition, from a practical perspective, minimizing L_{win} reduces computation time significantly.

We use a scalable window based on a spherical cap, defined as

$$W(\theta, l) = \begin{cases} 1, & \text{for} \quad \theta \leq \theta_c \\ 0, & \text{for} \quad \theta > \theta_c \end{cases}, \tag{2.67}$$

where $0 \leq \theta \leq \pi$, $\theta_c = \pi / \sqrt{l_s(l_s + 1)}$, and $l_s = l / f_s$, where the scaling parameter, $f_s \geq 1$, is the number of wavelengths (corresponding to l) that fit in the window. The spherical analogue to a Cartesian boxcar, a cap has many well known disadvantages. However, the window we use has only the first L_{win} coefficents of the harmonic expansion of the cap window, where L_{win} is the next integer greater than or equal to l_s. At l equal to the Nyquist degree, L_{nyq}, $L_{win} \simeq L_{nyq} / f_s$, and using equation 2.23 we find

$$L_{nyq} \simeq \frac{f_s}{f_s + 1} L_{obs}. \tag{2.68}$$

In addition to the issue of the local Nyquist degree, we have the constraint that our basis function should have zero-mean, i.e.,

$$\int_\Omega X_{lm}(\Omega)\, d\Omega = 0, \tag{2.69}$$

or more explicitly for a pole-centered window,

$$\int_\Omega \sum_{l_2=0}^{L_{win}} w_{l_2 0} Y_{l_2 0}(\Omega) Y_{lm}(\Omega)\, d\Omega = 0. \tag{2.70}$$

To satisfy this relation, it is sufficient (and possibly more restrictive than necessary) to require $w_{l_2=l,0} = 0$. We accomplish this by imposing $l_s < l$. From equation 2.68 we find that for $L_{obs} = 70$ and $f_s = 1$, $L_{nyq} = 35$; and for $L_{obs} = 90$ and $f_s = 2$, $L_{nyq} = 60$. Obviously, $f_s = 1$ provides optimum spatial resolution. However, when analyzing real data with noise, it is desirable to minimize potential bias by using $f > 1$, thereby localizing at length scales longer than the wavelength under consideration.

Examples of the windows and their spectra are shown in figure 2.1. In addition, examples of $W(\theta, L_{win})$, Y_{lm}, and X_{lm}, are shown for $l = 12$ and $f_s = 1$ and 4 in figures 2.2 and 2.3, respectively. We note that the spectrum of a spherical cap has multiple side lobes (for example, see 2.4). Our windows incorporate only coefficients within the first central lobe. As the windows get tighter spatially, the central lobe gets wider spectrally, and in the limit of a delta function, will gives flat spectrum, i.e., perfect spatial resolution with no spectral resolution. From figure 2.2 we see that a subset of the $X_{lm}(\Omega)$'s are nearly zero-valued. This behavior arises because our windows are pole-centered, and for a given l, $Y_{lm}(\Omega)$ has decreasing power near the pole with increasing m. We use this fact to reduce computation by modifying equation 2.64 to

$$m = 0, 1, \ldots M_{max}, \tag{2.71}$$

where we have neglected all $X_{lm}(\Omega)$'s with maximum RMS amplitude relative to the maximum RMS amplitude of $X_{l0}(\Omega)$ less than a specified threshold, here chosen to be 0.01. An increase in f_s will result in an increase in M_{max}.

The harmonic expansion of the windows are derived in the standard fashion, where

$$w_{l_2 0}(L_{win}) = \int_\Omega W(\theta, L_{win}) Y^*_{l_2 0}(\Omega)\, d\Omega. \tag{2.72}$$

Since $Y_{l0}(\Omega)$ terms do not depend on ϕ, we rewrite this explicitly in terms of Legendre

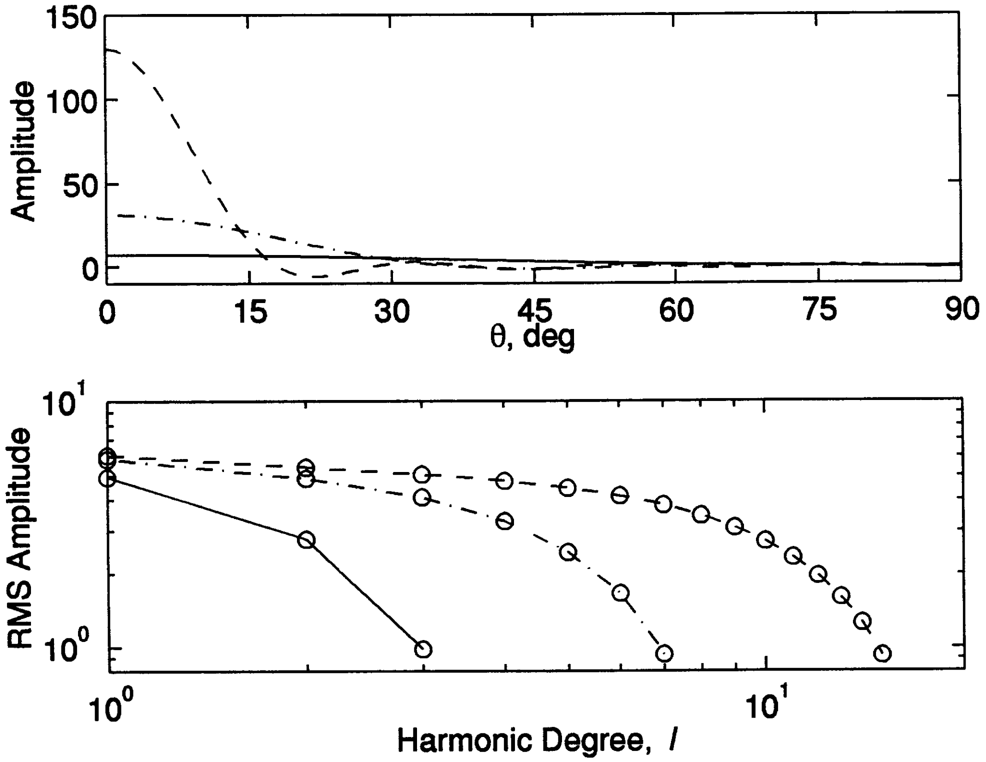

Figure 2.1: The spatial (top) and spectral (bottom) representation of $W(\theta, L_{win})$ for $L_{win} = 4, 8$, and 16 are shown by the solid, dash-dot, and dashed lines respectively.

polynomials as

$$w_{l_2 0}(L_{win}) = \sqrt{(2l_2+1)\pi}\int_0^{\pi} W(\theta, L_{win}) P_{l_2}(\cos\theta)\sin\theta\, d\theta. \tag{2.73}$$

For an aribitrary window, equation 2.73 is solved by numerical integration. However, using the identity

$$\int_{\theta_1}^{\theta_2} P_l(\cos\theta)\sin\theta\, d\theta = \left.\frac{P_{l-1}(\cos\theta) - P_{l+1}(\cos\theta)}{2l+1}\right|_{\theta_1}^{\theta_2}, \tag{2.74}$$

the coefficients for a cap with unit-amplitude can be calculated analytically, where

$$w_{00}^{c}(L_{win}) = \sqrt{\pi}(P_0(\cos\theta_c) - P_1(\cos\theta_c)) \tag{2.75}$$

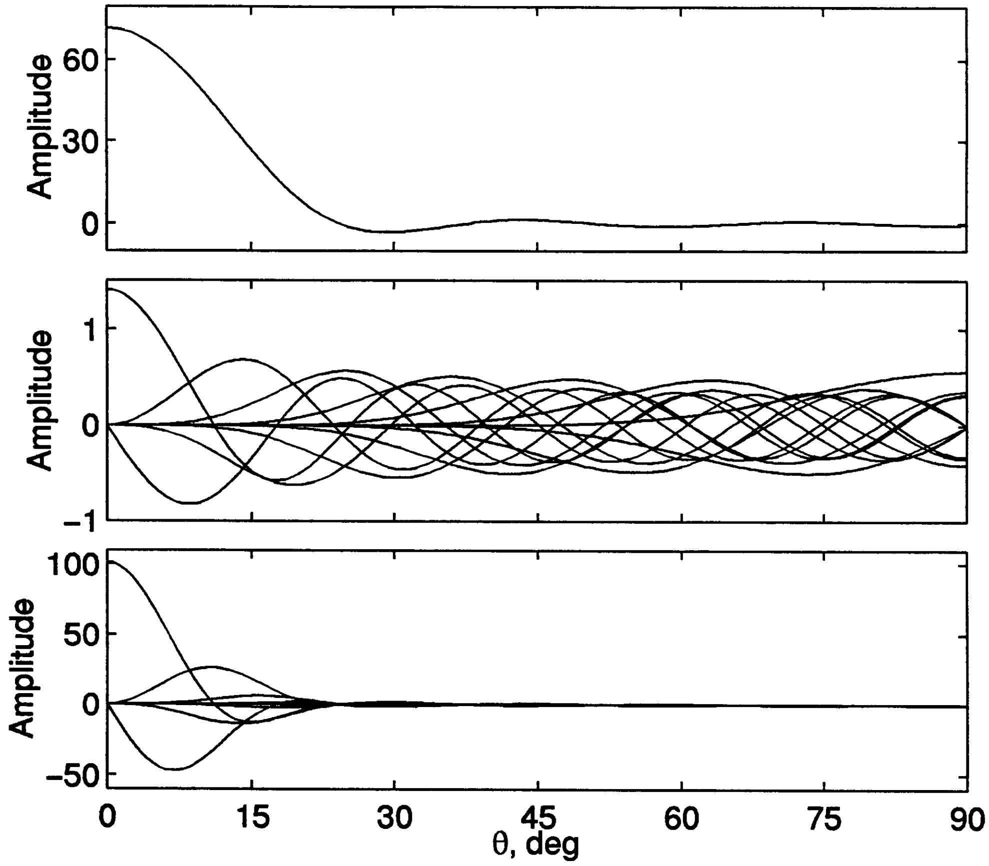

Figure 2.2: $W(\theta, L_{win})$ (top), pole-to-pole profiles of $Y_{lm}(\theta, 0)$ (middle) and $X_{lm}(\theta, 0)$ (bottom), for $l = 12$, $f_s = 1$, and $L_{win} = 11$.

and

$$w^c_{l_2 0}(L_{win}) = \sqrt{\frac{\pi}{2l_2 + 1}}(P_{l_2-1}(\cos\theta_c) - P_{l_2+1}(\cos\theta_c)). \tag{2.76}$$

In order to have a mean amplitude of one, w_{00} must equal $\sqrt{4\pi}$, and the remaining window coefficients are rescaled accordingly. We write the complete expression for the window coefficients as

$$w_{00}(L_{win}) = \sqrt{4\pi} \tag{2.77}$$

and

$$w_{l_2 0}(L_{win}) = \sqrt{\frac{4\pi}{2l_2 + 1}} \frac{P_{l_2-1}(\cos\theta_c) - P_{l_2+1}(\cos\theta_c))}{P_0(\cos\theta_c) - P_1(\cos\theta_c)}. \tag{2.78}$$

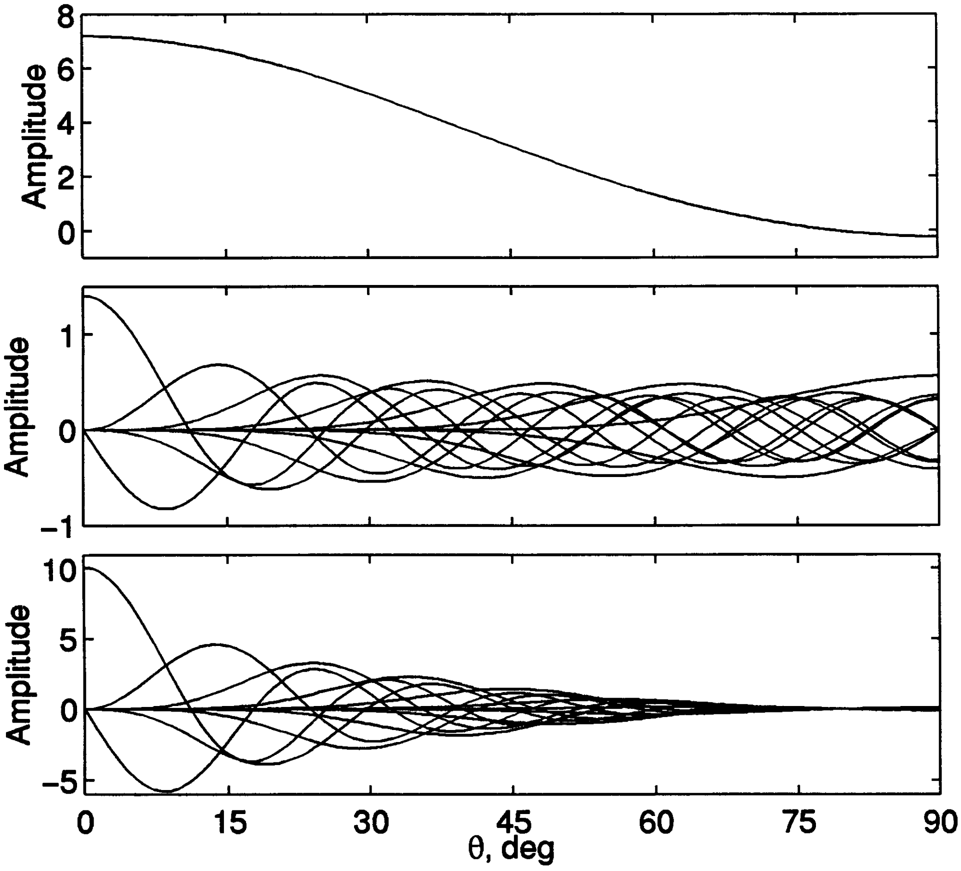

Figure 2.3: $W(\theta, L_{win})$ (top), pole-to-pole profiles of $Y_{lm}(\theta, 0)$ (middle) and $X_{lm}(\theta, 0)$ (bottom), for $l = 12$, $f_s = 4$, and $L_{win} = 3$.

As is evident from figure 2.1, these windows have sidelobes in the spatial domain with amplitudes less than 5 percent of the peak amplitude. Windows with better statistical properties surely exist, but the windows we have chosen satisfy our requirements of spectral compactness (crucial for maximizing L_{nyq}) and provide a simple tradeoff between spectral and spatial resolution.

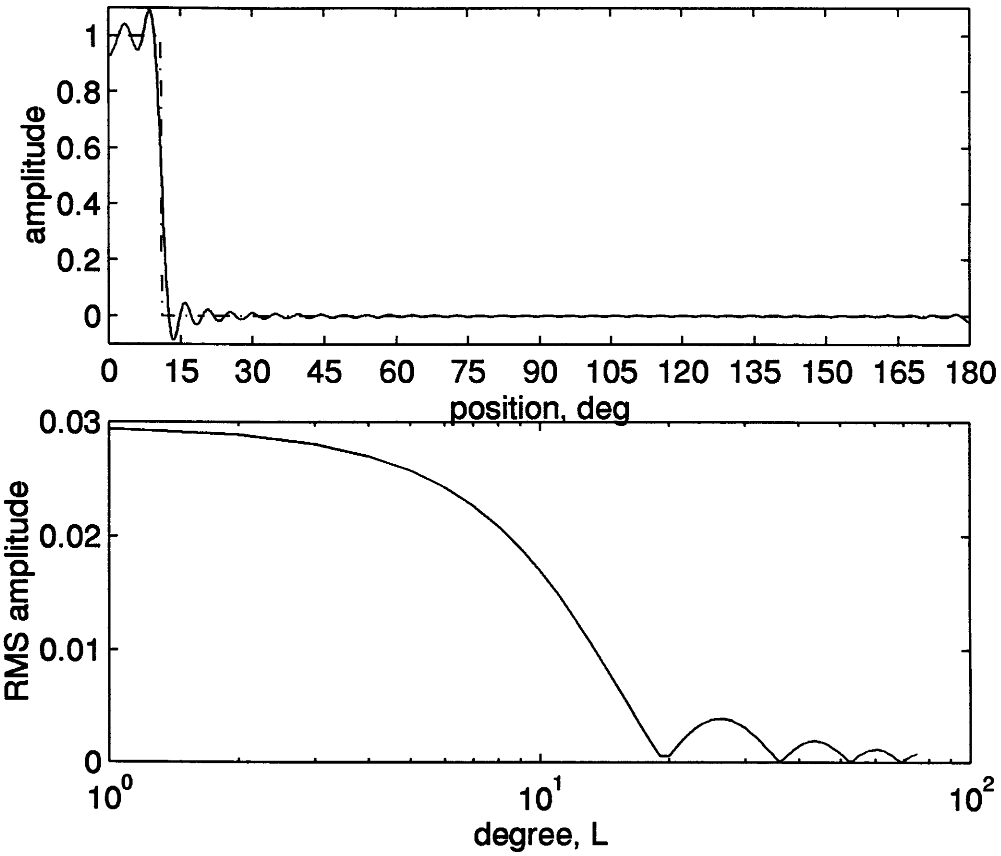

Figure 2.4: Longitudinal profile of a spherical cap (top with dash-dot line), the harmonic expansion of this function to $l = 75$ (top with solid line), and the RMS spectrum (bottom).

2.7 A Pictorial Dictionary

We show and discuss here results from application of our spherical localization technique to a variety of example fields. We first consider fields representing very localized structure such as spherical caps and equatorial annuli. We then consider fields consisting of a pure spherical harmonic. In each case, we highlight the tradeoff between spectral and spatial resolution, parameterized here by f_s.

At the top of figure 2.4, we show a pole-to-pole profile of a spherical cap with angular extent equivalent to the distance to the position of the first zero-crossing of $P_{12,0}(\cos\theta)$. A pole-to-pole profile of the spatial rendition of the degree 75 expansion of this field

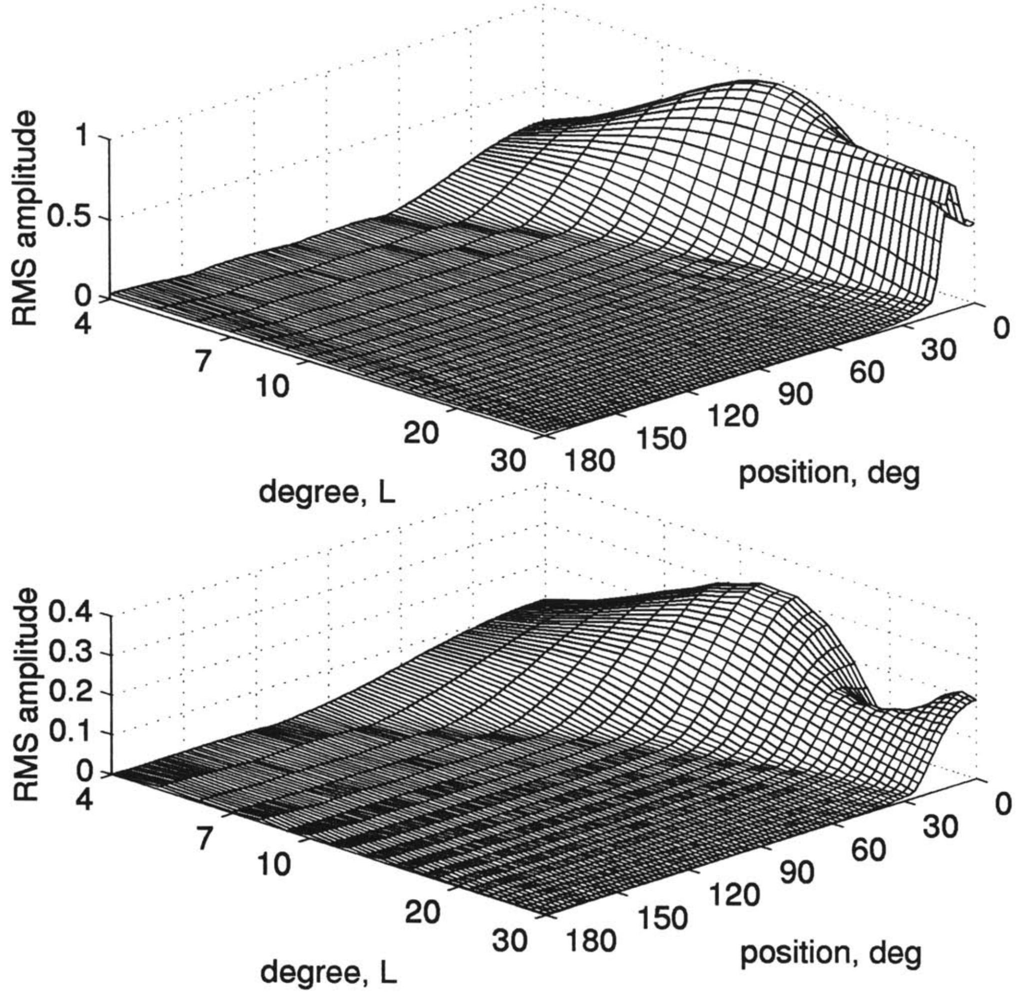

Figure 2.5: $S_l(\theta, 0)$ for the function shown in figure 2.4 using $f_s = 1$ (top) and $f_s = 2$ (bottom).

is also shown. The oscillations are Gibbs phenomena. The corresponding multi-lobed spectrum is shown at the bottom of figure 2.4. Since the field is axisymmetric, we need only consider the spectrogram on a pole-to-pole profile. This result is shown for $f_s = 1$ and $f_s = 2$ at the top and bottom, respectively, of figure 2.5. With $f_s = 1$ we have high spatial resolution, with the region of non-zero RMS amplitude more restricted to the region near the pole than with $f_s = 2$. However, while the spectral peak at $l = 12$ is clear in both spectrograms, it is more pronounced with $f_s = 2$. Futhermore, with

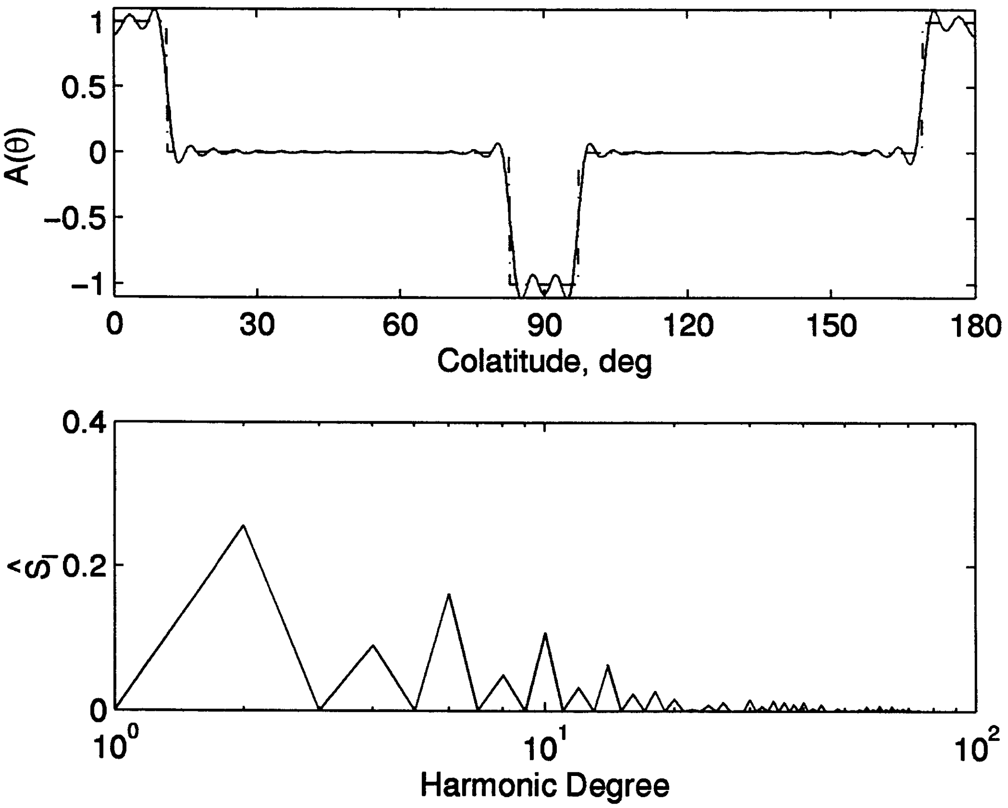

Figure 2.6: Longitudinal profile of a function composed of two spherical caps and an equatorial sheet (top with dash-dot line), the harmonic expansion of this function to $l = 75$ (top with solid line), and the RMS spectrum (bottom).

$f_s = 2$ we are able to resolve the second spectral lobe. It is worth noting that at high degree, with $f_s = 1$, we isolate the edges of the cap. Essentially, the spatial localization is sufficiently high, that when centered over the cap, we detect little variation in the signal.

Similar behavior is seen when we consider a field constructed with a spherical cap at each pole plus an equatorial annulus (figure 2.6). The size of each cap is the same as in figure 2.4, and the annulus has a width equivalent to the distance between the two zero-crossings of $P_{12,0}(\cos\theta)$ nearest to the equator. As is evident from figure 2.6, this function is even when considered globally, i.e., all the odd harmonics have zero amplitude. The spectrograms for this function, shown in figure 2.7, show the same

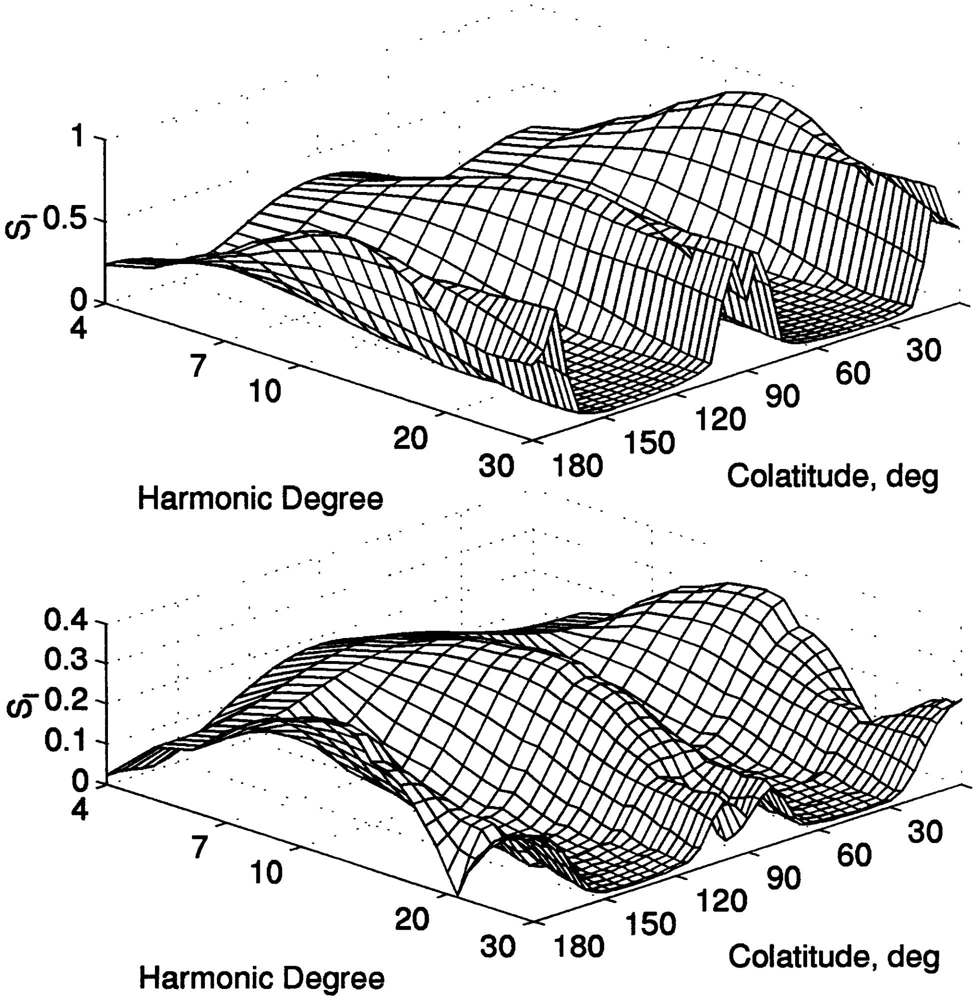

Figure 2.7: RMS amplitude, $S_l(\theta, 0)$, for the function shown in figure 2.6 using $f_s = 1$ (top) and $f_s = 2$ (bottom).

tradeoff between spatial and spectral resolution that we saw before. We also find that at middle and high degrees, the annuli and the cap have the same RMS amplitude, and that at length scales less than the separation distance between the caps the spectra near each are nearly identical to the spectra for the single cap.

We use the above example to demonstrate the effect of exceeding the Nyquist constraint from equation 2.23. At the top of figure 2.8 we show the spectrogram for the same field as in figure 2.6 but we have included coefficients only up to and including

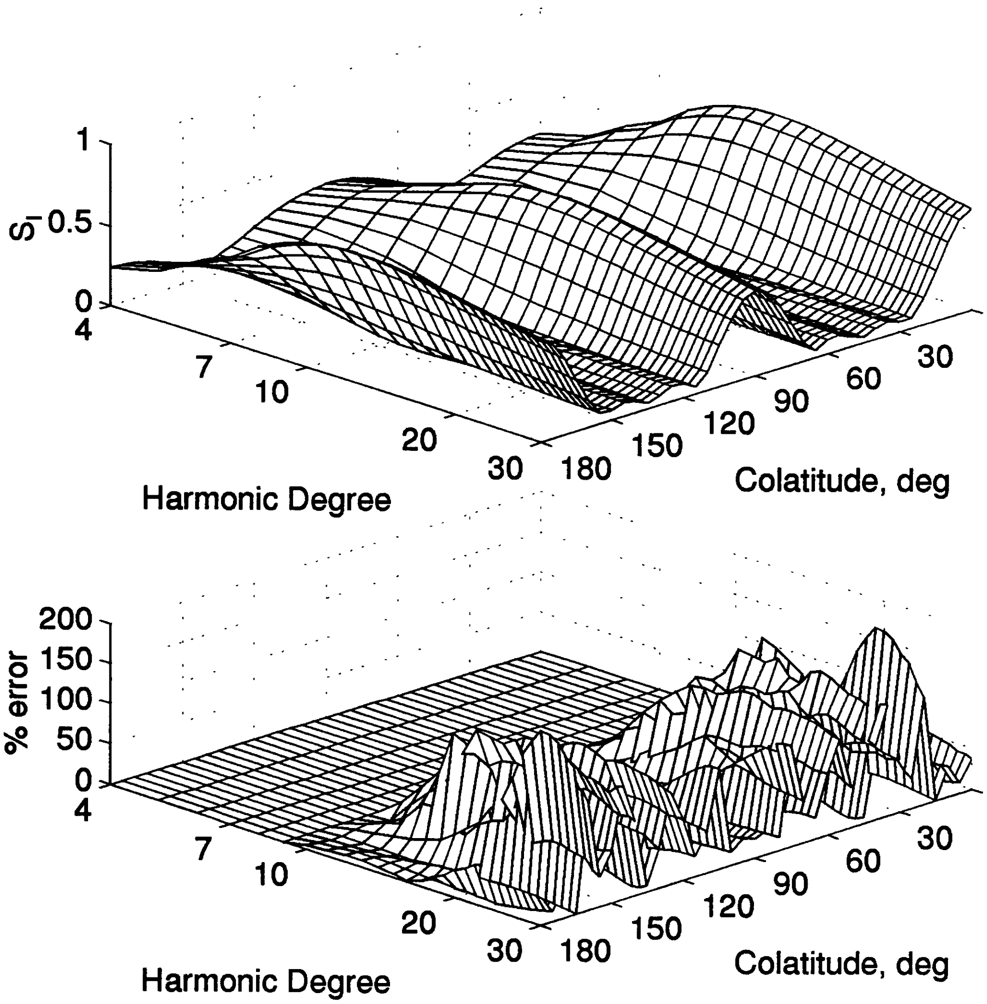

Figure 2.8: RMS amplitude, $S_l(\theta, 0)$, using $f_s = 1$ for the function shown in figure 2.6 with the input truncated at $l = 16$ (top) and the percent error of the RMS amplitude relative to the $L_{max} = 75$ expansion shown in figure 2.7 (bottom).

$l = 16$, which corresponds to $L_{nyq} = 8$ for $f_s = 1$. At the bottom of figure 2.8 the percent error relative to the $L_{max} = 75$ expansion (with $L_{nyq} = 35$) is shown. We see that the error rapidly increases when we exceed $l = 8$, but is zero-valued for $l \leq 8$.

As a final set of examples, we consider three purely harmonic fields. We consider different orders, m, of the harmonic corresponding to $l = 12$. We show the results of localizing purely zonal (figure 2.9), tesseral (figure 2.10), and sectoral (figure 2.10) harmonics. Results are shown for f_s ranging from 1 to 4. With tight spatial localization

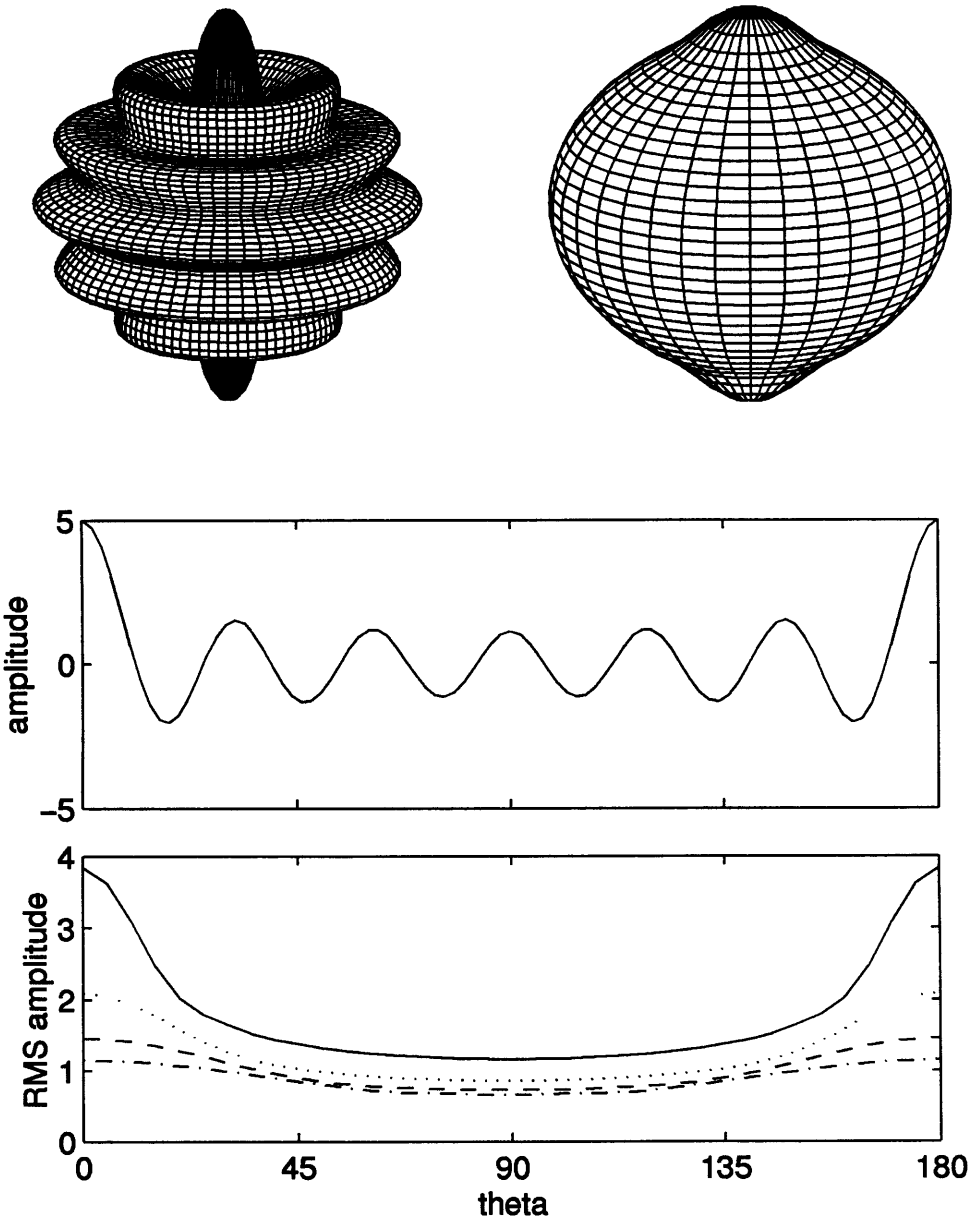

Figure 2.9: The original function $(4\pi)^{-2}Y_{12,0}(\Omega)$ (top left), the corresponding $S_{12}(\Omega)$ with $f_s = 1$ (top right), the pole-to-pole profile $(4\pi)^{-2}Y_{12,0}(\theta, 0)$ (middle), and the corresponding $S_{12}(\theta, 0)$ (bottom) with $f_s = 1$ to 4 shown by the solid, dotted, dashed, and dash-dot lines, respectively.

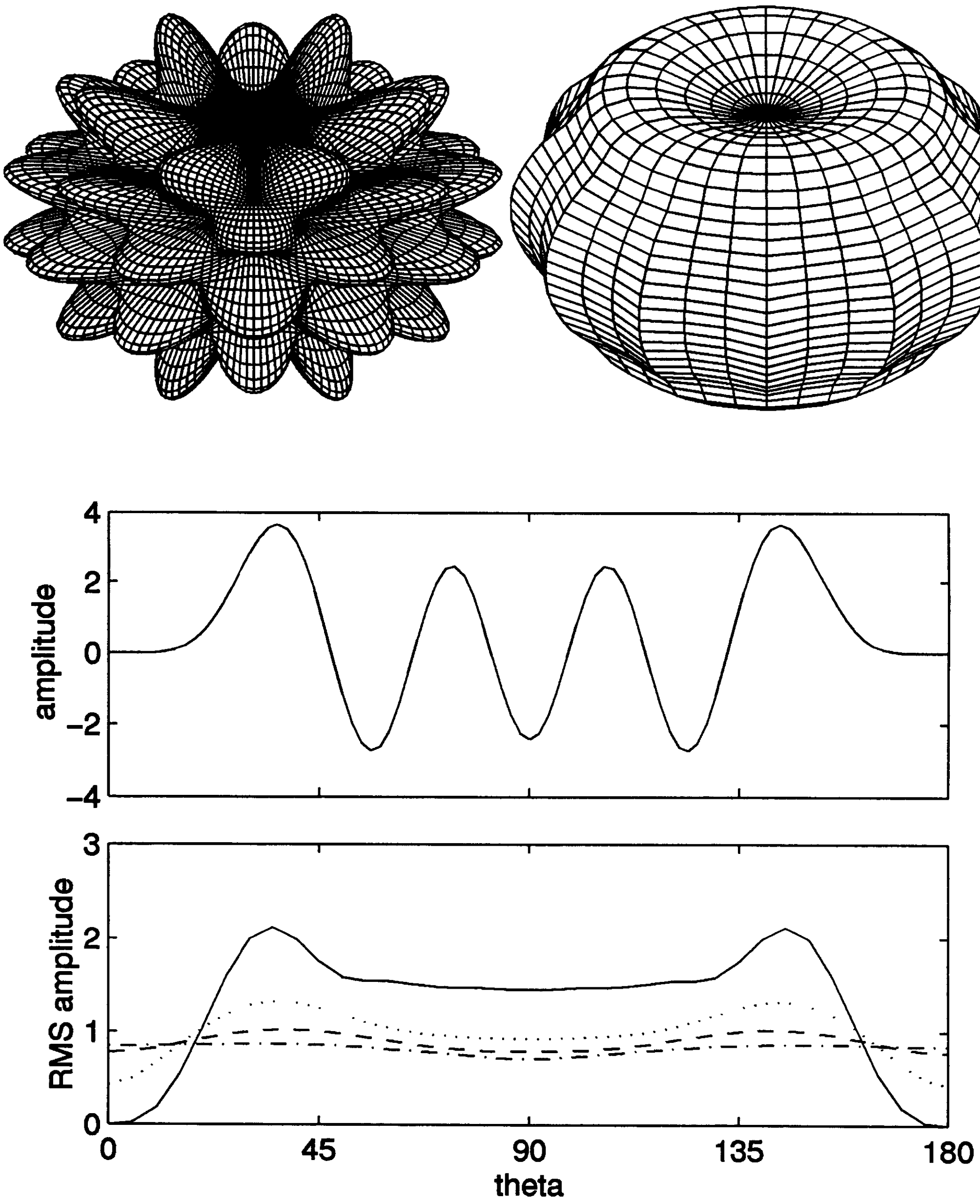

Figure 2.10: The original function $(2\pi)^{-2}[Y_{12,6}(\Omega)+Y_{12,-6}(\Omega)]$ (top left), the corresponding $S_{12}(\Omega)$ with $f_s = 1$ (top right), the pole-to-pole profile $(2\pi)^{-2}[Y_{12,6}(\theta,0)+Y_{12,-6}(\theta,0)]$ (middle), and the corresponding $S_{12}(\theta,0)$ (bottom) with $f_s = 1$ to 4 shown by the solid, dotted, dashed, and dash-dot lines, respectively.

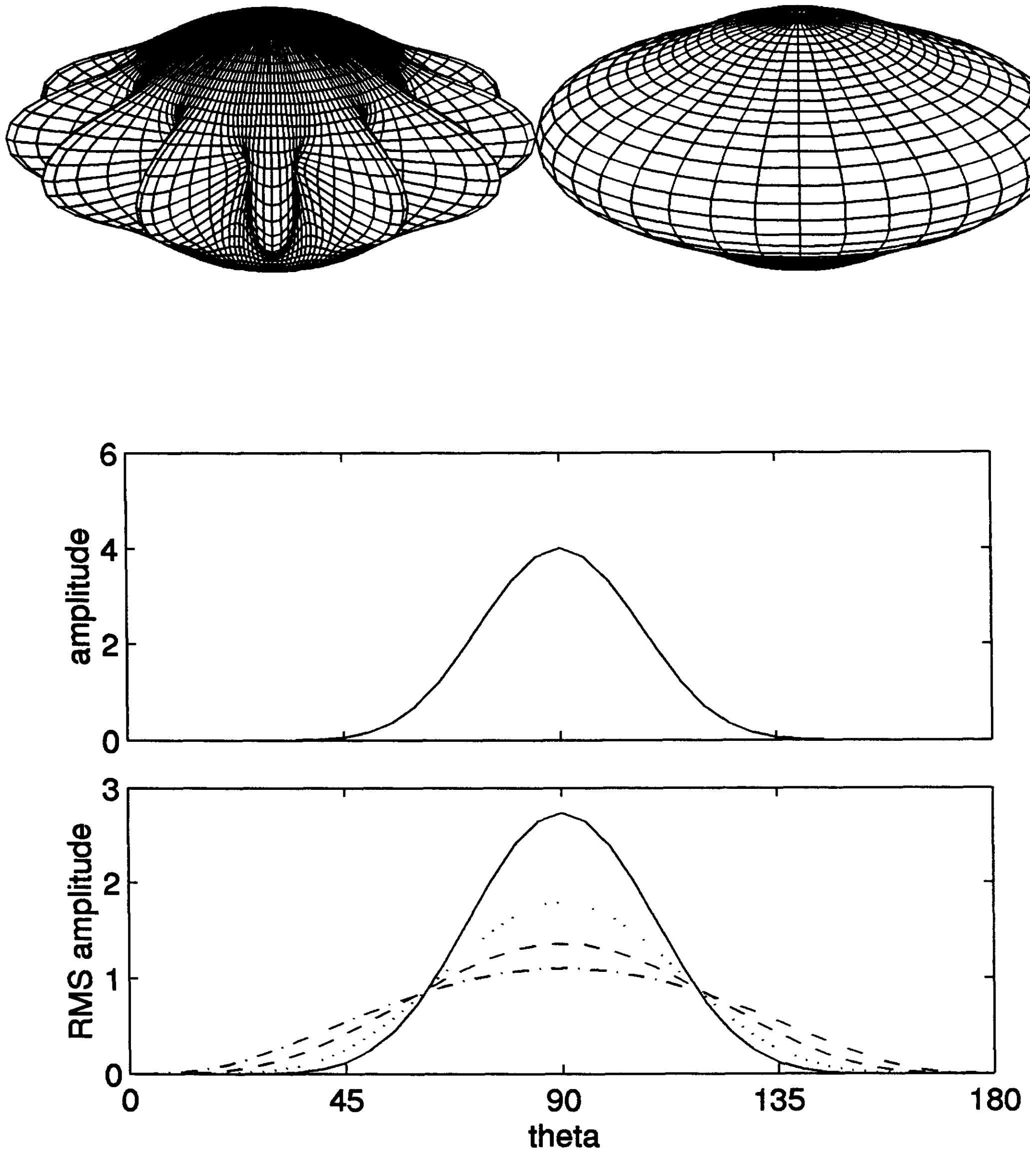

Figure 2.11: The original function $(2\pi)^{-2}[Y_{12,12}(\Omega) + Y_{12,-12}(\Omega)]$ (top left), the corresponding $S_{12}(\Omega)$ with $f_s = 1$ (top right), the pole-to-pole profile $(2\pi)^{-2}[Y_{12,12}(\theta,0) + Y_{12,-12}(\theta,0)]$ (middle), and the corresponding $S_{12}(\theta,0)$ (bottom) with $f_s = 1$ to 4 shown by the solid, dotted, dashed, and dash-dot lines, respectively.

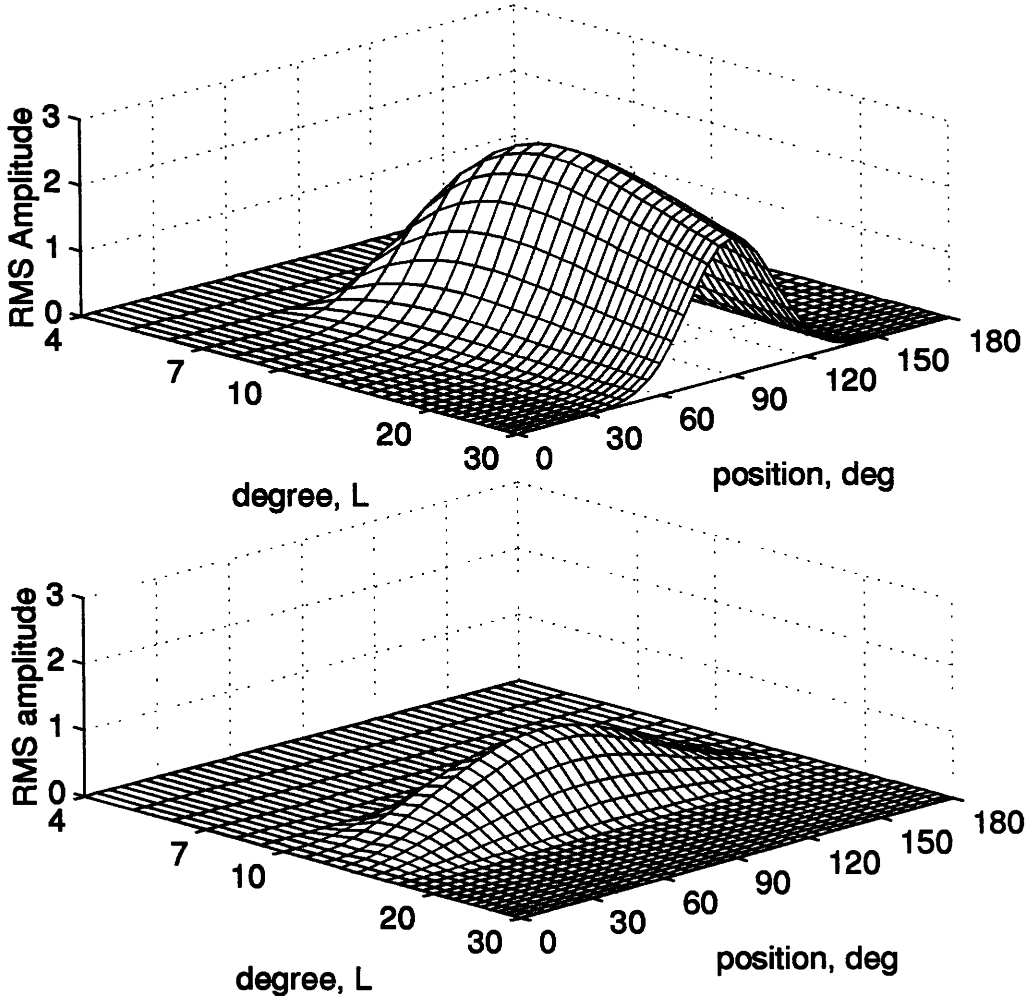

Figure 2.12: $S_l(\theta, 0)$ for the function shown in figure 2.11 using $f_s = 1$ (top) and $f_s = 2$ (bottom).

($f_s = 1$), we are very sensitive to the local structure, as is apparent with the high amplitudes of S_{12} at the pole in figure 2.9. As m increases, the power of each harmonic concentrates at the equator, and $S_l = 0$ at the poles. As expected, increasing f_s results in less spatial resolution, reaching the limiting case of perfect spectral resolution and no spatial resolution. We show the entire spectrogam for the sectoral input field using $f_s = 1$ and 2 in figure 2.12. The tradeoff between the spatial and spectral domains should be obvious. In practice, we generally use $f_s = 2$, which has proven to be an acceptable compromise for giving resolution in both domains.

2.8 Caveats

The method presented here is recent and has room for improvement. In particular, our choice of windows, while not arbitrary, lacks a robust justification. As a beginning, we are satisfied with reasonable control over the spatial localization (despite the obvious sidelobes) and the spectral compactness that is so crucial for the maximization of L_{nyq}. Future work should consider tailoring the windows for the data type being considered. In particular, there is the potential for bias in our method stemming from the analysis of data with red spectra. While we note this bias, we are not able to quantify it given the simplicity of our window construction. From the wavelet perspective, we have constructed a set of localized basis functions, $X_{lm}(\Omega)$, as the product of spatial windows and spherical harmonics. It may be desirable to formulate a localization method that constructs these basis functions directly. Indeed, as was noted previously in reference to figure 2.2, many of the $X_{lm}(\Omega)$'s do not contribute to the final result, suggesting the existence of a more efficient formulation. In other words, we would like a set of independent basis functions. The choice of basis will become more important in the future as the resolution of the global data sets increases and computational concerns become more of a factor.

Missing in our analysis is a discussion of the uncertainties in the derived statistical estimates. Only the error in the transfer function between two localized fields is presented here. While this is the error typically presented for two fields with independent harmonic coefficients free of errors, our localized coefficients are both correlated and themselves contain errors, so our error for the transfer function is an underestimate. From a practical perspective, we will analyze geoid and topography data. The harmonic representations of these global fields are rarely reported with errors for each coefficient. Future analyses should consider using the full covariance matrix derived in generating these fields (although for the high-degree fields now available this objective may be untenable). It should be of some comfort that the total error in the Earth's geoid is characterized by values less than 25 cm [*Nerem et al.*, 1994], significantly lower than the predictive ability of geodynamical models considered here. The situation is worse for the geoid on Venus, and we have made an attempt to include the expected strength of the geoid in our discussion of L_{nyq}, but we have not attempted to include errors from each harmonic coefficient.

Despite these warnings, the localization method used here provides new insights to the structure of many global geophysical fields. The method draws its strength from its simplicity and the similarities to conventional windowing techniques. The details of our approach rely on the coupling relationships between spherical harmonics. Possibly the most important outcome from our methdology is the existence of a localization Nyquist degree, L_{nyq}. In order to quantify L_{nyq}, we have used spatial windows with compact spectral representations. Indeed, for the standard fixed length-scale analyses common in most global geophysical studies, the issue of the finite spectral resolution of most global data sets is frequently overlooked or ignored.

Chapter 3

Topographic Compensation and Tectonics on Venus

3.1 Introduction

Much of the data analysis and discussion in this chapter is similar to that of *Simons et al.* [1994]. While the methods used here are considerably improved over those we used before, the main conclusions reached in *Simons et al.* [1994] are not changed, only expanded upon.

Although Venus and Earth are similar in size, density, and bulk composition [*Phillips and Malin*, 1983], radar images of the surface of Venus obtained by the recent Magellan mission show no evidence for global plate tectonics [*Solomon et al.*, 1991, 1992]. Thus, the surface manifestations of mantle convection are quite different on the two planets, a result plausibly attributed to the extreme dryness and high temperatures of the Venus surface [*Phillips and Malin*, 1983; *Phillips et al.*, 1991a; *Kaula*, 1990]. The high surface temperature makes the lithosphere on Venus more buoyant than its terrestrial counterpart and may inhibit the subduction process [*Phillips and Malin*, 1983]. Further, subduction requires throughgoing faulting of the lithosphere, and most models of spatially localized brittle faulting require the presence of water. In the absence of water, the lithosphere of Venus may not be capable of faulting on the scale necessary to create plate boundaries [*McKenzie*, 1977a].

Nevertheless, the composition of surface rocks, as determined at a handful of sites by the Venera and Vega landers, is similar to that of oceanic basalts [*Surkov et al.*, 1983, 1984, 1986, 1987]. Based on the earth-like abundances of the heat producing elements U, K, and Th, as well as cosmochemical considerations [*Basaltic Volcanism Study Project*, 1981] it is reasonable to consider a simple scaling of terrestrial heat loss estimates to Venus [*Solomon and Head*, 1982]. Such a scaling predicts a total heat loss of about 70 mWm^{-2} for Venus [*Solomon and Head*, 1982]. With no evidence for plate tectonics, we must ask how Venus loses its heat. Therefore, of primary interest is our ability, or lack thereof, to estimate the average thermal boundary layer (TBL) thickness of Venus.

Turcotte [1993] proposed a 300-km-thick TBL thickness on the basis of high spatial geoid-to-topography ratios (GTR) [e.g., *Smrekar and Phillips*, 1991], large effective elastic plate thickness estimates [e.g., *Johnson and Sandwell*, 1994], and the suggestion that the lithosphere has conductively cooled for the last 300 to 500 My. This last point was motivated by observations of impact crater density and degradation states suggesting that the surface of Venus has been relatively undisturbed for nearly a half billion years [*Phillips et al.*, 1991a, 1992; *Schaber et al.*, 1992; *Strom et al.*, 1994]. *Turcotte* [1993] interprets this result to be evidence for episodic plate tectonics, whereby the lithosphere conductively cools for several hundred million years and thickens to a value beyond that expected by marginal staiblity analysis, and then founders in a single short-lived event (frequently referred to as catastrophic overturn). *Parmentier and Hess* [1992] proposed a similar model, taking into account the effects of the depleted mantle layer that should develop in a system lacking a mechanism for wholesale lithospheric recycling. Assuming that our scaling from terrestrial values is reasonable, a 300-km-thick TBL does not permit sufficient heat to escape the planet, so there is need for episodic resurfacing whereby the heat is lost in brief but intense events. In contrast, *Solomon* [1993] proposed that the surface of Venus has experienced a monotonic decline in tectonic activity due to secular cooling and rheological nonlinearities. Without a catastrophic resurfacing event, this model requires a thinner lithosphere to permit sufficient heat loss. Thus, it is of particular interest to test if analysis of surface tectonics and geophysical observations can distinguish between an earth-like 100-km-thick TBL and one three times thicker.

The topography and gravity fields measured by the Magellan spacecraft, and the relation between them, constitute crucial data which we have used to develop models of the tectonic processes active on Venus. Variation in long-wavelength gravity and surface topography are primary expressions of the underlying structure, mechanical constitution, and dynamics of the mantle-lithosphere system [e.g., *Crough and Jurdy*, 1980; *Watts et al.*, 1980; *Hager and Richards*, 1989]. The processes associated with mantle convection, lithospheric deformation, and the development of crustal thickness variations are not mutually exclusive, and their expressions are frequently interrelated. We can constrain how each of these processes influences a given region and horizontal scale by considering how variations in geoid height relate to variations in topography.

Geoid and topography are typically related through an admittance function, estimates of which have been used on Earth to calculate effective elastic plate thicknesses, crustal thicknesses, and dynamic stresses imparted by the convecting mantle [e.g., *Dorman and Lewis*, 1970; *McKenzie*, 1977b; *McNutt*, 1980]. In its simplest usage, the admittance for a given area is the variation in geoid height divided by the variation in topography. Its sign and amplitude vary as a function of position and wavelength. At long wavelengths the geoid is most sensitive to processes associated with mantle convection. In the absence of significant long-wavelength topography associated with crustal thickness variations, a small or negative admittance value over a given area may imply that a low-viscosity channel is present beneath the lithosphere, decoupling it from underlying stresses in the convecting mantle [e.g., *Robinson and Parsons*, 1988a,b; *Kiefer*, 1993]. Such a situation may hold in oceanic regions on Earth [e.g., *Robinson and Parsons*, 1988a,b]. If crustal thickness variations are important in determining the geoid, then the admittance can be used to determine the mean crustal thickness over a region. In the absence of mantle convective processes, the admittance for such areas is positive and increases as the crustal thickness increases. More precisely, in a static compensation model, the admittance is linearly related to the first moment of the radial density distribution [*Ockendon and Turcotte*, 1977].

Before the Magellan mission [*Saunders et al.*, 1990; *Saunders and Pettengill*, 1991], tracking data from the Pioneer Venus Orbiter (PVO) indicated that the geoid height and topography of Venus are highly correlated on a planetary scale [*Sjogren et al.*, 1983; *Kiefer et al.*, 1986], but global analyses carried out with these data were limited to spherical harmonic degree 18 and less, and only global averages of the admittance were obtained. Several studies made use of line-of-sight (LOS) accelerations of the PVO spacecraft over limited geographic areas on Venus to demonstrate that the geoid height and topography correlate on shorter scales than could be represented with the global spherical harmonic fields then available, but such studies were limited to a few selected regions [e.g., *Herrick et al.*, 1989; *Smrekar and Phillips*, 1991; *Grimm and Phillips*, 1991, 1992]. More recently, with the new global gravity coverage, most investigators have switched to using only the spherical harmonic rendition of the gravity field [e.g., *Simons et al.*, 1994; *Smrekar*, 1994; *Grimm*, 1994a; *Phillips*, 1994; *McKenzie*, 1994; *Schubert et al.*, 1994].

We present maps of the geoid/topography admittance spectra for Venus from data recently obtained during the Magellan mission [*Ford and Pettengill*, 1992; *Konopliv and Sjogren*, 1994; *Konopliv*, 1995]. These maps demonstrate global variations in the admittance and constitute a guide to the depths and modes of compensation of topography associated with different large-scale features over much of Venus. Our results force us to address the issue of the evolution of the style of surface deformation over the past half billion years. We will show that a static compensation model fits the geoid/topography admittance spectra only over the highland plateaus, which encompass about 10 percent of the surface and may represent fossils of a now extinct tectonic regime. The failure of static models for the remaining 90 percent of the surface implies that admittance analyses that rely on spatial GTR ratios [e.g., *Smrekar and Phillips*, 1991; *Grimm and Phillips*, 1991, 1992; *Kucinskas and Turcotte*, 1994; *Schubert et al.*, 1994; *Moore and Schubert*, 1995], i.e., for which a single apparent depth of topographic compensation (ADC) at all wavelengths is assumed, will give misleading results when applied to regions with inherently dynamic signatures. The method used here will identify those few regions where a single ADC does explain the observations well. However, this can be done only after completion of the full spectral analysis. In addition, the localization method used here exposes the limits to which we can simultaneously analyze both the spatial and spectral behavior of the geoid given the finite resolution of the spherical harmonic degree and order 90 field currently available for Venus. These limits have been exceeded by most published analyses (especially given that until very recently, the available geoid models extended to degree and order 60.)

Since we do not have the luxury of a reliable *a priori* model of the interior density structure of Venus, we rely on numerical convection models to build intuition and to provide a self-consistent interpretation of the geoid and topography observations. We show that, due to the sensitivity of the geoid to the distribution of density anomalies and viscosity variations, admittances alone cannot be used to constrain the TBL thickness, and that there is no reason based on this evidence to favor a TBL thickness of 300 km over a more Earth-like 100 to 150 km. Furthermore, we also show that, contrary to most previous analyses, there is no reason to assume that Venus lacks an Earth-like mantle viscosity increase with depth.

3.2 A Brief Guide to Venus Surface Tectonics

The surface of Venus includes a wide range of geological structures. The global hypsometric profile is unimodal, unlike the bimodal distribution for the Earth [*Pettengill et al.*, 1980], reflecting the lack of an ocean/continent dichotomy. A reference map of global topography is shown in figure 3.1. Topography can be divided into highlands, lowlands, and plains, and in turn, highlands are generally subdivided into plateaus and long-wavelength swells.

The largest of the highland terrains is the equatorial region of Aphrodite Terra, which spans half the circumference of the planet. Western Aphrodite Terra consists of Ovda and Thetis Regiones, steep-flanked highlands rising approximately three kilometers above the planetary mean and characterized by pervasive, dominantly compressive deformational features [*Solomon et al.*, 1991, 1992]. In contrast, eastern Aphrodite Terra encompasses a broad rise, Atla Regio, topped by rift valleys and large volcanoes, with little evidence for compressional deformation [*Solomon et al.*, 1991, 1992; *Senske et al.*, 1992]. Beta and Eistla Regiones are each similarly characterized by a topographic rise, large volcanoes, and rifting [*McGill et al.*, 1981; *Solomon et al.*, 1991, 1992; *Senske et al.*, 1992; *Grimm and Phillips*, 1992]. Frequently associated with the volcanic and rift regions are chains of coronae, circular features consisting of concentric tectonic and topographic rings [*Pronin and Stofan*, 1990; *Squyres et al.*, 1992a]. Whether they each represent surface expressions of individual mantle plumes, or lithospheric subduction, or whether they are related to smaller scale phenomena, is currently unknown [*Squyres et al.*, 1992a; *Stofan et al.*, 1991; *Janes et al.*, 1992; *Sandwell and Schubert*, 1992a,b].

Ishtar Terra, which encompasses several mountain belts and blocks of highly deformed terrain, is the second largest compressionally deformed highland [*Barsukov et al.*, 1986; *Basilevsky*, 1986; *Pronin*, 1986; *Solomon et al.*, 1991, 1992; *Kaula et al.*, 1992]. Western Ishtar Terra consists of a plateau, Lakshmi Planum, approximately 2000 km in diameter and 3 to 4 km high covered by volcanic plains. The plateau is surrounded

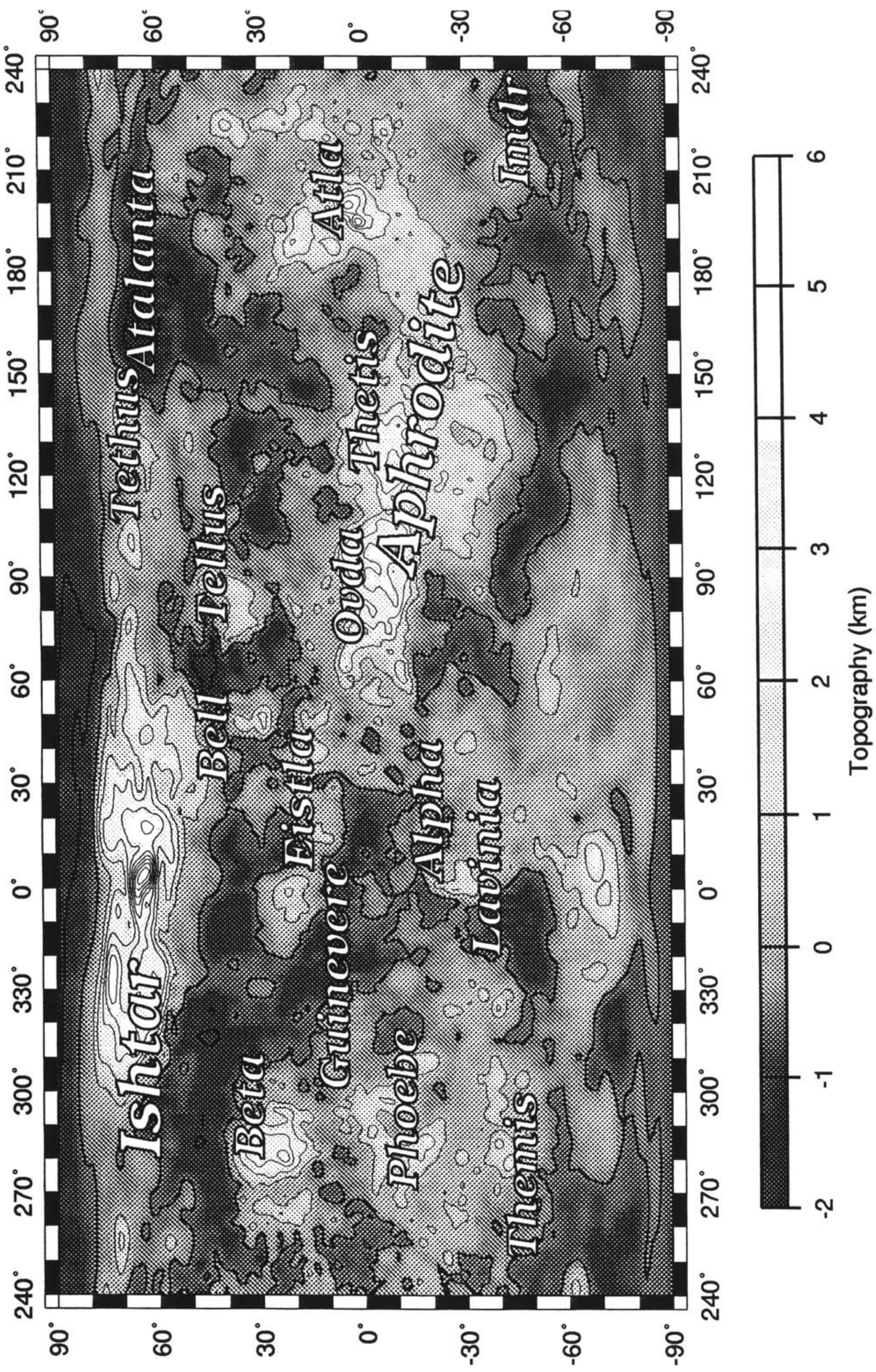

Figure 3.1: Image and contours of a spherical harmonic degree and order 120 expansion of topography with major physiographic provinces labeled for reference. Contours every 1 km; elevations ≥ 0.5 km use thin lines and elevations ≤ 0.5 km use thick lines (Cylindrical equidistant projection).

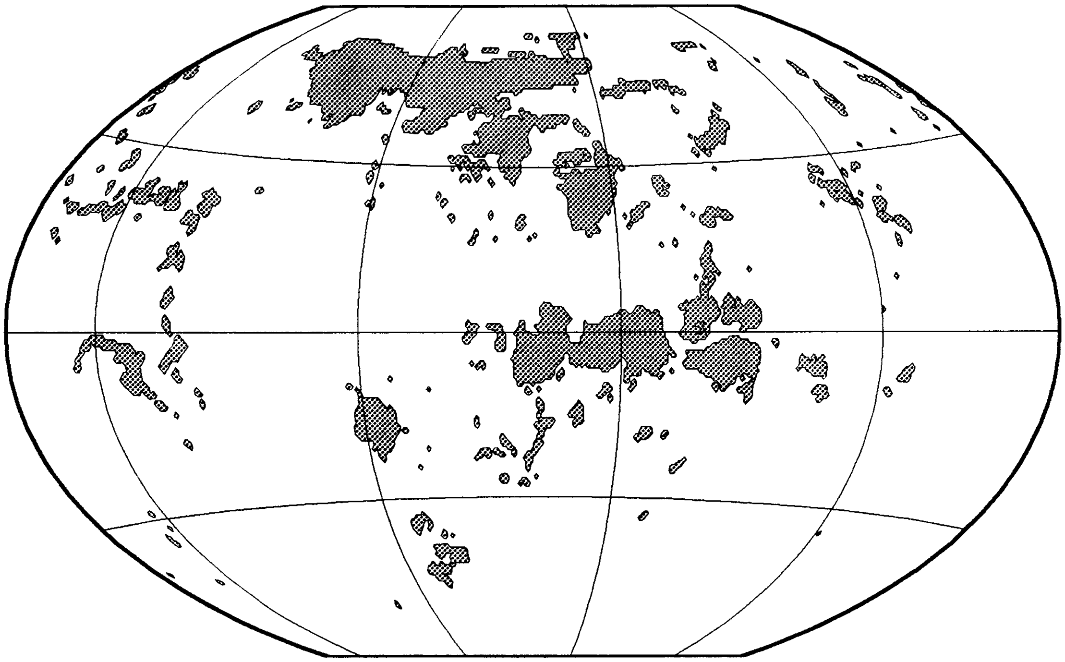

Figure 3.2: Global distribution of the highland plateaus and tesserae [*Price and Suppe*, 1995].

by a ring of mountains which reach a maximum elevation of 11 km above the planetary mean at Maxwell Montes. Models for the origin of Ishtar Terra include mantle upwelling, mantle downwelling, or response to a distant source of stress [*Pronin*, 1986; *Bindschadler and Parmentier*, 1990; *Bindschadler et al.*, 1990; *Grimm and Phillips*, 1991]. In addition to Aphrodite and Ishtar Terrae, there are many smaller highland plateaus, or tesserae, interpreted to be of compressive origin. Among these are Alpha and Tellus Regiones, which are steep sided, complexly deformed terranes with lateral dimensions of over a 1000 km [*Solomon and Head*, 1991; *Solomon et al.*, 1992; *Bindschadler et al.*, 1992b]. A global map of the distribution of highland plateaus and tessera terranes is shown in figure 3.2. This map is derived from analysis and interpretation of Magellan radar images by *Price and Suppe* [1995].

Plains and lowlands, the lowest of which are Atalanta and Lavinia Planitiae, lie between the highland terrains and make up most of the Venus surface. Ridge belts, compressional features with hundreds of meters of relief and dimensions of up to several thousand kilometers in length and hundreds of kilometers in width, are frequently associated with the lowest regions of the planet [*Zuber and Parmentier*, 1990; *Zuber*, 1990; *Solomon et al.*, 1992; *Squyres et al.*, 1992b]. The plains are generally interpreted to be covered by large volcanic lava flows and are sites for a multitude of volcanic land forms [e.g., *Head et al.*, 1991, 1992; *Guest et al.*, 1992].

By combining the topographic information with the highland plateau and tesserae map we are able to define a global tectonic regionalization. Topography greater than half a kilometer above the planetary mean is divided into highland plateaus and tesserae or highland volcanic swells (indicated by dark and light shading, respectively, on all subsequent global maps in this chapter). All remaining regions are lowlands and plains and show lower topographic relief than the highlands.

3.3 Global Geoid, Topography, and Admittance

The currently available spherical harmonic model of the geoid of Venus includes LOS data from orbital cycles 4 and 5 of the Magellan mission and has a maximum degree and order of 90 [*Konopliv and Sjogren*, 1994; *Konopliv*, 1995]. The spatial rendition of this field is shown in figure 3.3. This solution includes data from tracking of the spacecraft in a nearly circular orbit with an apoapsis of about 550 km and a periapsis of about 180 km [*Konopliv and Sjogren*, 1994]. The spherical harmonic expansion of the topography is taken from values gridded every 0.25° in latitude and longitude [*Ford and Pettengill*, 1992] and is complete to degree and order 360 [*Rappaport and Plaut*, 1994].

The close association of highlands and geoid highs is remarkable, suggesting perhaps that the geoid results from compensation of topography either isostatically [e.g., *Haxby and Turcotte*, 1978] or dynamically [e.g., *Richards and Hager*, 1984]. Here, isostatic compensation refers to the balancing of topographic loads with density variations at

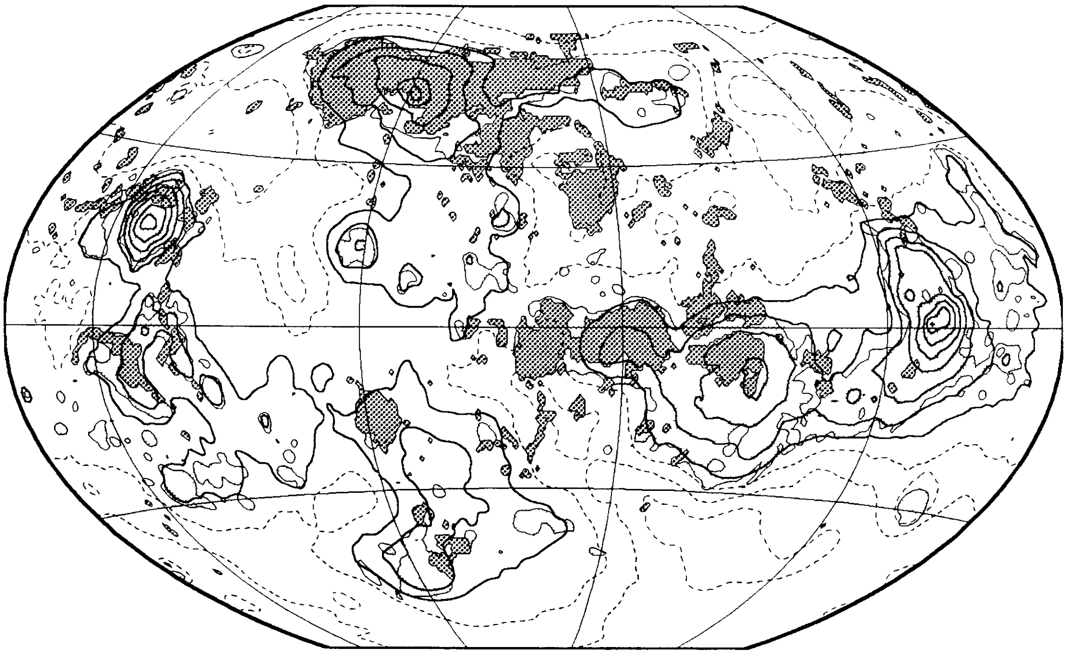

Figure 3.3: Global map of geoid model MGNP90LSAAP. Contours every 20 m, with $N(\Omega) \geq 10$ m and $N(\Omega) \leq -10$ m shown by solid and dashed lines, respectively. Unless stated otherwise, all global maps have elevations ≥ 0.5 km lightly shaded and highland plateaus and tesserae, which also have elevatons ≥ 0.5 km, darkly shaded for reference. Winkel Tripel projection centered at 60° E.

depth. These variations can be either at discrete interfaces, such as the crust-mantle boundary, or volumetrically distributed, such as contributions from the thermal and chemical structure of the interior. In contrast, dynamic compensation refers to surface topography supported by stresses from mantle flow.

We begin our analyses of topographic compensation on Venus by considering a set of simple static models. In figure 3.4 we show the isostatic geoid anomaly from 6 models where topography is treated as the result of a vertical load on a thin spherical plate with effective elastic plate thickness, T_e, and where a density contrast occurs at mean depth D across a crust-mantle interface that follows the deflection of the surface [*Kraus*, 1967]. We show results for $D = 25, 50,$ and 100 km and $T_e = 20$ and 40 km, where we have assumed a crustal density, ρ_c, of 2950 kg m^{-3} and a mantle density, ρ_m, of 3250 kg m^{-3}. Values of $D > 50$ km overcompensate the topography in Ovda Regio, Lakshmi

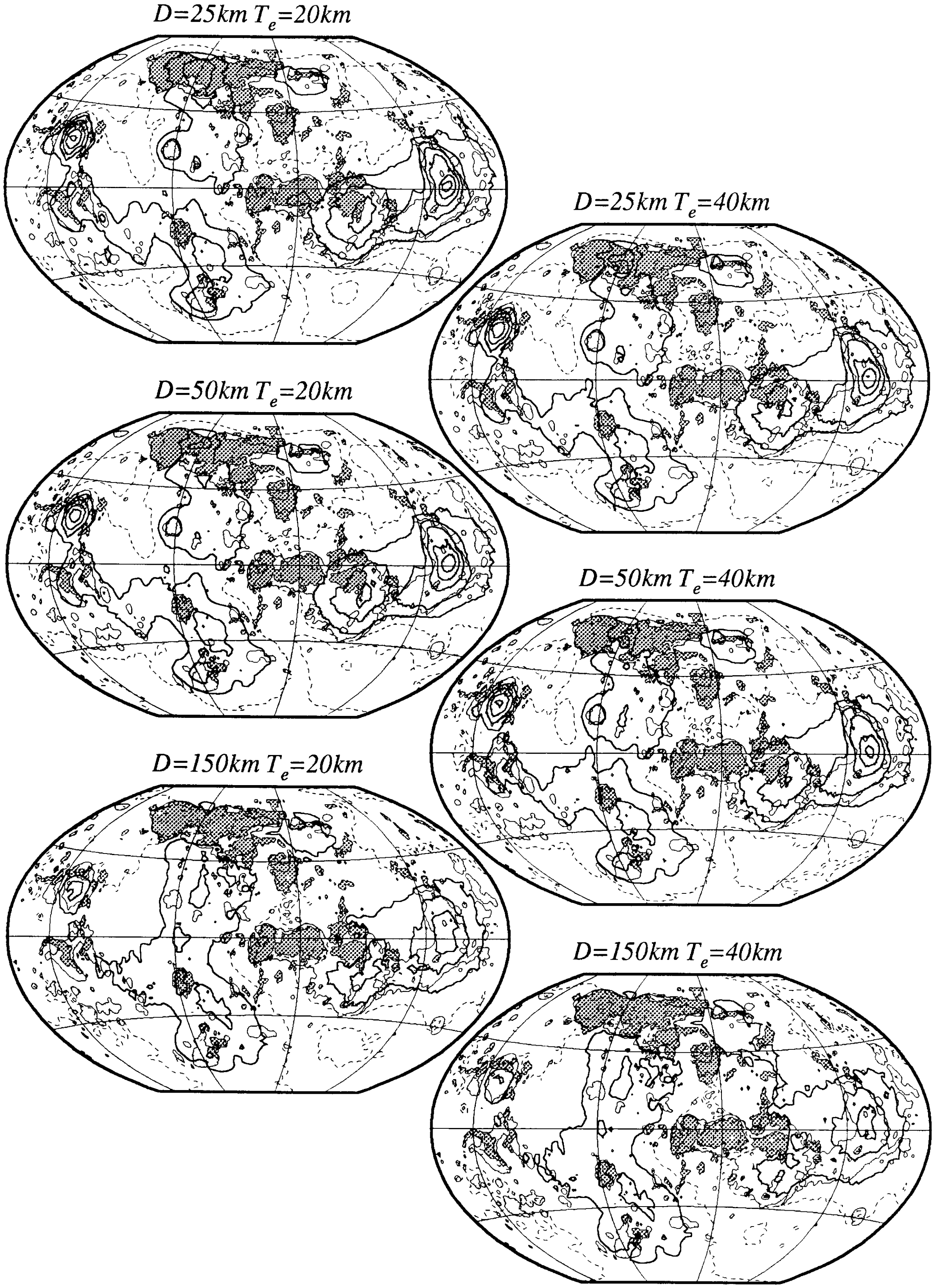

$D=25km\ T_e=20km$

$D=25km\ T_e=40km$

$D=50km\ T_e=20km$

$D=50km\ T_e=40km$

$D=150km\ T_e=20km$

$D=150km\ T_e=40km$

Figure 3.4: Maps of the isostatic geoid anomaly as a function of compensation depth, D, and elastic plate thickness, T_e. Contours every 20 m, with $N(\Omega) \geq 10$ m and $N(\Omega) \leq -10$ m shown by solid and dashed lines, respectively.

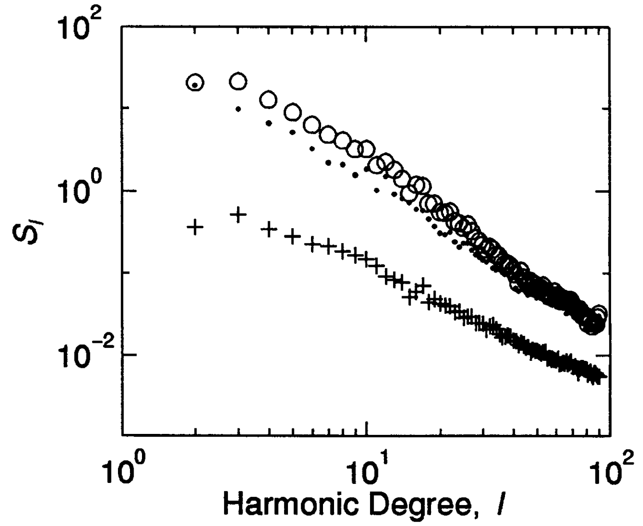

Figure 3.5: RMS amplitude spectra, $\hat{S}_l$, of geoid (circles), topography (crosses), and that part of the geoid which is not correlated with topography (dots).

Planum, and eastern Ishtar Terra. $D = 25$ km can account for about 70 percent of the total geoid anomaly in Ishtar Terra and all of the anomaly over Ovda Regio. $T_e = 40$ km does a better job than $T_e = 20$ km at reducing the anomaly over Maxwell Montes proper. For most other regions, we are unable to explain adequately the observed geoid with a single ADC model, even one with $D = 150$ km, a value considerably greater than any crustal thickness estimates for Venus, where the crustal thickness is limited by the basalt-to-eclogite phase transition, believed to occur at less than 100 km depth [*Anderson*, 1981]. Due to the red spectrum of the geoid and topography, the spatial analysis represented in figure 3.4 is dominated by the very longest wavelengths, and we are unable to evaluate the success of the single-ADC model for the smaller features.

In contrast to a purely spatial approach, we can also consider a purely spectral approach. In figure 3.5 we show rms amplitude *vs.* spherical harmonic degree for both geoid and topography. In figure 3.6 we show the degree correlation between the two fields, as well as the least squares estimate of the degree-dependent global admittance function. From the admittance function, we can construct a residual, or zero-correlation, geoid by

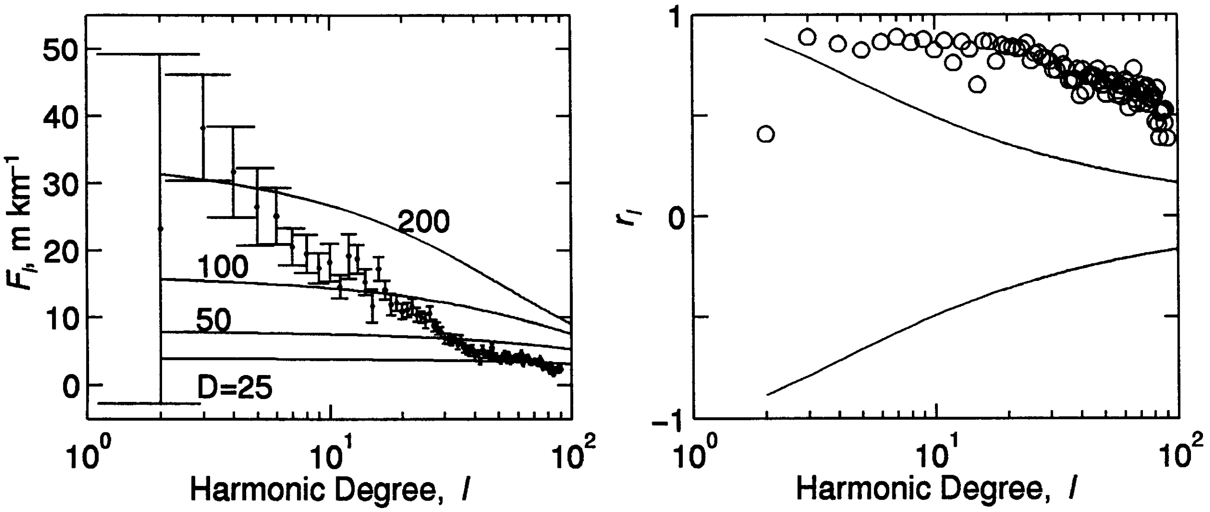

Figure 3.6: Left: Geoid/topography admittance, $\hat{F}_l$ with one standard deviation error bars. For reference, we show theoretical Airy curves for compensation at 25, 50, 100, and 200 km depth. Right: Degree correlation, $\hat{r}_l$, between geoid and topography for the observed geoid (circles). The 98 percent confidence limits are shown by the solid lines.

removing a synthetic field derived by multiplying each degree of the topography by the global admittance at that degree. The goal of this exercise is to quantify the ability of a globally determined parameter to explain the observed field locally. The best global estimate, $\hat{F}_l$, shows a certain amount of unphysical fluctuation from degree to degree. While we could attempt to fit a smooth curve to this spectrum, it would not effect our conclusions.

The spectrum of the residual geoid is shown in figure 3.5, and the spatial rendition of this field is shown in figure 3.7. From the global admittance spectrum, we see again that a single ADC does not fit the data when viewed globally, although there is a suggestion in figure 3.6 that an ADC of about 25 km fits the data for $l \geq 40$. From the residual map we see a strong correlation between the tesserae and those regions which are predicted to be overcompensated (i.e., regions which were associated with positive geoid anomalies in the original field and with negative geoid anomalies in the residual field). Specifically, the admittance calculated in this way predicts topography which is

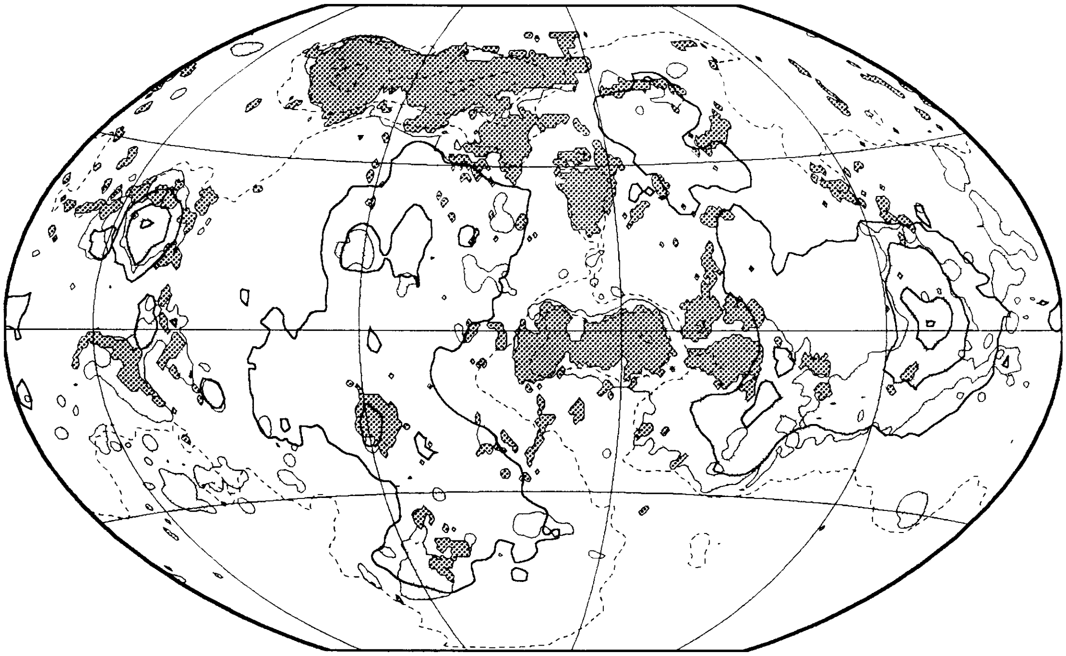

Figure 3.7: Residual geoid generated by removing that part of the geoid which is linearly related to topography in a degree by degree global sense. Contours every 20 m, $N(\Omega) \geq 10$ m and $N(\Omega) \leq -10$ m indicated by solid and dashed lines, respectively.

overcompensated in Ishtar Terra and western Aphrodite Terra and undercompensated in most other regions (figure 3.7). The residual map shows less small-scale structure than those in figure 3.4, but again, due to the dominance of the long wavelengths, it is hard to judge the success of this empirical admittance estimate spatially. The misfit of the large scale features stems from the spatial combination of different modes of compensation at long wavelengths. While the residual anomaly is uncorrelated with topography when viewed spectrally in a global sense, we see a high correlation when viewed locally (figure 3.7). This apparent contradiction arises because the geoid and topography are positively correlated for half the planet, and negatively correlated for the other half, resulting in a net correlation of zero. Given that using the global admittance predicts topography that is overcompensated in tesserae and plateaus and undercompensated at highland swells, plains, and lowlands, we conclude that the geoid signal from latter group dominates the total global signal.

3.4 Calculation of Local Admittance Estimates

In order to progress beyond the purely spectral or purely spatial approaches, we must consider methods to localize the geoid and topography data in the two domains simultaneously. We start by reviewing previous approaches to this problem. Historically, investigations of geoid-topography relations on Venus made use of geoid-to-topography ratios (GTR), which are spatial estimates of the covariance of geoid height and surface elevation over a finite region [e.g., *Smrekar and Phillips*, 1991; *Grimm and Phillips*, 1992; *Kucinskas and Turcotte*, 1994; *Schubert et al.*, 1994; *Moore and Schubert*, 1995]. The use of a single GTR relies on the premises that topography is locally compensated at one depth and that the spectra of the geoid and the topography are both white. If incorrect, as is indicated by the analysis at the beginning of this section, these premises can lead to erroneous conclusions. Furthermore, GTR analyses for both Earth and Venus have either included all wavelengths of the data [*Smrekar and Phillips*, 1991] or they have begun by bandpassing the geoid and topography to isolate wavelengths of approximately 600 to 2000 km [*Sandwell and Renkin*, 1988; *Sandwell and MacKenzie*, 1989; *Kucinskas and Turcotte*, 1994; *Moore and Schubert*, 1995]. Given the red spectra of these fields, the estimated GTR is then dominated by the longest wavelengths passed. Furthermore, spectral bandpassing followed by spatial localization can result in serious spatial aliasing, as discussed in chapter 2.

The admittance is similar to the GTR, but in the wavenumber domain. However, the assumption of a single compensation depth is not required because the admittance can vary with wavelength, as was shown in figure 3.6. Unlike GTR analyses, the approach taken here is first to localize in space, then in frequency, while only considering wavelengths less than the scale of spatial localization. Although some long-wavelength bias still exists due to the spatial windowing of data with red spectra, this bias is considerably less than from the GTR technique (and at least it is overt). Furthermore, as long as comparisons are made to models that have had the same windowing applied to them, we are not seriously affected by this bias. This realization is important since most of the forward models we use have parameters that vary with depth but not horizontal position. Given that we are looking for horizontal variations, it is crucial to window model predictions in exactly the same manner as the data. We note that while this windowing has a minimal effect for Airy forward models, it has a strong effect on regional compensation models. Previous analyses using spherical harmonic representations of the data have not compared windowed observational estimates with windowed forward models [*Phillips*, 1994; *Smrekar*, 1994; *Kucinskas and Turcotte*, 1994; *McKenzie*, 1994].

Following the practice in terrestrial studies [*Dorman and Lewis*, 1970], we assume that geoid and topography are linearly related and determine the admittance in a least squares sense using the method outlined in chapter 2. Strictly, the admittance then depends on the topography and that portion of the geoid that correlates with the topography. We use the localized representations of the geoid and topography and calculate the RMS amplitude anomaly, S_l, for each field, and the admittance, F_l, the error on the admittance, σ_{F_l}, and the correlation, r_l between the two fields using equations 2.58 through 2.61.

For the spatio-spectral localization, we use a scaling parameter, f_s, equal to 2. While not providing optimal spatial resolution, this choice permits us to extend our analysis to higher spectral resolution than with $f_s = 1$. On the basis of the Nyquist discussion in chapter 2, we have from equation 2.68

$$L_{nyq} \simeq \frac{f_s}{f_s + 1} L_{obs}. \tag{3.1}$$

With $f_s = 2$, $L_{nyq} = (2/3)L_{obs}$, and we can at best calculate the admittance up to a maximum degree and order of 60, or down to wavelengths of about 600 km for $L_{obs} = 90$. However, the geoid is not equally reliable at all points on the globe. Considerable variation in field quality exists due to variations in data coverage and spacecraft viewing

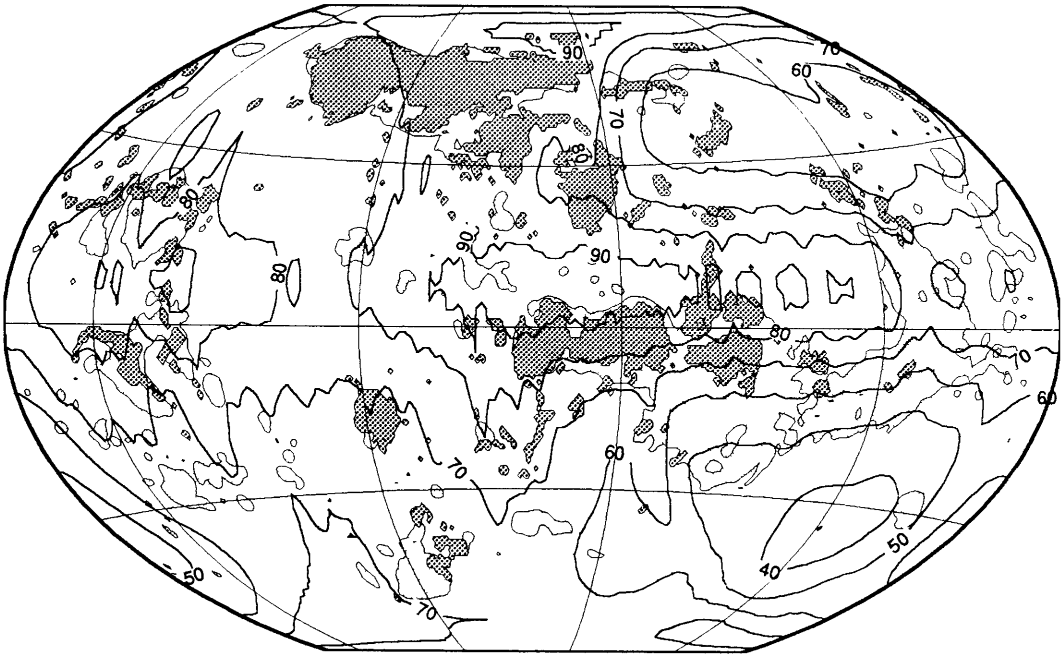

Figure 3.8: Global degree strength map for geoid model MGNP90LSAAP. Contours every 10 spherical harmonic degrees [*Konopliv*, 1995].

geometry. As an approximate estimate of the local reliability, we use the degree strength, defined by *Konopliv and Sjogren* [1995] as the degree at which the power of the total error at a given location and degree exceeds that predicted from application of Kaula's rule. The degree strength for MGNP90LSAAP is shown in figure 3.8. The large area of low degree strength near eastern Aphrodite Terra corresponds primarily to regions lacking periapsis coverage during the nearly circular orbit phase of the Magellan mission [*Konopliv and Sjogren*, 1994; *Konopliv*, 1995]. We equate degree strength with L_{obs}, which results in a position dependent value of L_{nyq}. The local estimate of L_{nyq} is really an upper bound. In the future, it would be wise to estimate the degree strength using the observed geoid as opposed to one based on a prediction from Kaula's rule. Furthermore, it may be more prudent to define the degree strength at the point when the error reaches some percent of the observed power. Many previously published admittance analyses exceed the Nyquist constraint by considering high-degree structure localized using windows having a large value of L_{win}, i.e., non-smooth, short-length-scale spatial windows [e.g., *Smrekar and Phillips*, 1991; *Grimm*, 1994a; *McKenzie*, 1994; *Smrekar*, 1994; *Phillips*, 1994; *Kucinskas and Turcotte*, 1994; *Schubert et al.*, 1994; *Moore and Schubert*, 1995].

3.5 Local Geoid, Topography, and Admittance

Our analysis produces localized spectra for all positions. We present these spectra as global maps for fixed l and as spectra for a set of single geographic locations. A location map for the individual spectra is given in figure 3.9. The global maps are presented as ΔS_l, i.e., deviations of S_l about $\overline{S_l}$, the global average value at each l. Thus, ΔS_l has negative as well as positive values. We apply this l-dependent shift to establish a useful baseline on which to compare results at different l; otherwise the red spectra characteristic of geoid and topography would dominate the figures. As shown in chapter 2, a purely harmonic input field would appear in the ΔS_l maps as having little or no spatial variation at the particular frequency of the input data, and an isolated discontinuity in the input data woud result in power at all degrees, centered at the position of the discontinuity.

Maps of ΔS_l using $f_s = 2$ for topography and geoid are shown in figures 3.10 and 3.11. At $l \leq 8$ the topography is dominated by Ishtar and Western Aphrodite Terrae. At higher l, the volcanic rises become much more significant, although the plateaus and regions of tesserae continue to have large topographic contributions, with a clear dominance of Maxwell Montes at all l. A very different picture appears in the maps of S_l for the geoid. The map of ΔS_4 is dominated by eastern Aphrodite Terra. At higher l, the maps are dominated by the volcanic rises, and all the plateaus and tesserae have very low values of ΔS_l. Although Maxwell Montes is an exception to this observation, it is also the region with the greatest topographic signal.

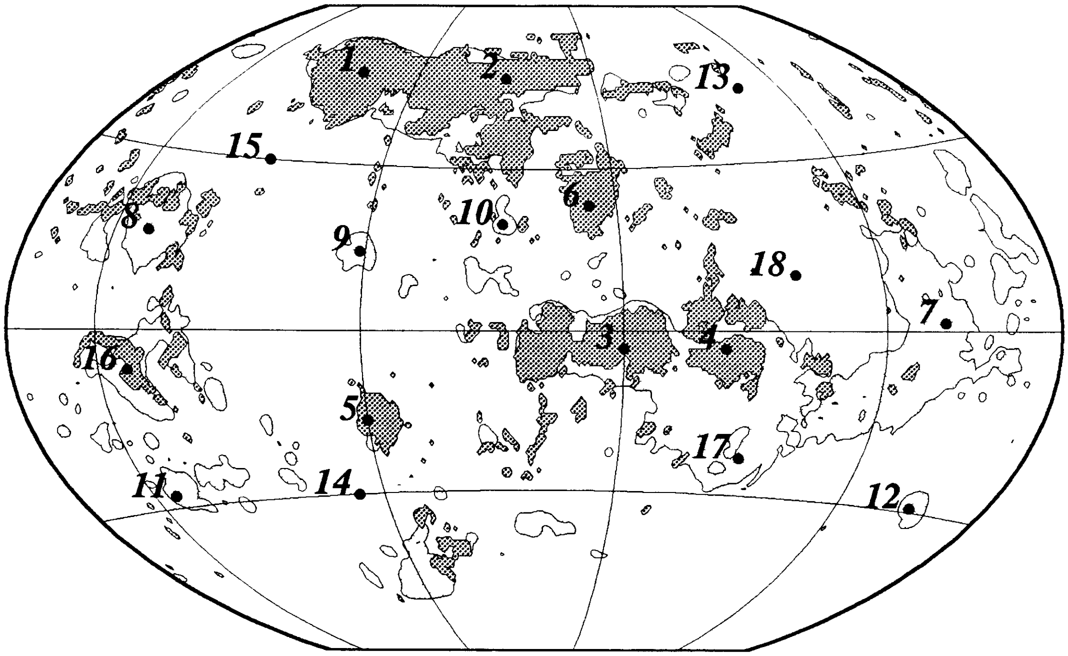

Figure 3.9: Location map the individual spectra shown in figures 3.13 to 3.15.

To further illuminate the relationship between geoid, topography, and tectonic regionalization, we calculate maps of the geoid/topography admittance (figure 3.12). Global and regional admittance values range from 1 to over 60 m km^{-1}, the latter value several times greater than the highest values found for Earth. As previously discussed, the global admittance is not well matched by an Airy model. The steady increase in admittance with decreasing degree l, however, is similar to predictions from models of mantle convection that ignore crustal thickness variations [e.g., *Kiefer et al.*, 1986]. The relationship to convective models is illustrated further in a later section. The local admittances at the highest degree considered here, as well as in global degree-by-degree analysis (figure 3.6), are consistent with an average crustal thickness of no more than about 25 km. From the ΔS_l maps of the geoid, we find that power at the largest length scales is dominated by Atla and Beta Regiones. These maps also show the clear distinction between the highland plateaus and the highland swells.

The admittance for the plateaus and tesserae is consistently lower than for the

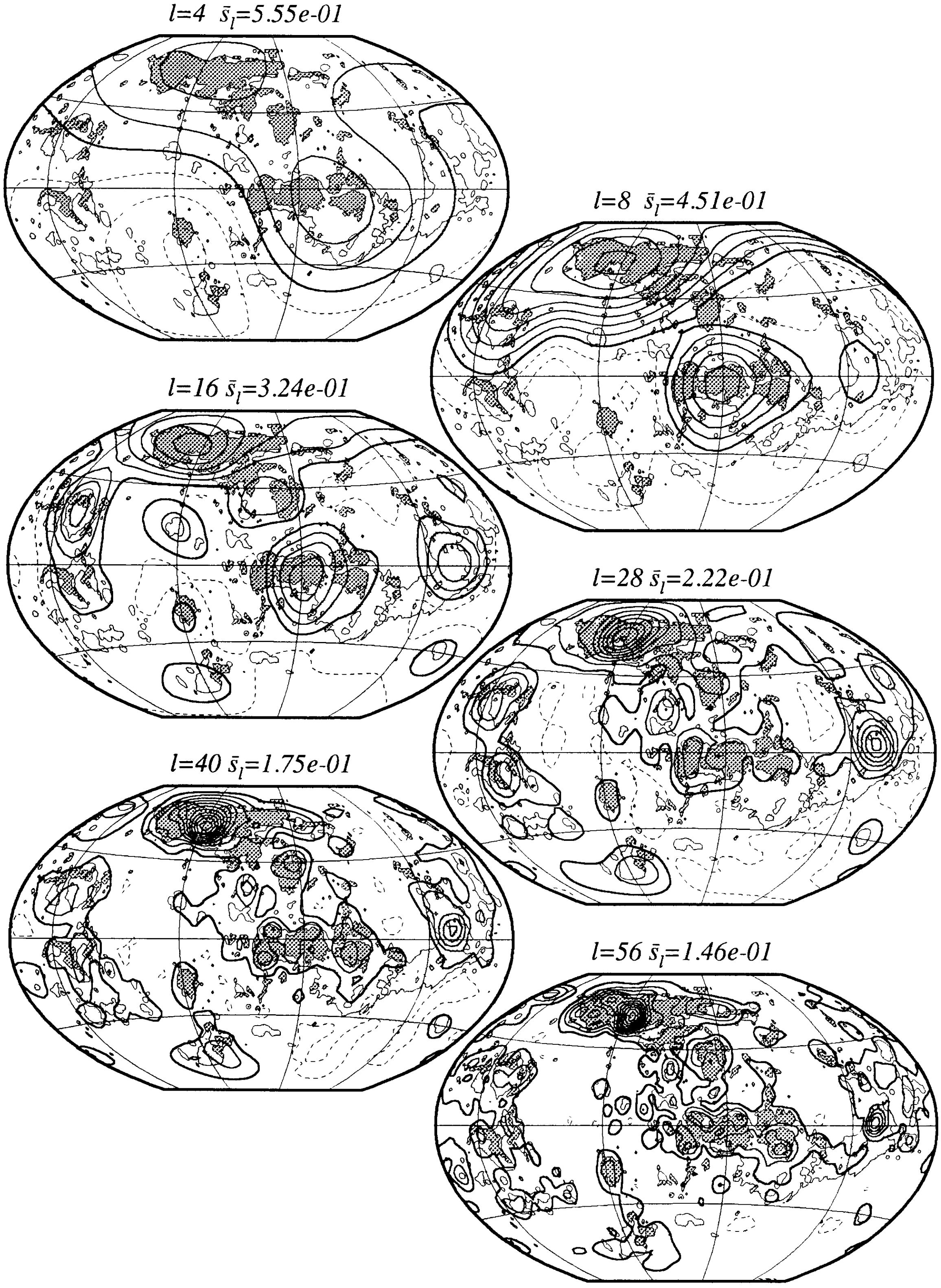

Figure 3.10: S_l of the topography with $f_s = 2$. All S_l maps are shown with thin lines for $\Delta S_l > 0$, thick lines for $\Delta S_l = 0$, and dashed lines for $\Delta S_l < 0$. Contour interval is 100 m.

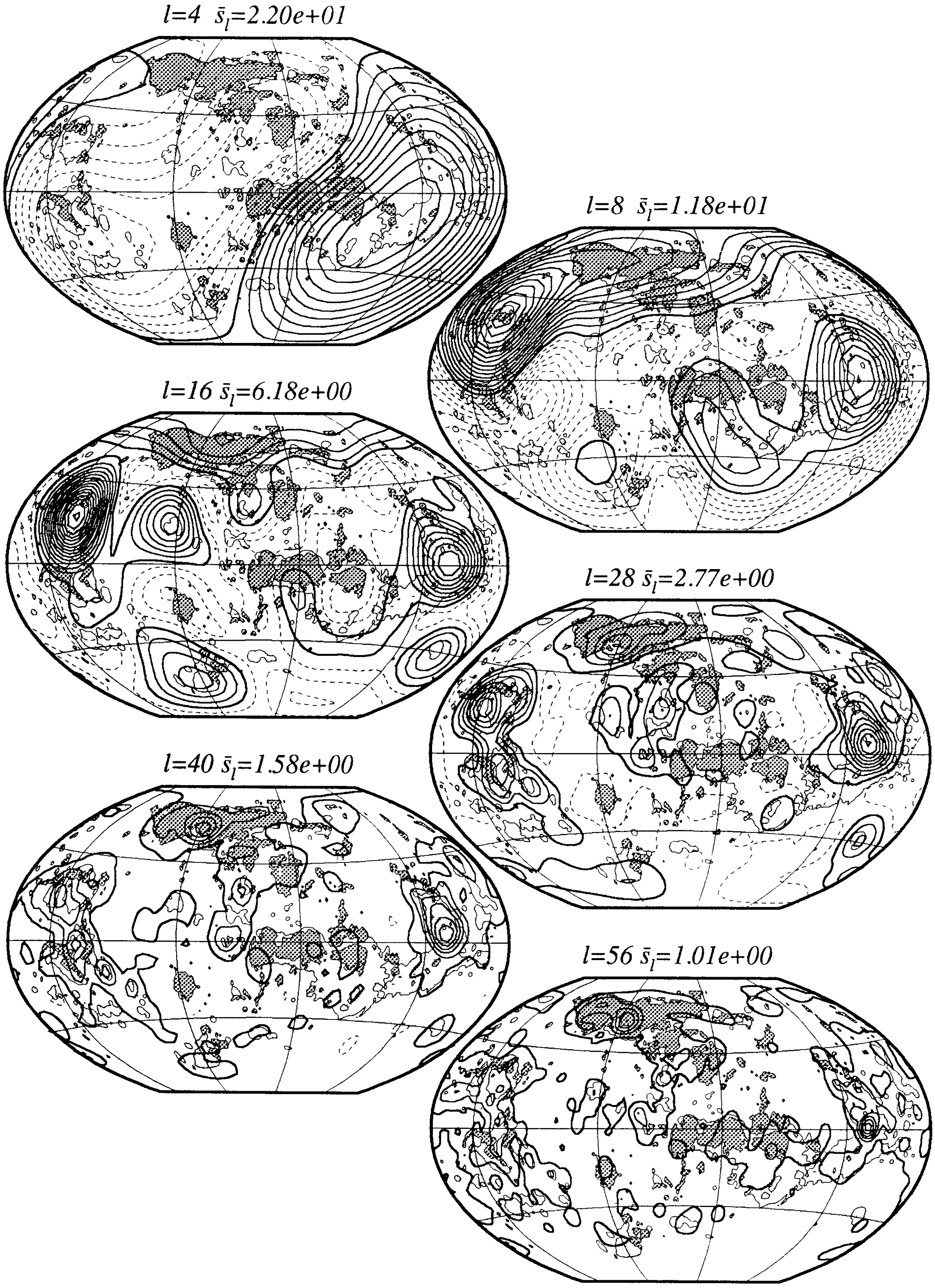
$l=4$ $\bar{s}_l=2.20e+01$

$l=8$ $\bar{s}_l=1.18e+01$

$l=16$ $\bar{s}_l=6.18e+00$

$l=28$ $\bar{s}_l=2.77e+00$

$l=40$ $\bar{s}_l=1.58e+00$

$l=56$ $\bar{s}_l=1.01e+00$

Figure 3.11: ΔS_l of the geoid with $f_s = 2$. Contour interval is 1 m.

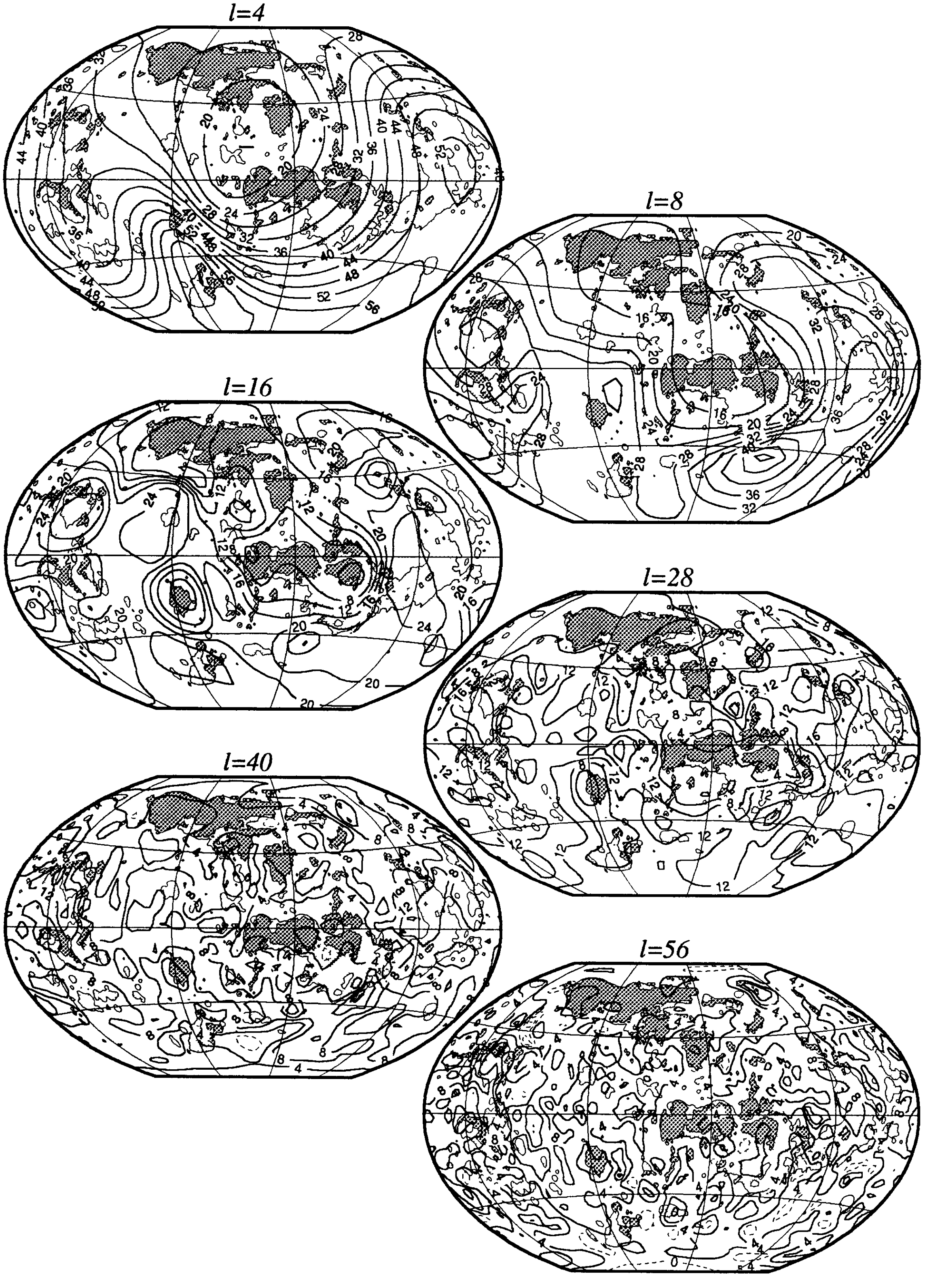

l=4

l=8

l=16

l=28

l=40

l=56

Figure 3.12: F_l with $f_s = 2$. Contour interval is 4 m km^{-1}, with $F_l > 0$ m km^{-1} and $F_l \leq 0$ m km^{-1} indicated with solid and dashed lines, respectively.

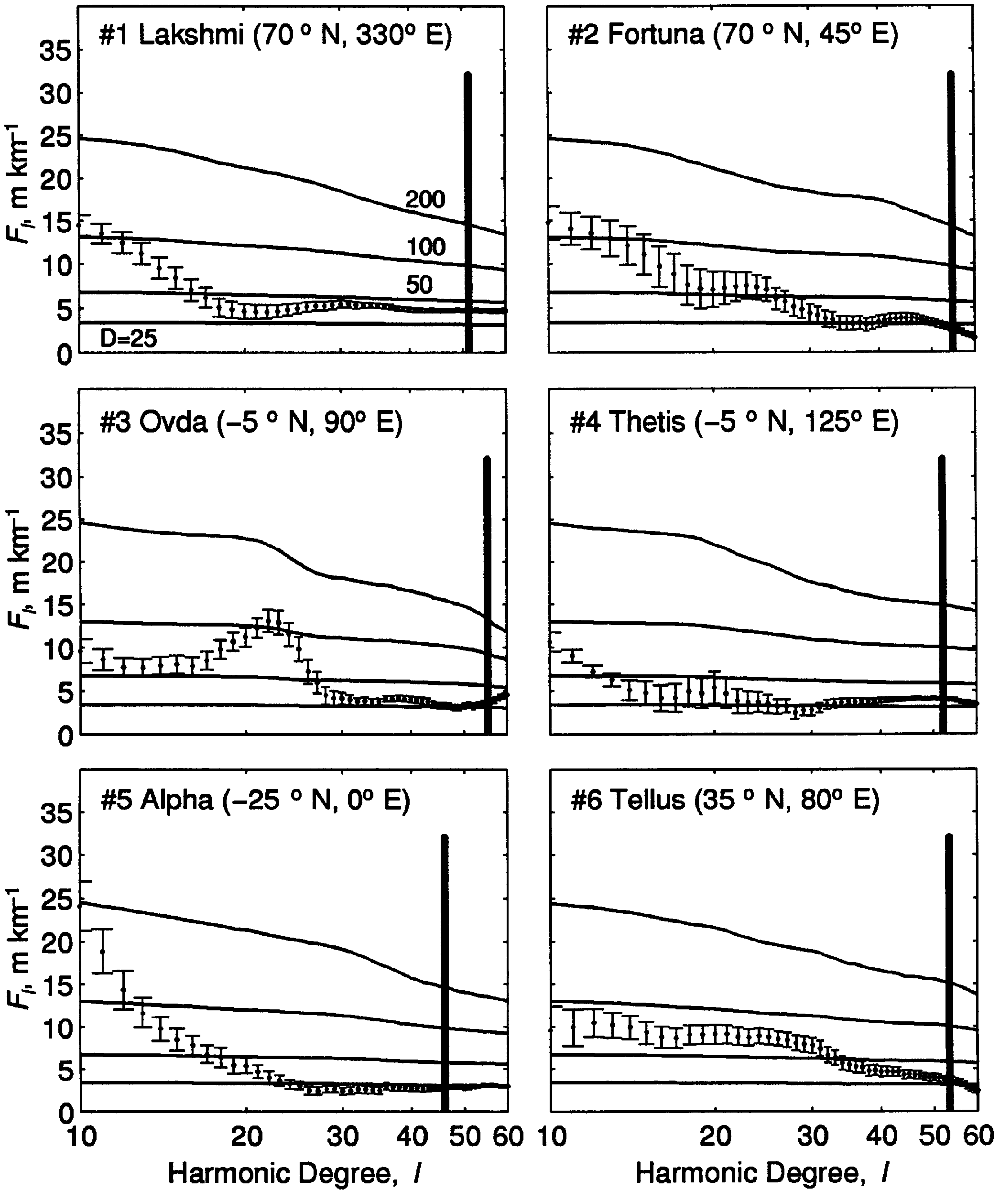

Figure 3.13: Geoid/topography admittance spectra for selected highland plateaus and tessera regions. For reference, theoretical Airy curves for compensation at 25, 50, 100, and 200 km, are shown by the thin lines. These reference curves are position-dependent since they include the windowing operation and are sensitive to the spectrum of the topography. The solid vertical line indicates the local Nyquist degree based on the degree strength map shown in figure 3.8.

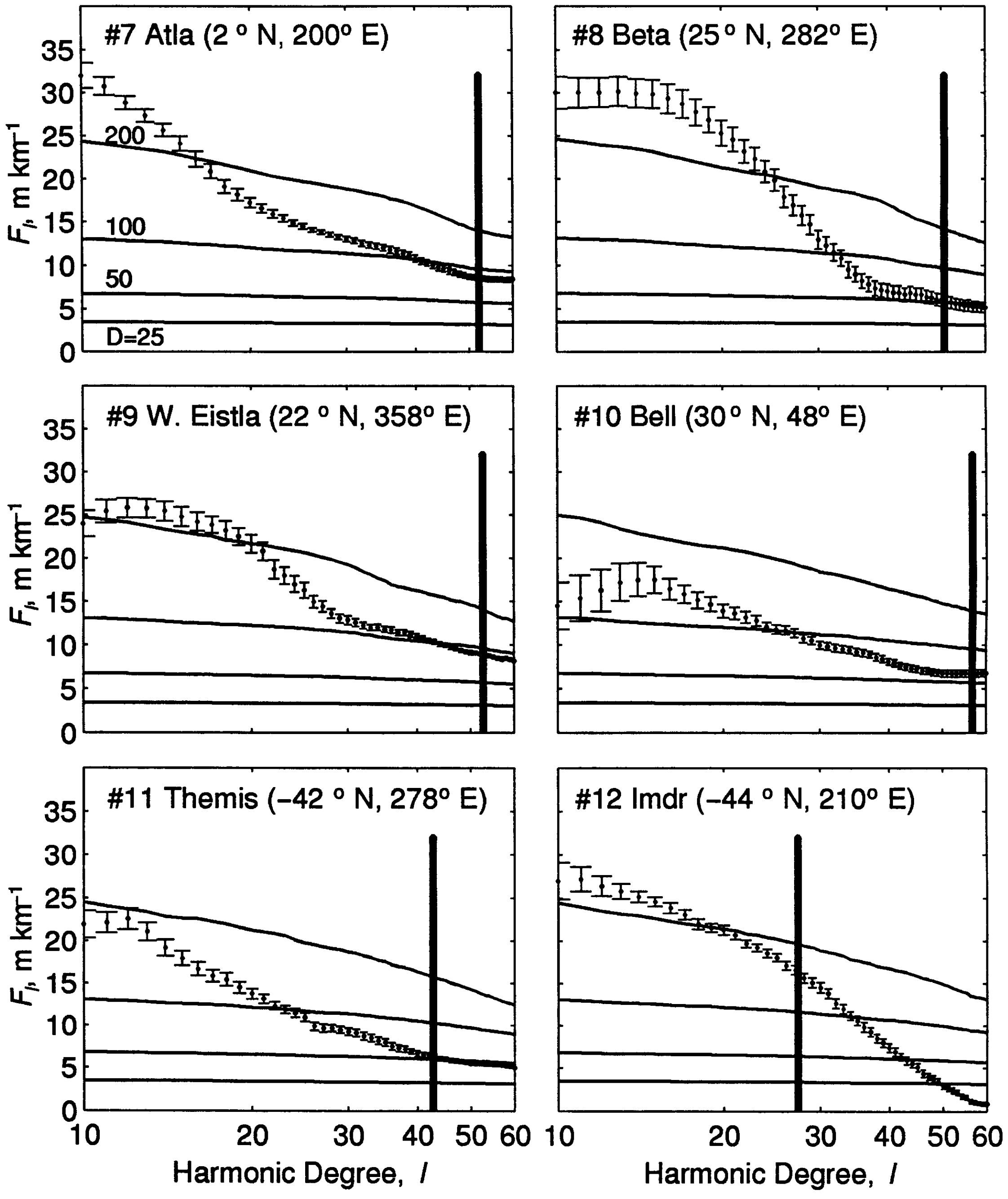

Figure 3.14: Same as figure 3.13 for selected highland swells.

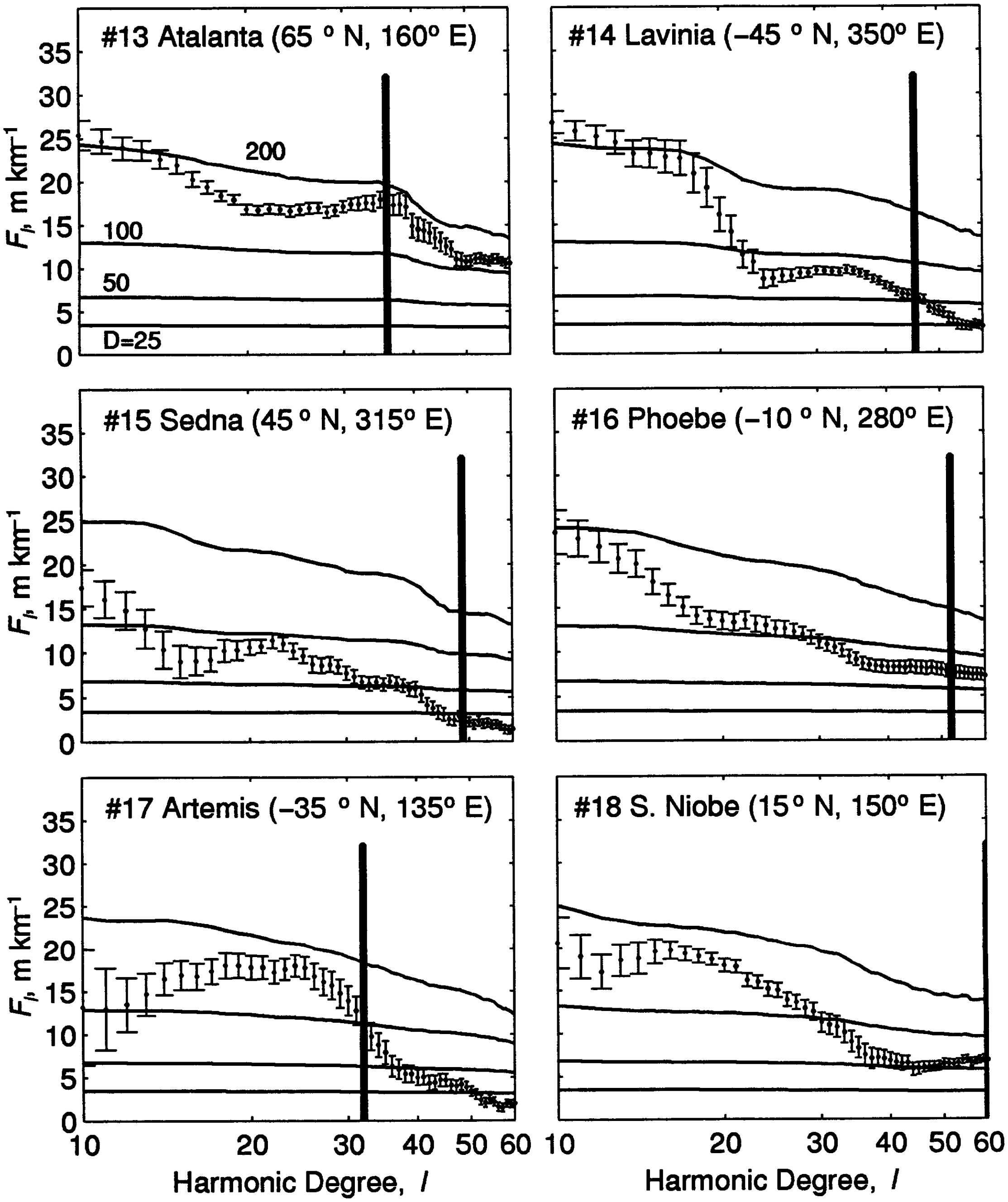

Figure 3.15: Same as figure 3.13 for selected lowlands and planitiae.

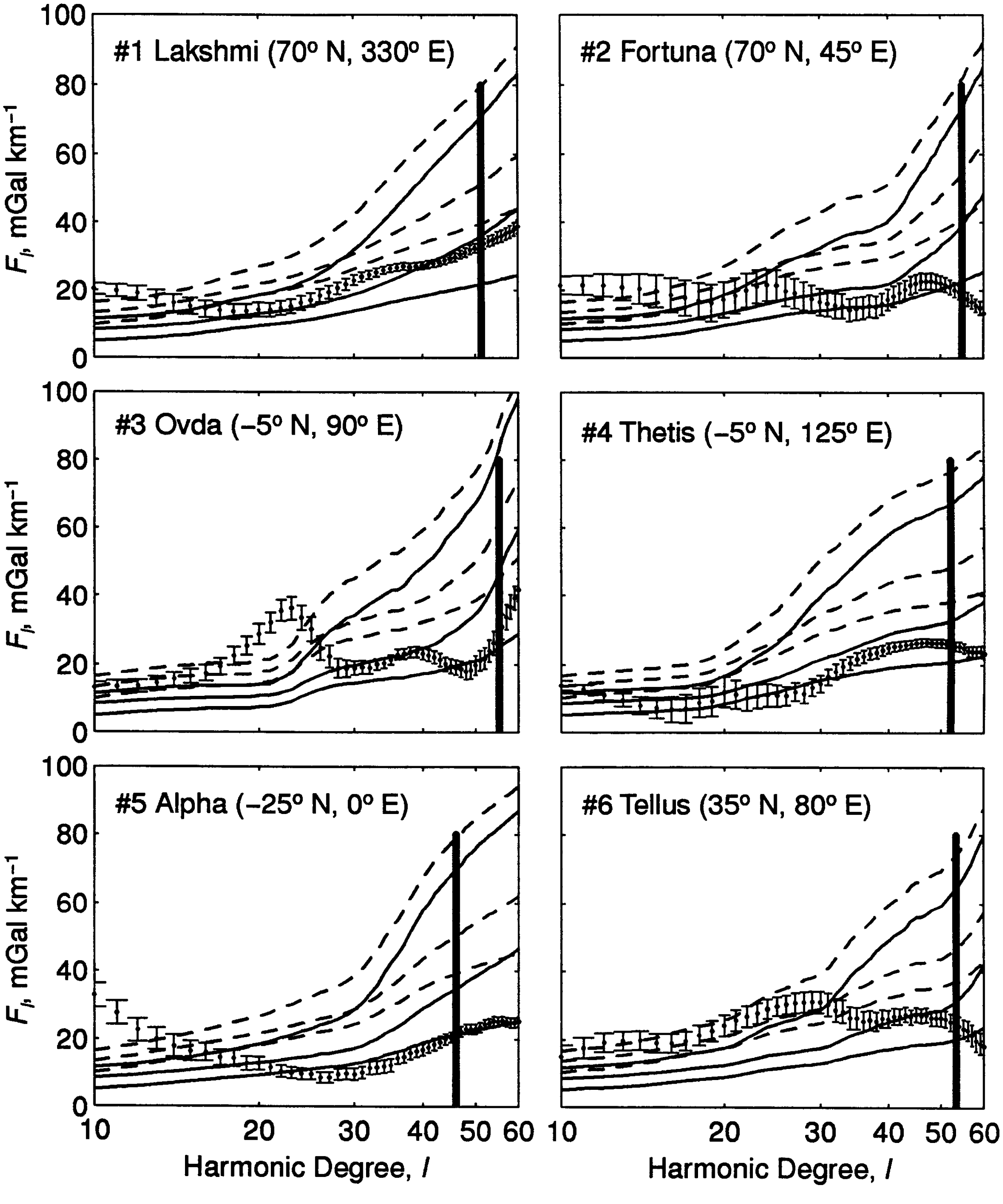

Figure 3.16: Gravity/topography admittance spectra for selected highland plateaus and tessera regions. Theoretical curves for compensation at depths of 25 (solid line) and 50 (dashed line) with effective elastic plate thicknesses of 0, 20, and 40 km (in order of increasing admittance) are shown for reference. The solid vertical line indicates the local Nyquist degree based on the degree strength map shown in figure 3.8.

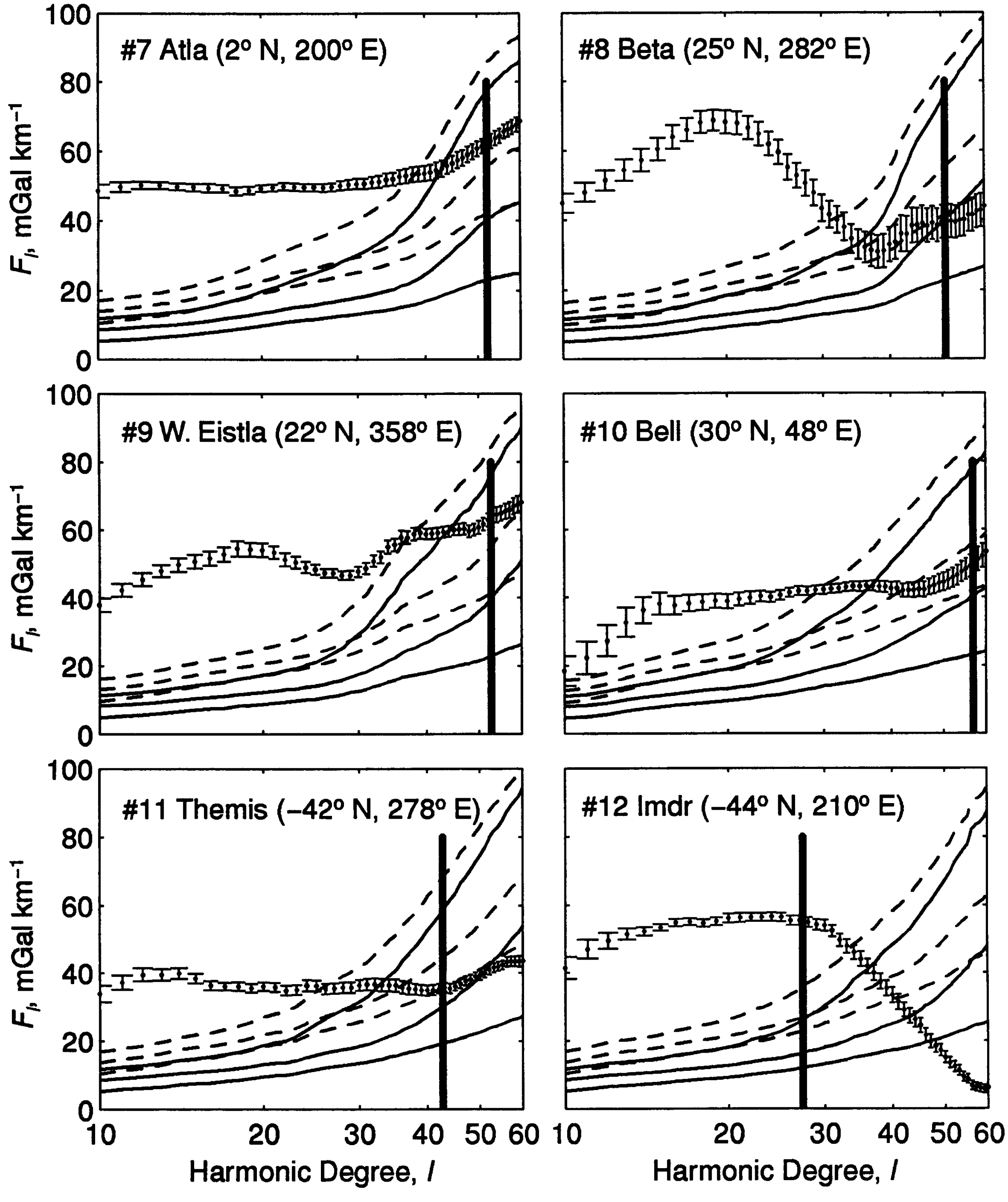

Figure 3.17: Same as figure 3.16 for selected highland swells.

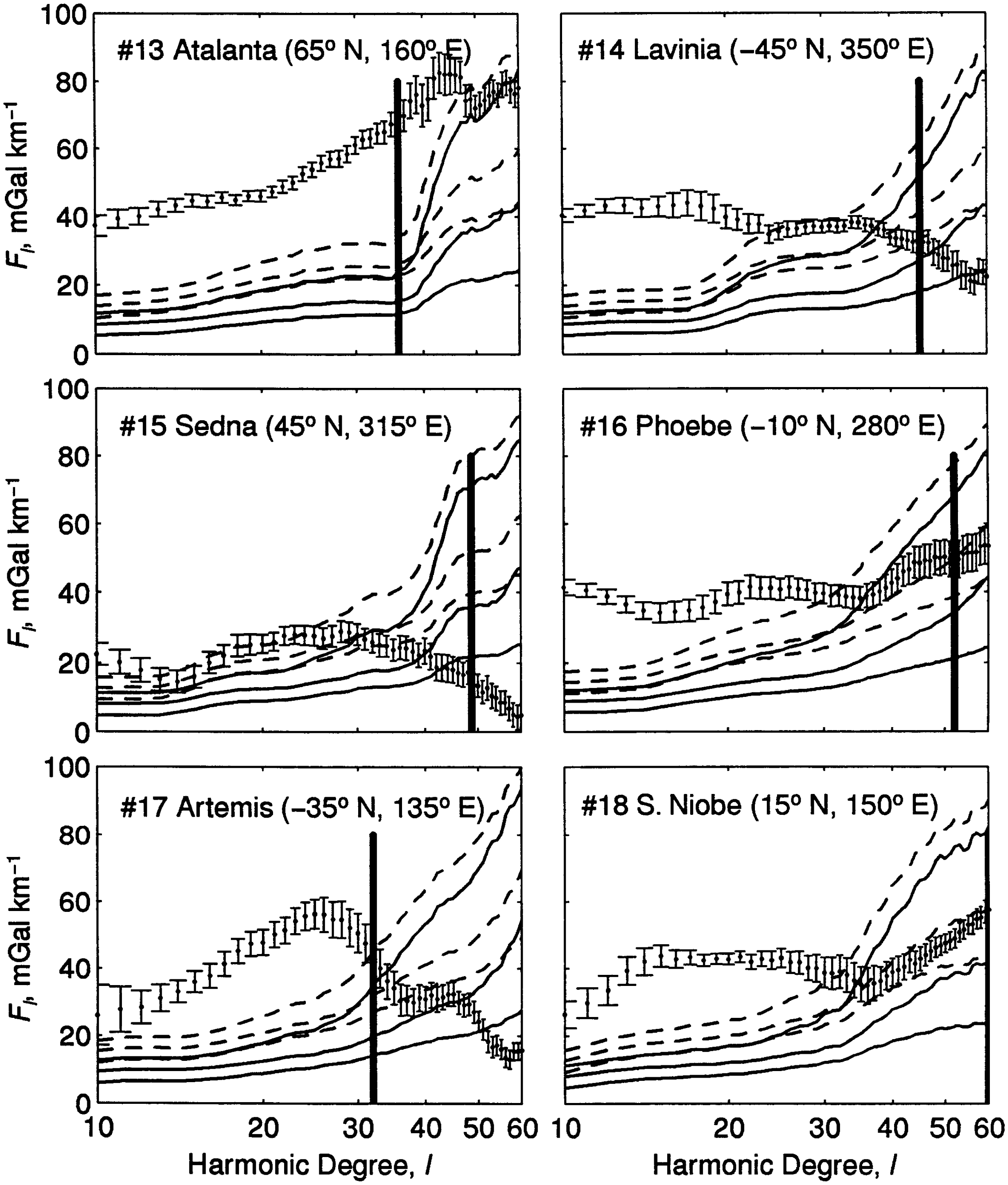

Figure 3.18: Same as figure 3.16 for selected lowlands and planitiae.

swells. Eastern and western Ishtar Terra (figure 3.13, frames 1 and 2) have admittances of about 5 m km^{-1} for $l \geq 18$ ($\lambda \leq 2000$) km, corresponding to an ADC of about 40 km. Convective processes are not required to explain such admittance values. This ADC value differs from an earlier estimate of 180 ± 20 km [*Grimm and Phillips*, 1991], presumably because the admittance derived here incorporates low-elevation data from the nearly circular orbit of Magellan. Aphrodite Terra can be divided into two regions. To the west of 135°E in Ovda and Thetis Regiones (figure 3.13, frames 3 and 4), admittances are 3 to 7 m km^{-1}, whereas to the east in Atla Regio (figure 3.14, frame 7), the admittances are much higher, with values of 20 to 30 m km^{-1}. These values are substantially lower than those computed for previous long wavelength ADC estimates of 70 and 230 km for western and eastern Aphrodite, respectively [*Herrick et al.*, 1989]. We note the bump in the admittance spectrum for Ovda Regio centered at $l = 18$ for which we have no explanation. The admittance for Tellus Regio (figure 3.13, frame 6) is similar to that of Ishtar and western Aphrodite Regiones, all about 4 m km^{-1} for high l. Although Alpha Regio (figure 3.13, frame 5) is also similar to these areas for $l \geq 25$, the admittance increases at small l. This difference at low degrees arises because Alpha has a lateral extent of only about 1500 km, so that longer wavelengths mostly sample the surrounding plains (especially with $f_s = 2$).

The highland swells have much higher admittance values than do the highland plateaus. At long wavelengths, the admittance for Beta Regio (figure 3.14, frame 8) of about 30 m km^{-1} at $l \leq 18$ agrees well with a previous estimate of 31 ± 2 km obtained from PVO data [*Smrekar and Phillips*, 1991]. High admittances are also found in Atla and Eistla Regiones (figure 3.14, frame 9). At degrees between 10 and 20, the results for Eistla agree with those of an earlier regional analysis [*Grimm and Phillips*, 1992], but at higher degrees, the admittances are less, and the implied ADC is shallower. Many of the previous local analyses display this long-wavelength bias. In Bell Regio (figure 3.14, frame 10), for instance, our admittance of about 18 m km^{-1} at long-wavelengths agrees with the result of an earlier regional model [*Smrekar and Phillips*, 1991], but decreases significantly at shorter wavelengths. This bias in previous estimates stems from an implicit reliance on an Airy isostatic model, which our results suggest is not generally valid and, as noted earlier, from the dominance of the long wavelengths given the red spectra of geoid and topography.

None of the admittance estimates for Atalanta, Lavinia Planitia and the other lowlands and plains (figure 3.15) fit a single ADC model. Their spectral behavior is qualitatively similar to that seen in convection calculations, as is discussed later, but it is not possible at this point to say anything quantitative about topographic compensation in these areas on the basis of admittance estimates alone.

In order to avoid biases induced by windowing data with red spectra, *McKenzie* [1994] has suggested that studies of compensation mechanisms should not make use of geoid data but should be restricted to analyses of the gravity field. For completeness, we repeat the preceding analysis using the gravity field instead of the geoid. The local gravity/topography admittance spectra are shown in figures 3.16, 3.17, and 3.18. For reference, we compare the observed admittance estimates with those predicted from models which include elastic support, i.e., models in which the topography is that of a top-loaded plate of elastic thickness T_e and crustal thickness D. The six reference models are for $D = 25$ and 50 km and $T_e = 0$, 20, and 40 km. A value of the elastic plate thickness such that $0 < T_e < D$ implies that only the upper portion of the crust can support finite stresses and that the lower crust is ductile. The difference in the reference curves as a function of region underscores the need to apply the same localization to both the data and the models.

The conclusion that topography in the tesserae and plateaus is primarily Airy compensated is unchanged, as are the ADC estimates. We note that for a few of these regions, there is a suggestion from the slight upturn in F_l at large l that elastic support may play a role in topographic compensation. However, given that our local L_{nyq} probably overestimates the local resolution of the gravity field, it is not clear which spectral features at short length scales are due to elastic support and which are due to noise. We therefore restrict ourselves to concluding that at the time of formation of the topography of the tesserae and compressive plateaus T_e was locally at most 20 km. Not only is this estimate, e.g., for Lakshmi Planum, consistent with the 11 to 18 km estimates of T_e found beneath the Freyja Montes foredeep *Solomon and Head* [1990], but larger values of T_e would presumably be evident in the admittance spectra at length scales resolvable with the current gravity field.

In contrast to the tesserae and plateaus, there is little evidence in the gravity/topography admittances for elastic support over the swells, lowlands and plains. Many of these regions, such as Atla, Themis, and Imdr Regiones, as well as Lavinia Planitia, are remarkable for the flatness of their gravity/topography admittance spectra, with values that range from 40 to 60 mGal km^{-1} depending on the region.

3.6 Interpretation of the Local Admittance

The admittance at all wavelengths is consistently nonnegative for the entire portion of Venus for which the geoid is well resolved and the admittance well constrained. In addition, the mean admittance values for Venus for $10 \geq l \geq 60$ exceed the maximum values observed for the Earth in the same degree range (see chapter 4). High values of admittance from earlier global and regional analyses formed the basis for the hypothesis that Venus lacks an upper mantle low-viscosity zone and thus experiences strong coupling between motions of the convecting mantle and the overlying lithosphere [*Kiefer et al.*, 1986; *Kiefer and Hager*, 1991a,b; *Phillips*, 1990; *Smrekar and Phillips*, 1991]. While these new admittance estimates are consistent with the hypothesis of convective coupling, we will show that it is not possible to distinguish between models with and without a low-viscosity upper mantle.

First, however, we must address the issue of coupling between mantle flow and crustal deformation. There are three types of geological provinces that are important in this discussion: the high plateaus and tesserae, the highland swells, and the plains and lowlands. As described previously, high plateaus and tesserae are regions that are characterized by pervasive compressional features which, together with the large topographic relief, suggest that the crust has deformed (thickened) in response to horizontal shortening. This category includes Western Aphrodite, Ishtar Terra, and the other large tessera regions, such as Alpha and Tellus Regiones. The admittances in these areas suggest crustal thicknesses of between 25 and 50 km. We ask whether these regions represent the surface expression of active crustal shortening and mantle downwelling.

In contrast, on the basis of large admittance values and evidence for extensive volcanism, it is generally accepted that the highland rises Beta, Atla, Bell, Eistla, Imdr, and Themis Regiones overlie sites of mantle upwelling; their high topography results principally from a combination of vertical tractions on the base of the lithosphere and crustal thickening by volcanism and magmatic intrusion. We note that there is no evidence for significant extensional thinning of the crust over regions of upwelling mantle. Impact craters in regions of postulated mantle upwelling show only limited amounts of strain [*Grimm*, 1994b]. What strain is evident in these regions occurs primarily across rifts, which show only limited amounts of horizontal separation. In addition, except for isolated volcanic edifices, rifts show little evidence for voluminous magmatism [*Senske et al.*, 1992], in support of the view that the crust and lithosphere have not thinned sufficiently to generate widespread pressure-release melting.

The plains and lowlands, like the highland rises, have high admittance values that are not well matched by single ADC models. Tectonism in these regions is limited and concentrated at the ridge-belts and wrinkle ridges [*Solomon et al.*, 1992]. However, as with the highland plateaus, we ask whether these regions are the surface expression of mantle downwelling (incipient or fully developed), or whether they are unrelated to the planform of upper mantle flow. In other words, we ask whether mantle downwelling is associated with the lowlands and plains, with some or all of the tesserae and high plateaus, or with all of these provinces.

A model in which the crust acts only as a passive tracer, such that essentially all long-wavelength topography is simply the result of the vertical tractions associated with mantle convection, can fit the observed geoid and topography over the swells and lowlands. In this model, highland swells overlie sites of mantle upwelling, and lowlands overlie sites of mantle downwelling. In such a model, the ridge belts in the lowlands are most likely the expression of limited lithospheric strain induced by mantle downwelling [*Zuber*, 1987; *Zuber and Parmentier*, 1990; *Zuber*, 1990]. However, a model without substantial crustal deformation induced by mantle flow can not explain the large-scale compressional features seen in radar images of the highland plateaus and the pervasive deformation recorded in the tesserae. Thus, this model can only be viable if such regions are postulated to have formed during a now extinct phase of tectonic deformation.

In contrast, if some or all of the compressional highlands can be related to present mantle flow patterns — that is, if the crust currently experiences significant deformation in response to mantle-convective tractions — then the issue of the origin of the lowlands remains. The lowlands have previously been hypothesized to be regions of incipient or fully developed downgoing mantle flow, which eventually mature to states resembling western Aphrodite Terra or Ishtar Terra [*Bindschadler and Parmentier*, 1990; *Bindschadler et al.*, 1990; *Bindschadler and Head*, 1991; *Bindschadler et al.*, 1992b,a; *Zuber*, 1990]. To accomplish such a metamorphosis, the topography must change sign (relative to the global mean elevation) during the evolution of the convective downwelling. The sign of the topography would be dominated by vertical convective stresses (surface depression) in the early stages of evolution and by crustal thickening effects (high topography) in the later stages [*Bindschadler and Parmentier*, 1990]. In the absence of a mechanism by which the sign of the geoid anomaly from a given convective phenomenon changes at the same time as that of the topography, this scenario involves an early lowland period during which admittance is of one sign (for example, negative), a brief period with no appreciable topographic expression when the admittance is unbounded (or the geoid and topography are incoherent), and a late highland period when the admittance has a sign opposite to that of the lowland period (for example, positive) [*Bindschadler and Parmentier*, 1990]. Because observed admittances for both lowlands and highlands are positive and bounded, this model is inconsistent with observation.

By this reasoning, in a model which includes significant convection-driven crustal deformation in the recent past, lowlands must overlie regions where there is no substantial vertical component of upper mantle flow, and a source of stress other than localized downwelling is required to form the ridge belts. One possibility is that the lithospheric instabilities believed to generate the ridge belts arise from shear tractions at the base of the lithosphere. However, this mechanism for ridge belt formation has yet to be explored in detail. In addition, the consistently positive values of admittance, together with observations of crustal deformation, suggest either that surface elevation over downwellings in this model always be positive, or that our present view of Venus includes no juvenile features. If we reject the latter hypothesis by an appeal to uniformitarianism, then the thickening of crust and any buoyant residuum must always be sufficient to overcome the effects of surface downwarping by flow in the underlying mantle.

On the other hand, topography over mantle upwelling must also be positive, requiring that mantle convective uplift and magmatic additions to crustal volume dominate the effects of convectively induced crustal extension and thinning. One possible solution to this apparent paradox is that over mantle upwellings the crust is shielded from convective shear tractions by the strong mantle portion of the lithosphere, such that crustal thinning is either negligible or outweighed by constructional volcanism and magmatic intrusion. In contrast to upwellings, where rising plumes impinge on the base of the lithosphere, the development of convective downwelling instabilities would involve the entire lithospheric boundary layer. In this downwelling scenario, the crust would not be shielded from convective tractions but would deform with the rest of the lithosphere as the instability grows.

Since we reject the model in which lowlands become highland plateaus, the issue of the location of active mantle downwelling revolves around the possibility that the surface manifestation of convection on Venus has dramatically changed in the past. In fact, the density of impact craters on the surface of Venus indicates an average surface age of 300 to 500 million years [*Phillips et al.*, 1991b, 1992; *Schaber et al.*, 1992; *Strom et al.*, 1994]. Furthermore, the low density of craters modified by volcanic flows or deformation suggests that the rate of removal or modification of impact craters has been markedly lower since 500 Ma than before that time [*Phillips et al.*, 1991b, 1992; *Schaber et al.*, 1992; *Strom et al.*, 1994]. Therefore, although the premise that mantle convection couples to the lithosphere provides a basis for our interpretation of the admittance maps, we should distinguish between models in which the styles of surface deformation have been similar for much more than 300 to 500 million years and models in which a significant change occurred at about 500 Ma. We refer to these two classes of models as a steady regime and a variable regime, respectively (figure 3.19). Under a steady regime, all observed surface deformational features can be related to currently active processes. In contrast, under a variable regime, some observed tectonic features are products of processes no longer occurring.

With these definitions, we would categorize Earth as being in a steady regime and Venus in a variable regime. While much of the continents on Earth are old and can be considered as inactive, the processes associated with their formation (e.g., accretion of island arcs and continental collisions) are ongoing processes. We find that the highland plateaus on Venus, like old continents on Earth, are remnants of previous high crustal strain prior to 500 Ma. But in contrast to Earth, the lack of geologic evidence for active tessera formation and the positive and bounded admittances at all length scales and

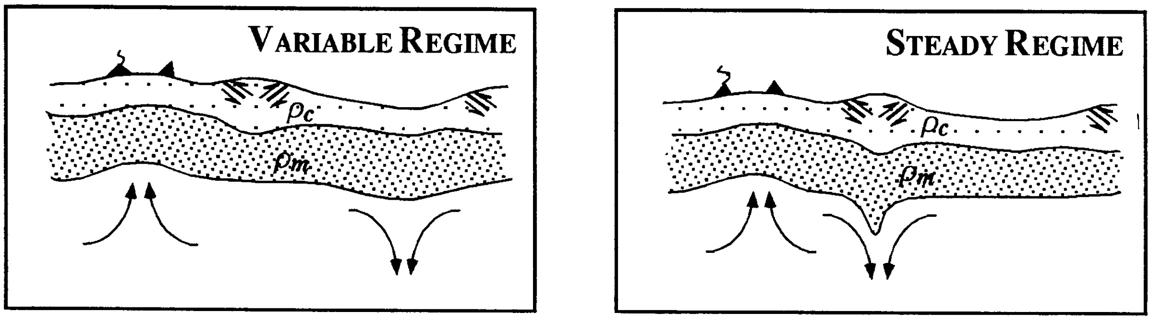

Figure 3.19: Schematic illustration of the two permissible regimes that are consistent with the geoid/topography admittance constraints: The variable regime (left) and the steady regime (right). Curving arrows indicate direction of mantle flow, ρ_c and ρ_m indicate regions with crustal and mantle densities, respectively, and thrust faults symbols denote highland plateaus and tesserae.

positions suggests that the processes responsible for their formation are no longer present. This model for the evolution of the style of crust-mantle coupling on Venus is favored by the results of several recent studies. The tesserae have a higher density of impact craters larger than 16 km in diameter than do the plains, and only one-sixth of the large impact craters in the tesserae have been significantly deformed [*Ivanov and Basilevsky*, 1993]; these results suggest that recent tectonic activity has not been widespread in these regions. Further, new laboratory measurements indicate that the strength of crustal rocks under dry Venus-like conditions is much greater than previously recognized [*Mackwell et al.*, 1995], implying that the large topographic relief and steep slopes found in the crustal plateaus and mountain belts can be maintained over longer time periods than previously assumed on the basis of the high surface temperature and the estimated strength of crustal rocks on Earth. Consistent with these new measurement of creep strength are Earth-like estimates of the thickness of the elastic lithosphere on Venus from the flexural response to volcanic and tectonic loading [e.g., *Johnson and Sandwell*, 1994].

3.7 Mantle Viscosity and Lithosphere Thickness

In the preceding sections, we conclude that the geoid and topography data over approximately 90 percent of the surface are dominated by vertical convective tractions on the base of the lithosphere. Given this inference, we essentially have a crude map of vertical mantle flow in the venusian mantle. Ideally, we could use the admittance estimates to constrain the thermal boundary layer thickness, a necessary parameter in order to constrain heat flow and thermal evolution models. We can already forsee difficulties, however, on the basis of previous theoretical studies that have shown the nonlinear sensitivity of the geoid and topography to the distribution of viscosity and buoyancy forces [e.g., *Richards and Hager*, 1984; *Ricard et al.*, 1984; *Revenaugh and Parsons*, 1987]. These studies are based on the analysis of the dynamic response functions, or kernels, which relate internal density variations to geoid and topography. For flow in a cylindrical domain (r, θ) with only radial variations in viscosity, this relationship can be written as

$$N_l = \frac{4\pi\gamma a}{2l g_0} \int_c^a G_l(r)\, \delta\rho_l(r)\, dr, \tag{3.2}$$

where r is the radius, a and c are the outer and inner radii of the mantle, respectively, N_l, is the geoid, U_l is the geoid kernel at a given radius, $\delta\rho_l$ is the harmonic decomposition of density variations at a given radius, g_0 is the mean gravitational attraction at the surface, and γ is the gravitational constant. A similar expression holds for the topography. The derivation of the kernels for a cylindrical geometry used here can be found in appendix B.

The geoid kernels are very sensitive to variations in mantle viscosity [e.g., *Hager*, 1984; *Richards and Hager*, 1984]. Examples of both topography and geoid kernels are shown for three different viscosity profiles in figures 3.20, 3.21, and 3.22. Each of these figures shows the predicted geoid, topography, and admittance response as a function of harmonic degree and depth of an infinitesimally thin mass sheet. It is worth noting

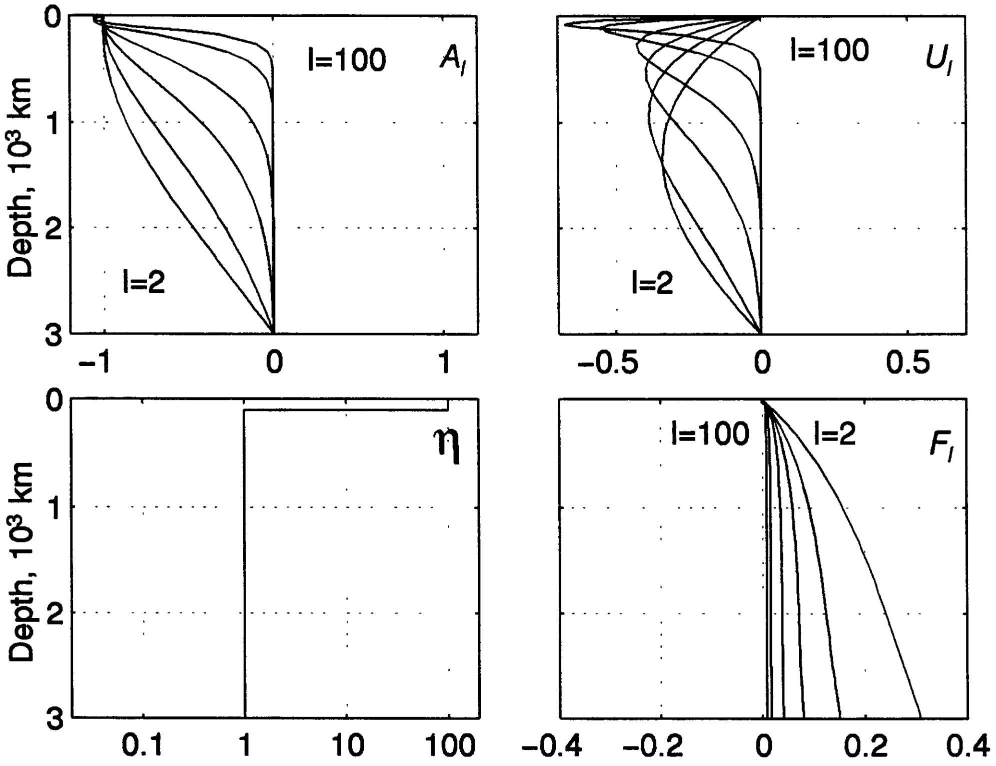

Figure 3.20: Dynamic response kernels for a cylindrical self-gravitating planet. The viscosity model is shown at the bottom left. This model is isoviscous except for a 100-km-thick high-viscosity lid. Topography kernels, A_l, and geoid kernels, U_l, for angular order $l = [2, 5, 10, 30, 50, 100]$ ($l = 2\pi R/\lambda$) are shown top left and top right respectively. The admittance response, F_l, for a sheet mass at a single depth is shown at the bottom right.

that although a given density model can be convolved with the geoid and topography kernels to generate complete spatial fields, the same can not be done for the admittance since it is the ratio of the total geoid and topography fields.

Figure 3.20 shows that for an isoviscous system with a high-viscosity lid, (which is very similar to a model with no lid), a positive density anomaly will generate negative geoid and topography anomalies, and the admittance will therefore always be positive [*Richards and Hager*, 1984]. The topography kernels remain negative for all models in which viscosity only varies with depth. As shown in figures 3.21 and 3.22, this behavior is not true for the geoid kernels. An increase in viscosity with depth can cause the geoid

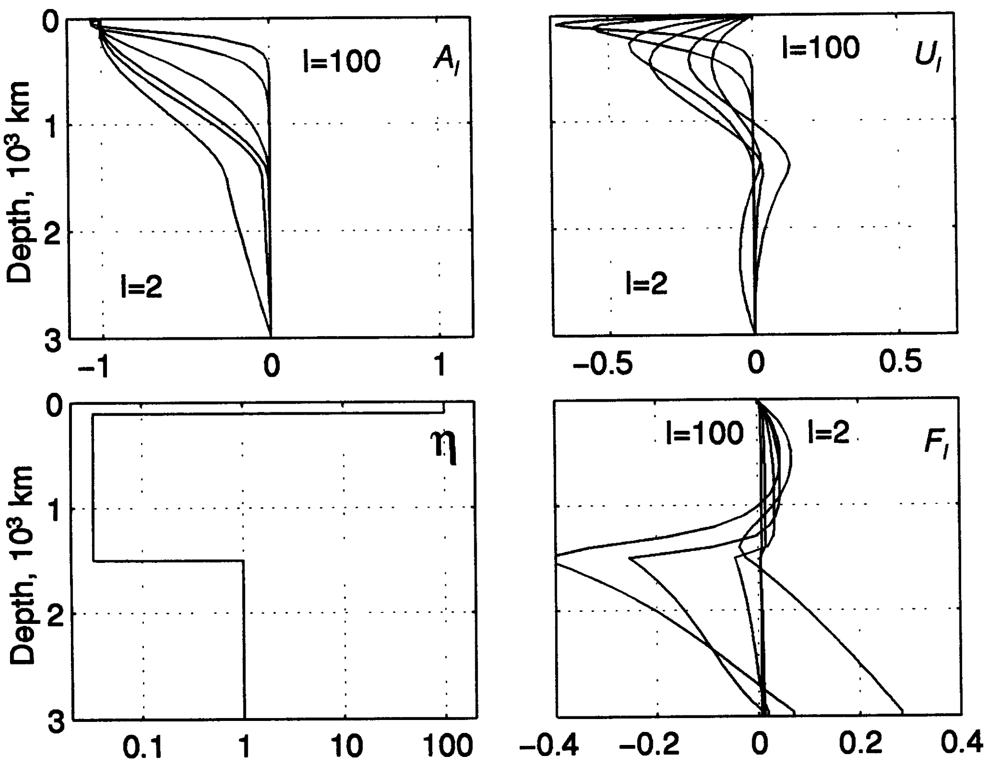

Figure 3.21: Same as in figure 3.20 but with a 30-fold increase in viscosity at 1500 km depth and a 3000-fold increase between the upper mantle and the lid.

kernels to switch sign, so that the final sign (at different length scales) of the complete geoid, and therefore the admittance, is sensitive to both the depths of driving density anomalies and their spectral distributions.

Here we employ a finite element convection model to investigate the viability of using long-wavelength admittance spectra to constrain the TBL thickness and the variation of mantle viscosity with depth. Our model is based on the Cartesian finite-element code developed by *King et al.* [1990] for Boussinesq convection and modified to a cylindrical (r, θ) computational domain by *Zhong and Gurnis* [1993]. From this convection model we calculate topography, geoid, and the resulting admittance as a function of position and wavelength. We use a single density model which we convolve with different viscosity models to show that GTRs and single-ADC models fail to represent our dynamic models

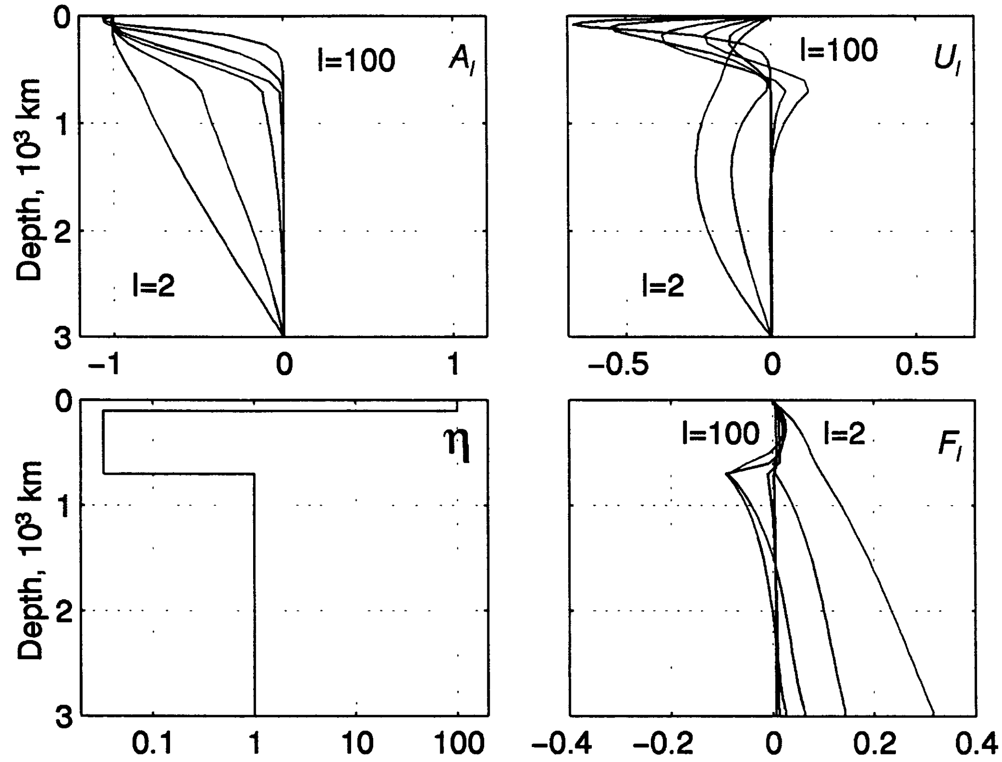

Figure 3.22: Same as in figure 3.21 but with the 30-fold increase in viscosity at 700 km depth.

well. The goal of this exercise is not to provide a match between observed admittances and those calculated from a convection model, nor is it an attempt to investigate fully the effect of the numerous parameters involved on geoid and topography; rather we simply use this model to illustrate that once dynamic stresses are considered, the relationship between admittances and interior density contrasts is sufficiently non-unique that we cannot make inferences regarding the TBL thickness and viscosity structure without additional information.

Our temperature structure is shown in figure 3.23. In generating this snapshot we have applied boundary conditions of no horizontal velocity at the top surface and no shear stress at the bottom surface. The calculation is done using an isoviscous mantle, a Rayleigh number for bottom heating of 10^6, and sufficient internal heat production

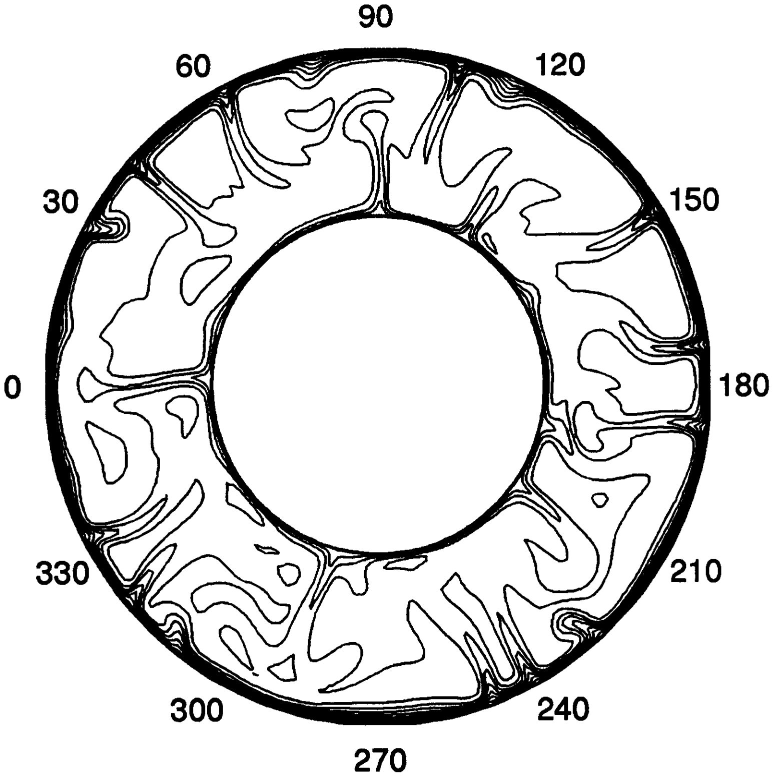

Figure 3.23: Input temperature structure derived from a numerical convection model. Temperature contours are every 250°C.

such that in steady state this model has between 60 and 70 percent internal heating. The model is constructed in this way to provide a density structure that is characteristic of mantle convection in a system with negligible horizontal surface motions, as is appropriate for Venus. We investigate the affects of assuming different radial viscosity models by convolving the temperature (density) field with the previously discussed response kernels. We see in figure 3.24 that even models with a low-viscosity upper mantle generate geoid anomalies with 100's of meters of peak to peak amplitude, and that the characteristic length scales of the features are not affected. As is expected from the kernels, the topography is mostly sensitive to the viscosity variation at shallow depths, and therefore is not affected greatly by the increase in viscosity between the upper and lower mantle. When viewed spatially, we see that topography and geoid are positively

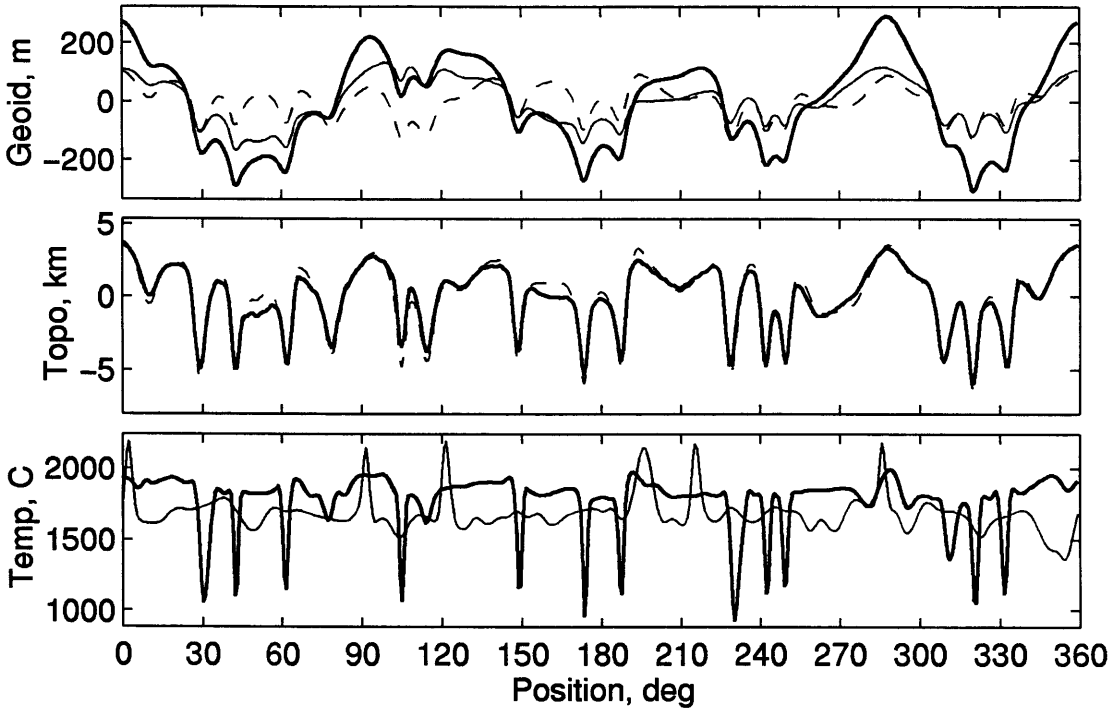

Figure 3.24: Geoid (top) and topography (middle) derived by convolving the temperature field shown in figure 3.23 with three viscosity models; no upper mantle low-viscosity zone (thick line), thin low-viscosity zone (thin line), and thick low-viscosity zone (dashed line). The topography for the first two solutions are not distinguishable on this plot. Bottom: Temperature profiles at constant depths of 500 km (thick line) and 2500 km (thin line).

correlated for all three viscosity models.

Localized geoid/topography and gravity/topography admittance spectra using a conventional wavelet method are shown in figures 3.25 and 3.26 for two regions overlying upwelling mantle and two regions overlying downwelling mantle. The model admittances are not as smooth as the observed admittances for Venus, presumably because the observed admittances are calculated by averaging over azimuths, which is not possible with our two-dimensional model. The geoid/topography admittance spectra over the four regions are very similar, exhibiting the rapid increase in F_l with decreasing l that is characteristic of most of Venus. The effect of a low-viscosity upper mantle, or more explicitly, an increase in viscosity with depth, is to decrease the admittance at low degree.

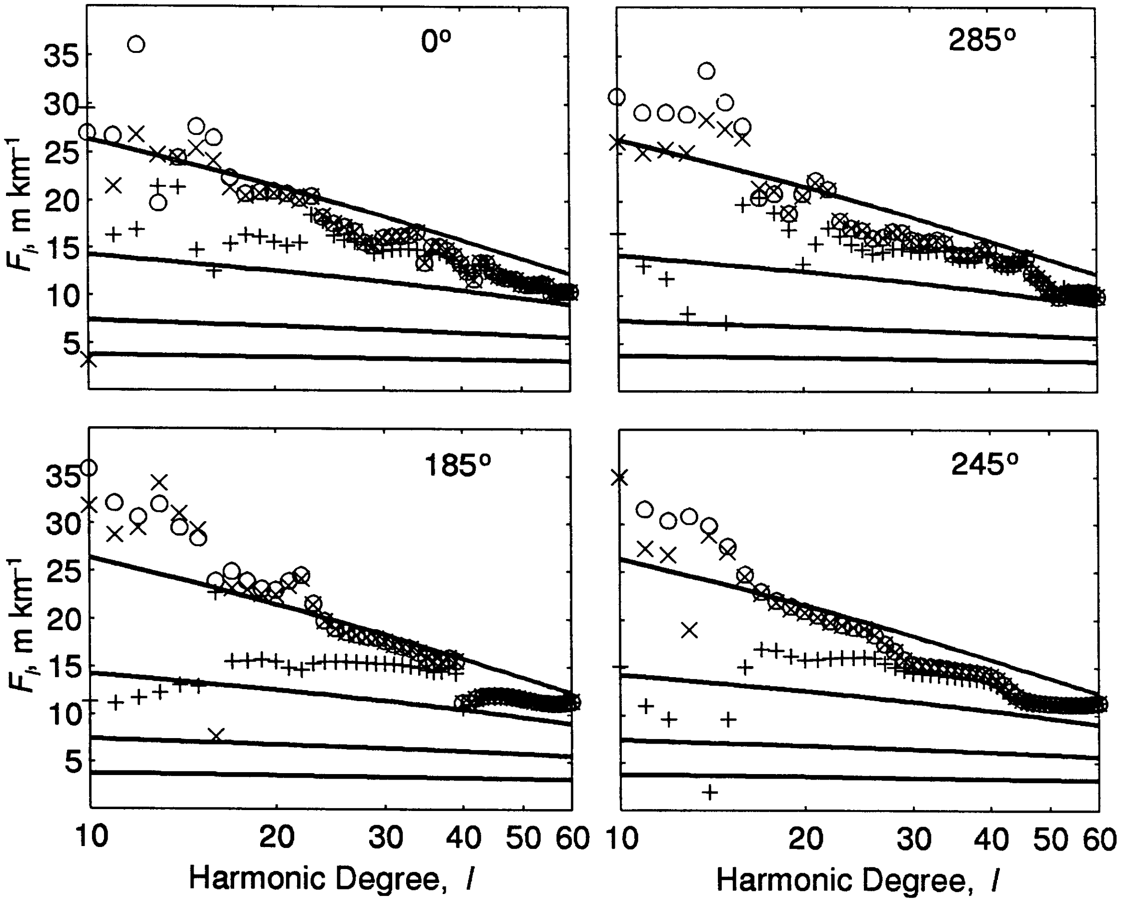

Figure 3.25: Localized geoid/topography admittance spectra for three viscosity models: no upper mantle low-viscosity zone (circles), thin low-viscosity zone (plusses), and thick low-viscosity zone (crosses). The location of each spectrum is indicated at the top right hand corner of each frame. Top frames are for regions of upwelling mantle and bottom frames for regions of downwelling mantle. Spectra for Airy compensation at depths of 25, 50, 100, and 200 km are shown for reference.

As the depth of the increase in viscosity becomes shallower, the admittance deviates from a model with no weak upper mantle at progressively greater values of l. However, in all cases F_l is positive. While not conclusive, it is interesting to note that the observed geoid/topography admittance over many regions on Venus also exhibits flattening at low degree. This behavior may suggest that the venusian mantle indeed has a low-viscosity upper mantle. Indeed, if the jump in viscosity believed to occur between the upper and lower mantle on Earth is related to phase changes, it is not unreasonable to expect the

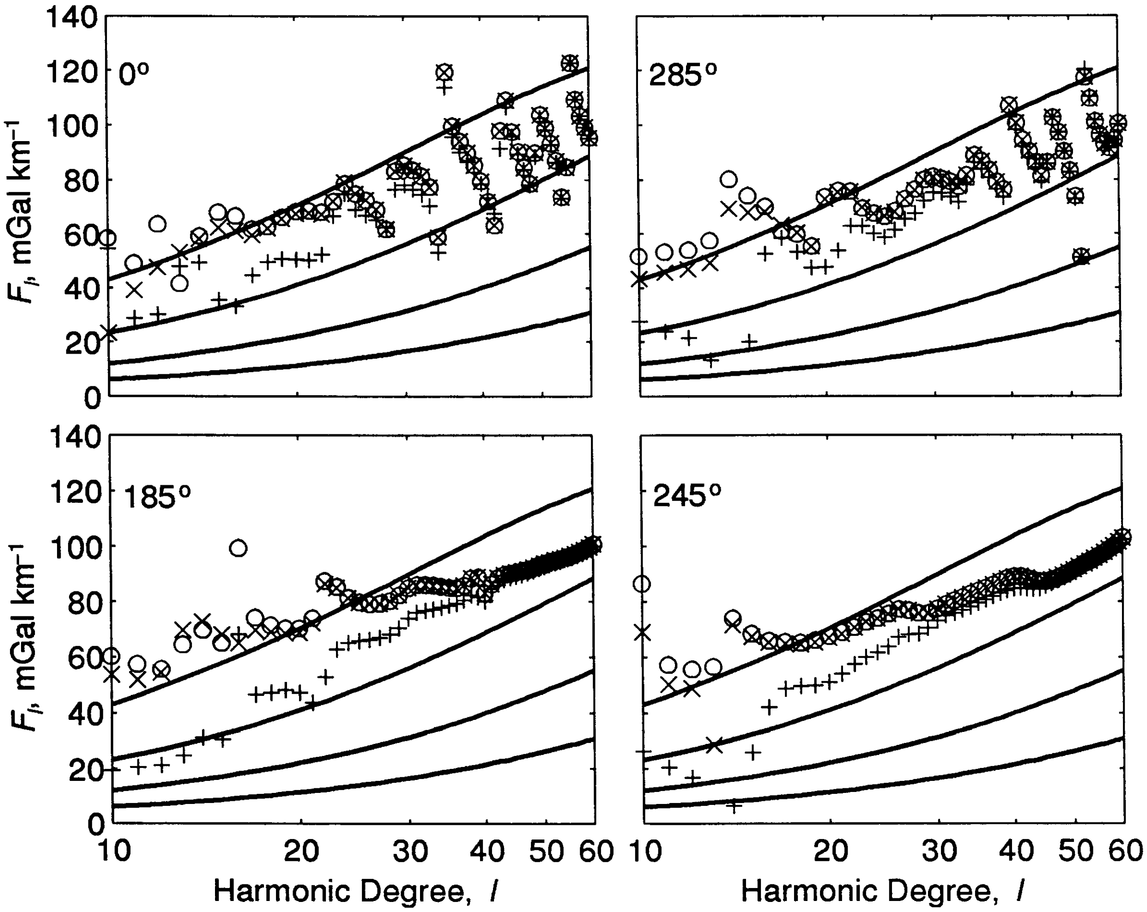

Figure 3.26: Same as figure 3.25 but for gravity/topography admittances.

same jump on Venus.

None of the spectra follow that predicted for a single compensation depth, and by logical extension, the admittance spectra cannot be interpreted in the context of an Airy compensation model. GTRs or other single-ADC models will fail to estimate the TBL thickness because they are static models that do not account for dynamic stresses induced by mantle flow. We note that static compensation models include thermal or Pratt isostasy. We have interpreted the observed admittances in the context of a model in which highland plateaus are remnants of an earlier regime of high crustal strain, the crust does not thicken or thin significantly in response to mantle-convective tractions, and most long-wavelength topography not associated with the earlier regime arises from normal convective tractions at the base of the lithosphere. Given the modelling results presented here, this scenario is able to match qualitatively the slope of the observed admittance specra. However, these values cannot be used to constrain the average TBL thickness on Venus without additional constraints.

Estimates of the effective elastic plate thickness can constrain the TBL thickness [e.g., *McNutt and Menard*, 1982; *McNutt*, 1984; *McNutt and Judge*, 1990]. Published estimates of mechanical plate thickness, T_m, based on elastic plate modelling span a range of 15 to 60 km for coronae, rifts, and volcanoes. If we assume that this depth corresponds to a mantle temperature of 750°C, that the surface is at 500°C, and the interior temperature is 1250°C, we predict a TBL thickness of 50 to 150 km. We also note that the volcanoes have an average surface age between one half and one fourth the average (300 to 500 Ma) age of the plains [*Namiki and Solomon*, 1994], and overlie lithosphere with estimated T_m values in the middle of the 15 to 60 km range [*McGovern*, 1995]. Furthermore, a 50 to 150 km TBL thickness is within a factor of two of that estimated by scaling terrestrial heat flow to Venus [*Solomon and Head*, 1982], assuming that both planets have identical heat production per unit mass and a similar radial distribution of heat producing elements, and that heat loss is solely by steady-state conduction through the lithosphere. Given these assumptions, the estimates of T_m, and the realization that single GTRs or admittance values do not constrain TBL thickness, a 100- to 150-km-thick TBL cannot be rejected on the basis of current geophysical inferences. Furthermore, a 300-km-thick TBL is neither required nor favored by any geophysical observation.

3.8 Conclusions

From the relationship between gravity and topography on Venus, we find that topographic compensation over the highland plateaus and tesserae can be simply explained as the result of Airy isostasy with local mean crustal thicknesses averaging about 25 km and reaching maximum values of about 50 km. Furthermore, at the time of formation the effective elastic plate thickness in these regions was probably less than about 20-km-thick. Because of the consistency with gravity, cratering, and geologic data, we conclude the crust does not thicken or thin significantly in response to present convective tractions. It then follows that the compressional highlands and tesserae are products of past, rather than current, mantle processes, and most other long-wavelength topographic features are principally the result of vertical tractions at the base of the lithosphere.

If this model of topographic compensation is correct, then we are effectively presented with a crude spatial map of the vertical convective motions in the upper mantle. While it is tempting to use admittance estimates to constrain the TBL thickness and mantle viscosity structure, because of the inherent non-linearities involved in mantle dynamics, such efforts are doomed to be inconclusive without a prior model of the interior density structure of the planet. Counter to analyses conducted by others, a qualitative comparison of observed and model-derived admittance spectra suggests that an Earth-like radial viscosity structure and TBL thickness is plausible, and that there is no geophysical evidence that suggests otherwise.

Chapter 4

Localizing Earth's Geoid

4.1 Introduction

Using high resolution global geoid models, we can investigate how different physical processes contribute to the geoid as a function of length scale and position. In this chapter, we begin with a first attempt at non-parametric spatio-spectral localization of the Earth's geoid on a global scale, and discuss the implications for different processes that contribute to the geoid at length scales greater than 800 km. With the guidance and intuition provided by the non-parametric analysis, we use the localization method to provide a decomposition of the geoid parameterized in terms of the known spatial distribution of selected tectonic processes.

The best currently available global model of the geoid for studies of the solid earth, JGM-2G, extends to spherical harmonic degree and order 70 and is based on a combination of satellite tracking data, surface gravimetry, and satellite altimetry observations [*Nerem et al.*, 1994, 1995]. Higher resolution fields exist, but they incorporate topographic information as a constraint in their construction [e.g., *Rapp et al.*, 1991]. The spatial rendition of JGM-2G, referenced to the hydrostatic equilibrium figure [*Nakiboglu*, 1982], is shown in figure 4.1 and the global root-mean-squared amplitude, $\hat{S}_l$, of the geoid

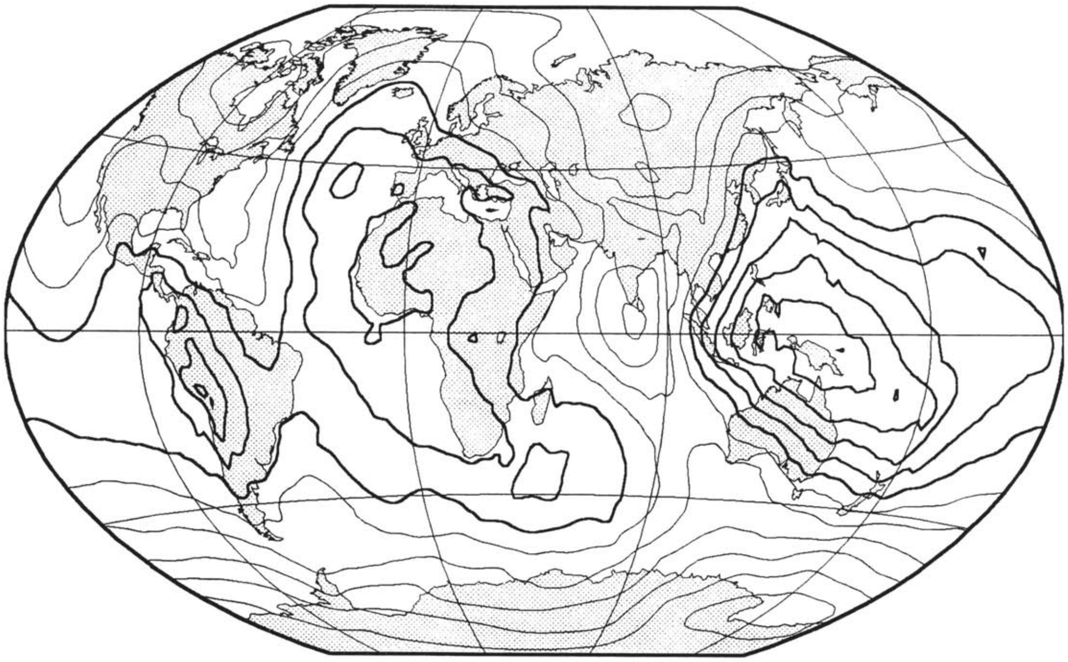

Figure 4.1: Global map of geoid model JGM-2G. Contours every 20 m, $N \geq 10$ m indicated by thick lines and $N \leq -10$ m by thin lines. Unless stated otherwise, all global maps use a Winkel Tripel projection centered at 45° E.

as a function of degree is shown in figure 4.2.

As observed by *Nerem et al.* [1994, 1995], the $\hat{S}_l$ spectrum does not decay with a spectral slope of -2 as predicted by Kaula's rule [*Kaula*, 1963]. In fact, $\hat{S}_l$ has a change in slope around $l = 13$, with a spectral slope of 2.3 for $l \leq 12$ and of 1.6 for $l \geq 13$. This difference from previous geoid models occurs because JGM-2G is the first such model for which sufficient data exist to eliminate the need for damping the geoid solution using Kaula's rule [*Nerem et al.*, 1994]. We do not explore the physical significance of the break in spectral slope here; we note only that wavelengths corresponding to $l = 13$ equal the depth to the base of the mantle and that removing the effect of isostatically compensated topography on the geoid does not appreciably change these spectral characteristics.

Most of the total variance of the geoid can be explained by fluid dynamical models of the mantle [e.g., *Richards and Hager*, 1984; *Ricard et al.*, 1984; *Hager and Clayton*,

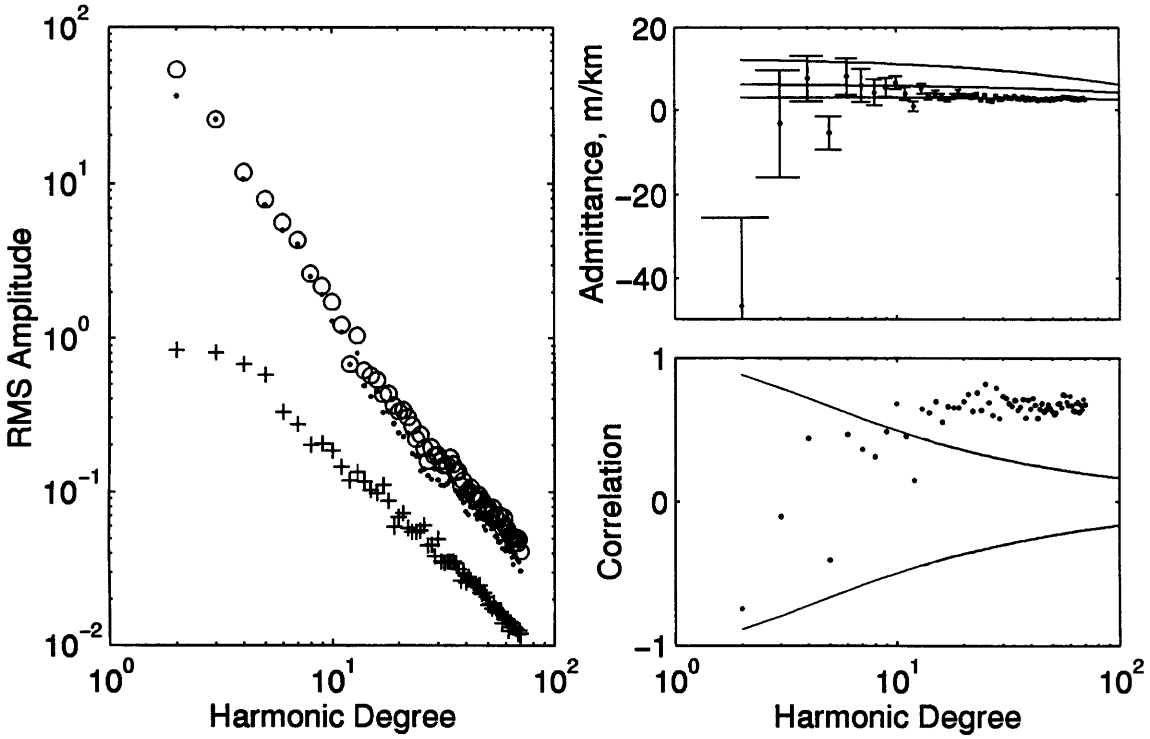

Figure 4.2: Left: RMS amplitude spectra of geoid (circles), topography (crosses), and that part of the geoid which is not correlated with topography (dots). Top Right: Global geoid/topography admittance estimates compared with theoretical Airy admittance curves from equation 4.1 for compensation at 25, 50, and 100 km depth (in order of increasing admittance). Bottom Right: Degree correlation of observed geoid and topography (dots). 98 percent confidence levels are indicated by solid lines.

1989; *Forte et al.*, 1994]. These models depend on the magnitude and location of mantle density anomalies and on the spatial variation of viscosity. A model with only radial variations of viscosity convolved with an assumed model of the density anomalies due to subducting lithosphere and those inferred from seismic tomography can explain 90 percent of the total global variance in the geoid [e.g., *Hager and Clayton*, 1989; *Hager and Richards*, 1989; *Forte et al.*, 1994]. The details of the best fit radial viscosity model are non-unique, but generally incorporate a viscosity increase going from the upper to the lower portions of the mantle, as well as a moderately high-viscosity surface layer [e.g., *Hager*, 1984; *Richards and Hager*, 1988; *Forte et al.*, 1994]. The viscosity model and

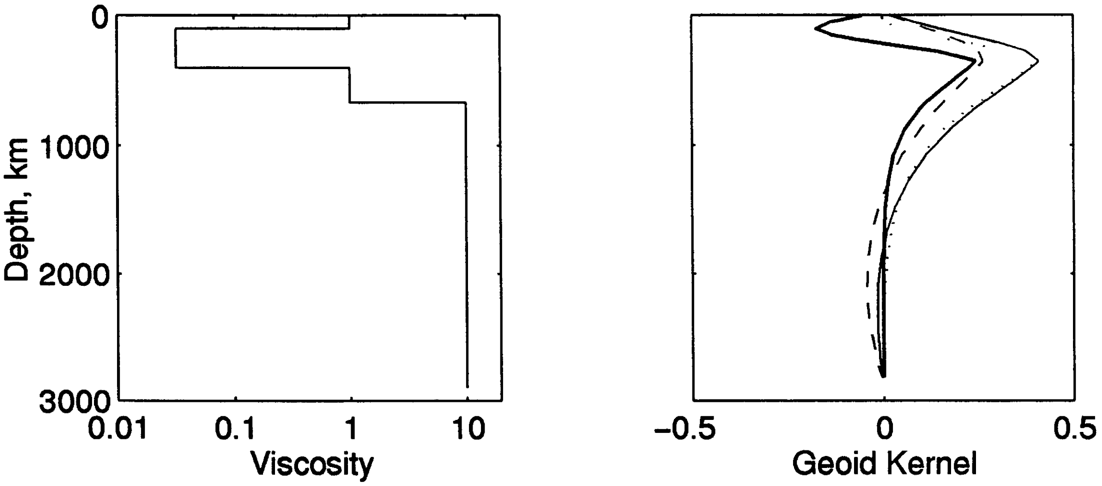

Figure 4.3: Left: The favored radial viscosity model of *Hager and Clayton* [1989]. Right: The corresponding geoid response kernels for l =2 (dashed line), 4 (thin solid line), 8 (dotted line), and 16 (thick solid line).

corresponding geoid response kernels for one such successful model is shown in figure 4.3 [*Hager and Clayton*, 1989]. The salient feature of this model is the increase in viscosity with depth, which causes the geoid kernels at the lowest degrees to be positive in the upper mantle (i.e., a positive density anomaly would produce a positive geoid anomaly) and negative in the lower mantle.

It is worth noting that the success of a given flow model is usually measured by global variance reduction. However, because of the red spectrum of the geoid, most of the variance reduction is accomplished by matching the longest wavelengths of the geoid. In particular, the aforementioned 90 percent variance reduction is found using only the $l = 2, 3, 4$ components from global seismic tomography models and $l = 2$ through 9 of the subduction model [e.g., *Hager and Richards*, 1989]. While convective processes undoubtedly contribute to the higher degrees of the geoid, their inclusion in the current generation of flow models increases the variance of the geoid [e.g., *Hager and Richards*, 1989].

In addition to global flow models, we can consider the global covariance of geoid with topography. At $l < 10$ the global correlation, $\hat{r}_l$, between the two fields is either anticorrelated or insignificant (figure 4.2). However, at higher degrees the global correlation is positive and significant above the 98 percent confidence level [e.g., *Rapp*, 1982]. The global geoid/topography admittance, $\hat{F}_l$, at these shorter wavelengths is consistent with an Airy compensation model, with compensation at depths of about 25 km (figure 4.2). However, this estimate is deceptive since it is global, combining a multitude of tectonic provinces. The geoid predicted by using the global admittance fails to reduce the degree variance of the geoid markedly, as is shown by the $\hat{S}_l$ spectra of the residual field (figure 4.2).

Given that the geoid model is complete to degree and order 70, we would like to develop a description of the geoid that includes both the longest and the shortest wavelengths, one that permits us to evaluate the success of synthetic models as a function of position and length scale. With this perspective, we can isolate where and at what length scales to look for anomalous signal related to specific geologic regions and phenomena. We begin with an attempt to explain the observed localized structure using a series of simple forward models, consisting of crustal thickness variations, ocean-continent differences, and oceanic plate cooling. We also include the effects of oceanic trenches, which we treat as uncompensated [*Chase and McNutt*, 1982].

At long wavelengths the localized geoid is dominated to a greater extent by processes associated with mantle convection and to a lesser extent by the effects of incomplete glacial rebound. The gravity signature of these processes has been the focus of extensive modelling efforts. Here, we take a different approach by using the localization transform to perform a tectonic decomposition of the gravity field. In other words, given an *a priori* estimate of the spatial distribution of a tectonic phenomenon (e.g., subduction zones, hotspots, and ice melting history), we determine the global average of the geoid which is locally correlated with each phenomenon. Limited by the resolution of the observed geoid, our slab, hotspot, and glacial rebound geoids extend to $l = 46$. We compare our slab and hotspot geoids with those derived by dynamic flow modelling, although due to limitations in the flow models, this comparsion can only be done at low harmonic degree. Similarly, we develop a glacial rebound geoid that represents the minimum geoid anomaly that can be expected from incomplete glacial rebound and compare our rebound geoid with predictions made from published viscosity models.

4.2 Observed Geoid and Topography

For illustrative purposes, we begin with localizing a spherical harmonic rendition of topography. Here, and in all subsequent use of topography, we use the spherical harmonic degree and order 360 expansion of equivalent rock topography (ERT360) derived by ***Pavlis and Rapp*** [1990], in which ice and water are replaced with the equivalent mass of crustal rock.

Our analysis produces localized spectra, S_l, for all positions. We present these spectra as global maps for fixed l and as spectrograms of S_l versus position along great circle profiles. The maps and spectrograms are presented as ΔS_l, i.e., deviations of S_l about $\overline{S_l}$, the global average value at each l. Thus, ΔS_l has negative as well as positive values. We apply this l-dependent shift to establish a useful baseline on which to compare results at different l; otherwise the red spectra characteristic of geoid and topography would dominate the figures. As shown in chapter 2, a purely harmonic input field would appear in the ΔS_l maps as as having little or no spatial variation at the particular frequency of the input data, and an isolated discontinuity in the input data would result in power at all degrees, centered at the position of the discontinuity.

The ΔS_l spectra do not vary rapidly with l; therefore we only show maps for selected l. The maps for ERT360, using a scaling parameter, f_s, equal to 1 and 2, are shown in figures 4.4 and 4.5, respectively. ΔS_l estimates with $f_s = 1$ have more spatial resolution and less spectral resolution than the $f_s = 2$ estimates. $f_s = 1$ also has a localization

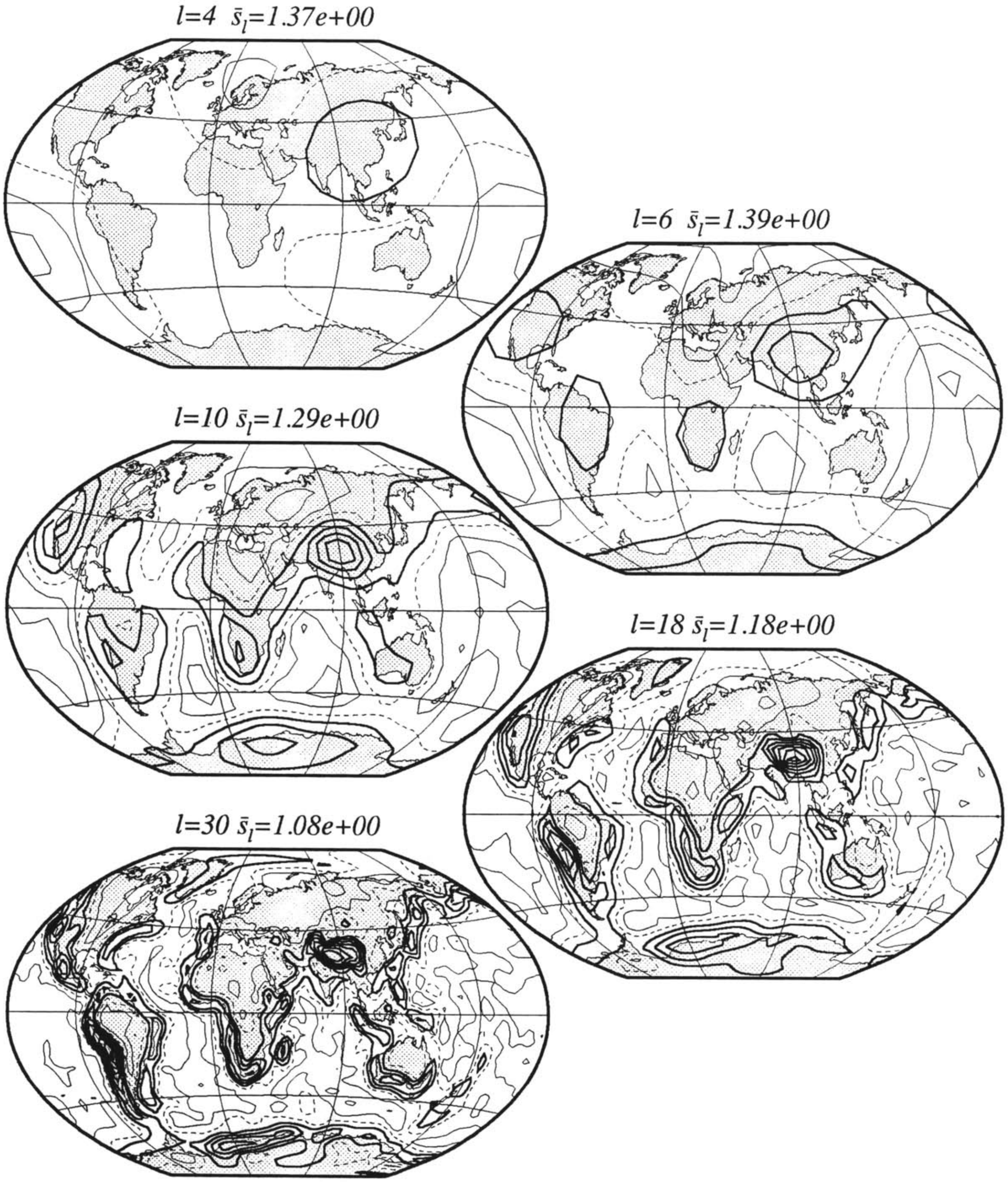

Figure 4.4: ΔS_l of topography with $f_s = 1$. Contour interval is 400 m. All ΔS_l maps are shown with thick lines for $\Delta S_l > 0$, dashed line for $\Delta S_l = 0$, and thin lines for $\Delta S_l < 0$.

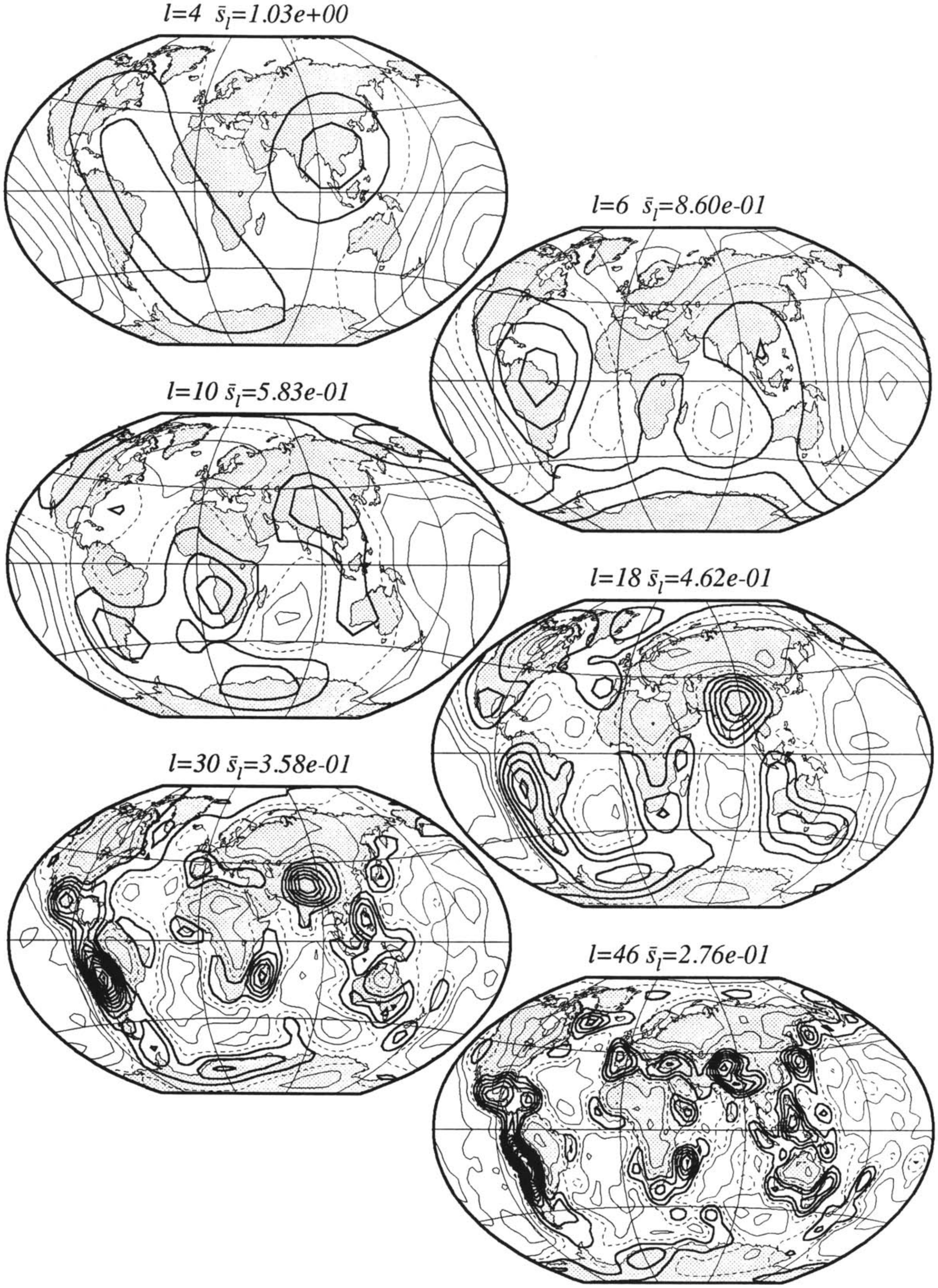

Figure 4.5: ΔS_l of topography with $f_s = 2$. Contour interval is 100 m.

Nyquist degree, L_{nyq}, of 35 in contrast to a value of 46 for $f_s = 2$. We emphasize that ΔS_l is a measure of the variation, but not the sign, of the original signal. At the highest l shown, the localization operator becomes a discontinuity detector, isolating ocean-continent boundaries, oceanic trenches, and regions of steep mountainous terrain. All of these regions can effectively be considered as step or delta functions. ΔS_l has minima at high l in the middle of continents and oceanic basins, both of which are regions with relatively little topographic variation. At lower l, ΔS_l is high over most of the continents and is lowest over the Pacific.

Maps of ΔS_l for JGM-2G, using $f_s = 1$ and 2, are shown in figures 4.6 and 4.7, respectively. For $f_s = 1$ at $l = 4$, we see a tennis ball pattern, with a broad maximum spanning nearly from pole to pole and passing over central Asia, Indonesia, Australia, and Antarctica, and a broad equatorial minimum spanning from Africa to the central Pacific. We find a similar pattern when using $f_s = 2$. Regions of subduction are associated with ΔS_l highs at all scales and for both values of f_s. In particular, they dominate the geoid for $l < 10$, which is consistent with the conclusions reached from a global analysis [*Hager*, 1984].

We also find ΔS_l maxima at $l \geq 6$ over Hudson Bay and Antarctica, presumably attributable to the mass deficiencies caused by incomplete rebound from the last deglaciation. For $l \geq 18$, there are ΔS_l maxima over the Andes, the Tibetan plateau, and regions north of the plateau. In addition, a clear maximum south of India for $l \geq 10$, over the so-called "Sri Lankan low", is seen with $f_s = 1$ but not with $f_s = 2$. To explain this dependence on f_s we must recognize that as f_s gets smaller, we approach a situation where localization returns the spatial magnitude of the geoid, i.e., the absolute value of the original signal convolved with a spatial delta function. However, as f_s gets larger, we are able to localize the characteristic length scales much better, enabling us to resolve a large amplitude but short length-scale feature over the Himalaya and Tibet, as well as a large length scale feature over most of central Asia and the Indian Ocean. The Sri

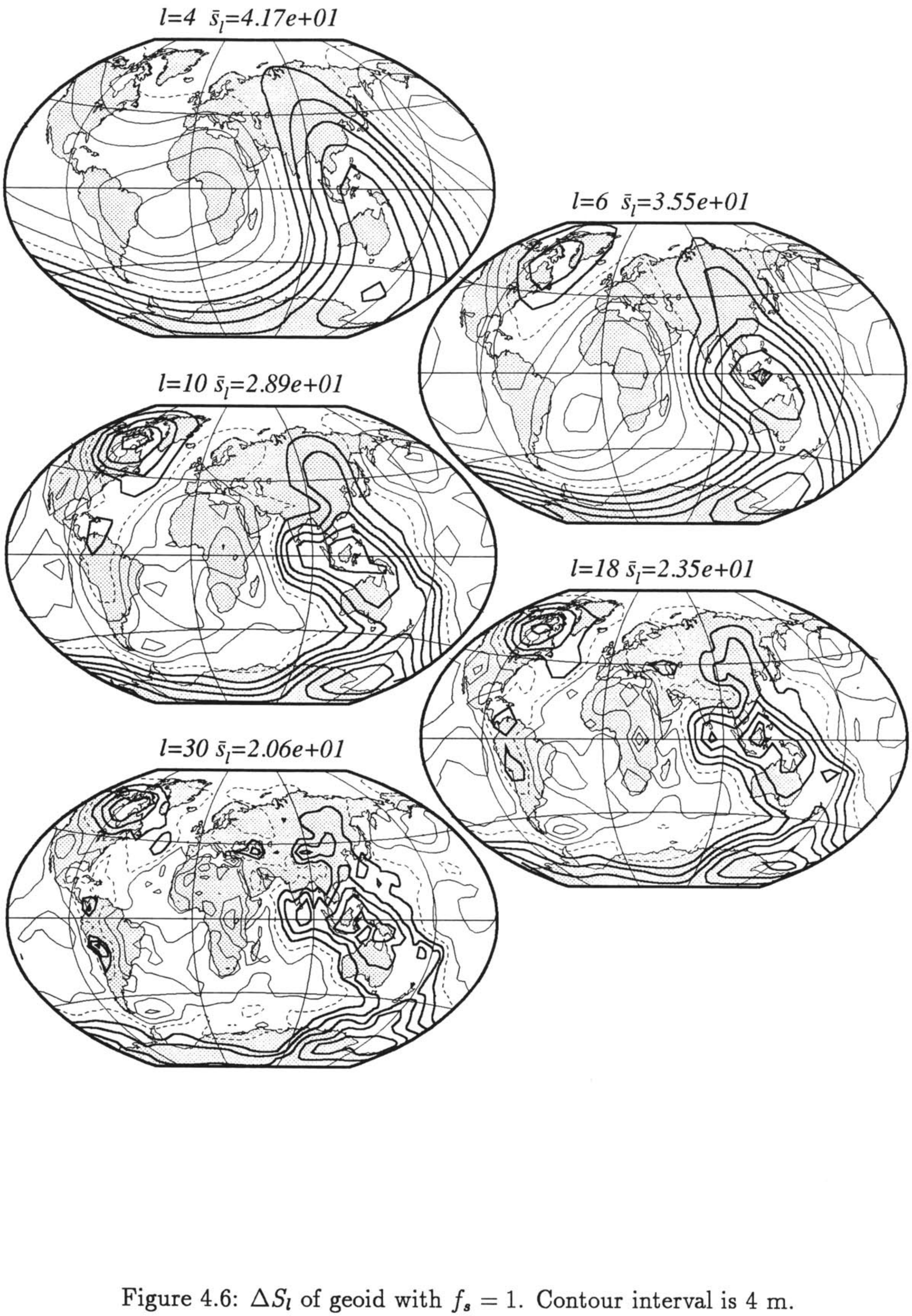

$l=4$ $\bar{s}_l=4.17e+01$

$l=6$ $\bar{s}_l=3.55e+01$

$l=10$ $\bar{s}_l=2.89e+01$

$l=18$ $\bar{s}_l=2.35e+01$

$l=30$ $\bar{s}_l=2.06e+01$

Figure 4.6: ΔS_l of geoid with $f_s = 1$. Contour interval is 4 m.

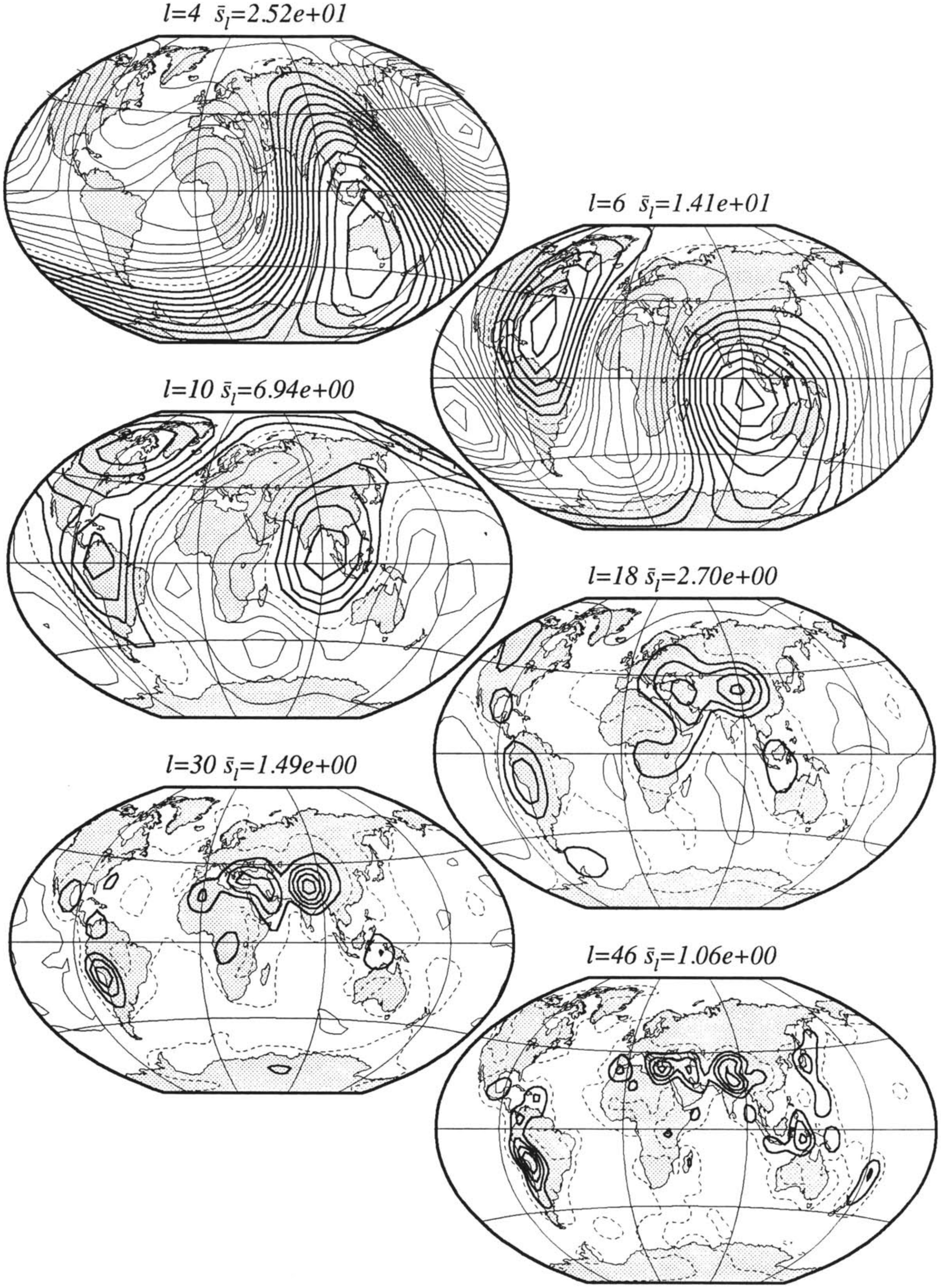

Figure 4.7: ΔS_l of geoid with $f_s = 2$. Contour interval is 1 m.

Lankan low is discussed further in the description of the spectrograms.

At high l, we find what appears to be better spatial localization using $f_s = 2$, with clear maxima over all the trenches. The unexpected apparent increase in spatial resolution with increased f_s stems from the long wavelength bias is introduced by spectrally smoothing the red spectrum that is characteristic of the geoid. The higher the value of f_s, the less bias introduced. Alternatively, instead of the geoid, one can consider the gravity field which, although still red, has a spectral slope which is decreased by a factor of $(l+1)$. ΔS_l for the gravity field with f_s equal to 1 and 2 is shown in figures 4.8 and 4.9, respectively. As expected, comparing the two maps for $l = 30$, we find that $f_s = 1$ has better spatial resolution than $f_s = 2$.

We next consider the ΔS_l spectrograms of the geoid using $f_s = 2$ for seven great circle profiles. The location of each spectrogram is indicated in figure 4.10. The spectrograms are labelled A through G, and referred to as SpA, SpB, and so on (figures 4.11 through 4.17). For each path we show the geoid in an oblique Mercator projection for which the equator is the great circle path, a profile of the geoid along the path, and the spectrogram. We emphasize that the geoid profile is shown only for reference, and that the analysis is fully two-dimensional.

Regions containing steep gradients in the geoid (and topography), such as the Andes (SpA, figure 4.11), the Himalaya (SpB, SpD, and SpE, figures 4.12, 4.14 and 4.15), and Central America (SpB, figure 4.12), are all characterized by spatially localized spectral ridges, reminiscent of the examples containing discontinuities shown in chapters 1 and 2. It is notable that these spectral ridges extend up to wavelengths associated with $l = 10$. In other words, the processes associated with these short length-scale features have clear signatures at wavelengths as great as 4000 km.

By inspection of the geoid profile or the spectrogram (SpD, figure 4.14), it appears that the Sri Lankan low may be the result of combining a short length-scale positive anomaly over Tibet and a longer length-scale positive anomaly in the Southern Indian

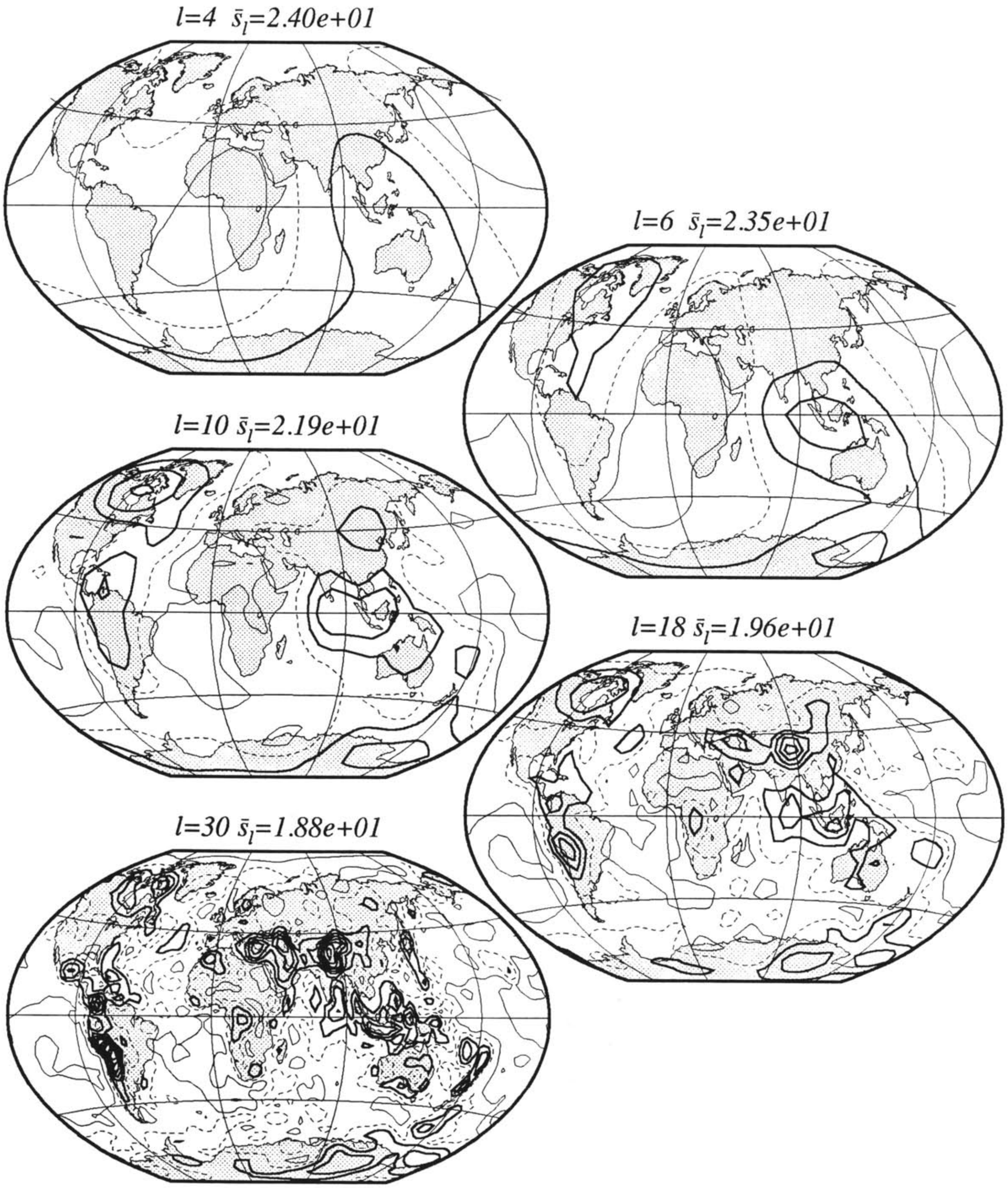

Figure 4.8: ΔS_l of gravity with $f_s = 1$. Contour interval is 8 mGal.

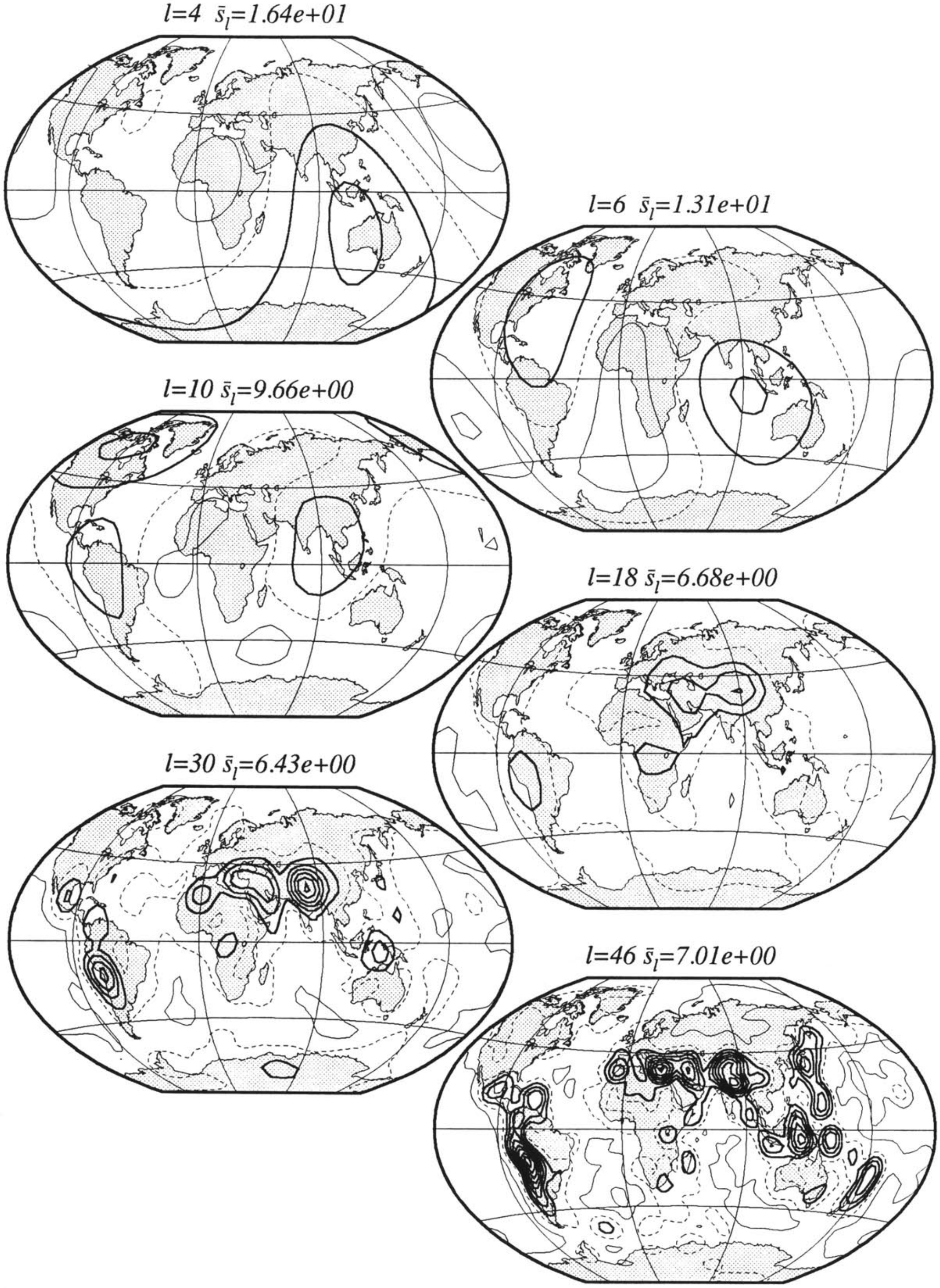

Figure 4.9: ΔS_l of gravity with $f_s = 2$. Contour interval is 4 mGal.

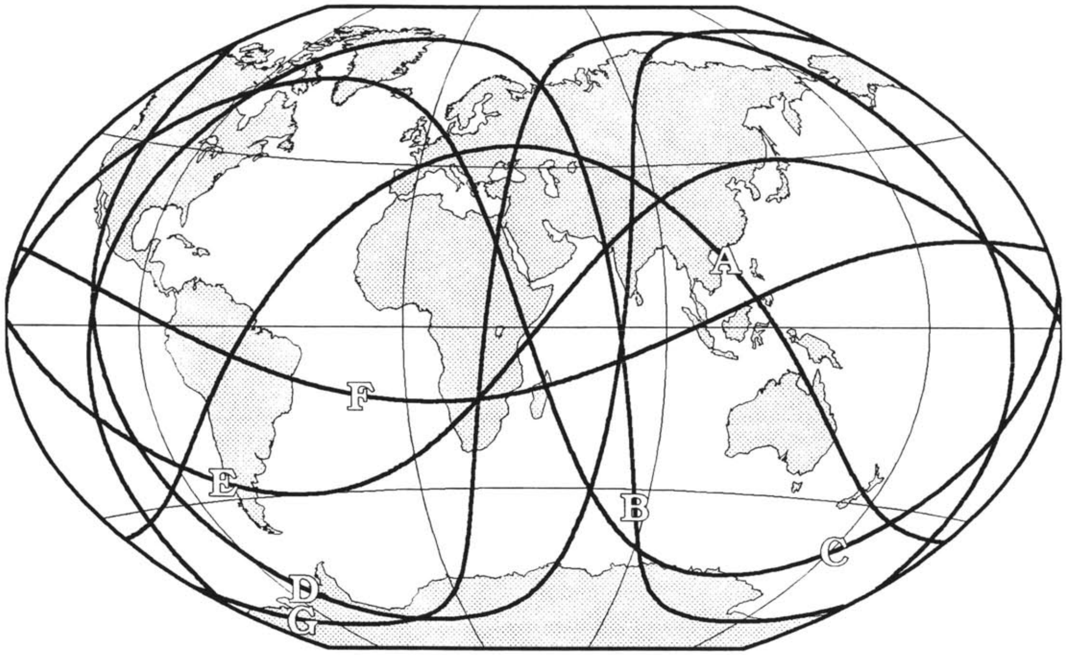

Figure 4.10: Location of great circle profiles shown in figures 4.11 through 4.17.

Ocean. The former is probably related to crustal thickness variations and the latter is possibly related to the swell responsible for Kerguelen and the other hotspots in the region. This hypothesis differs from previously proposed explanations for the Sri Lankan geoid low which include the effect of topography at the core-mantle boundary [*Bowin*, 1986, 1991] and small-scale convection in the upper mantle [*Stark and Forsyth*, 1983; *Phipps Morgan et al.*, 1995]. Thus, given the results presented here, instead of looking for structure in the mantle at the scale of the Sri Lankan low (about 2000 km) centered south of India, one should consider structures at much shorter scales centered over Tibet as well as larger structures on the scale of the Southern Indian Ocean.

Hudson Bay (SpB and SpC) is characterized by a geoid anomaly that is localized both in space and in length scale, with a peak ΔS_l value at $l \approx 9$ corresponding to length scales of about 4000 km. The negative geoid and free-air anomalies in this region have been the focus of extensive analysis in the context of Pleistocene deglaciation models

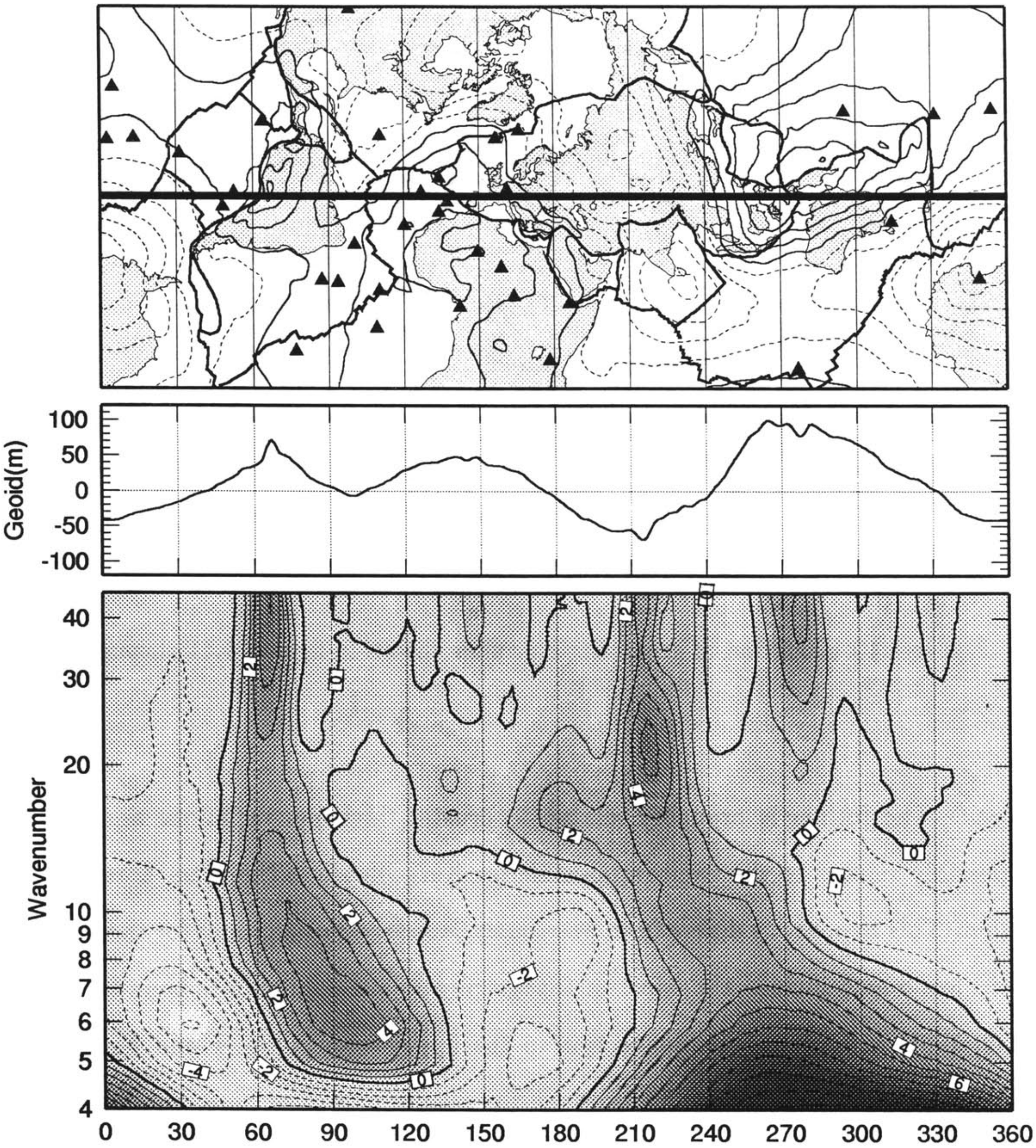

Figure 4.11: Great circle profile A (SpA). Figures 4.11 through 4.17 are presented identically. Top: Location map including plate boundaries, hotspots (triangles), and the geoid contoured at 20 m intervals, with $N \geq 10$ m indicated by solid lines and $N \leq 10$ m by dashed lines. Middle: Geoid profile along great circle path. Bottom: ΔS_l as a function of l and position in degrees along the great circle. $\Delta S_l > 0$ indicated by thin lines, $\Delta S_l = 0$ by thick lines, and $\Delta S_l < 0$ by dashed lines. Contour interval is 1 m.

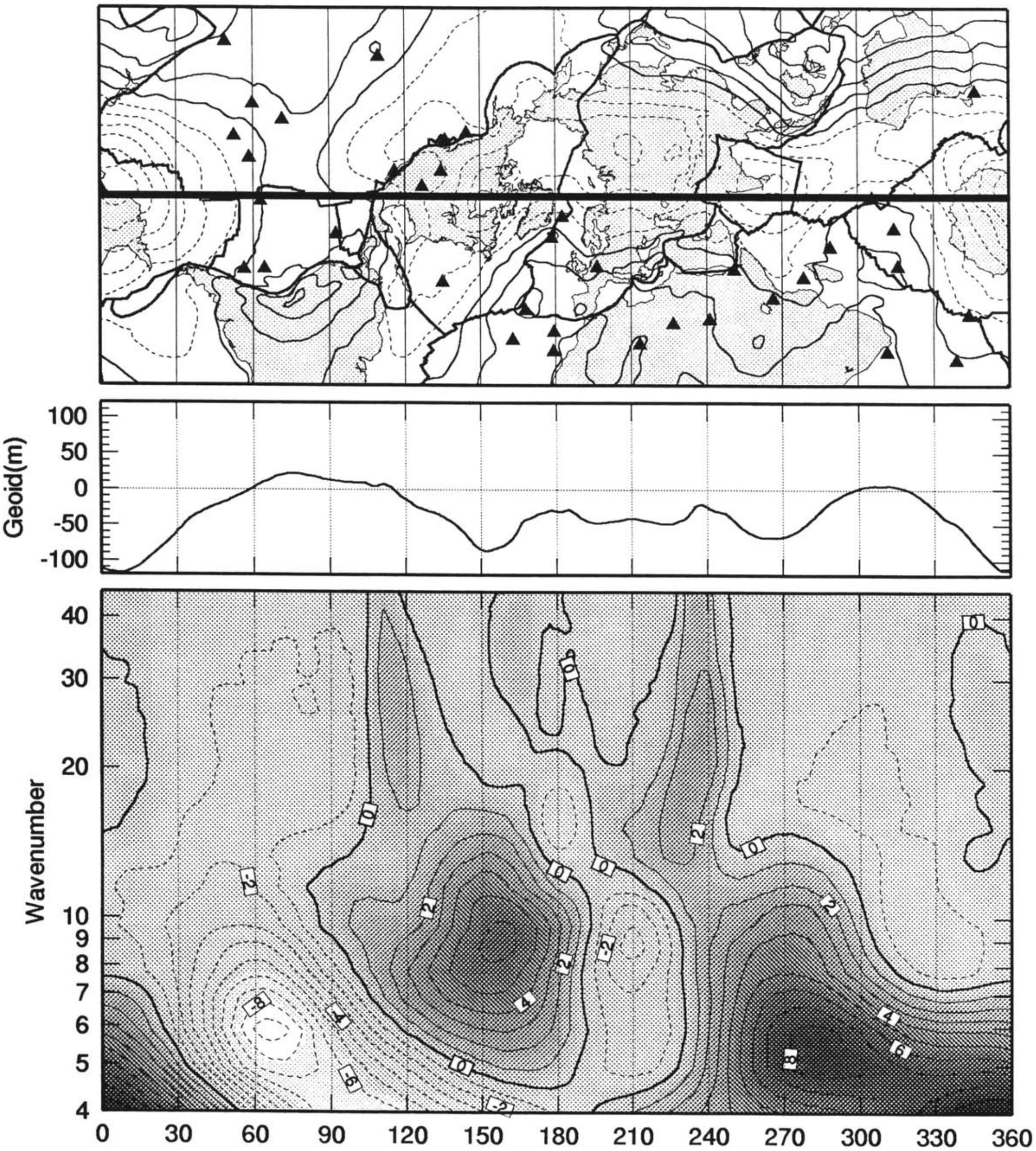

Figure 4.12: Great circle profile B (SpB).

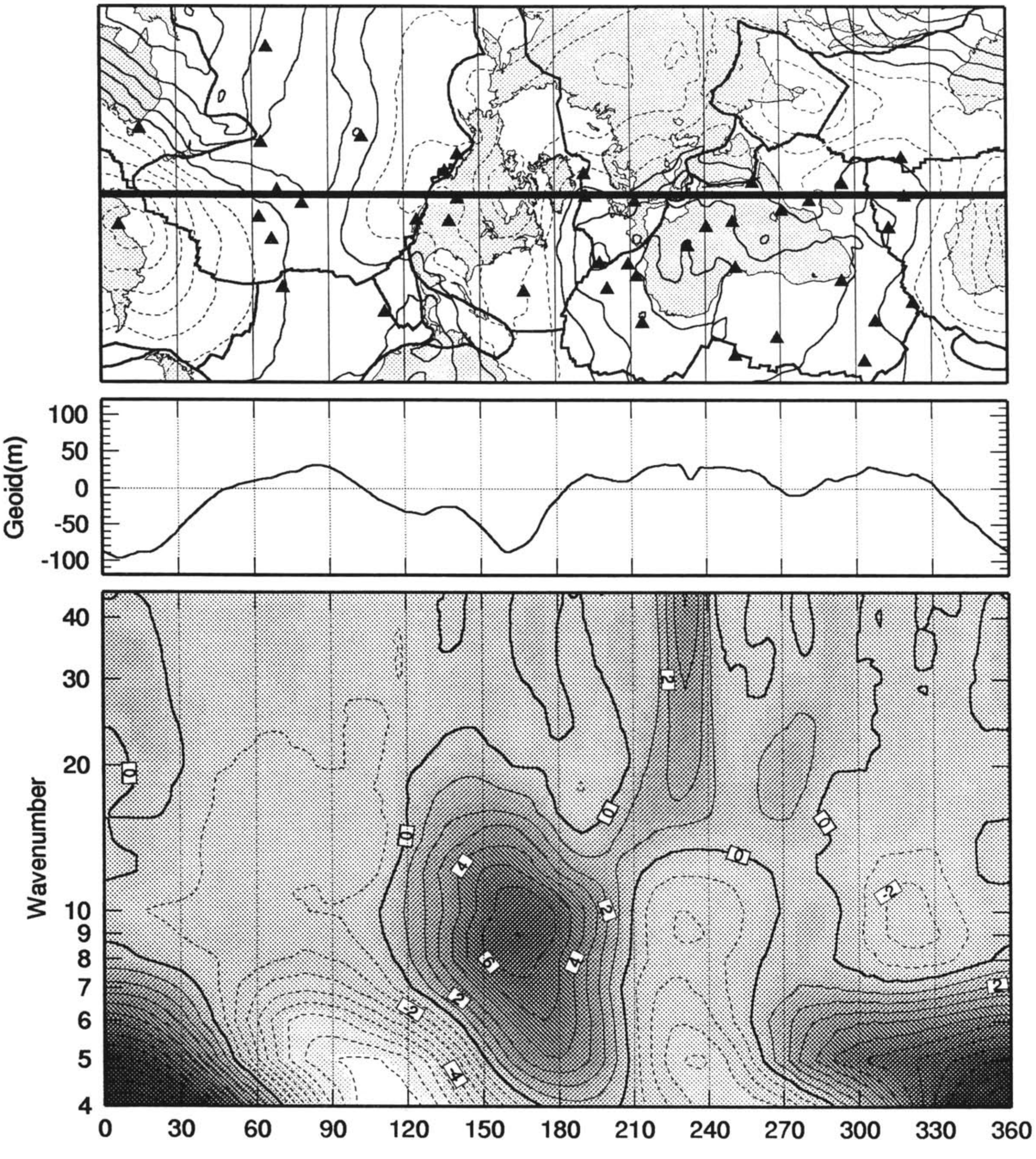

Figure 4.13: Great circle profile C (SpC).

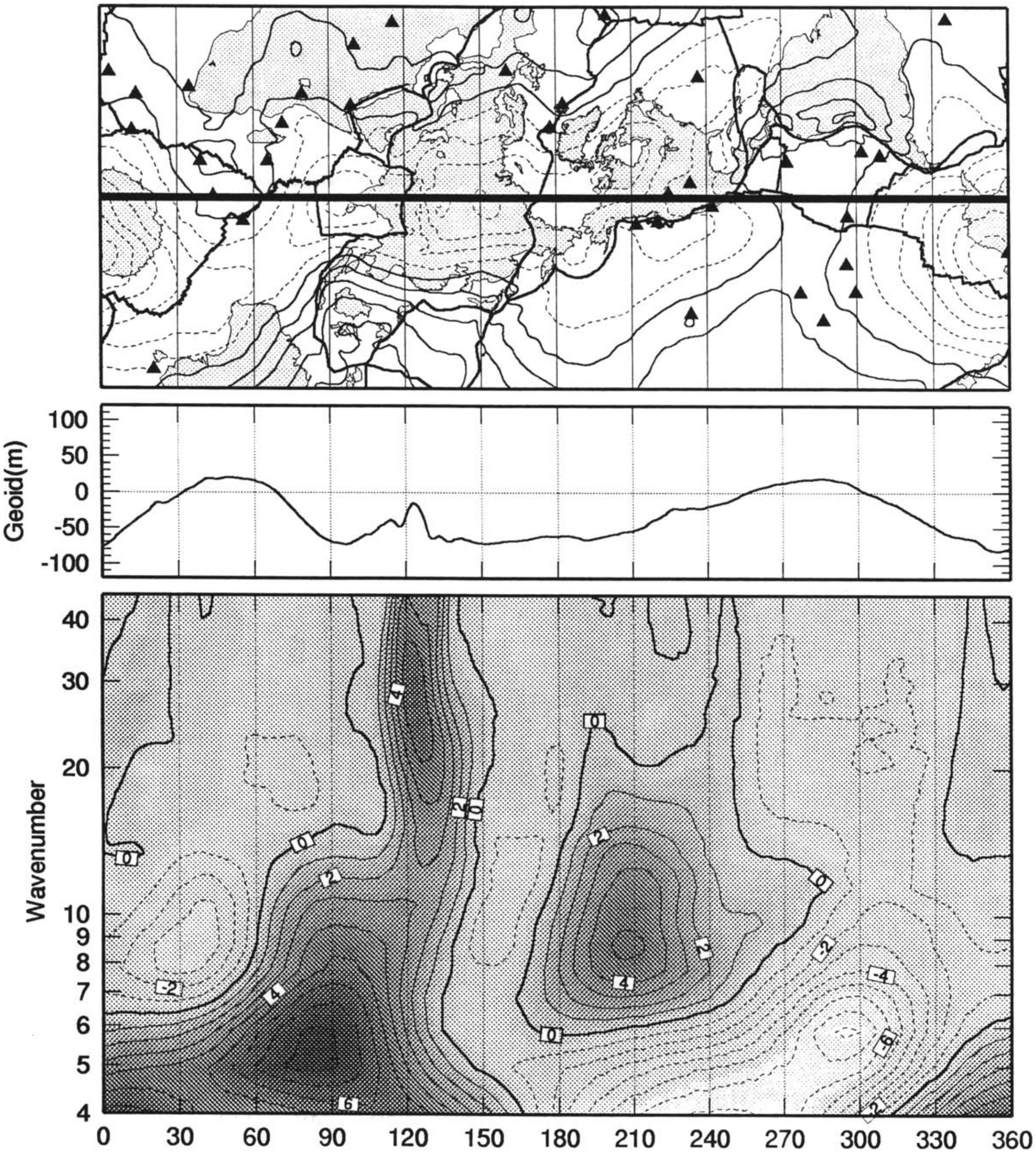

Figure 4.14: Great circle profile D (SpD).

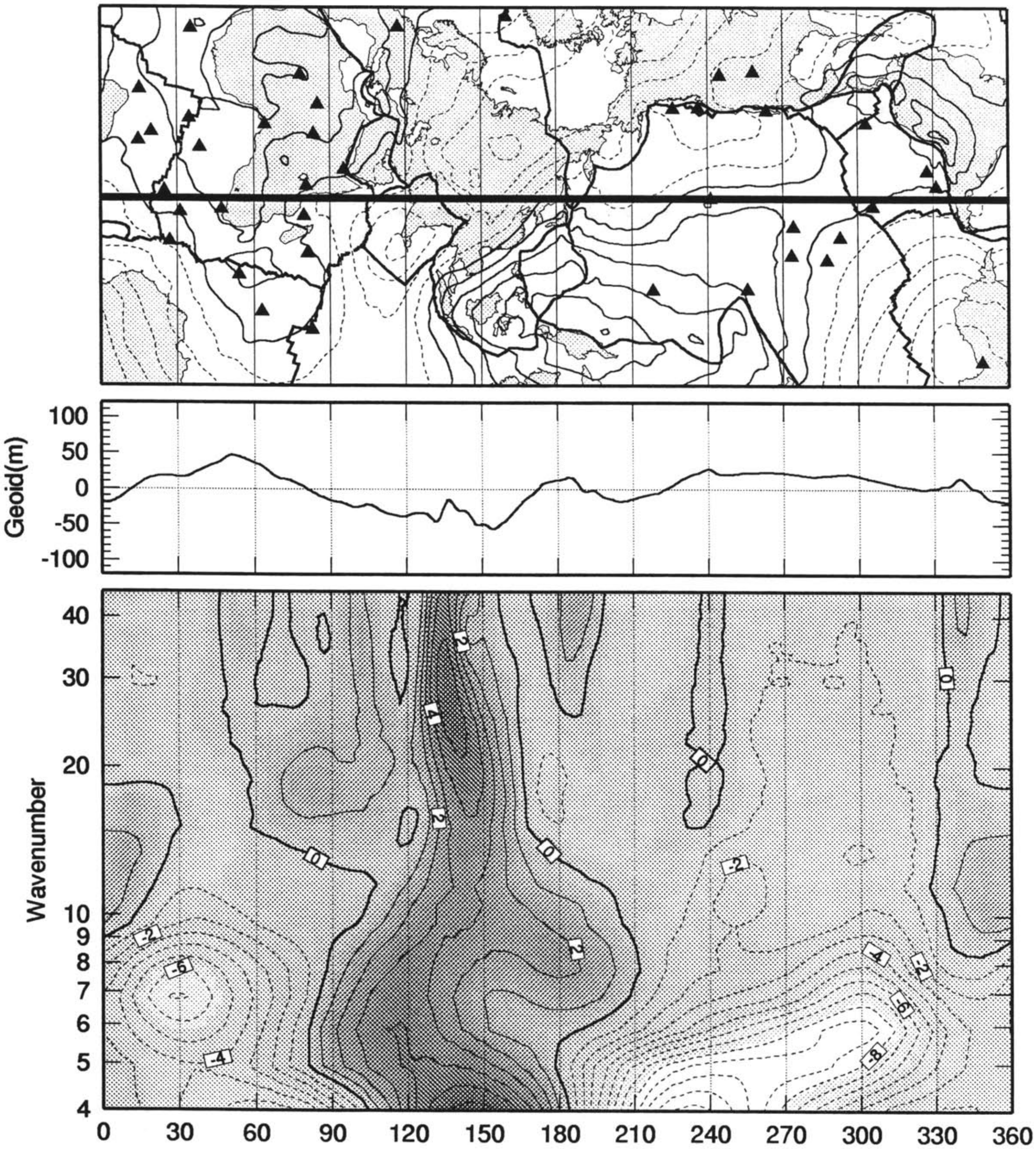

Figure 4.15: Great circle profile E (SpE).

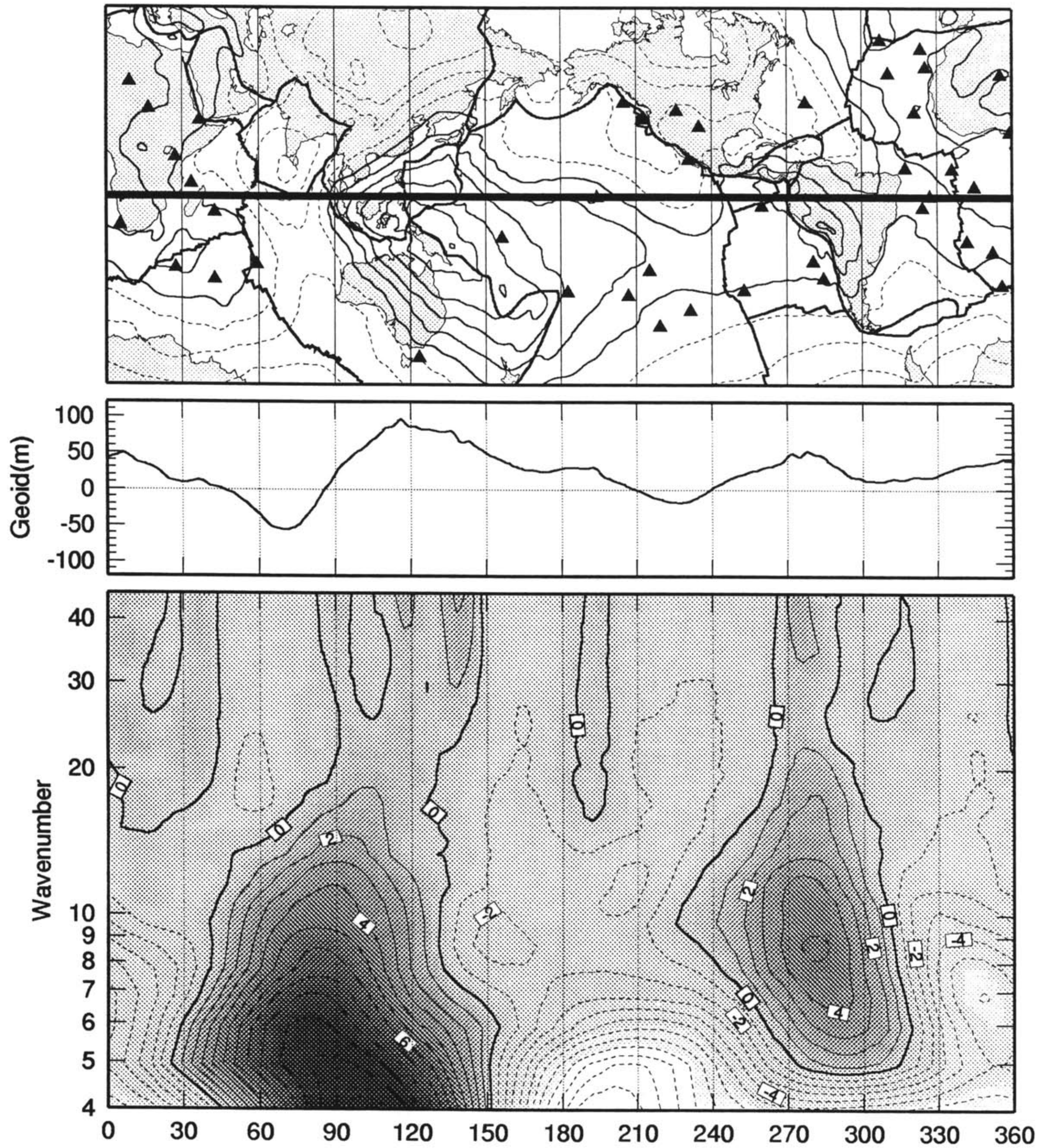

Figure 4.16: Great circle profile F (SpF).

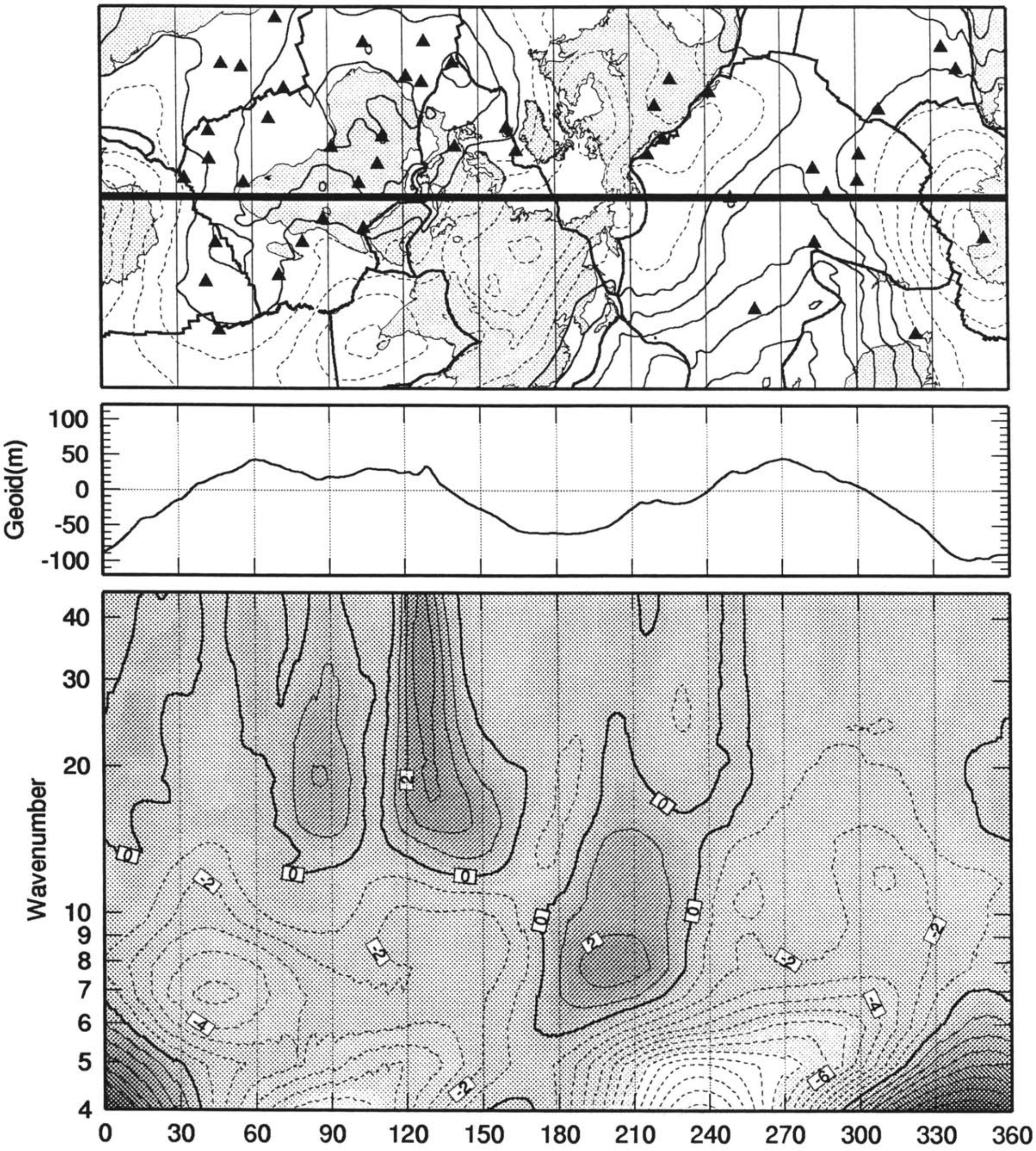

Figure 4.17: Great circle profile G (SpG).

in order to constrain the viscosity structure of the mantle [e.g., *Walcott*, 1972, 1973; *Nakiboglu and Lambeck*, 1981; *Mitrovica and Peltier*, 1989; *James*, 1992]. These analyses were conducted either in the purely spatial or the purely spectral domains and are susceptible to the previously discussed pitfalls of these approaches. For example, *Mitrovica and Peltier* [1989] compared their model predictions with the observed geoid bandpassed to leave only $10 \geq l \geq 22$, therefore missing most of the signal. We suggest that the success or failure of their earth model should not be judged with this filtered geoid, but rather in the localized domain. In contrast to *Mitrovica and Peltier* [1989], *Peltier et al.* [1992] interpret the negative gravity anomaly over Hudson Bay as entirely due to the influence of mantle convection. While there is probably a convective component to the total anomaly in this region, there is no other continental region with a similar anomaly, and we will show later that a significant portion of this anomaly can be accounted for by predicitions made from models of glacial rebound.

As previously noted, subduction zones are characterized by large ΔS_l maxima centered at $l < 10$ (SpA, SpD, SpE, and SpG). For the same areas, there is usually a lower amplitude maximum in the spectrograms at high values of l, which we associate with the mass deficiences in oceanic trenches.

Many of the known hotspot provinces also appear as ΔS_l highs (or at least regions with $\Delta S_l > 0$.) This relation is true for Hawaii (SpE), for l less than about 15, as well as for the African hotspots, the Azores (SpA), and Kerguelen (SpC). Surprisingly, Iceland is not clearly associated with $\Delta S_l > 0$. Over the region known as the South Pacific Superswell [*McNutt and Judge*, 1990], we find no anomalously large geoid variation at the length scales considered here. Indeed, the Superswell appears as a minimum on all the ΔS_l maps. The lack of localized anomalies in this region suggests that the negative geoid anomaly in the Superswell [*McNutt and Judge*, 1990] is not related to local processes, but is instead low because it lies between geoid highs associated with subduction zones on both sides of the Pacific, as well as a possible high associated the Hawaiian Swell.

Previously, a high correlation between the spherical harmonic expansion of hotspot locations and the geoid has been found at $l = 6$ [*Richards and Hager*, 1988; *Cazenave and Thoraval*, 1994]. *Cazenave and Thoraval* [1994] suggested that the $l = 6$ mantle flow is reponsible for the Atlantic and African hotspots, as well as the Superswell. Surprisingly, we find higher than average values of S_6 only over the north Atlantic. Furthermore, it is not clear the extent to which the north Atlantic ΔS_6 high is controlled by glacial rebound signal over Hudson bay, or by the separation distance ($\approx$ 7000 km) between Hudson Bay and the locally strong signal over the Central Andes, which corresponds to wavelengths associated with $l = 6$.

We can hypothesize physical reasons for the various highs in the ΔS_l estimates described above. In particular, the maxima associated with the regions of large topographic gradient are likely due to crustal thickness variations. Furthermore, we might expect that the signal due to cooling of the oceanic plates would reduce or even mask the signal from deeper processes. In an attempt to reduce such complications, we construct a series of residual geoids, each designed to account for signal that is believed to be approximately understood. We begin with static compensation models, including Airy models, with compensation at discrete interfaces, as well as Pratt models, with compensation by distributed density variations, here presumed to be thermal in nature.

4.3 Static Topographic Compensation Models

Our first synthetic geoid is constructed by assuming that all topography is compensated at a single depth, D, and that the surface material has a single density, ρ. The geoid/topography admittance for such a model can be written as [e.g., *Phillips and Lambeck*, 1980; *Hager*, 1983],

$$F_l = h_l \frac{4\pi G \rho R}{g(2l+1)} \left[1 - \left(1 - \frac{D}{R} \right)^l \right], \tag{4.1}$$

where R is the planetary radius, G is the universal gravitational constant, g is gravitational acceleration, and h_l is the isostatic Love number, well approximated by $h_l = (l + 0.6)/l$ [*Hager*, 1983]. In order to appraise the success of our synthetic model, we apply the localization operator to the residual geoid. We present the results for compensation at 30 km (figures 4.18 and 4.19) and 70 km (figures 4.20 and 4.21), with $\rho = 2700\ \mathrm{kg\,m^{-3}}$. For $D = 30$ km, $f_s = 2$, and $l \geq 18$, S_l magnitudes are greatly reduced, as indicated by the change in $\overline{S_l}$ as well as the near complete disappearance of the maxima over the central Andes, and a reduction of ΔS_l over Tibet. For $l < 18$, there is little difference in the maps before and after correction for compensation. Increasing D to 70 km successfully removes most of the signal over Tibet, but increases the variance in most other areas, as is evidenced by the increase in $\overline{S_l}$. Similar results hold for $f_s = 1$. However, we find that $\overline{S_l}$ increases for all l relative to the original field because of the coupled effects of the long wavelength bias and the failure of the single compensation model to explain the long wavelength signal. As with Tibet, we find that deeper compensation is more successful at reducing ΔS_l over the Bolivian Andes. This is not evident with $f_s = 2$ because of the reduced spatial resolution.

A model with compensation at a single depth for the whole planet is inappropriate, as is the assumption of a single density. We therefore improve our static compensation model by including the effects of cooling of oceanic plates, differences in continental and oceanic crustal densities, and by permitting crustal thicknesses, h_c, to vary such that isostasy is maintained while matching the observed topography [*Shapiro and Hager*, 1995]. Similar isostatic corrections to the geoid have been constructed before [e.g., *Chase and McNutt*, 1982; *Hager*, 1983; *Richards and Hager*, 1988; *Pavlis and Rapp*, 1990] using various assumptions including a single crustal compensation depth or a single crustal density, and most have been limited to low harmonic degree. Following the methodology outlined by *Hager* [1983], and further expanded upon by *Shapiro and Hager* [1995], the isostatic correction assumes a reference density structure of mature, 120-Myr-old oceanic

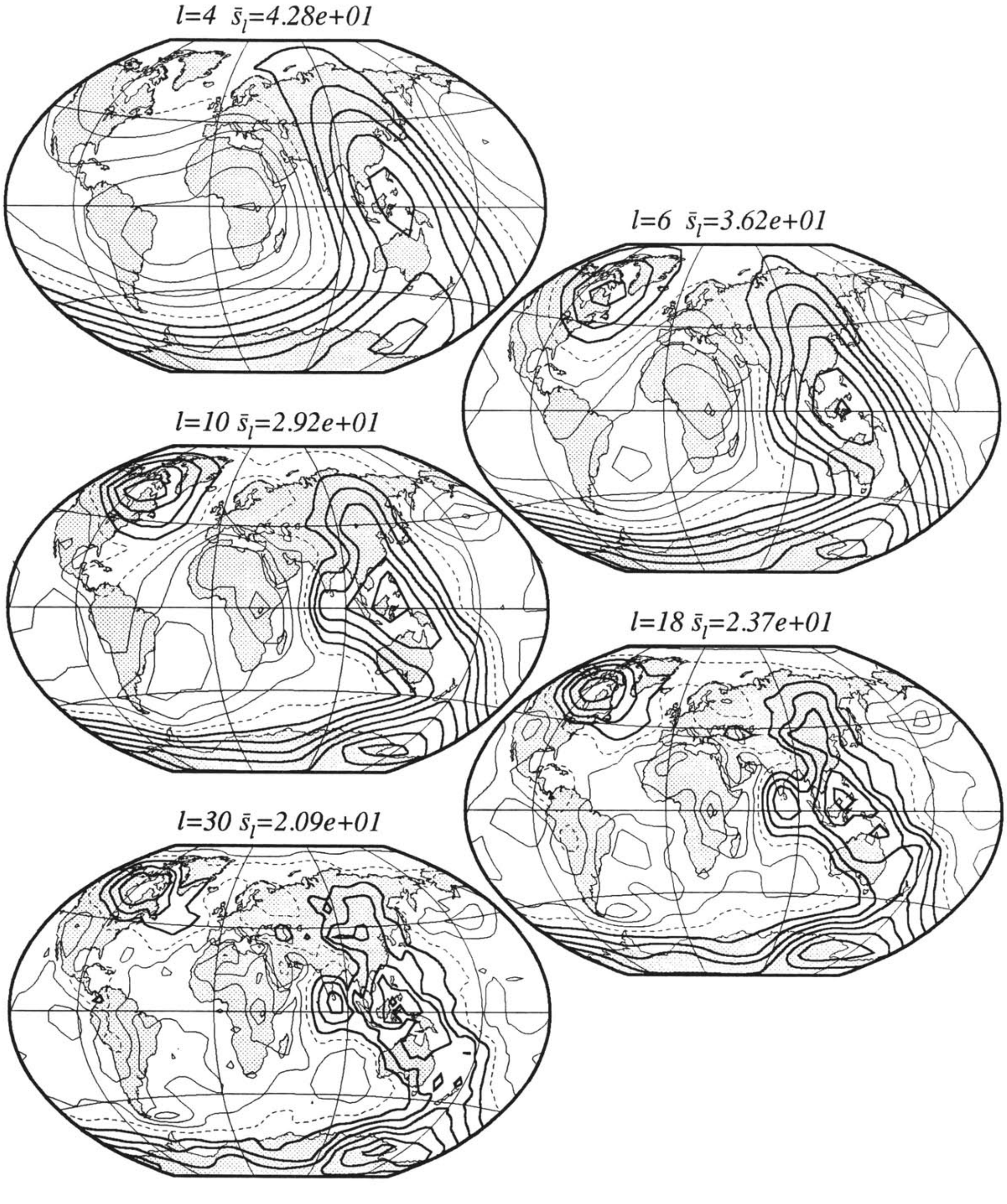

$l=4$ $\bar{s}_l=4.28e+01$

$l=6$ $\bar{s}_l=3.62e+01$

$l=10$ $\bar{s}_l=2.92e+01$

$l=18$ $\bar{s}_l=2.37e+01$

$l=30$ $\bar{s}_l=2.09e+01$

Figure 4.18: ΔS_l of residual geoid with $f_s = 1$, assuming all topography is compensated at 30 km depth. 4 m contour interval.

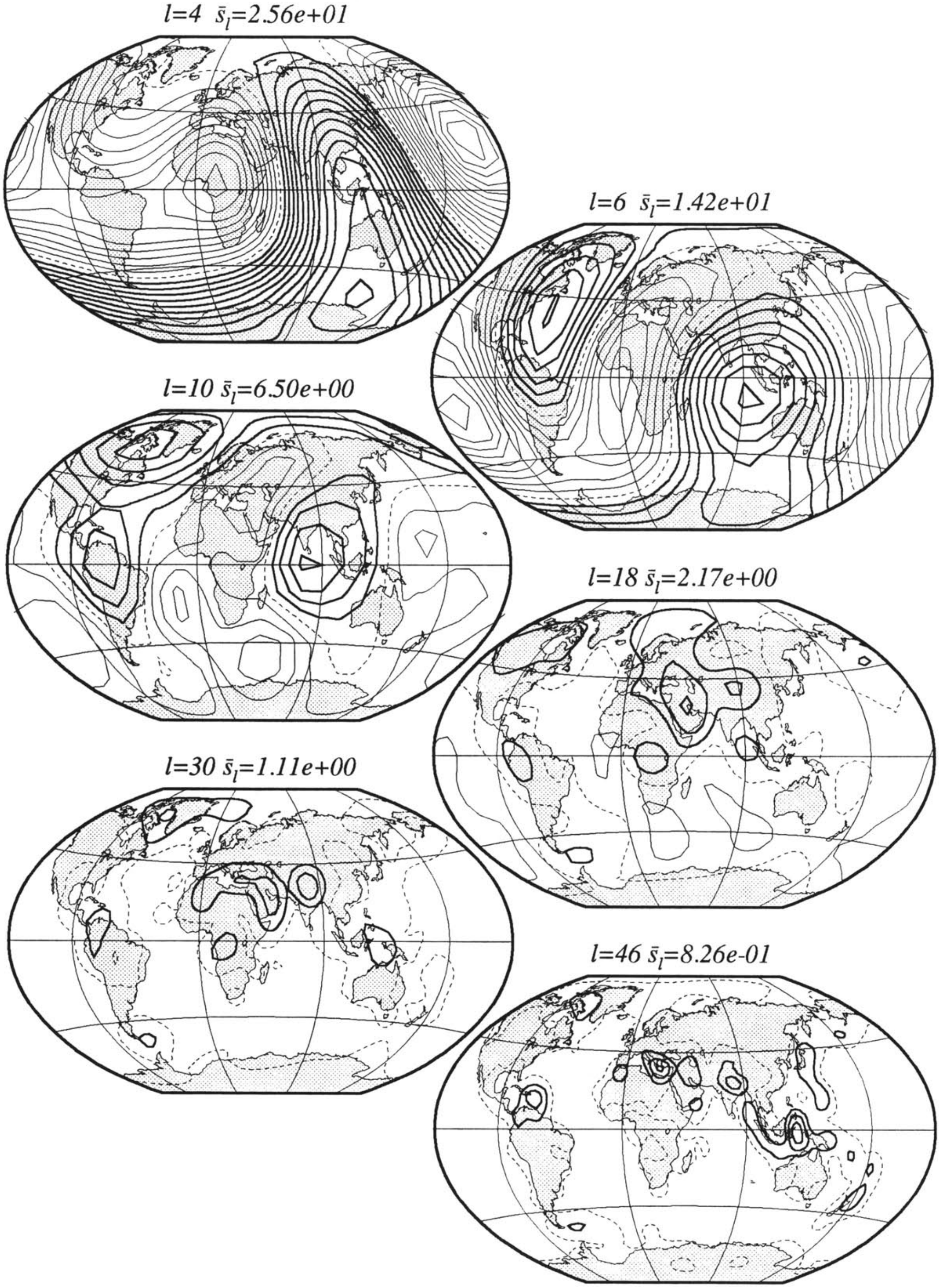

Figure 4.19: ΔS_l of residual geoid with $f_s = 2$, assuming all topography is compensated at 30 km depth. 1 m contour interval.

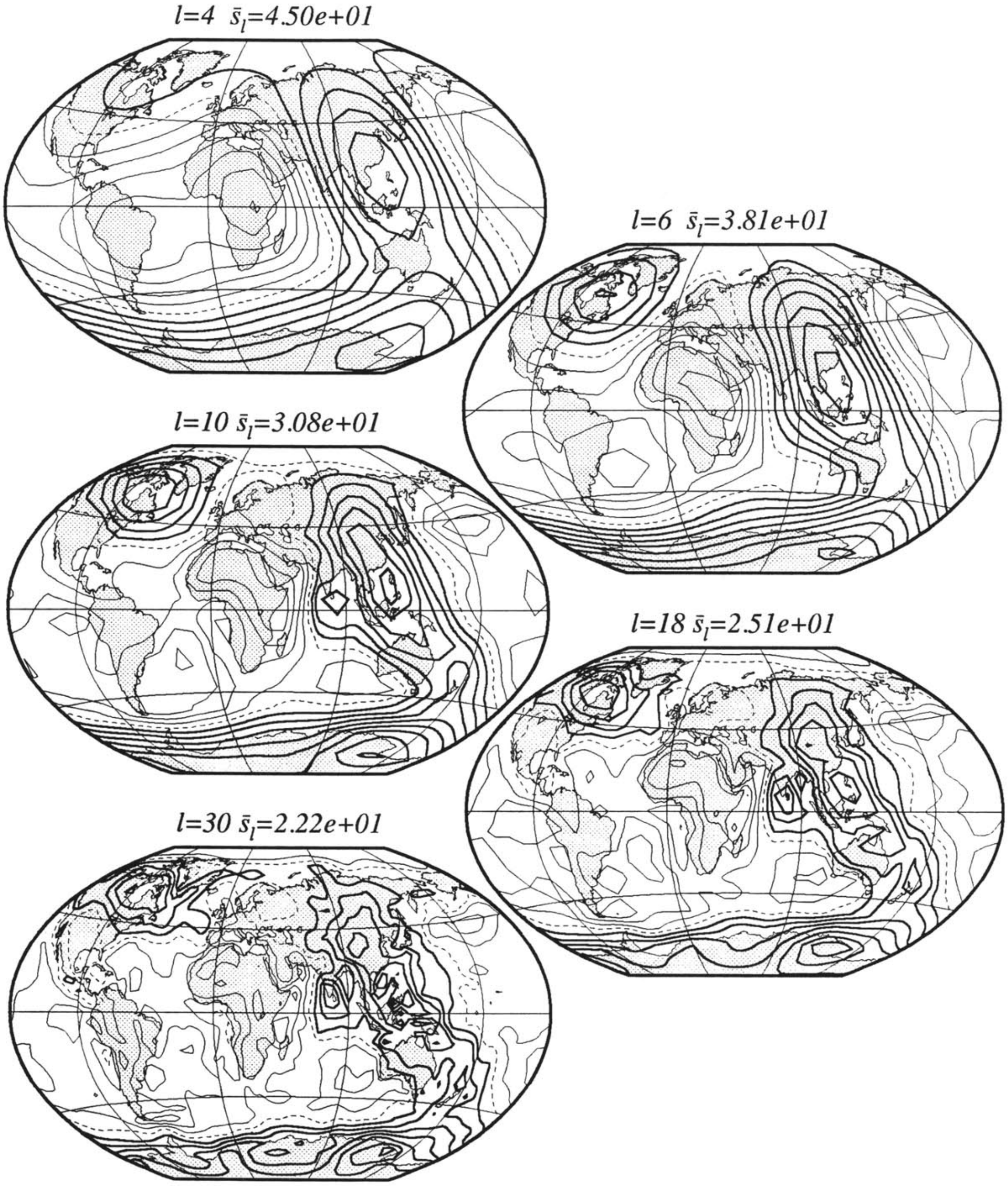

$l=4$ $\bar{s}_l=4.50e+01$

$l=6$ $\bar{s}_l=3.81e+01$

$l=10$ $\bar{s}_l=3.08e+01$

$l=18$ $\bar{s}_l=2.51e+01$

$l=30$ $\bar{s}_l=2.22e+01$

Figure 4.20: ΔS_l of residual geoid with $f_s = 1$, assuming all topography is compensated at 70 km depth. 4 m contour interval.

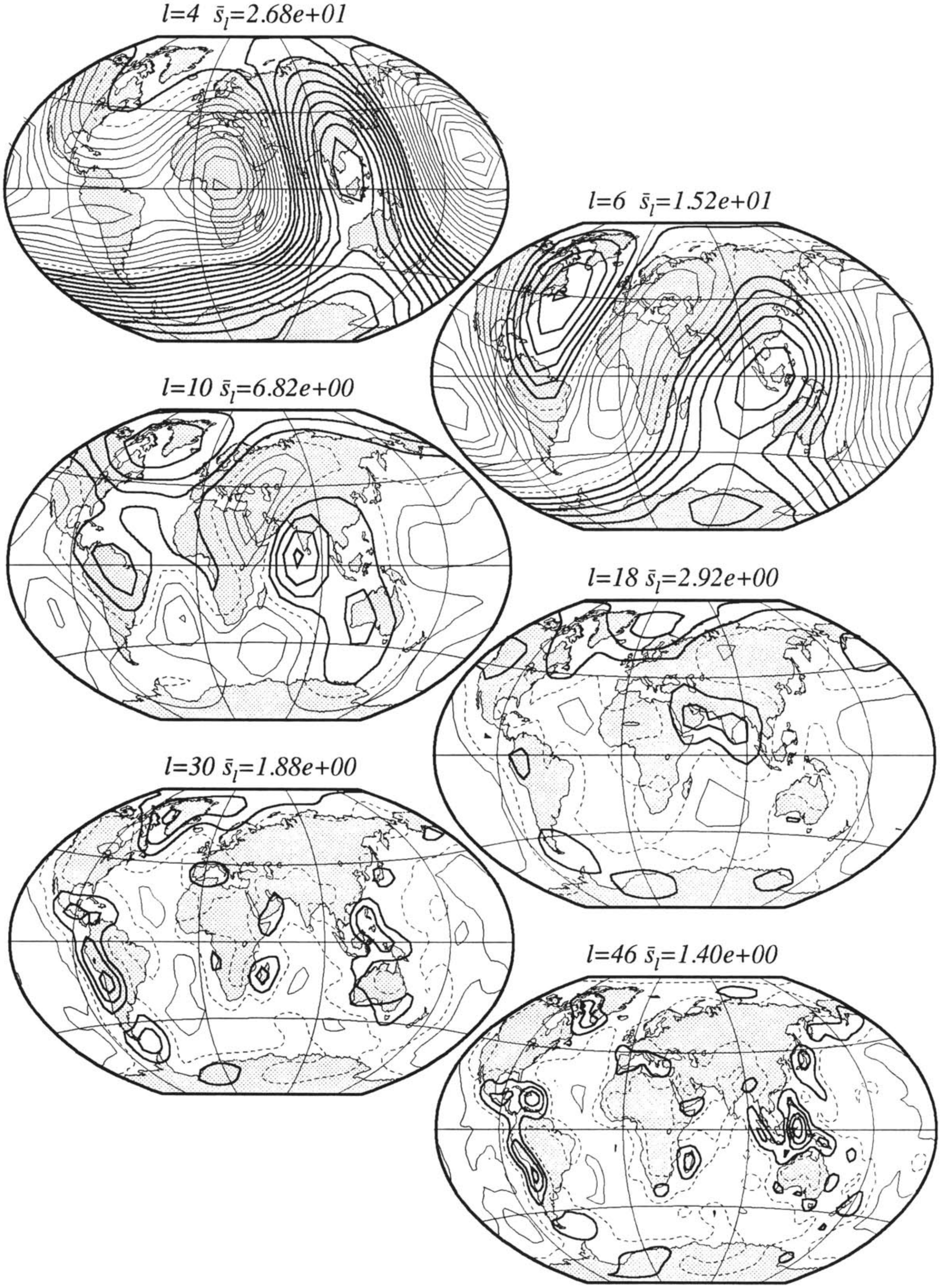

Figure 4.21: ΔS_l of residual geoid with $f_s = 2$, assuming all topography is compensated at 70 km depth. 1 m contour interval.

lithosphere with 7-km-thick crust. The temperature as a function of depth and oceanic age is given assuming a plate model [*McKenzie*, 1967a; *Parsons and Sclater*, 1977]. The age information is taken from a 5° by 5° compilation of oceanic ages by *Mauk* [1977], and the temperature structure of the continents is assumed to be that of old oceans. It is likely that there are significant compositional effects on the density structure of the continents; in particular, the upper 400 km of the continental mantle may be chemically distinct from the oceanic mantle, with the difference in instrinsic density offset by a thermal effect on density [*Jordan*, 1978]. No attempt is made to correct for these effects, since our model assumes that the continents have the same geotherm as old oceans, and isostasy is enforced relative to the old oceans.

The geotherm information is interpolated to a finer 2.5° by 2.5° latitude and longitude grid on which is included the effects of isostatic compensation of topography. This last step is done by fixing the crustal density and the temperature structure, and varying crustal thickness to simultaneously maintain isostasy and match the observed topography [*Shapiro and Hager*, 1995]. Densities of 2700, 2950, and 3300 $\mathrm{kg\,m^{-3}}$ for continental crust, oceanic crust, and mantle material, respectively, are assumed. Adopted thermal plate parameters include a temperature of 1300°C at 120 km depth, a coefficient of volumetric thermal expansion of $3.3 \times 10^{-5}\,{}^{\circ}\mathrm{C}^{-1}$, and a thermal diffusivity of 1.0×10^{-6} $\mathrm{m\,s^{-2}}$ [*Parsons and Sclater*, 1977].

The final crustal thickness derived by this isostatic model is shown in figure 4.22. The continents are generally characterized by crustal thicknesses on the order of 35 km, consistent with recent compilations of global variation in crustal thickness [*Durrheim and Mooney*, 1994; *Christensen and Mooney*, 1995]. We note that a few areas, especially regions of continental extension (e.g., the Basin and Range Province) and oceanic swells (e.g., Hawaii), have topography which may in reality be partially compensated by distributed density anomalies due to variations in the regional thermal gradient. The isostatic model adopted here will compensate these regions with variations in h_c. While

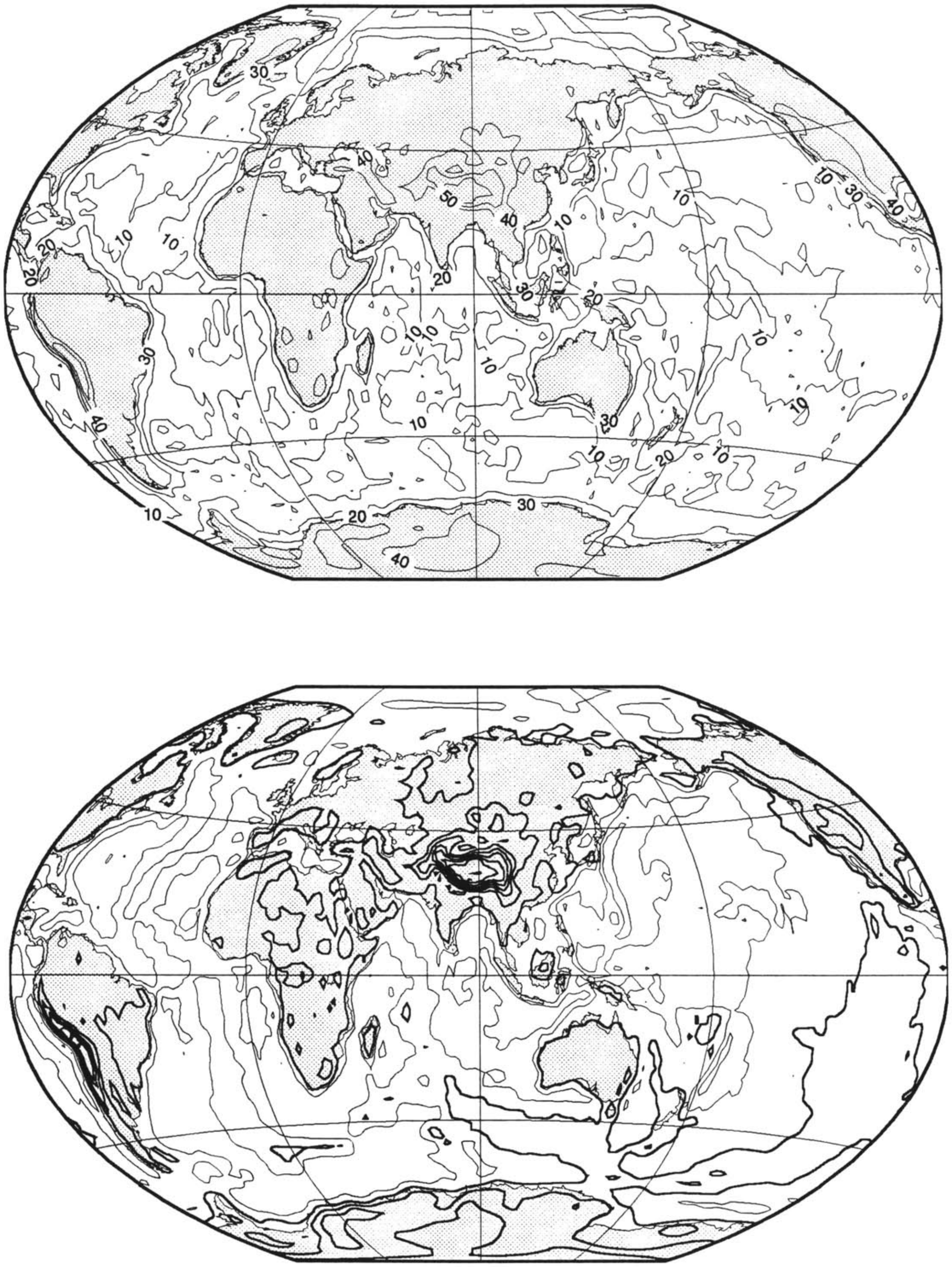

Figure 4.22: Top: Derived crustal thickness (km). Bottom: Synthetic geoid from plate cooling effects, crustal thickness variations, and oceanic trenches. 4 m contour interval, with $N(\Omega) \leq 2$ m and $N(\Omega) \geq 2$ m indicated by thin and thick lines, respectively.

this procedure leads to erroneous estimates of h_c, the effect on the geoid is small, since for a given topographic load, Airy and Pratt models give similar geoid anomalies if the Airy compensation depth is half the Pratt compensation depth. We also note the 55 to 65 km thick crust in Tibet and the Bolivian Andes. While such values are considerably greater than the thickness of the average continental crust, they are not as great as found in the global compilations nor as indicated by regional investigations. In particular, crustal thickness estimates in Tibet range as high as 80 km [e.g., *Molnar*, 1988]. Indeed, given our reliance on topography, any convectively induced dynamic topography will result in an underestimation of the crustal thickness variation [e.g., *Molnar et al.*, 1993]. This point will become important in our discussion of the residual geoid. Instead of deriving crustal thickness variations, we could attempt to use global compilations of such variations. However, since the data coverage is highly non-uniform and the appopriate density for the lower crust is uncertain, we found it preferable to derive an internally consistent crustal thickness model.

In addition to the effects of statically compensated topography, we also correct for oceanic trenches. We approximate this effect by assuming that all the relief in the trenches (measured relative to the abyssal plains) is completely uncompensated. The location of the trenches is taken from a compilation by *Lithgow-Bertelloni et al.* [1993]. In practice, we assume that all trenches are 100 km wide and have 6 km of relief. This relief is slightly larger than average by approximately 2 km [e.g., *Jarrard*, 1986], in order to offset the effect of compensating the trenches in the isostatic model [*Chase and McNutt*, 1982]. The global variance reduction achieved by removing the isostatic and trench geoid model (ITGM) is shown in figure 4.23, as is the correlation of the residual geoid with topography. Globally, ITGM results in a 30 to 60 percent variance reduction for $l > 15$, and adequately removes that part of the geoid which is correlated with topography. Note, however, that this geoid also results in a variance increase at the lowest degrees. Figure 4.22 and 4.24 show the spatial rendition of ITGM and the

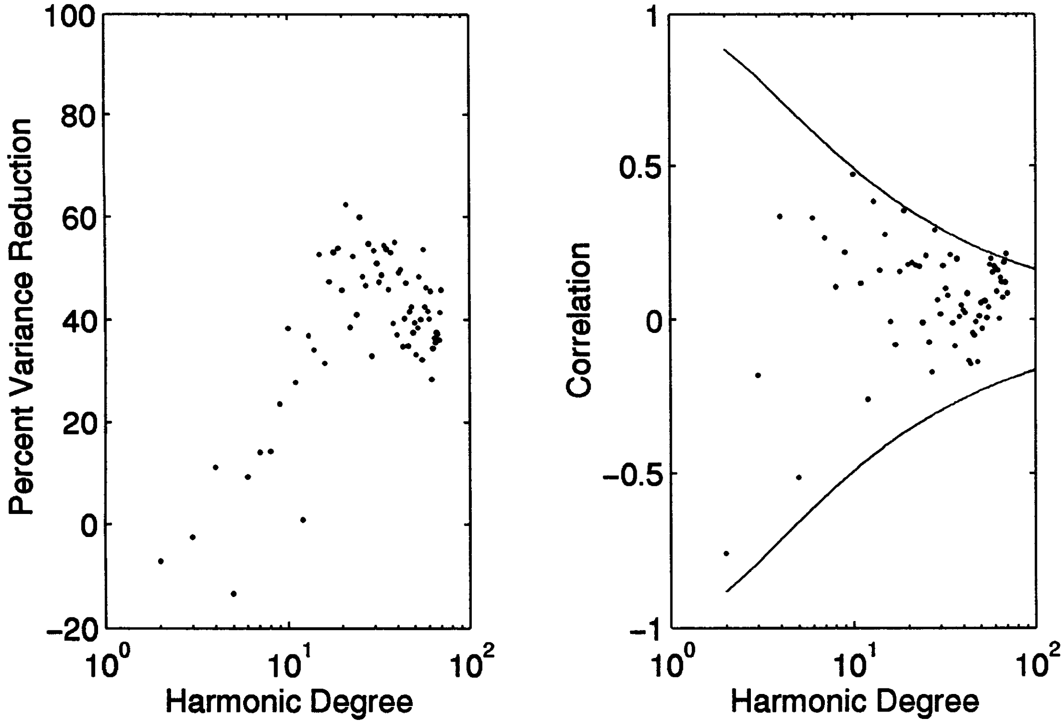

Figure 4.23: Left: Global variance reduction of the geoid resulting from the removal of the geoid predicted from a static topographic compensation model and a model of oceanic trenches. Right: The degree correlation of topography with the residual geoid, along with the 98 percent confidence limits.

ΔS_l maps of the residual geoid with ITGM removed, respectively. As expected from the global spectra, $\overline{S_l}$ is significantly reduced for $l \geq 18$, with variance reductions of between 30 and 45 percent. The local variance over Tibet and the Andes is reduced by 85 to 90 percent. The success of this model underscores the fact that crustal thickness variations can have non-trivial contributions to the geoid regionally up to $l \approx 10$ (or length scales of 4000 km) (see also *Le Stunff and Ricard* [1995]).

The failures of ITGM at short length-scales include locally high ΔS_l values centered south of Greece, over the Caribbean plate, and at the confluence of the subduction zones between Indonesia and New Guinea. These regions are either not included in our subduction zone correction (Greece) or the actual geometry and the processes involved are considerably more complex than assumed in ITGM.

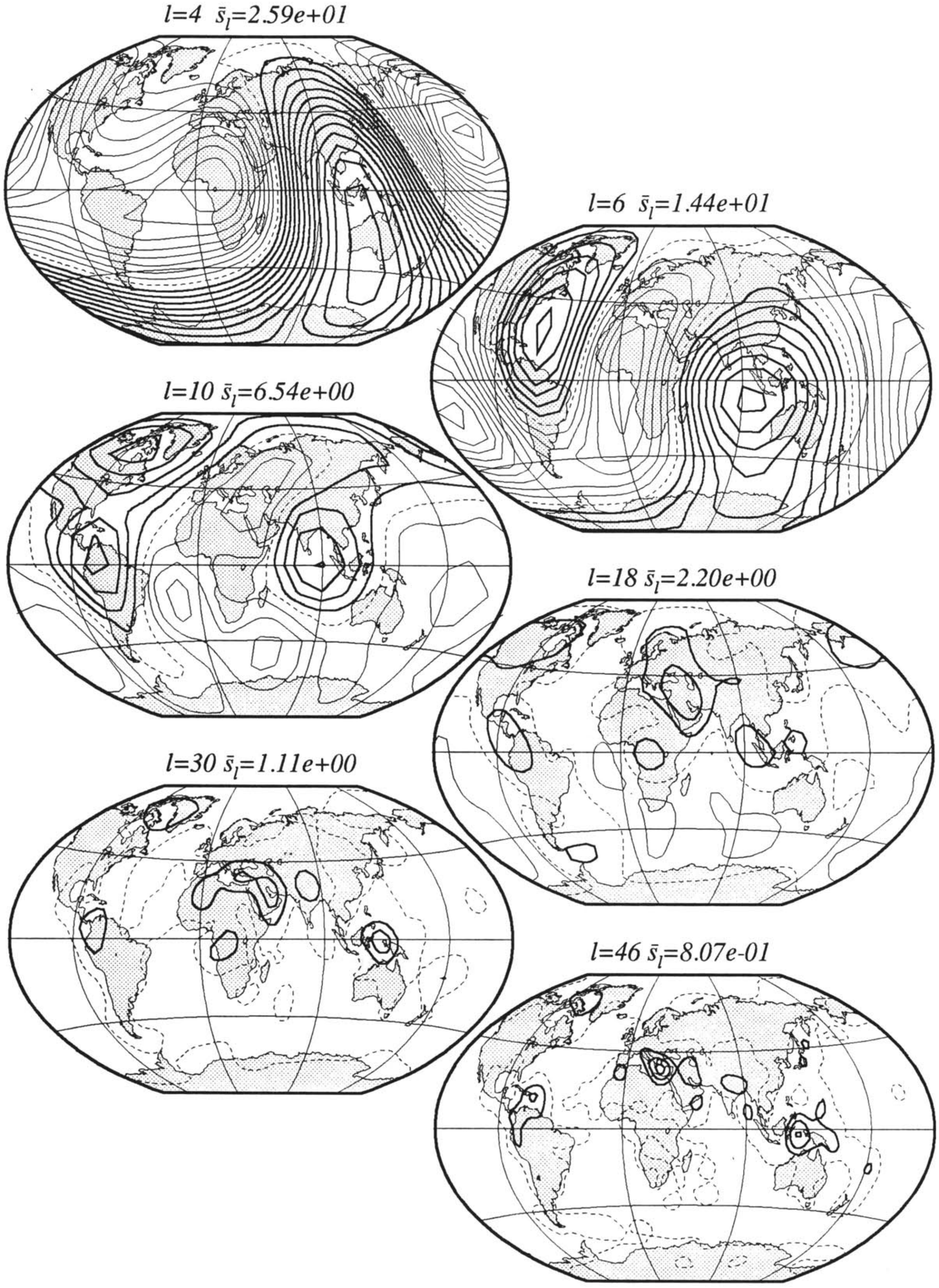

Figure 4.24: ΔS_l of residual geoid with $f_s = 2$, assuming oceanic trenches are uncompensated and all remaining topography is isostatically compensated. 1 m contour interval.

4.4 Local Inversion for the Dynamic Geoid

In the previous section we demonstrated that static compensation mechanisms significantly reduce the variance in the geoid at high l globally, and at medium l for selected regions. However, at low l, representing most of the total variance, the geoid is dominated by convective processes. In particular, the ΔS_l maps show a correlation between subduction zones and ΔS_l highs. In addition, after removal of modelled slab effects, there is a correlation between the residual geoid and the distributions of hotspots, implying an association between geoid highs and hot upwelling mantle [e.g., *Richards and Hager*, 1988]. These correlations are well known [e.g., *Crough and Jurdy*, 1980; *Hager*, 1984], and served as the impetus for the development of a series of dynamic flow calculations that assume a model of the density distribution in the mantle (based on seismic tomography or a geodynamic model), and attempt to match the observed geoid by varying the mantle viscosity structure. To match the observed geoid high over subduction zones and hotspots, these flow models require a 30 to 50 fold increase in viscosity between the upper and lower mantle [e.g., *Hager*, 1984], and that most of the mass anomalies correlated with the hotspot distribution be located in the lower mantle [e.g., *Dziewonski*, 1984; *Hager et al.*, 1985]. These inferences follow directly from the geoid response kernels shown in figure 4.3 [*Richards and Hager*, 1984; *Hager and Richards*, 1989]. Such flow calculations successfully account for about 90 percent of the total variance in the long wavelength geoid [e.g., *Hager*, 1984; *Hager and Clayton*, 1989; *Ricard and Vigny*, 1989; *Forte and Peltier*, 1991; *Forte et al.*, 1994]. In addition to the dynamic geoid associated with mantle convection, the estimates of ΔS_l suggest that in local regions (e.g., Hudson Bay) there may be significant contributions to the geoid from incomplete isostatic adjustment following the last deglaciation event approximately 20 ky ago.

Unfortunately, it is difficult to separate the contributions of each of these processes. Furthermore, unlike the static compensation models considered earlier, dynamic compensation models are highly nonlinear, with a strong dependence on the rheological structure assumed. Dynamic flow calculations are limited to considering radial variations in viscosity, yet the effects of lateral variations become significant at $l > 4$ [e.g., *Richards and Hager*, 1989; *Ribe*, 1992; *Zhang and Christensen*, 1993; *Forte and Peltier*, 1994], as was illustrated in the introduction (figure 1.1). However, it is reasonable to assume that, despite our current inability to model these processes at large l, they should express themselves in the geoid at $l > 4$. Furthermore, a limitation on the implementation of these dynamic models has been their reliance on global variance reduction (total or l-dependent) to determine their success. By necessity, this reliance implies that one is also modelling geoid anomalies which are unrelated to the process being considered.

Here, we take a different approach to constraining the dynamic contributions to the geoid — one which is based on the local correlation between the observed geoid and the spatial distribution of each of the tectonic processes in question. For example, consider a function on the sphere which has a value of one for regions within a short distance of a subduction zone and is zero elsewhere. Using the global linear transfer function, $\hat{F}_l$, between this slab function and the geoid, we could attempt to predict the long wavelength geoid associated with slabs. As mentioned previously, a global analysis can be contaminated by trying to account for anomalies that are not related to subduction processes, such as the geoid highs in the North Atlantic and in the Southwestern Indian Ocean, and the low over Hudson Bay. This contamination may not be a big concern if our only interest were determining the geoid related to slabs, since the geoid anomalies associated with subduction zones are among the largest on the Earth. However, we are also interested in the geoid signal related to processes that do not dominate the observed geoid when viewed globally. Indeed, *O'Connell* [1971] found no significant global correlation between the observed geoid and that expected from a model of deglaciation.

To circumvent these problems, we calculate the local l-dependent transfer function, $F_l(\Omega)$, between a harmonic expansion of a given tectonic distribution function, $T(\Omega)$, and the observed geoid, $N(\Omega)$, over the entire planet. We derive a single global transfer function, $\tilde{F}_l$, by spatially averaging the local estimates weighted by the local variance, $\sigma^2_{\Psi\Psi}(\Omega, l)$, of $T(\Omega)$. We can then convolve $\tilde{F}_l$ with $T(\Omega)$ to create a predicted geoid. Alternatively, this procedure can be viewed as the estimation of a single global transfer function for a given l using the ensemble of all the localized coefficients of both $T(\Omega)$ and $N(\Omega)$. These two approaches are identical, providing an averaging algorithm bridging the local and global domains. The local approach for a single tectonic distribution function can be written as

$$\tilde{F}_l = \frac{\int_\Omega F_l(\Omega)\sigma^2_{\Psi\Psi}(\Omega, l)\, d\Omega}{\int_\Omega \sigma^2_{\Psi\Psi}(\Omega, l)\, d\Omega}. \tag{4.2}$$

By the definition of F_l, we can also write equation 4.2 as

$$\tilde{F}_l = \frac{\int_\Omega \sigma^2_{\Psi\Gamma}(\Omega, l)\, d\Omega}{\int_\Omega \sigma^2_{\Psi\Psi}(\Omega, l)\, d\Omega}, \tag{4.3}$$

where Γ is the localized rendition of $N(\Omega)$. Equation 4.3 is the equivalent global approach to equation 4.2. We evaluate equation 4.3 using the relation

$$\int_\Omega \sigma^2_{\Psi\Gamma}(\Omega, l)\, d\Omega = (2l+1)\sum_{l_1}\sum_{m_1} a^*_{l_1 m_1} b_{l_1 m_1} \sum_{l_2} w^{\odot 2}_{l_2} \begin{pmatrix} l_1 & l_2 & l \\ 0 & 0 & 0 \end{pmatrix}^2 . \tag{4.4}$$

which can be derived in a manner analogous to equation 2.54. If the window expansion has only an $l_2 = 0$ term (i.e., no spatial localization), then the 3-j term in equation 4.4 will have a non-zero value only if $l_1 = l$, and equation 4.4 reduces to the unlocalized expression for the covariance function, equation 2.43. Alternatively, we can view equation 4.4 as a form of convolution of the global variance spectrum (i.e., the sum over m_1) with the window spectrum.

Before considering real data, we first apply equation 4.3 to synthetic data. In figure 4.25 we show the result of filtering the polar cap and equatorial sheet function shown in figure 2.6 and then estimating the filter using the original function as $T(\Omega)$ and the

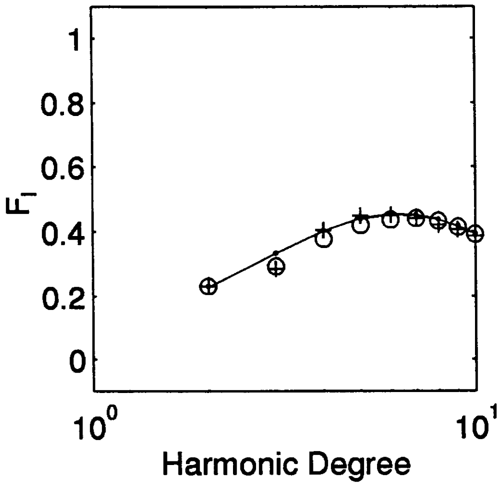

Figure 4.25: The applied transfer function, F_l, (solid line), and that found by inversion of the filtered versions of the test function shown in figure 2.6 (crosses) and the slab distribution function (open circles). See text for a description of F_l.

filtered field as data. The choice of the filter is not important here, but will be discussed when we address subduction zone processes. As indicated by the crosses, the inversion using localization estimates the filter reasonably well. The largest diferences occur at odd degrees where the input function has no power.

We consider three transfer functions, one for the glacial rebound geoid, $\tilde{F}_l^G$, one for the subduction geoid, $\tilde{F}_l^S$, and one for the hotspot related geoid, $\tilde{F}_l^H$. These transfer functions will be considered separately as well as simultaneously. In practice, we attempt to start with a model with spectral decay similar to that of the observed geoid. For example, our slab distribution function is not simply zero or one as in the example above, but is taken as the static geoid calculated assuming an average dip, length, and density anomaly for all slabs, and scaled by a spatially varying parameter, with a value between zero and one, that reflects the presence of a slab and its magnitude relative to other slabs. Similarly, our glacial rebound distribution function is not simply a spatial rendition of the change of ice thickness with time, but rather the gravity field predicted by instant deglaciation with no relaxation. All the estimates of $\tilde{F}_l$ that follow are made relative to ITGM. The estimates are made using free air gravity, rather than the geoid, in order to reduce biases. The results, however, do not differ significantly when calculated using the geoid.

Glacial Rebound

We begin our localized decomposition of the gravity field by considering the anomaly due to incomplete isostatic adjustment after the last Pleistocene glaciation event. The change in ice thickness over the last 18 ky is shown in figure 4.26. Also shown is the predicted geoid, $N^{inst}(\Omega)$, and the predicted gravity field, both constructed assuming isostatic equilibrium before deglaciation, uniform redistribution of the melted ice load over the ocean basins, and no isostatic relaxation during or following deglaciation. We note that in this model the redistributed melt water does not actually conform to the geoid since we are neglecting self-gravitation. While this assumption would be a serious defect for a study of relative sea levels, it is a second order effect for geoid analyses. The assumption of no isostatic relaxation is identical to assuming instant deglaciation and calculating the geoid immediately after the melting event. The estimates of ice distribution and magnitude are taken directly from the ICE-3G deglaciation history [*Tushingham and Peltier*, 1991]. While the primary use of this deglaciation model in our study is as a tectonic distribution function, we note that since strandlines and gravity data are used as constraints in its construction, the actual melting history incorporates an *a priori* Earth model [*Tushingham and Peltier*, 1991].

We estimate two sets values for $\tilde{F}_l^G$. The first is relative to the non-hydrostatic geoid, N^{hyd}, and the second is relative to the geoid referenced to the best fitting ellipsoid, N^{ell} (figure 4.27). Relative to N^{hyd}, N^{ell} has the c_{20} coefficient removed and the c_{40} coefficient reduced. When using N^{ell}, we reference both N^{inst} and N^{obs} to the best fitting ellipsoid. We consider both N^{hyd} and N^{ell} because we will find that localization fails at the longest wavelengths, causing us to correlate N^{inst} with signals unrelated

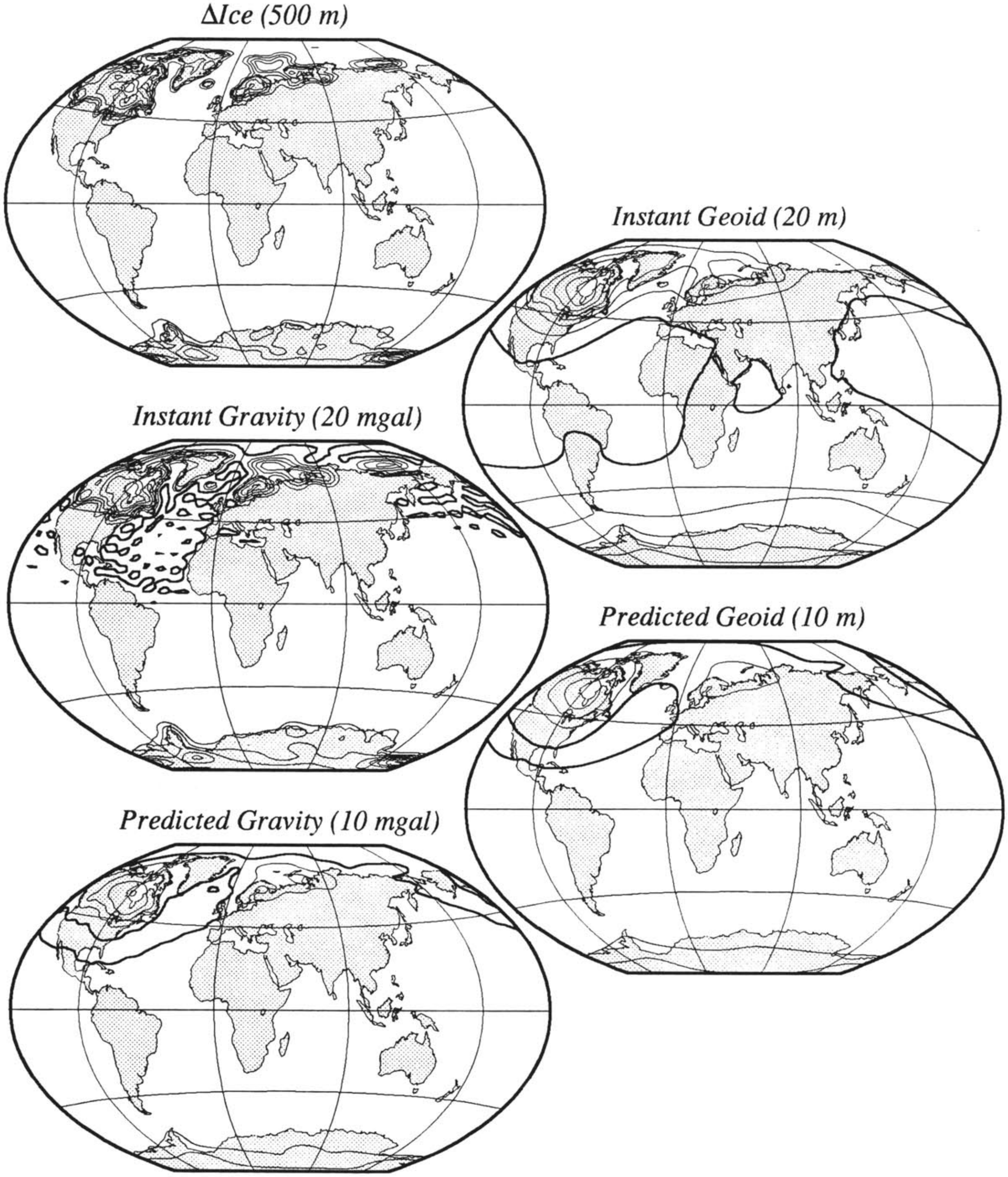

ΔIce (500 m)

Instant Geoid (20 m)

Instant Gravity (20 mgal)

Predicted Geoid (10 m)

Predicted Gravity (10 mgal)

Figure 4.26: From top to bottom: Change in ice thickness over the last 18 ky, geoid and gravity anomalies predicted by assuming instant deglaciation, and the predicted geoid and gravity from the locally weighted correlation between N^{inst} and the geoid (l = 3 to 45) referenced to the best fitting ellipsoid. Contour intervals are indicated above each map and are staggered about zero by half an interval.

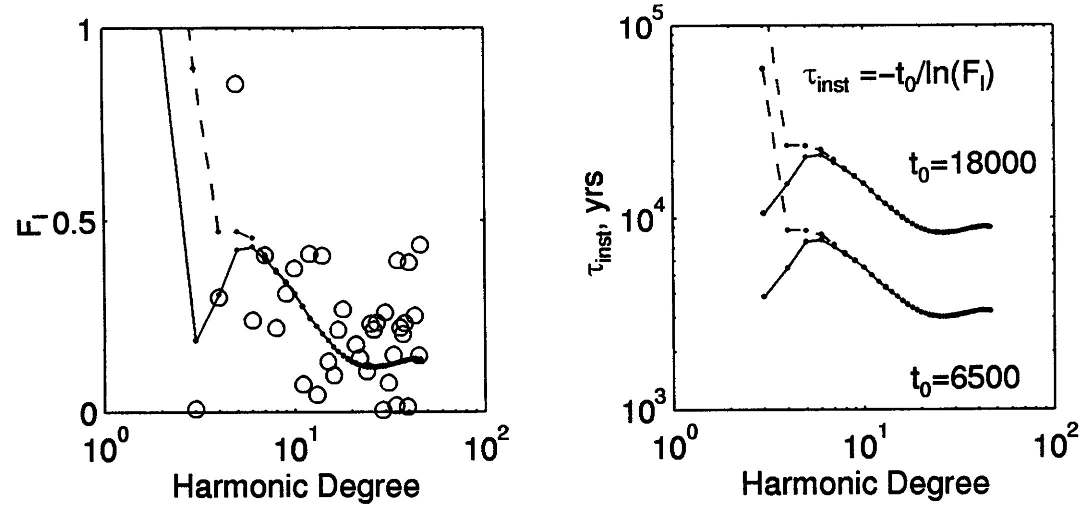

Figure 4.27: $\tilde{F}_l^G$ (left) and τ_{inst} (right) versus harmonic degree for N^{inst} relative to N^{hyd} and N^{ell}, indicated by dashed and solid lines, respectively. The open circles (left) indicate the global estimate $\hat{F}_l^G$ between N^{inst} and N^{hyd}.

to glacial rebound. In particular, since N^{inst} is focussed at the poles, it will have a significant contribution from the c_{20} term. Thus, using N^{ell} will damp correlations at $l = 2$. Here, we are effectively pursuing the rationale that the difference between N^{ell} and N^{hyd} (corresponding to a little less than 100 m of equatorial bulge) is most likely attributable to processes other than glacial rebound. Candidate processes include the effect of internal density contrasts of convective origin and the delayed readjustment of the hydrostatic figure to changes in rotation rate [e.g., *O'Connell*, 1971]. In addition, we must remember that it is difficult to isolate different sources of signal in the $l = 2$ components of the geoid. Furthermore, we use $f_s = 2$, which suggests that localization could be problematic for $l \leq 4$. For comparison with conventional techniques, we also show in figure 4.27 the global estimate, $\hat{F}_l^G$, which does not take into account the spatial distribution of deglaciation. The global estimates show considerable scatter reflecting the presence of unrelated processes.

Since our initial distribution function, N^{inst}, is the maximum geoid anomaly possible, we should find that $\tilde{F}_l^G < 1$ for all l. $\tilde{F}_l^G$ would equal one only if there were no relaxation, and would be constant for all l and less than one if the relaxation were not dependent on the wavelength of the disturbance. At the lowest degrees, we find that $\tilde{F}_l^G > 1$; on the basis of the arguments just described, such values are probably indicative of a limitation in the localization procedure. Furthermore, for both estimates of $\tilde{F}_l^G$, we must also remember that localization reduces the spectral resolution, thus any difficulties at $l = 2$ could bleed into the neighboring degrees. Therefore, we interpret the values of $\tilde{F}_l^G$ relative to N^{hyd} at $l \leq 5$ as artifacts. Similarly, we also reject the estimate of $\tilde{F}_2^G$ estimated relative to N^{ell}. However, we can not arbitrarily reject all estimates in which $\tilde{F}_l^G$ increases with decreasing l, an issue to which we return later.

Given a value of $\tilde{F}_l^G$, we can estimate the effective relaxation time, τ_{inst}, for the rebounding process. For an exponentially decaying displacement of initial amplitude a_l^o, (equivalent to N^{inst}), the transfer function between the initial amplitude at a time t_o before the present (bp) and the amplitude at the present can be written as $\tilde{F}_l^G = (a_l/a_l^o)e^{(-t_o/\tau_{inst})}$, which can be solved for τ_{inst}, giving $\tau_{inst} = -t_o/\ln \tilde{F}_l^G$. The conversion from $\tilde{F}_l^G$ to τ_{inst} is shown in figure 4.27. We show τ_{inst} for t_o equal to 18 ky bp and 6.5 ky bp, spanning the period of greatest change in ice volume, and therefore approximately bounding the true value of τ for the actual extended melting history.

In order to understand the form of the relaxation time curve, it is worth considering the simple end member models of a viscous half space and a viscous channel. These are the two original models used to interpret glacial rebound data [e.g., *Haskell*, 1937; *Van Bemmelen and Berlage*, 1935]. For relaxation of a surface disturbance over a viscous half space, the relaxation time is proportional to the wavenumber, k. However, for a layered system, the relaxation time can increase with decreasing wavenumber [e.g., *Cathles*, 1975]. This effect is illustrated in figure 4.28, which shows the non-dimensional relaxation time, τ^*, as a function of non-dimensional wavenumber, k^*, for a planar channel with depth, D, viscosity, η, density, ρ, and wavelength, λ [e.g., *Cathles*, 1975].

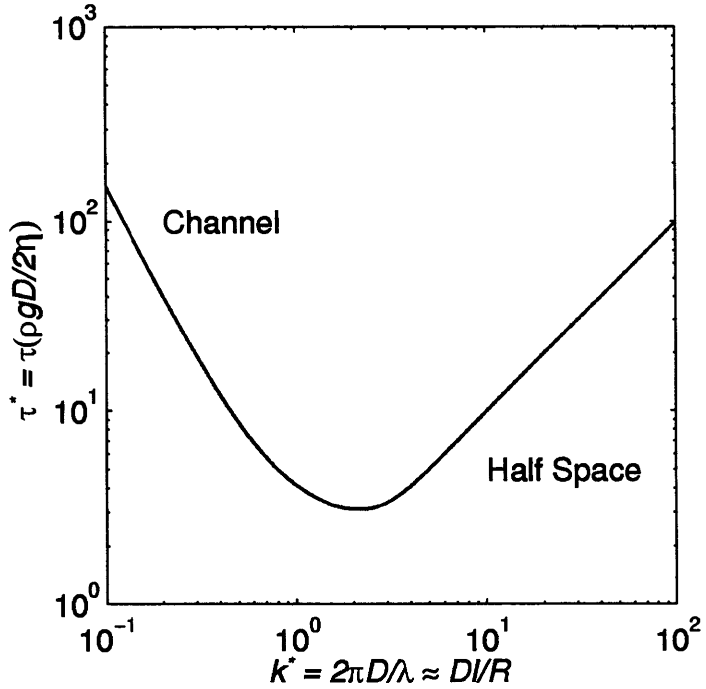

Figure 4.28: Non-dimensional relaxation time, τ^*, as a function of non-dimensional wavenumber, k^*.

For large k^*, τ^* decays as with a half space model, but at smaller k^* the flow sees the bottom of the channel and the relaxation time increases with decreasing k^* [e.g., *Cathles*, 1975]. We can use figure 4.28 to form a crude interpretation of the observed relaxation curve shown in figure 4.27. Going from high to low l we find that τ decreases to a minimum between $l = 20$ and $l = 30$, corresponding to wavelengths of 1300 to 1900 km. The minimum relaxation time in figure 4.28 occurs at $k^* \approx 2$, which corresponds to a layer depth, D, of 450 to 650 km, or approximately the transition between the upper and lower mantle. As with the channel model, continued decrease in l is accompanied by an increase in τ_{inst}. However, for $l \leq 6$ τ_{inst} decreases, reflecting the participation of the lower mantle in the rebound flow.

Since we rejected the estimates of $\tilde{F}_l^G$ at the lowest l, we must do the same for the estimates of τ_{inst}. However, we note that a less extreme increase in τ_{inst} with decreasing l

at long wavelengths is not impossible, and could reflect the existence of thin layers within or at the base of the mantle (e.g., a compositionally distinct D'' layer). Indeed, we will find such an increase in τ_{inst} in the simultaneous inversions. To quantify the allowable change in relaxation time from degree to degree we return to the simple channel model. In particular, for small k^*, τ^* is inversely proportional to the square of the wavenumber. Therefore, we can write the limiting case of the increase in $\tilde{F}_l^G$ with decreasing l as

$$\tilde{F}_{l-1}^G = (\tilde{F}_l^G)^{(l-1)^2/l^2}. \qquad (4.5)$$

Because of the difficulties at the longest wavelengths, we only show the spatial rendition of the predicted gravity and geoid anomalies from the inversion for $\tilde{F}_l^G$ relating N^{inst} to the observed N^{ell} for $l = 3$ to 46 (figure 4.26). Over Hudson Bay, this procedure predicts a peak gravity anomaly of -35 mGal and a peak geoid anomaly of -31 m. The latter value agrees reasonably well with the -37 m geoid anomaly prediction from the model of *Mitrovica and Peltier* [1989], but the former is in contrast to the gravity anomaly estimate of *James* [1992] of less than 10 mGal (both models use ICE-3G).

However, from a data analysis perspective, the peak anomaly is a dangerous quantity to use when judging the success of a given Earth model since two predictions may differ only at the very longest wavelengths and be identical at the shorter wavelengths which contain the higher sensitivity to deglaciation. Yet the longest wavelength are the hardest to localize. In our case, for $l > 5$ the two estimates are indistinguishable (figure 4.27) but diverge rapidly at lower degrees. Furthermore, two different models may predict the same peak anomaly as observed, but with very different spectral behaviour. We will demonstrate later that this is likely the case for the viscosity model of *Mitrovica and Peltier* [1989].

Predicted relaxation time spectra for a suite of proposed mantle viscosity models can be calculated [e.g., *Hager*, 1991] and compared with the bounds on the relaxation times provided by the gravity analysis. However, given that our inferred relaxation spectra are derived by a localization procedure which causes spectral smearing, anything more than a crude comparison can not be made. A true comparison requires submitting the ice history to the relaxation process and localizing the predictions in the same manner as the data. This requirement is crucial to recognize since the gravity data need to be localized to limit sensitivity to other tectonic processes. Therefore, despite the fact that most forward models are global and encompass only a single tectonic process, the models can be accurately judged only after submitting them to the same filtering as the data. We will make such a comparison with the estimates of $\tilde{F}_l^G$ from the simultaneous inversions.

Subduction Zones

Our slab distribution function is the static geoid derived from an *a priori* slab model similar to that used in the dynamic geoid modelling of *Hager* [1984], *Hager and Clayton* [1989], and *Hager and Richards* [1989], except that our model extends out to $l = 70$. The location of subducting slabs is determined by the location of slab seismicity [*Hager*, 1984]. The width of the surface projection of each slab is taken from the assumption that each slab penetrates into the mantle with a 60° dip, has a thickness of 125 km, and extends to 800 km depth. Slabs associated with seismicity at depths greater than 300 km are given an effective density of one, and slabs with no deep seismicity are given an effective density of one half [*Hager*, 1984]. The absolute scaling (i.e., density) of the slab function is not important, since we are calculating a transfer function which is free to shift up and down as required. We emphasize that at a fixed l the geoid estimated through localization will always have the same spatial pattern as the distribution function since we are calculating an l-dependent filter. The anticipated improvement achieved by localization is that the estimated amplitude of this filter is preferentially weighted to regions with slabs.

The estimates of $\tilde{F}_l^S$ for both N^{hyd} and N^{ell} are shown in figure 4.29, as are the

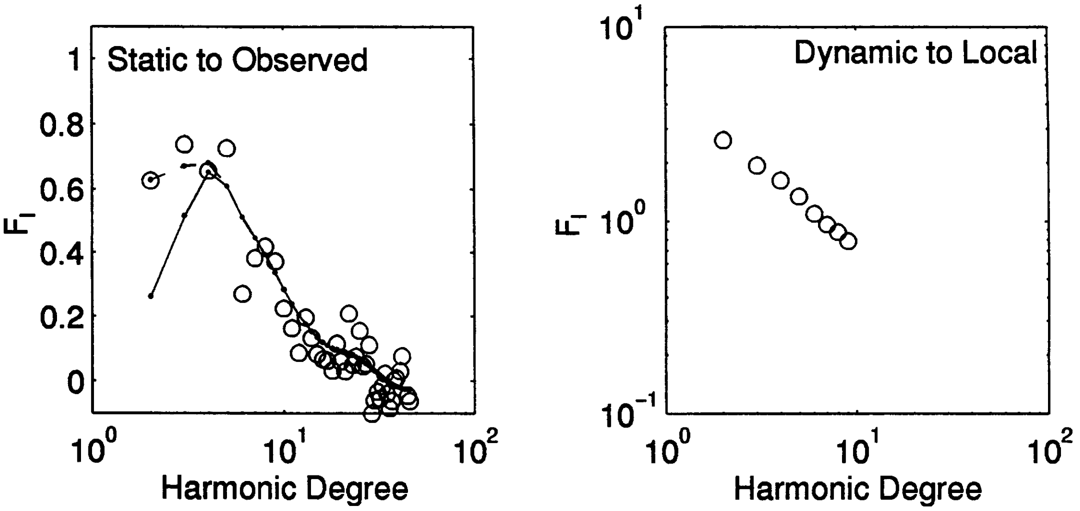

Figure 4.29: Left: $\tilde{F}_l^S$ for the static slab geoid relative to N^{hyd} and N^{ell}, indicated by dashed and solid lines, respectively. Also shown (open circles) is the global estimate, $\hat{F}_l^S$, relative to N^{hyd}. Right: The transfer function between the predicted geoid from dynamic flow modelling and localization relative to N^{hyd}.

global estimates $\hat{F}_l^S$. The predicted geoid and resulting residual fields are shown in figure 4.30. At low l, $\tilde{F}_l^S$ is similar to a smoothed version of $\hat{F}_l^S$, however at higher degrees $\tilde{F}_l^S$ is generally greater than $\hat{F}_l^S$. In the spatial domain we estimate geoid highs of over 70 m (N^{hyd}) and 50 m (N^{ell}) over the western Pacific subduction zones and over 70 m (N^{hyd}) and 30 m (N^{ell}) over the South American subduction zone. Geoid lows more negative than -30 m are predicted in the central Pacific and of less than -10 m in the Indian Ocean.

It is instructive to compare our slab geoid derived by localization methods with that predicted from a dynamic flow model (figures 4.29 and 4.31). The relationship between the geoid kernels and the geoid can be written as

$$N_{lm} = \frac{4\pi\gamma a}{g_0(2l+1)} \int_{r_1}^{r_2} G_l(r)\, \delta\rho_{lm}(r)\, dr \tag{4.6}$$

where N^{lm} is a harmonic coefficient of the geoid, G^l is the kernel, $\delta\rho_{lm}$ is the harmonic

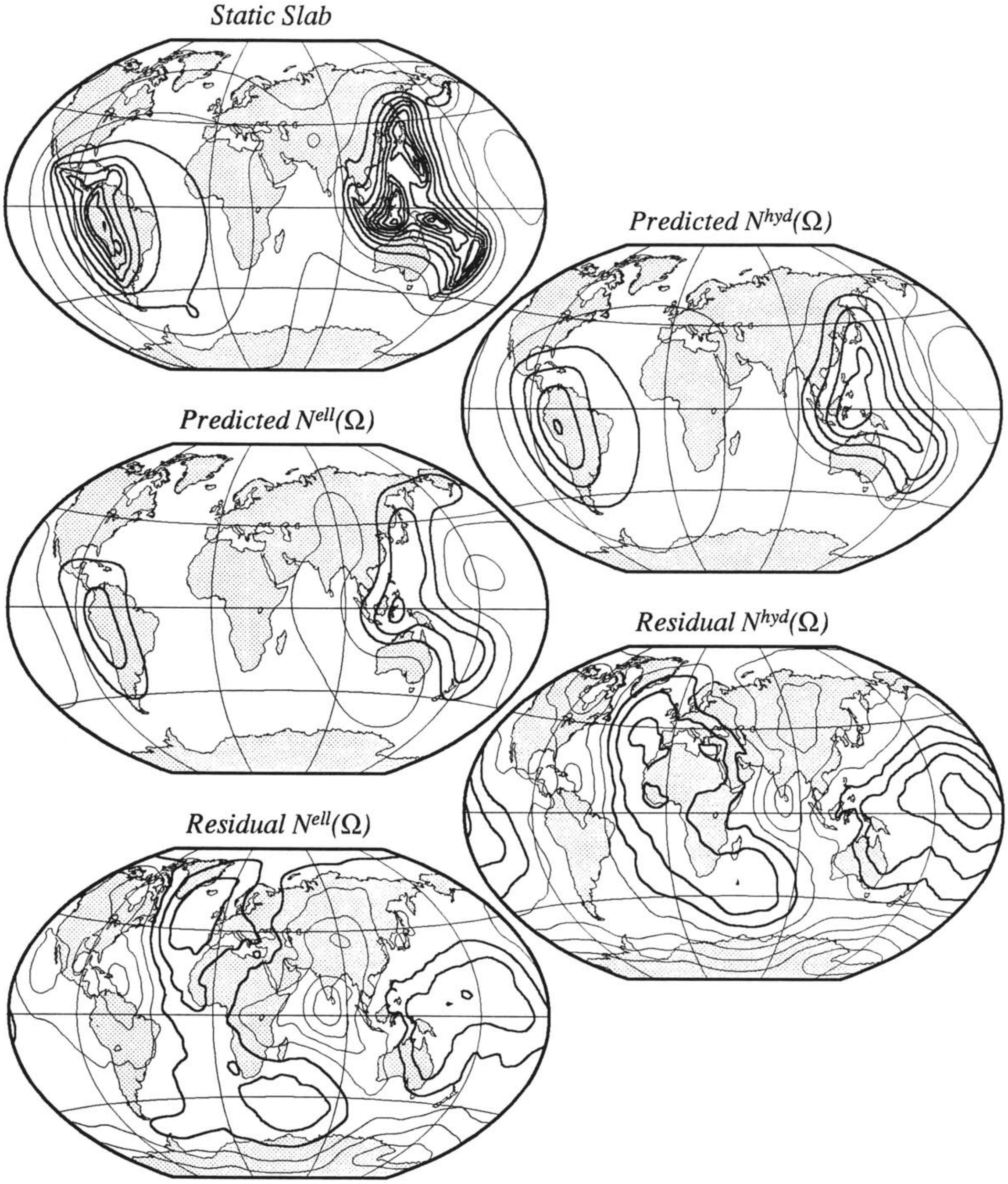

Static Slab

Predicted $N^{hyd}(\Omega)$

Predicted $N^{ell}(\Omega)$

Residual $N^{hyd}(\Omega)$

Residual $N^{ell}(\Omega)$

Figure 4.30: From top to bottom: The static slab geoid, N^{stat}, the slab geoid predicted by localization of N^{stat} relative to N^{hyd} and N^{ell}, along with the corresponding residual geoid anomalies. 20 m contour interval, staggered about zero by half an interval.

expansion of the density anomaly, γ is the gravitational constant, a is the planetary radius, and g_0 is the vertical gravity field at the surface. For a static geoid model with no dynamic topography, $G_l(r) = (r/a)^{l+2}$. To compare with the dynamic flow calculations we use the preferred viscosity model of *Hager and Richards* [1989] (figure 4.3) convolved with the slab density function that forms the basis of our slab distribution function and was constructed following the approach of *Hager* [1984]. The viscosity model was originally derived attempting to fit N^{hyd} in the degree band 2 to 9 [*Hager and Richards*, 1989].

Since the slab density model is independent of r for depths less than 800 km and is zero for depth greater than 800 km, we can write the expected transfer function relating the static geoid to that predicted by the viscosity model as

$$F_l = \frac{(l+3)/a}{1-(r_1/r_2)^{l+3}} \int_{r_1}^{r_2} G_l(r)\, dr, \tag{4.7}$$

where r_1 and r_2 correspond to 800 km depth and the surface, respectively. This filter is shown in figure 4.25, as is the result of inverting for the filter after it has been applied to the slab distribution function. The global transfer function, $\hat{F}_l$, between the dynamic slab geoid and our localization geoid in this degree band provides a quantitative measure of the difference between the two models. Since the flow model geoid and the localization geoid use the same tectonic distribution function and since both methods result in an l-dependent filter, the degree correlation between these models always has a value of one. The absolute scaling used in either the flow modelling or in constructing $T(\Omega)$ is a free parameter implying that the $\hat{F}_l$ spectra between the dynamic and localization geoids can be translated up and down arbitrarily. However, in our case both models use the same density contrast of 64 kgm^{-3} for the slabs and are therefore directly comparable to each other. We find that at $l = 4$ and 5, where the slab distribution function has a spectral peak [e.g., *Richards and Hager*, 1988], the two models differ by less than a

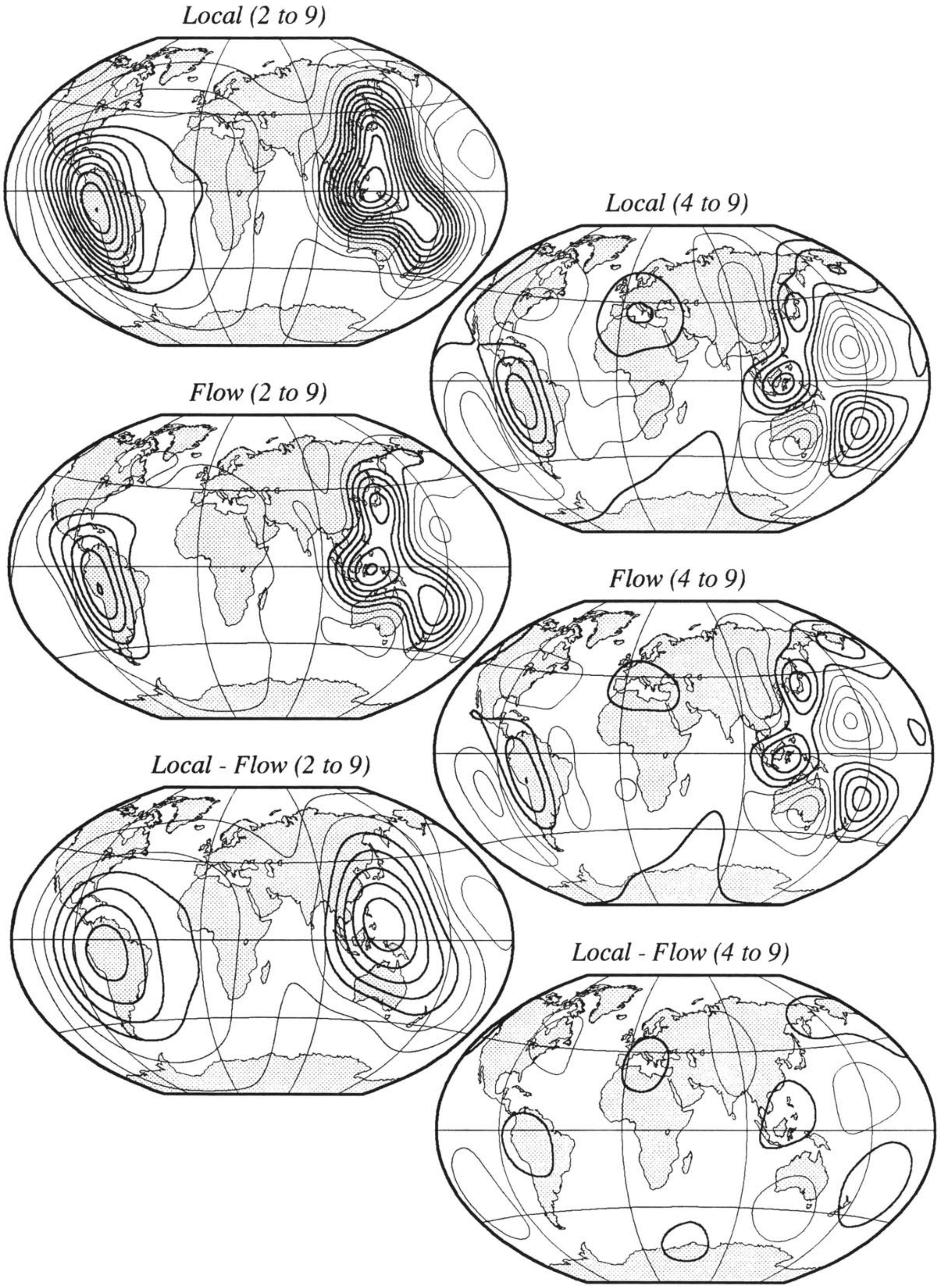

Local (2 to 9)

Local (4 to 9)

Flow (2 to 9)

Flow (4 to 9)

Local - Flow (2 to 9)

Local - Flow (4 to 9)

Figure 4.31: The predicted slab geoid from localization and dynamic flow modelling, as well as the difference between the two predictions in the degree band 2 to 9 (left) and 4 to 9 (right). 8 m contour interval, staggered about zero by half an interval

factor of 2. If the geoid were completely described by the flow model, then the value of $\hat{F}_l$ spectra would be a constant value of one. Changing the slope of the spectra could be achieved by changing the viscosity model, a task which is not pursued here.

The spatial rendition of the localization and flow-derived geoids are remarkably similar (of course, we started with the same distribution function), differing primarily at the lowest degree (figure 4.31). We expect that where there is spectral power in the slab distribution function, the localization geoid will have a larger amplitude than the flow-derived geoid. This difference arises because both methods are effectively least-squares estimates of an l-dependent filter (this is explicit in the localization procedure, or implicit with the flow modelling which is judged by global variance reduction), and the localization procedure reduces the effect of "noise", coming in the form of geoid anomalies unrelated to subduction zones.

Hotspots

In this section, we estimate the geoid associated with the processes reponsible for the formation of hotspots. Unlike the case of glacial rebound or subduction zones, we can not design a tectonic basis function which is based on a geophysical quantity (such as the instant unloading geoid or the static slab geoid). Instead, we consider a compilation of hotspot locations and treat each hotspot as a delta function. The spherical harmonic expansion of the compilation is reddened by dividing the coefficients by $(2l+1)$ in order to give a spectrum which is characteristic of the geoid. We apply this procedure to the hotspot compilations from *Richards et al.* [1988](RHS88) and from *Sleep* [1990](S90), as well as a modified version of the *Sleep* [1990] compilation (S95) (table 4.1). S90 differs from RHS88 in that it combines several hotspots believed to result from the same deep structure. Furthermore, S90 includes only the most robust continental hotspots that are not likely the result of passive rifting [*Sleep*, 1990]. S90 was compiled in order to calculate the buoyancy flux associated with each hotspot. We use this flux estimate

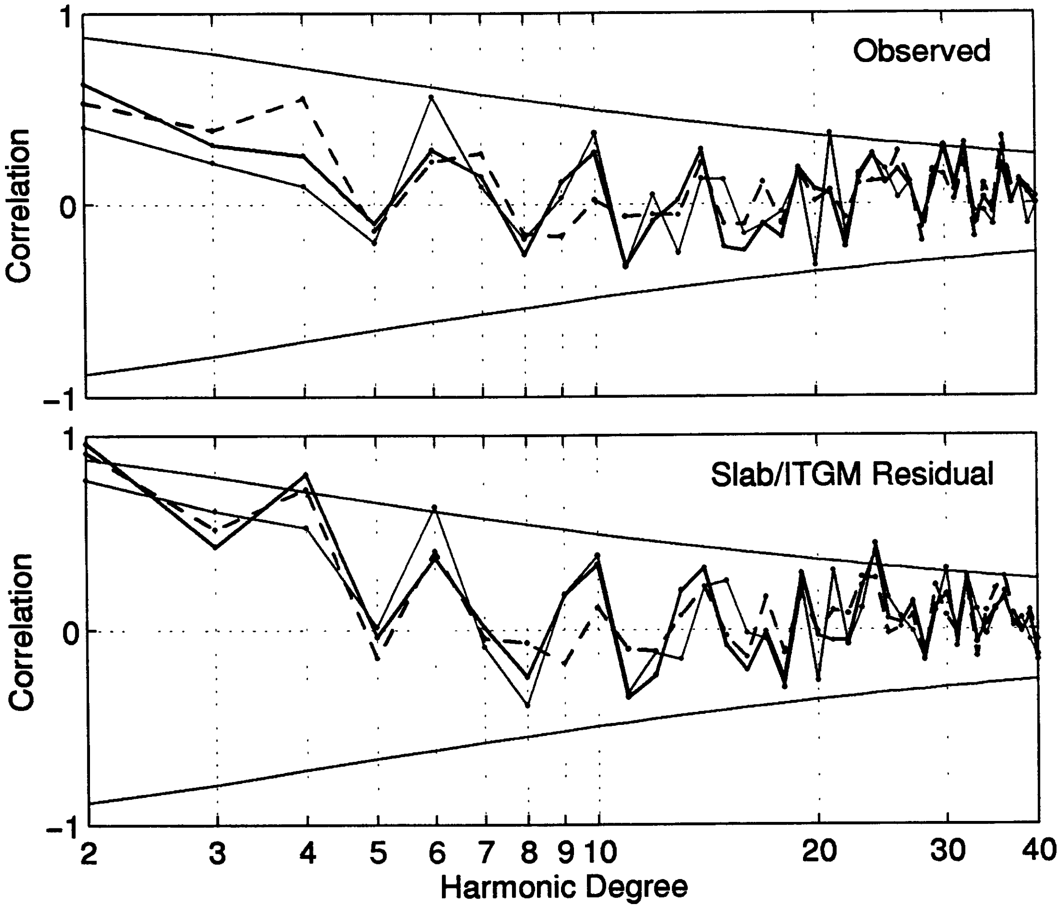

Figure 4.32: Global degree correlations between the hotspot distributions and the global geoid (top) and the residual geoid after removal of ITGM and the predicted slab geoid (bottom). Dashed lines correspond to RHS88, thin lines to S90, and thick lines to S95. 98 percent confidence levels are shown for reference.

for relative scaling of each hotspot. However, we note a cirucularity in this approach since geoid data was used to estimate the flux. We address this circularity with S95 which uses the S90 compilation but with a unit weight for all hotspots. In addition, S95 differs from S90 in that we have removed hotspots with small buoyancy flux (less than 0.5 Mgs^{-1}), and we have added the Vema and Erebus hotspots.

The global correlation between the three hotspot distribution functions and the observed geoid is shown in figure 4.32, as is the correlation with the residual geoid after removal of ITGM and our predicted subduction geoid. Previously, a high correlation

Lat °N	Lon °E	Weight[1]	Weight[2]	Weight[3]	Name
12	42	1.0	1.2	1.0	Afar, Ethiopia
-17	-25	1.0	–	–	Arnold
-8	-14	1.0	–	–	Ascension
38	-28	1.0	0.3	–	Azores
30	-65	1.0	1.1	1.0	Bermuda
-54	4	1.0	0.4	–	Bouvet
53	-135	1.0	0.3	–	Bowie, Kodiak
4	9	1.0	–	–	Cameroon
28	-17	1.0	1.0	1.0	Canary
15	-24	1.0	1.6	1.0	Cape Verde
3	167	1.0	1.6	1.0	Caroline
-35	80	1.0	–	–	Christmas, Amsterdam
46	-128	1.0	0.3	–	Cobb, Juan de Fuca
-12	44	1.0	–	–	Comores
-45	50	1.0	0.5	1.0	Crozet
-42	0	1.0	0.5	1.0	Discovery, Cape
-27	-109	1.0	3.3	1.0	Easter
50	7	1.0	–	–	Eifel
-78	167	1.0	–	1.0	Erebus
-4	-32	1.0	0.5	1.0	Fernando
0	-91	1.0	1.0	1.0	Galapagos
27	-113	1.0	0.3	–	Guadalupe, Baja
20	-155	1.0	8.7	1.0	Hawaii
20	6	1.0	0.9	1.0	Hoggar
64	-20	1.0	1.4	1.0	Iceland
72	-8	1.0	–	–	Jan Mayen
13	24	1.0	–	–	Jebel Marra, Darfur
-34	-79	1.0	1.6	1.0	Juan Fernandez
-49	69	1.0	0.5	1.0	Kerguelen
-3	36	1.0	–	–	Lake Victoria
-53	-138	–	0.9	1.0	Louisville
33	-17	1.0	–	–	Madeira
-11	-139	1.0	3.3	1.0	Marquesas
-29	-140	1.0	3.3	1.0	MacDonald, Cook-Austral
-45	5	–	0.5	1.0	Meteor
29	-29	1.0	0.5	1.0	New England, Great Meteor
-27	-129	1.0	3.3	1.0	Pitcairn, Gambire
37	-104	1.0	–	1.0	Raton, New Mexico
-21	56	1.0	1.9	1.0	Reunion
-15	-168	1.0	1.6	1.0	Samoa
-27	-80	1.0	1.6	1.0	San Felix
-16	-6	1.0	0.5	1.0	Saint Helena
-18	-148	1.0	3.3	1.0	Tahiti, Society
-40	150	1.0	2.7	1.0	Tasman
21	17	1.0	–	–	Tibesti
-21	-29	1.0	0.5	1.0	Trinidade, Martin Vaz
-37	-12	1.0	1.7	1.0	Tristan de Cunha
-32	16	1.0	–	1.0	Vema
45	-111	1.0	1.5	1.0	Yellowstone

Table 4.1: Location and relative weighting of hotspots from the compilations of [1] *Richards et al.*, [1988], [2] *Sleep*, [1990], and [3] this work. The weighting for *Sleep*, [1990] is equal to his estimate of buoyancy flux in Mgs^{-1}.

between RHS88 and the residual geoid after removal of the modelled slab signature has been noted [e.g. *Richards and Hager*, 1988]. This correlation is not clearly evident here (at least above the 98 percent confidence level). Furthermore, there is a lot of scatter in the correlation spectra suggesting that any global correlations are not robust. We investigate the relationship further by considering the localized relationship between hotspots and the geoid.

The estimates of $\tilde{F}_l^H$ for the three hotspot distributions are shown in figure 4.33, and the spatial renditions of the predicted geoids are shown in figures 4.34, 4.35, and 4.36. The spatial representations of the estimated hotspot geoid for the different distribution functions are very similar, with geoid highs of between 30 and 60 m over the central Pacific and the Atlantic hotspots, and distinct geoid lows estimated over South America and central Asia. The residual geoids still have positive geoid anomalies over the Indian Ocean hotspots, as well as the North Atlantic hotspots. These residuals suggest that the hotspots in these regions should be given larger relative weights in the construction of the distribution function.

On a linear scale, $\tilde{F}_l^H$ is dominated by the longest wavelengths (figure 4.33, left). When viewed on a logarithmic scale (figure 4.33, right) we find that the $\tilde{F}_l^H$ may be divided into two regions. We interpret the low degree portion as related to the deep processes responsible for swells and often associated with multiple hotspots. In contrast, we associate the high degree portion of $\tilde{F}_l^H$ to be the average response associated with individual hotspots. This separation was evident in the spectrograms of the geoid (e.g., over Hawaii). The minimum $\tilde{F}_l^H$ that separates these two parts of the spectrum occurs at $l \approx 13$, or at length scales similar to the depth of the mantle. We reiterate that the estimates of $\tilde{F}_l^H$ can not be directly related to a physical process since the hotspot distribution represents only selected position on the globe and not an inherent physical quantity such as density.

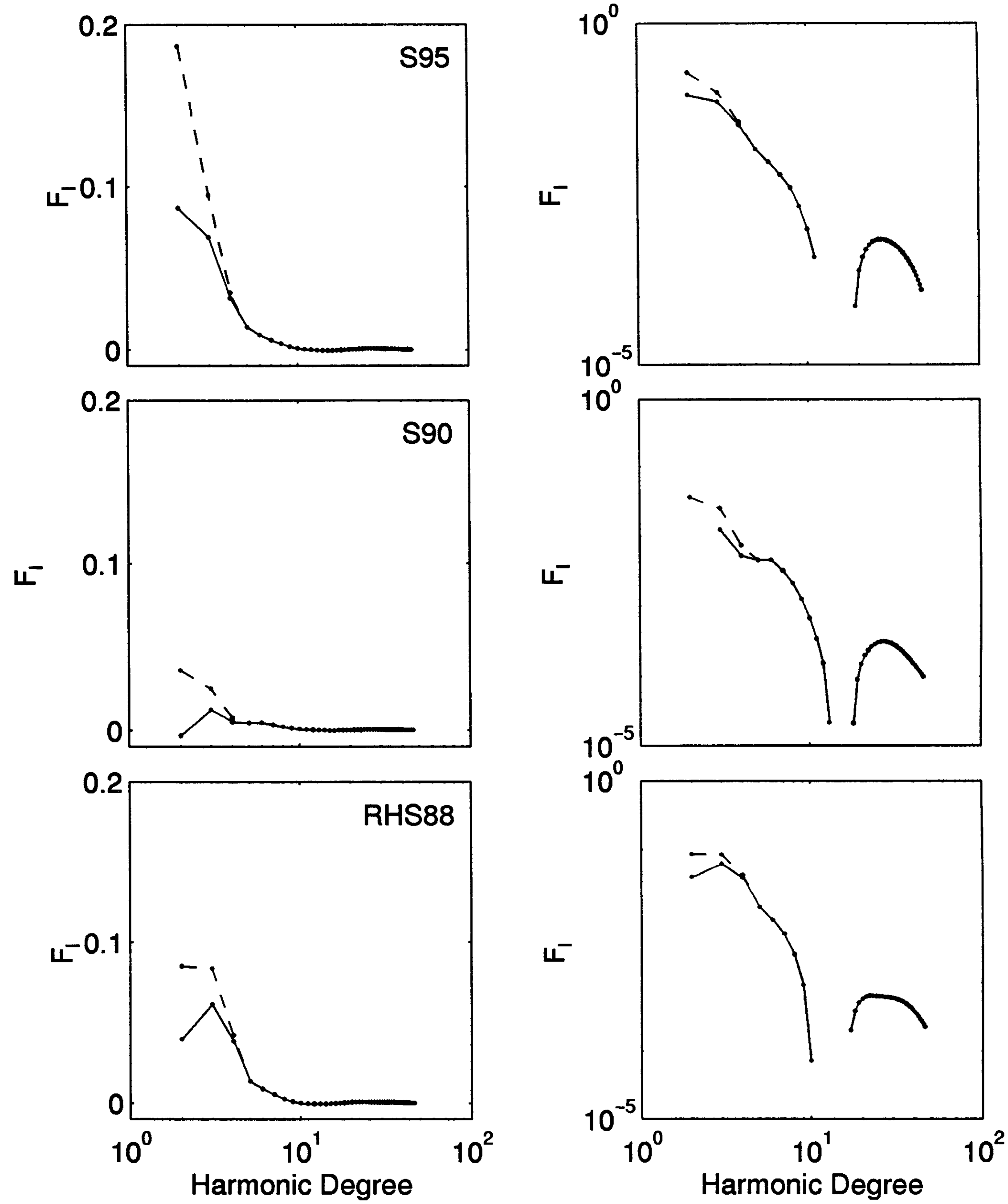

Figure 4.33: $\tilde{F}_l^H$ for the three hotspot distribution functions relative to N^{hyd} (dashed lines) and N^{ell} (solid lines). Frames on the left have semilog axes and frames on the right have loglog axes.

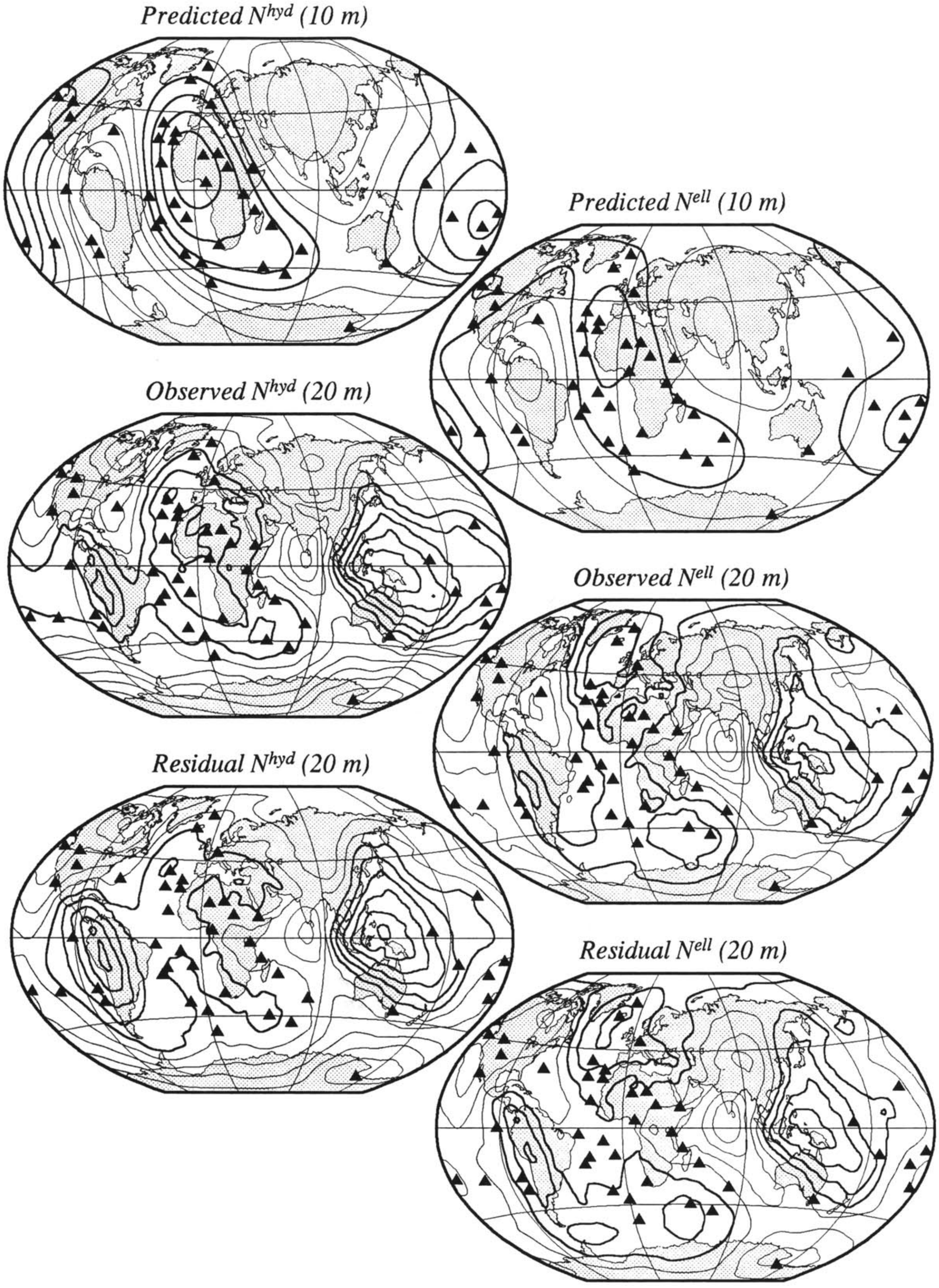
Predicted N^{hyd} (10 m)

Predicted N^{ell} (10 m)

Observed N^{hyd} (20 m)

Observed N^{ell} (20 m)

Residual N^{hyd} (20 m)

Residual N^{ell} (20 m)

Figure 4.34: From top to bottom: Geoid predicted from localization of RHS88, the observed geoid, and the corresponding residual geoid. Contour intervals are labeled and are staggered about zero by half an interval. Triangles indicate RHS88 hotspot locations.

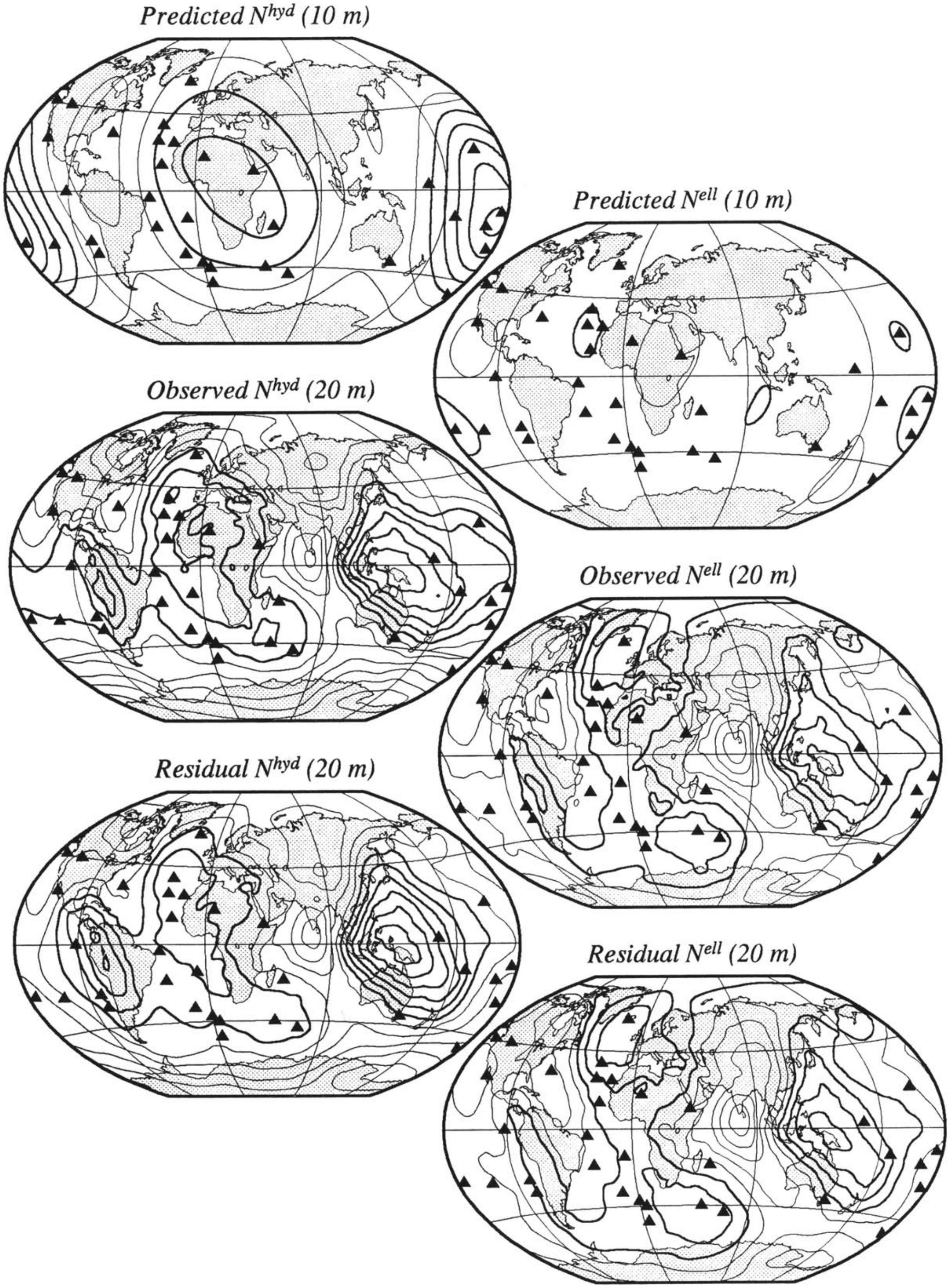

Figure 4.35: Same as 4.34 but for S90

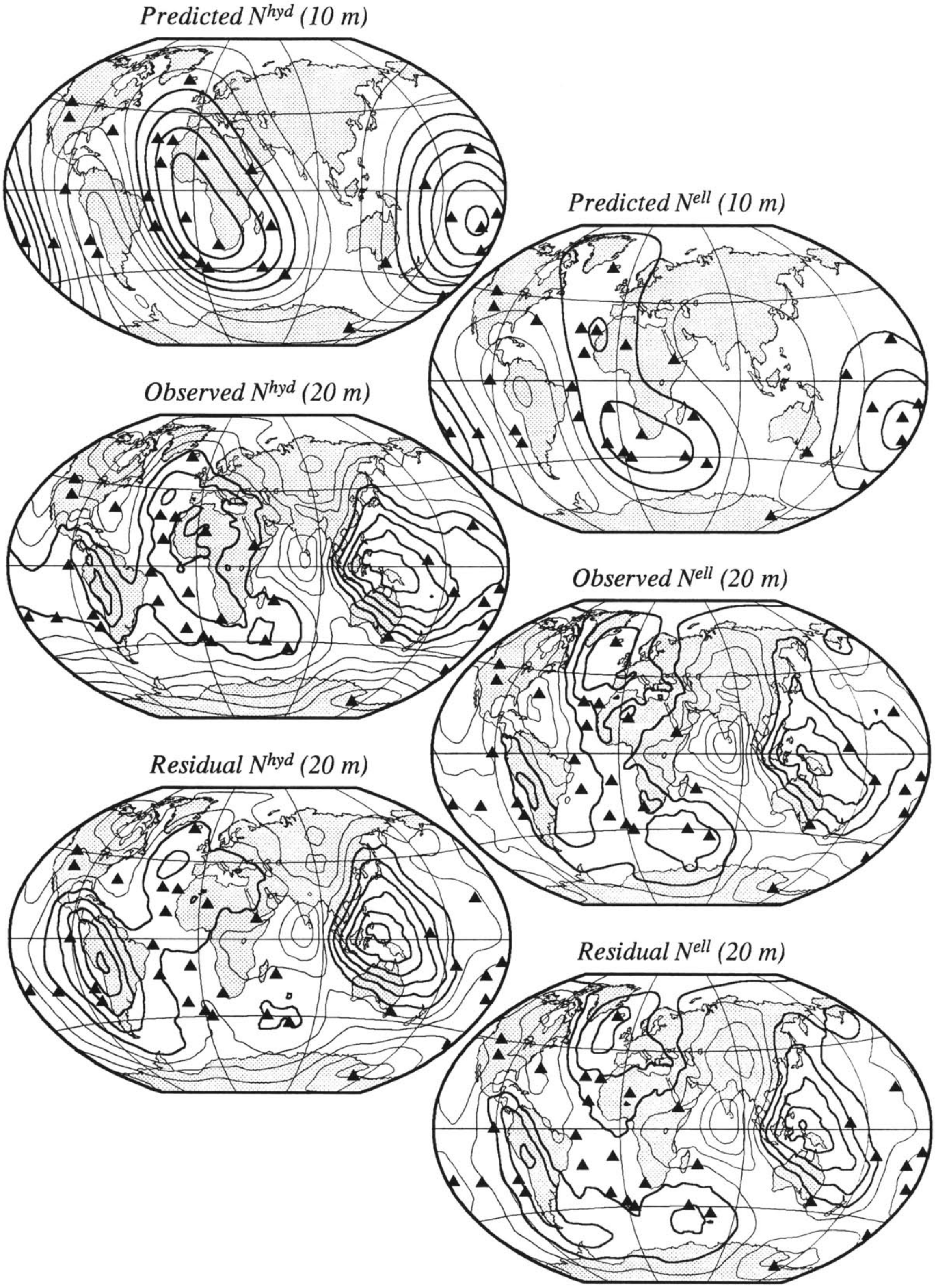

Predicted N^{hyd} (10 m)

Predicted N^{ell} (10 m)

Observed N^{hyd} (20 m)

Observed N^{ell} (20 m)

Residual N^{hyd} (20 m)

Residual N^{ell} (20 m)

Figure 4.36: Same as 4.34 but for S95

Simultaneous Inversion

Clearly, there may be a trade off between the geoid anomaly attributed to different tectonic distributions. For instance, the slab geoid predicts a geoid high over South America and the hotspot geoid predicts a geoid low in the same region. To get a measure of this interdependence, we consider a simultaneous estimation of $\tilde{F_l}^G$, $\tilde{F_l}^S$, and $\tilde{F_l}^H$. For a discrete set of locations, Ω_i, $i = 1 \cdots p$, the inversion can be written (using the global approach) as

$$\begin{pmatrix} g_{l0}(\Omega_1) & s_{l0}(\Omega_1) & h_{l0}(\Omega_1) \\ \vdots & \vdots & \vdots \\ g_{ll}(\Omega_1) & s_{ll}(\Omega_1) & h_{ll}(\Omega_1) \\ \vdots & \vdots & \vdots \\ g_{l0}(\Omega_p) & s_{l0}(\Omega_p) & h_{l0}(\Omega_p) \\ \vdots & \vdots & \vdots \\ g_{ll}(\Omega_p) & s_{ll}(\Omega_p) & h_{ll}(\Omega_p) \end{pmatrix} \begin{pmatrix} \tilde{F_l}^G \\ \tilde{F_l}^S \\ \tilde{F_l}^H \end{pmatrix} = \begin{pmatrix} n_{l0}(\Omega_1) \\ \vdots \\ n_{ll}(\Omega_1) \\ \vdots \\ n_{l0}(\Omega_p) \\ \vdots \\ n_{ll}(\Omega_p) \end{pmatrix}. \tag{4.8}$$

where g, s, h, and n are the localized representations of the glacial, subduction, hotspot, and observed geoids, respectively. Since our data exist as continuous spatial variables for the entire surface of the planet, and in order to take advantage of the harmonic coupling relations, it is most efficient to write equation 4.8 in terms of the normal equations in the continuous limit (i.e., $p \to \infty$), resulting in

$$\begin{pmatrix} \int_\Omega \sigma^2_{gg}(\Omega, l)\, d\Omega & \int_\Omega \sigma^2_{gs}(\Omega, l)\, d\Omega & \int_\Omega \sigma^2_{gh}(\Omega, l)\, d\Omega \\ \int_\Omega \sigma^2_{sg}(\Omega, l)\, d\Omega & \int_\Omega \sigma^2_{ss}(\Omega, l)\, d\Omega & \int_\Omega \sigma^2_{sh}(\Omega, l)\, d\Omega \\ \int_\Omega \sigma^2_{hg}(\Omega, l)\, d\Omega & \int_\Omega \sigma^2_{hs}(\Omega, l)\, d\Omega & \int_\Omega \sigma^2_{hh}(\Omega, l)\, d\Omega \end{pmatrix} \begin{pmatrix} \tilde{F_l}^G \\ \tilde{F_l}^S \\ \tilde{F_l}^H \end{pmatrix} = \begin{pmatrix} \int_\Omega \sigma^2_{ng}(\Omega, l)\, d\Omega \\ \int_\Omega \sigma^2_{ns}(\Omega, l)\, d\Omega \\ \int_\Omega \sigma^2_{nh}(\Omega, l)\, d\Omega \end{pmatrix}, \tag{4.9}$$

which can be rapidly solved using equation 4.4. As should be expected, this system reduces to equation 4.3 when estimating a single $\tilde{F}_l$.

We present the results for inversions using all three hotspot compilations relative to N^{hyd} (figures 4.37 through 4.50). In addition to the estimates of $\tilde{F}_l$, we also show the predicted relaxation times from the glacial geoid estimation, the global transfer function relating the dynamic flow geoid to the localized geoid, and the correlation between the estimates of the three transfer functions. We also present the spatial renditions of the predicted geoids along with their corresponding residual fields. Finally, we show the global variance reduction achieved by each model as well as S_l maps of the residual geoids using f_s equal to 1 and 2.

Generally, we find few differences between the individual and the simultaneous inversions. The primary difference is the trade off between the three sources for the $l \leq 5$ signal, as is indicated by plot of r_l. On the basis of the channel flow arguments made previously, we can not rule out the possibility that the observed increase in $\tilde{F}_l^G$ at the lowest degrees for the models using RHS88 and S95 is due to relaxation of a relatively thin viscous layer somewhere within or at the bottom of the mantle.

The residual geoids for the three models are similar, differing primarily in the amount of the low l signal taken up by the hotspot geoid. It is instructive to consider the global l-dependent variance reduction as well as the individual contributions from glacial, subduction, and hotspot geoids, including the effect of ITGM. In this global perspective, the geoid anomaly associated with glacial rebound only has significant effect at $l = 5$, accounting for nearly a fourth the variance at that degree. For RHS88 and S95, the hotspot geoid is only significant ($\geq$ 25 percent) at $l = 2$. In contrast, for all three models, the subduction geoid reduces the variance at multiple degrees with a notable impact at $l = 2$ through 5. The combined geoid model accounts for over half the variance at all l, and up to 99 percent of the geoid at selected degrees. We point out that the total variance reduction can be greater than the sum of the variance reductions

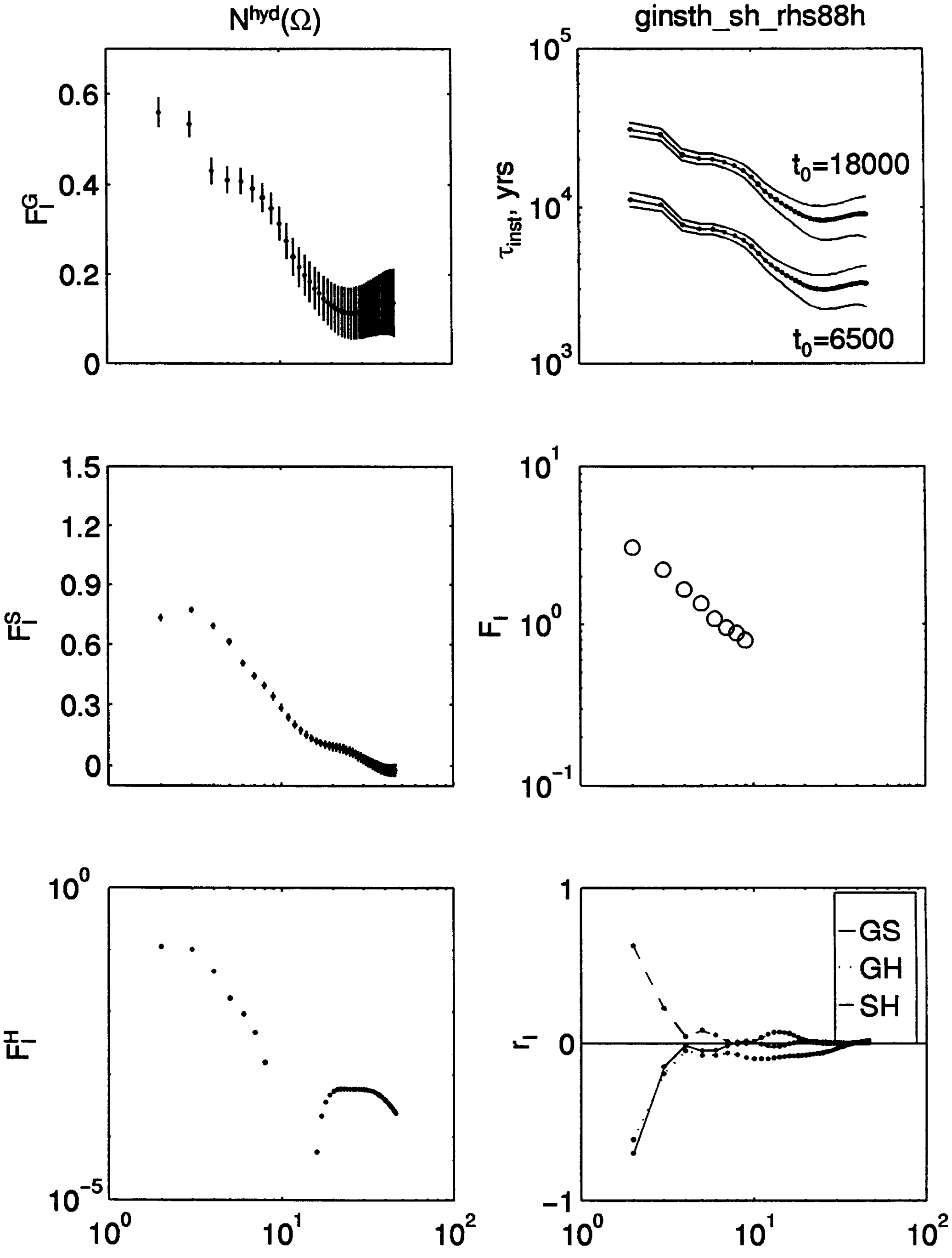

Figure 4.37: From top to bottom, left to right: $\tilde{F}_l^G$, predicted relaxation times, $\tilde{F}_l^S$, $\hat{F}_l$ between the flow derived and localized slab geoids, $\tilde{F}_l^H$, and the correlations between estimates of $\tilde{F}_l^G$, $\tilde{F}_l^S$ and, $\tilde{F}_l^H$. Errors are one standard deviation, and all estimates are relative to N^{hyd}.

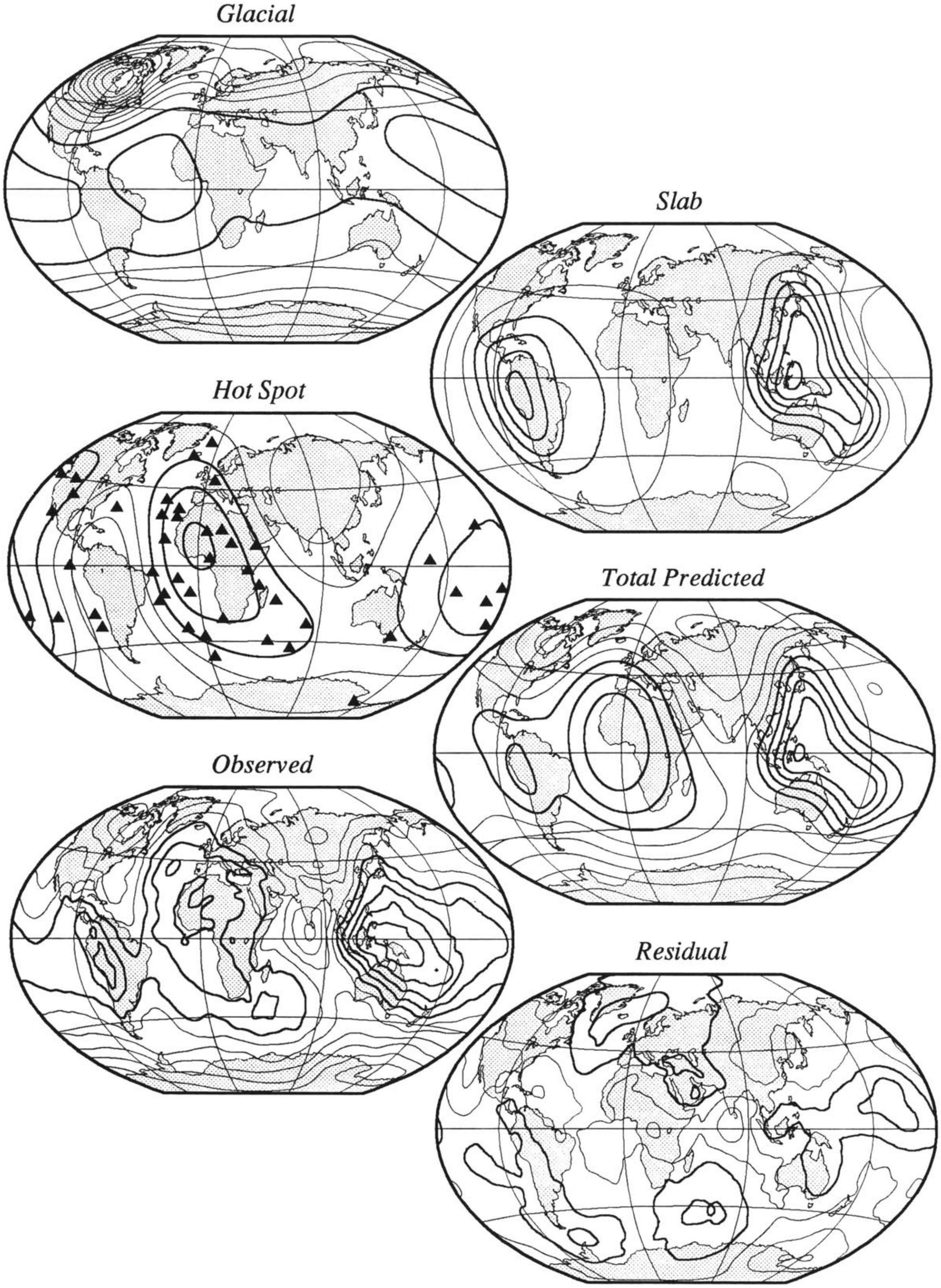

Figure 4.38: Predicted and residual geoids for $l = 2$ to 46 from simultaneous local inversion relative to N^{hyd}. 20 m contour interval, except for the glacial geoid which has a 6 m interval.

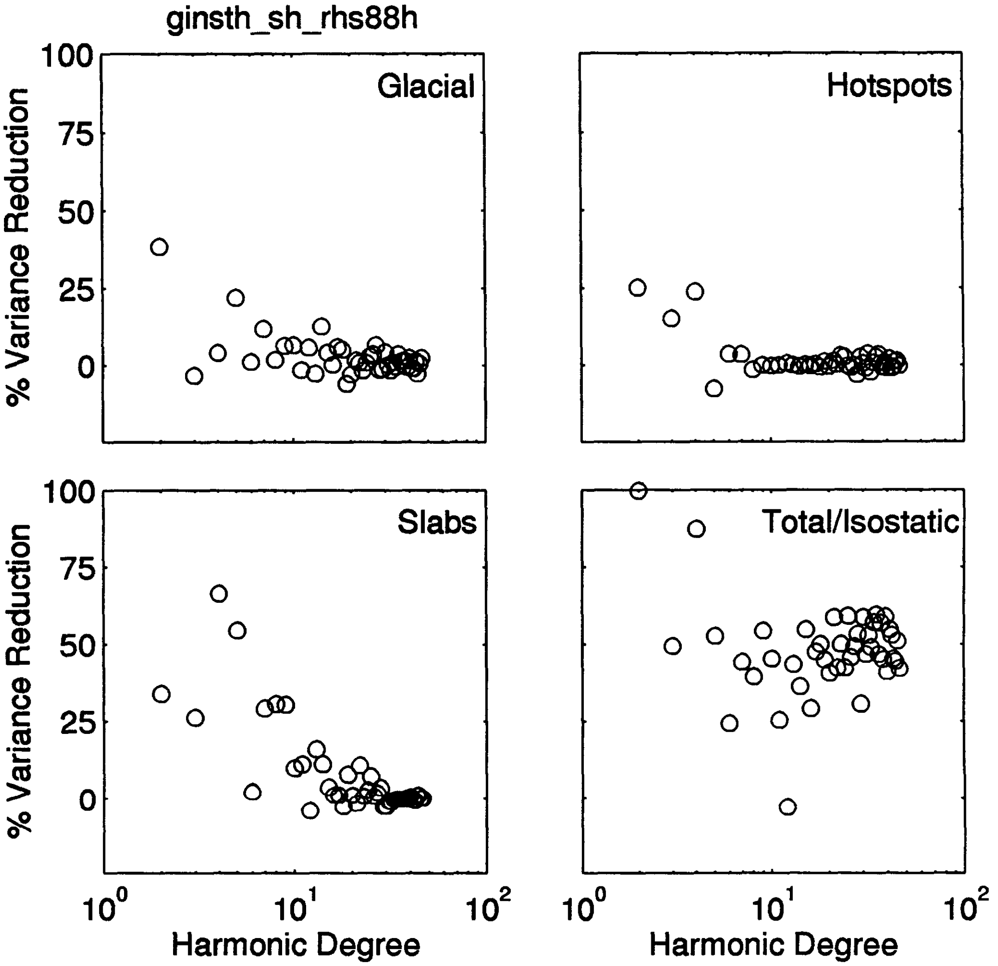

Figure 4.39: Individual contributions to the global variance reduction of N^{hyd} from the simulataneous inversion using RHS88. The total variance reduction at the bottom left includes the effects of ITGM.

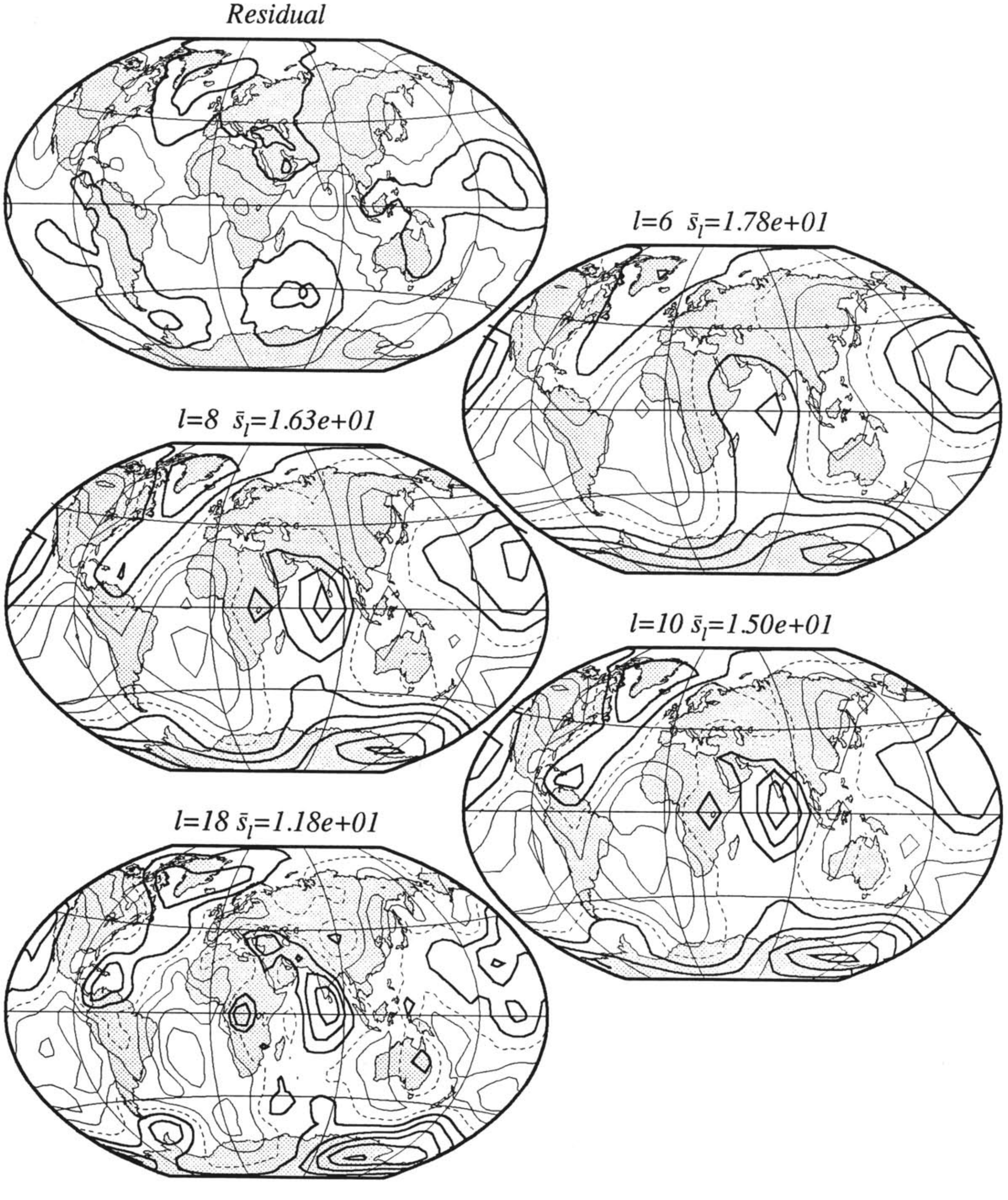

Residual

$l=6$ $\bar{s}_l=1.78e+01$

$l=8$ $\bar{s}_l=1.63e+01$

$l=10$ $\bar{s}_l=1.50e+01$

$l=18$ $\bar{s}_l=1.18e+01$

Figure 4.40: ΔS_l of Top left: The residual geoid from the model using RHS88, 20 m contour interval staggered about zero by half an interval. Remaining frames: ΔS_l of the residual geoid using $f_s = 1$, 3 m contour interval.

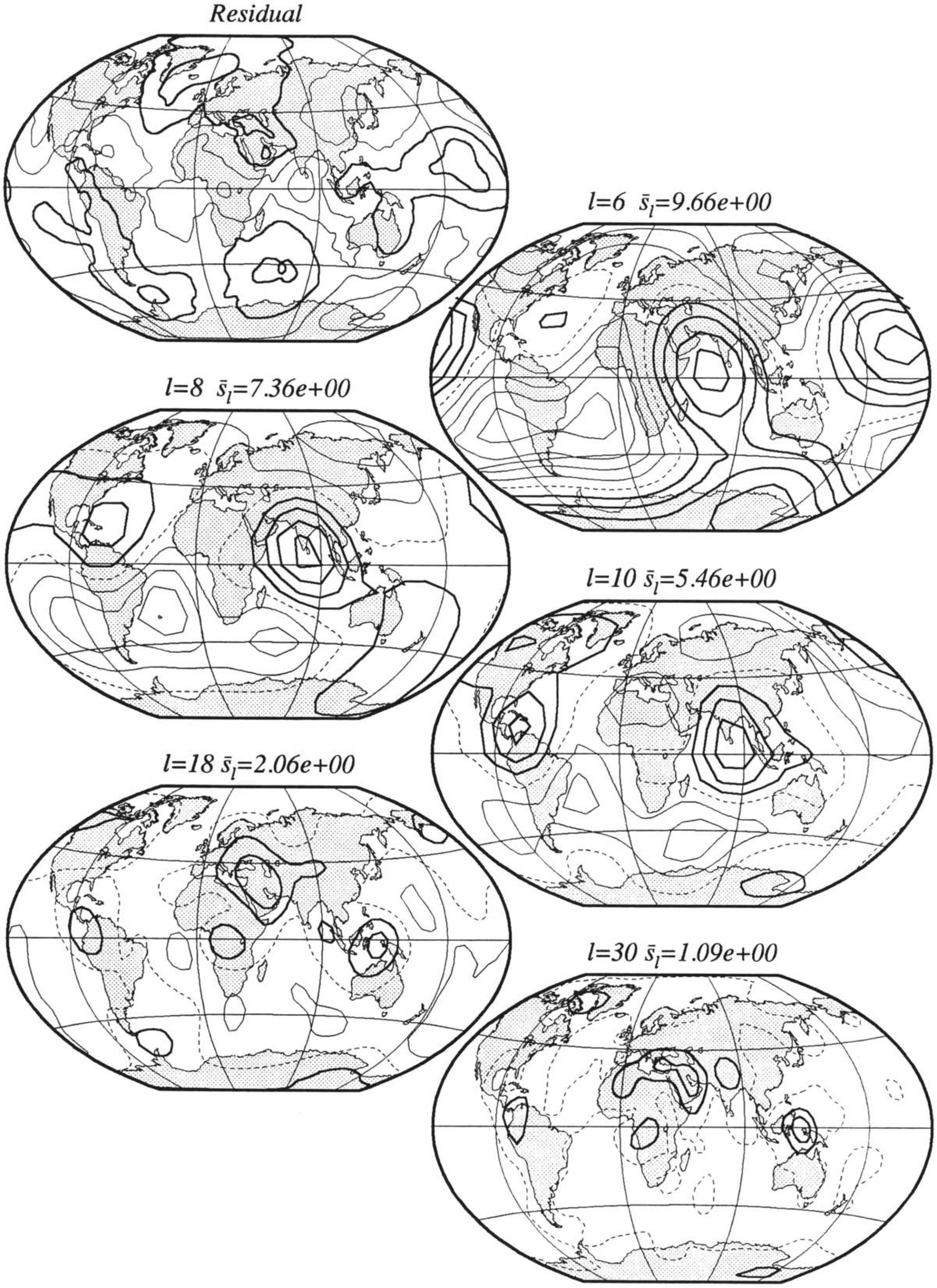

Residual

$l=6$ $\bar{s}_l=9.66e+00$

$l=8$ $\bar{s}_l=7.36e+00$

$l=10$ $\bar{s}_l=5.46e+00$

$l=18$ $\bar{s}_l=2.06e+00$

$l=30$ $\bar{s}_l=1.09e+00$

Figure 4.41: ΔS_l of Top left: The residual geoid from the model using RHS88, 20 m contour interval staggered about zero by half an interval. Remaining frames: ΔS_l of the residual geoid using $f_s = 2$, 1 m contour interval.

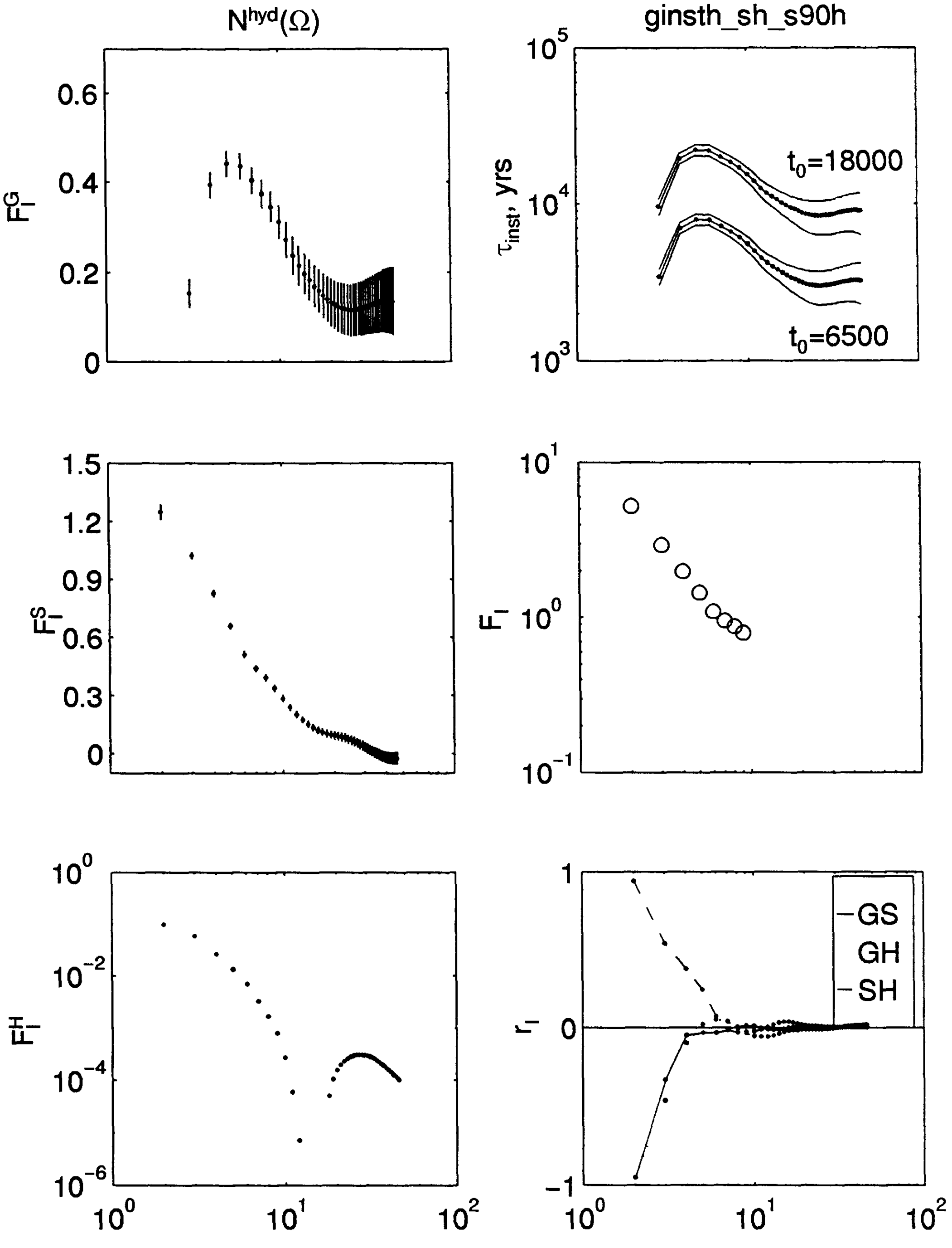

Figure 4.42: Same as figure 4.37 but using the hotspot compilation S90.

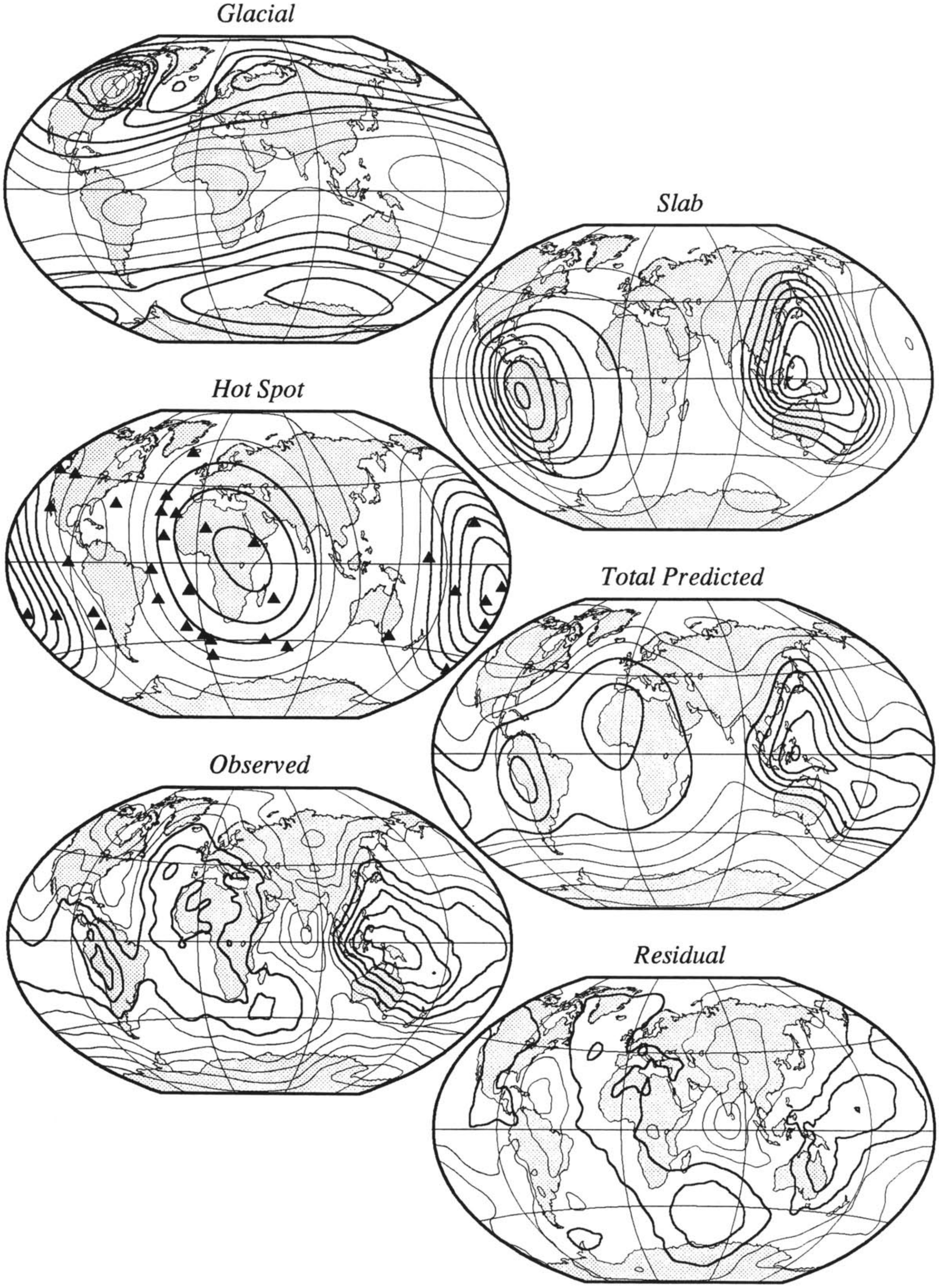

Figure 4.43: Same as figure 4.38 but using the hotspot compilation S90.

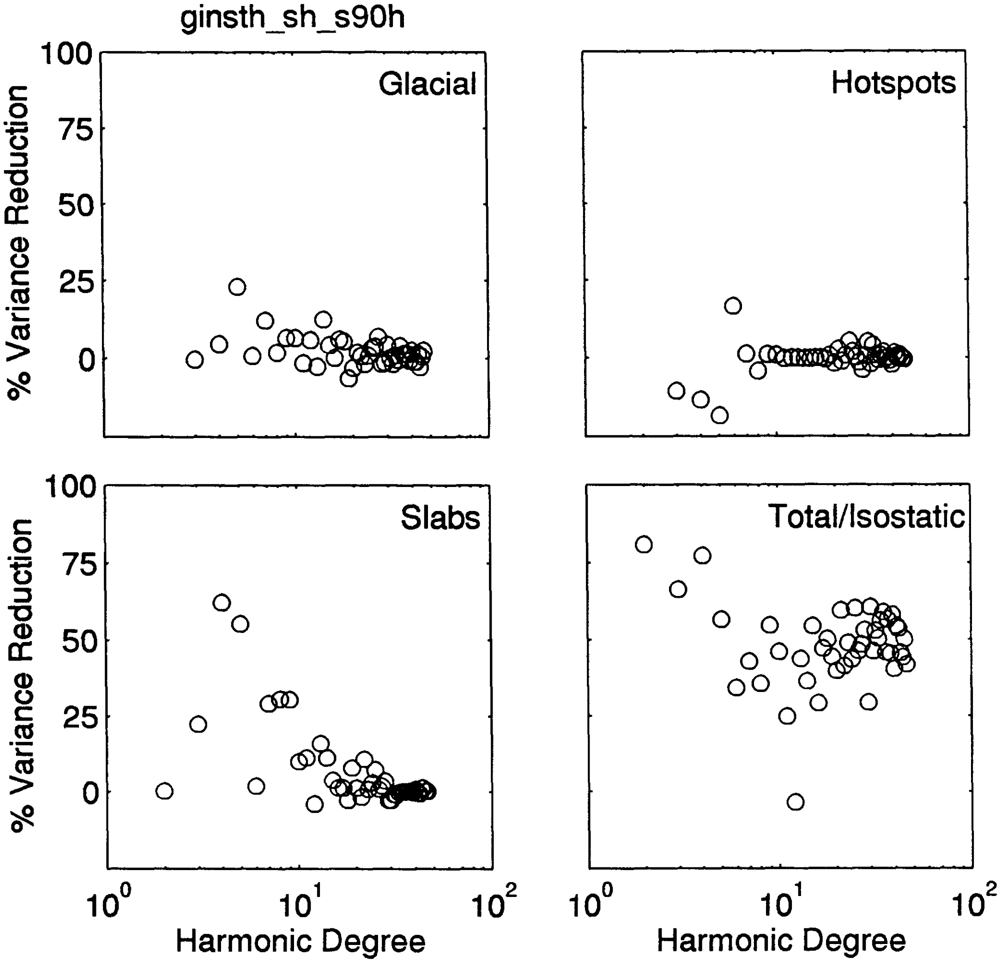

Figure 4.44: Same as figure 4.39 but using the hotspot compilation S90.

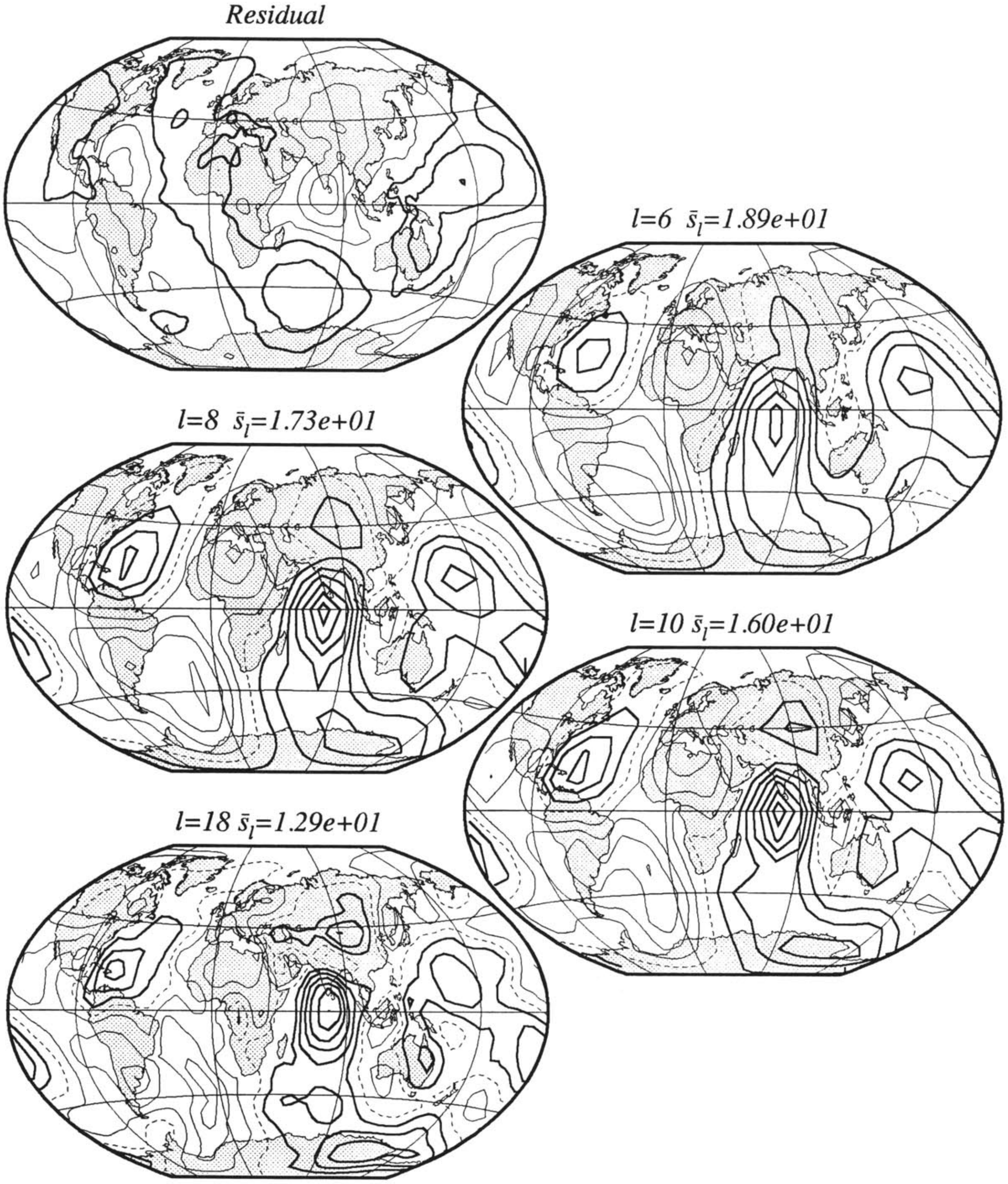

Figure 4.45: ΔS_l of Top left: The residual geoid from the model using S90, 20 m contour interval staggered about zero by half an interval. Remaining frames: ΔS_l of the residual geoid using $f_s = 1$, 3 m contour interval.

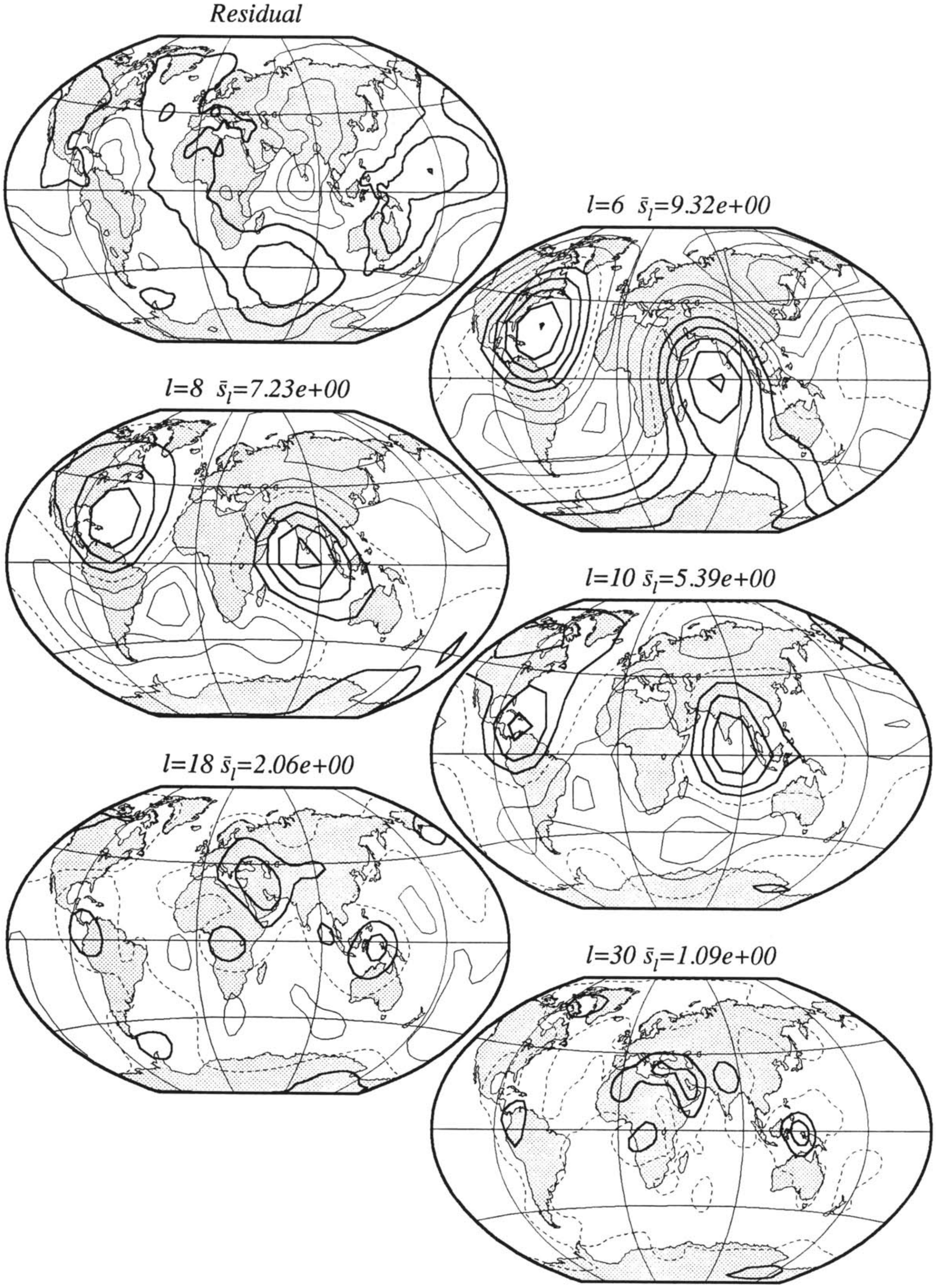

Figure 4.46: ΔS_l of Top left: The residual geoid from the model using S90, 20 m contour interval staggered about zero by half an interval. Remaining frames: ΔS_l of the residual geoid using $f_s = 2$, 1 m contour interval.

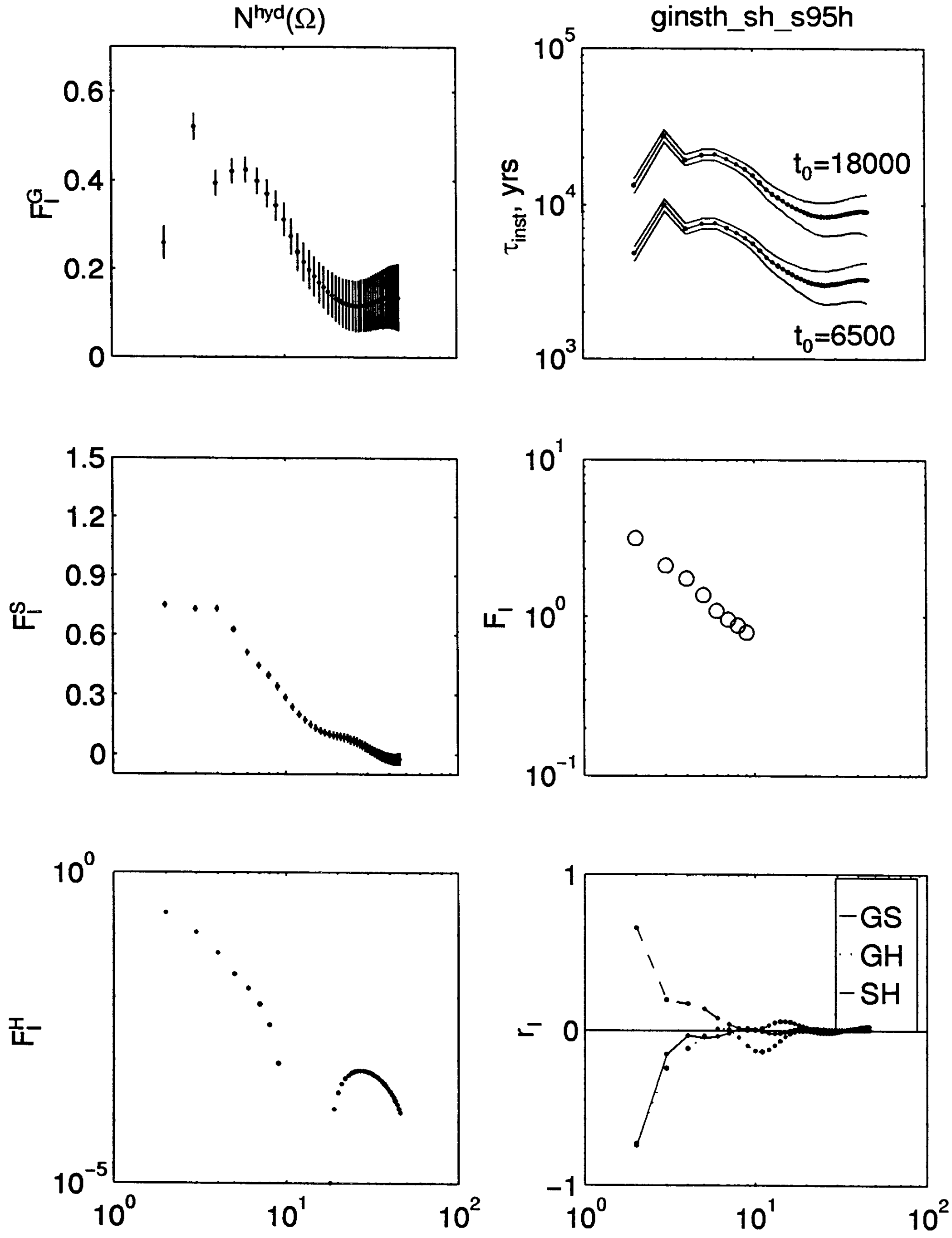

Figure 4.47: Same as figure 4.37 but using the hotspot compilation S95.

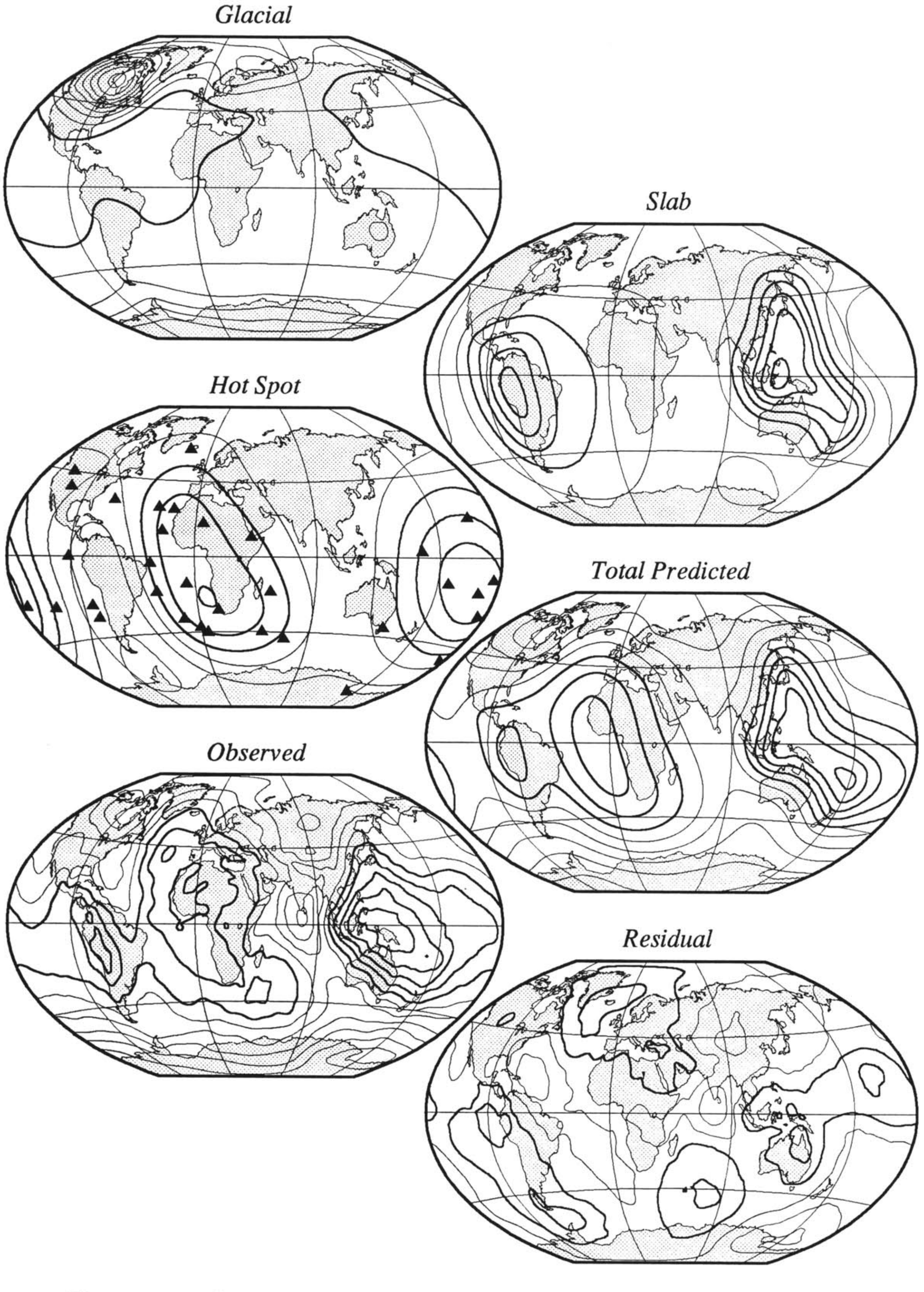

Figure 4.48: Same as figure 4.38 but using the hotspot compilation S95.

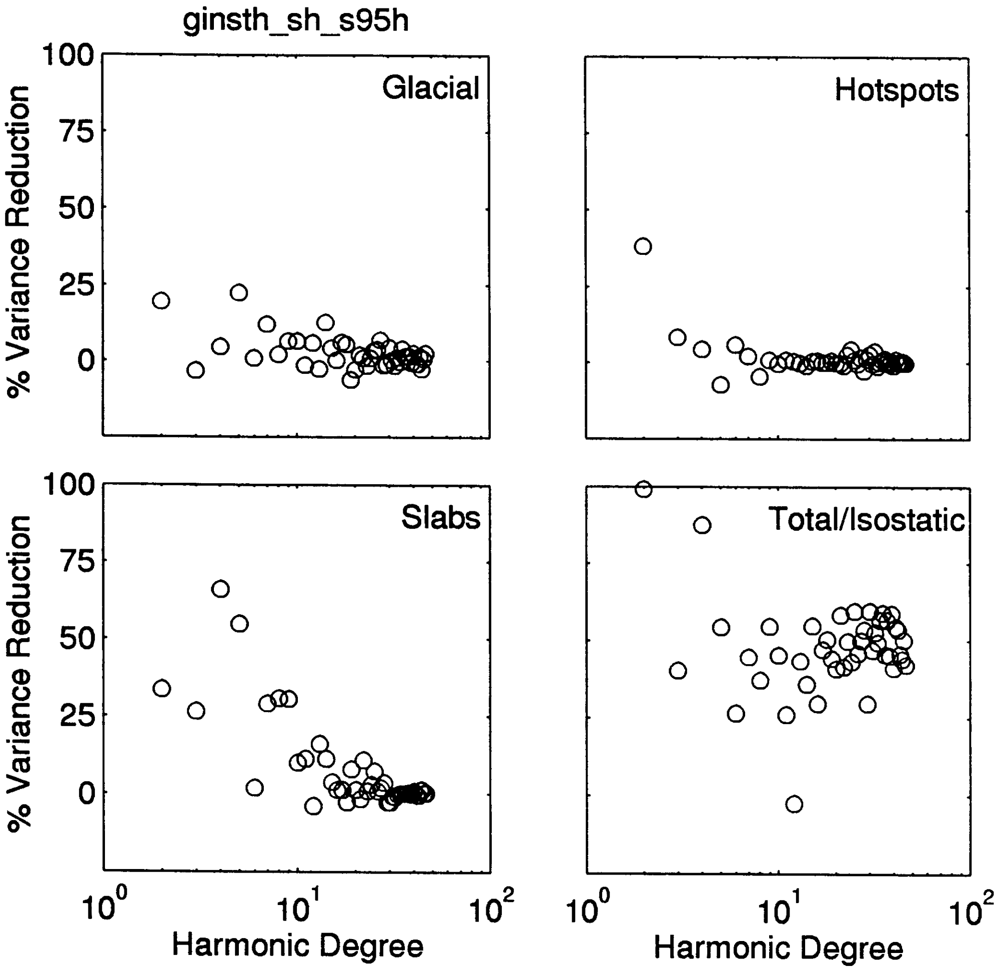

Figure 4.49: Same as figure 4.39 but using the hotspot compilation S95.

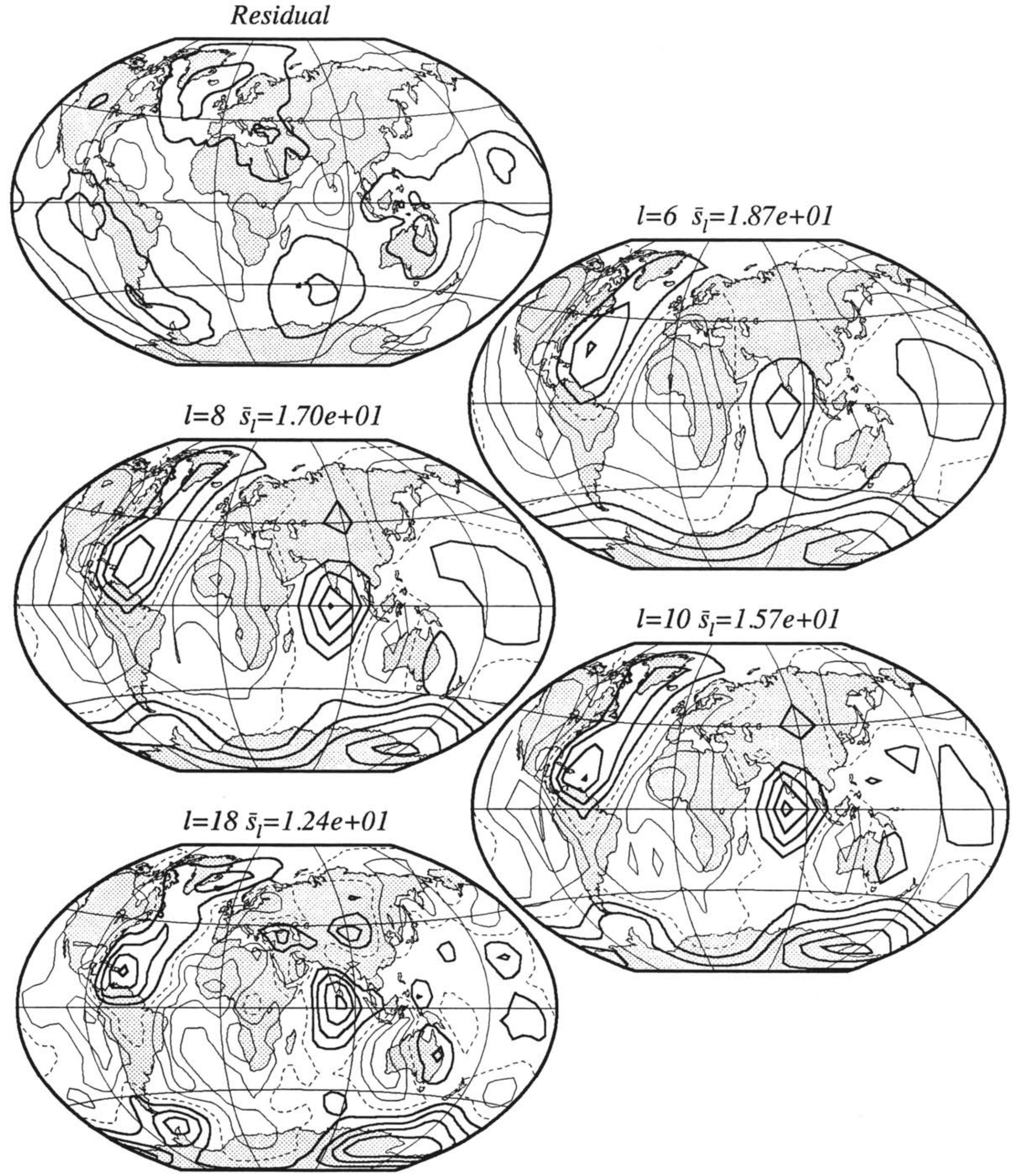

Residual

$l=6$ $\bar{s}_l=1.87e+01$

$l=8$ $\bar{s}_l=1.70e+01$

$l=10$ $\bar{s}_l=1.57e+01$

$l=18$ $\bar{s}_l=1.24e+01$

Figure 4.50: ΔS_l of Top left: The residual geoid from the model using S95, 20 m contour interval staggered about zero by half an interval. Remaining frames: ΔS_l of the residual geoid using $f_s = 1$, 3 m contour interval.

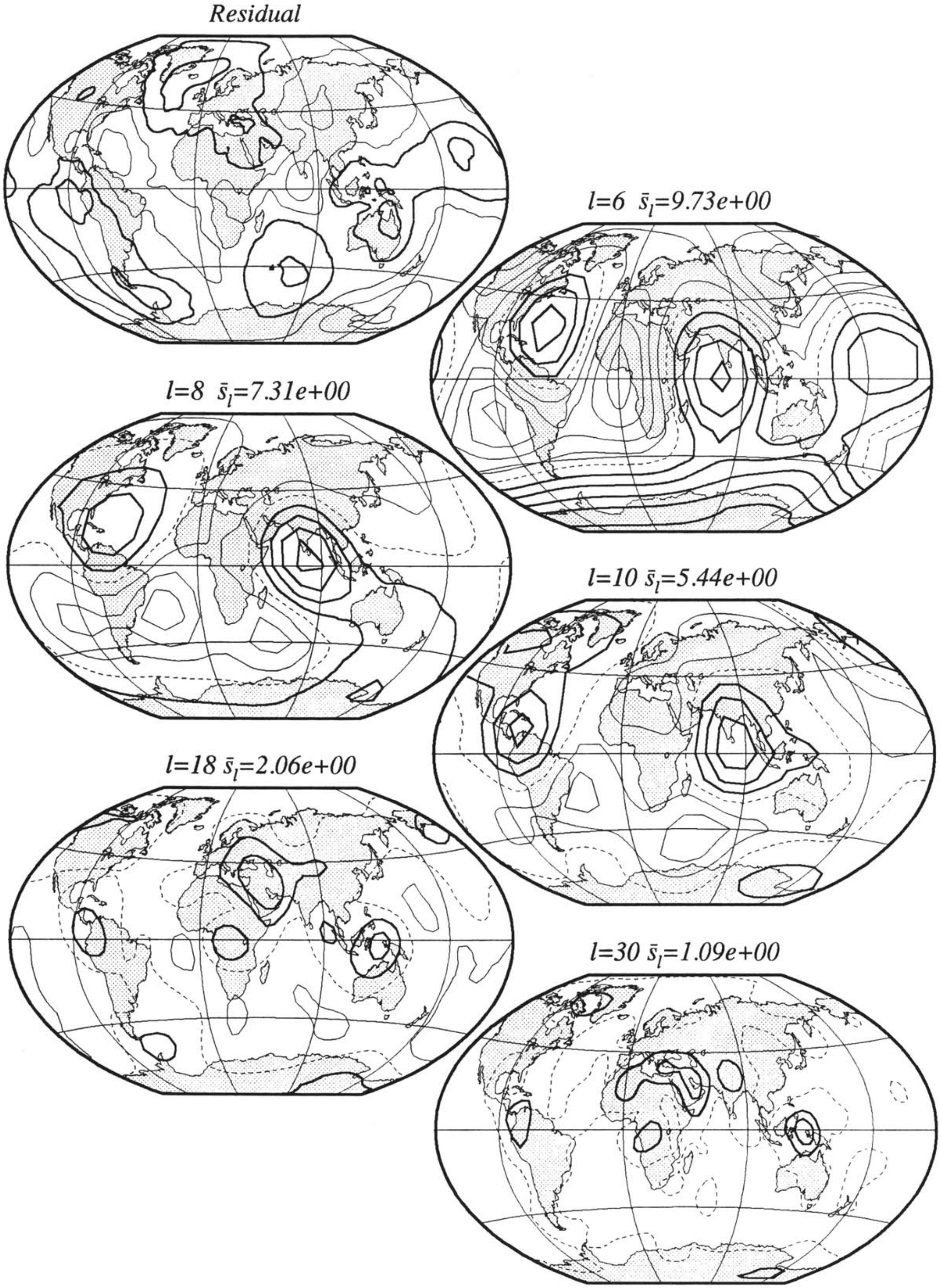

Figure 4.51: ΔS_l of Top left: The residual geoid from the model using S95, 20 m contour interval staggered about zero by half an interval. Remaining frames: ΔS_l of the residual geoid using $f_s = 2$, 1 m contour interval.

from each of the three contributing sources.

A more appropriate measure of the success of our final geoid is made through localization. The maps of ΔS_l of the residual geoid using f_s equal to 1 and 2 should be compared with the original localizaton of the geoid shown in figures 4.6 and 4.7, while remembering to take into account the change in $\overline{S_l}$. There is a large ΔS_l anomaly at long wavelengths over the central Pacific for the S88 and S95 model which is not present in the S90 model, probably a reflection of the increased weighting of the Hawaiian hotspot in the S90 compilation. There is also a large ΔS_l anomaly in all the models corresponding to a geoid low in the residual centered over the Carribean. This anomaly is possibly due to our slab function inadequately representing the subduction process or the hotspot distribution function in this region. All the models have a high ΔS_l anomaly over western Antarctica. The possible sources for the Antarctic anomaly are numerous, many of which are due to the effects of poor data coverage in the parts of our modelling which rely on accurate ice thickness estimates in Antarctica. In particular, this errors could affect both the ERT360 topography model and the ICE-3G deglaciation history.

At $l = 6$ and 10, we find a prominent residual over most of the Indian Ocean. Previously, we discussed the issue of the Sri Lankan geoid low. It is still apparent in the residual geoid, although the relative amplitude has been reduced by over 50 percent. The existence of this residual anomaly may stem from an underestimation of the crustal thickness in Tibet and the neglect of support of topography by the finite strength of the lithosphere (i.e., elasticity), which has been shown be to significant in this region [e.g., *Molnar*, 1988]. Furthermore, there remains a geoid high in the southern Indian Ocean which is associated with multiple hotspots. This anomaly could be accounted for with a more sophisticated hotspot distribution function. We hypothesize that reduction of these two geoid anomalies would further reduce the amplitude of the relative geoid low south of India.

We compare our predictions of the glacial geoid (here using the result from the

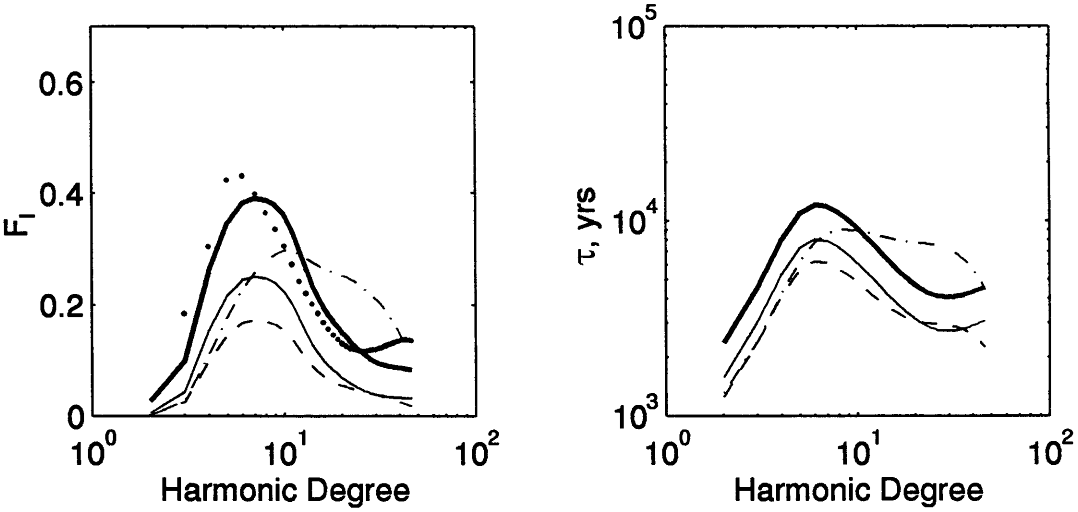

Figure 4.52: Left: $\tilde{F}_l^M$ for the viscosity models MP (dash dot line), LJN (dashed line), HS1 (thin solid line), and HS2 (thick solid line), as well as $\tilde{F}_l^G$ from localization (dots). Right: Relaxation times from MP, LJN, HS1, and HS2 (not localized) [*Hager*, 1992]. Same line conventions.

individual inversion relative to N^{ell}) with that predicted from published rheological models. Following the approach of *Hager* [1991], we calculate the relaxation spectrum (figure 4.52) for a series of models using a propagator matrix technique. Each relaxation spectrum is convolved with the ICE-3G deglaciation history to generate a predicted geoid, N^{mod}. The globally averaged local transfer function between N^{inst} and N^{mod}, $\tilde{F}_l^M$ is then compared with the $\tilde{F}_l^G$. Two of the viscosity models we use were derived from glacial rebound data whereas the third is based on the previously discussed viscosity model from *Hager and Clayton* [1989], which was derived from convection modelling. The first two models have two layers corresponding to the upper and lower mantle, with viscosities, η_{um} and η_{lm}, respectively. In addition, each model has a surface elastic layer of thickness, h. The first model, MP, is from *Mitrovica and Peltier* [1989] and was designed to fit the observed geoid anomaly over Hudson Bay. This model has $\eta_{um} = 10^{21}$ Pa s, $\eta_{lm} = 4.1 \times 10^{21}$ Pa s, and $h = 120$ km. The second model, LJN, is from *Lambeck et al.* [1990] and was designed to fit observations of sea level rise in

Europe. This model has $\eta_{um} = 3.5 \times 10^{20}$ Pa s, $\eta_{lm} = 4.7 \times 10^{21}$ Pa s, and $h = 100$ km. The third model, HS1, has the same relative variations as the model shown in figure 4.3. However, since this model was derived from models of subduction processes in oceanic environments, we increase the viscosity in the asthenosphere by an order of magnitude on the basis of our prejudice that continental upper mantle has a higher average viscosity than the corresponding oceanic upper mantle [e.g., *Shapiro*, 1995]. Dynamic flow models are sensitive only to relative viscosity variations and not absolute viscosity. The absolute viscosity can be estimated by calculating the advected heat flux derived by the predicted mantle flow, which is calculated using the density field inferred from a seismic tomography model [e.g., *Hager and Clayton*, 1989]. Using this calibration, *Hager* [1991] found that an abolute viscosity for the lower mantle of $\eta_{lm} = 6 \times 10^{21}$ Pa s. We note however that this approach is sensitive to the damping and spectral truncation intrinsic to the global seismic tomography models [*Hager*, 1991].

$\tilde{F}_l^M$ for all three viscosity models is substantially less than $\tilde{F}_l^G$ (figure 4.52). Model MP has a peak value occurring at higher degrees than either our prediction or the other forward models. MP also has a different characteristic spectral decay at high l. We speculate that the shift in the peak value results from the previously mentioned reliance on spectral windowing (passing $l = 10$ through 22), followed by spatial analysis. The relatively high values of $\tilde{F}_l^M$ from model MP at high degree is probably the result of trying to match the peak spatial anomaly with power at high degrees. The simplest way to reconcile the other estimates of $\tilde{F}_l^M$ with $\tilde{F}_l^G$ is to increase the absolute viscosity, having the effect of increasing the relaxation time. We have generated a new model, HS2, by increasing the viscosity used in HS1 by 50 percent. This model does reasonably well at matching $\tilde{F}_l^G$ (figure 4.52).

Unfortunately, while model HS2 can fit the geoid data near $l = 8$, it would not be able to fit the sea level data used in constructing LJN. Given that our localization estimate is controlled by the $l \approx 8$ anomaly over Hudson Bay, which lies in the middle of a continental shield, whereas LJN is derived using sea level data on the continental margin, we interpret the differences between the two models as evidence for lateral variations in upper mantle viscosity. Alternatively, because the change in ice load over Fennoscandia has a characteristic length scale about half that over Hudson Bay, the sea level data used in model LJN may not provide a constraint on the long wavelength relaxation times. Therefore, while not attempted here, it may be possible to determine a singe radial viscosity model that fits both the gravity data over Hudson Bay and the European sea level data.

4.5 Summary and Conclusions

Using a non-parameteric approach, we have provided a localized description of Earth's global gravity field, and in the process made the distinction between characteristic wavelengths and characteristic length scales. The first conclusion from this analysis is that variations in crustal thickness can have significant effects on the geoid up to wavelengths of about 4000 km in limited geographic regions, such as Tibet and the Andes. This result suggests that the use of geoid data in modelling dynamic processes related to mantle convection in these regions [e.g., *Russo and Silver*, 1994; *Phipps Morgan et al.*, 1995] should begin by correcting for these static compensation effects.

Besides static compensation mechanisms, we find large local variance at long wavelength associated with subduction zones and regions subject to post-glacial rebound. Surprisingly, the non-parametric approach finds no significant geoid variation at long wavelengths associated with regions of proposed mantle upwelling. In particular, we found no evidence for a strongly negative geoid anomaly over the South Pacific Superswell. In fact, this area is remarkable for appearing as a minimum in the estimates of ΔS_l of the geoid. Similarly, the global $l = 6$ correlation between hotspots and the geoid does not express itself in the localized variance estimates.

The signal associated with hotspots is further constrained by the parametric inversions which attempt to determine a global hotspot-related geoid based on local correlations of the hotspot distribution function and the observed geoid. Depending on the hotspot compilation used, the predicted geoid from this analysis can reduce the global variance significantly at $l = 2$, in agreement with previous correlations of hotspots with the geoid at this degree [e.g., *Richards and Hager*, 1988; *Cazenave et al.*, 1989]. However, our localization hotspot geoids do not significantly reduce the variance at $l = 6$. Furthermore, the residual geoid after removal of our final predicted geoid shows a strong positive anomaly over the central Pacific Ocean, possibly related to the Hawaiian swell. This region also appears as a high in the map of ΔS_l of the residual at $l = 6$. As mentioned earlier, the strong localized geoid anomalies in South America and Hudson Bay are separated by distances roughly corresponding to $l = 6$. As there are a large number of hotspots occurring in the regions between these two areas, we hypothesize that the global $l = 6$ correlation between the hotspots and the observed geoid is controlled by this coincidental distribution of the North Atlantic hotspots and by the large geoid anomaly in the central Pacific.

In addition to the hotspot geoid, we estimated the geoid related to subduction processes. At long wavelengths, the predicted geoid from this analysis agrees surprisingly well with predictions from dynamic flow modelling. However, we have assumed a very simple structure for our slab distribution function. Future analysis could use new high resolution tomographic results [e.g., *Fukao et al.*, 1992; *van der Hilst and Seno*, 1993; *van der Hilst*, 1995] or a more sophisticated geodynamic reconstruction [e.g., *Lithgow-Bertelloni et al.*, 1993]. We must emphasize, however, that localization is not a physical model and therefore does not provide the same kind of information as flow modelling. In particular, it does not directly supply any information regarding viscosity structure. With respect to flow modelling, the results in this chapter suggest that additional insights could be derived by the integration of the two techniques. Specifically, the success of a given flow model should be made in the localized domain. For simple density models that are effectively independent of depth, such as our slab function, the flow modelling should be made relative to that portion of the geoid which is locally correlated with the density function, as opposed to the complete geoid. Finally, localization should provide a tool in the developement of regional dynamic models that attempt to determine constraints on local structure, as opposed to global averages. Of course, such regional models are subject to the inherent limitations on spectral resolution that we have expressed in terms of the local Nyquist condition.

Chapter 5

The Sister Planets

In the preceeding chapters we have attempted to construct a bridge between the purely spatial and purely spectral approaches to analyzing harmonic renditions of globally defined data. This bridge comes in the form of a spatio-spectral localization operator which can be viewed either as the harmonic decomposition of spatially windowed data, or as the projection of the data onto a set of localized basis functions. The formalism behind this operator provides quantitative limits on our ability to simultaneously determine variations in the spatial and spectral domains — limits which are particularly important to determine when manipulating data with finite global spectral resolution.

We have used our localization approach to study the different modes of topographic compensation at length scales greater than 800 km on both Earth and Venus, as well as to determine constraints from the gravity field on the extent to which convective processes within both planets manifest themselves at the surface. Due to lack of prior knowledge regarding the behavior of the gravity field of either planet in the localized domain, we began with a non-parametric approach, providing a guide to the spatial regions that are associated with significant variations in the gravity field at different wavelengths.

For Venus we found that geoid and topography are not only positively correlated at all wavelengths when viewed globally, but also when viewed locally. Combined with geologic evidence, we are able to use the local correlations between the two fields to separate the topography into two classes. Tesserae and crustal plateaus, representing about 10 percent of the surface area, are consistent with a model in which topography is supported by crustal thickness variations. In contrast, the geoid over the remaining 90 percent of the surface is consistent with a model in which most of the topography stems from convectively-induced normal tractions at the base of the lithosphere. Thus, the geoid effectively provides a crude map of the vertical motions in the upper mantle of Venus.

In contrast to Venus, the structure of the geoid on Earth is much more complex — most of the topography is supported by variations in crustal density and thickness, and the long wavelength geoid is globally dominated by convective processes, with geoid highs associated with both upwellings and downwellings [e.g. *Richards and Hager*, 1988]. Based on dynamic flow modelling with seismically inferred or *a priori* density models, we can match the observed geoid and constrain the radial viscosity structure of the Earth, an experiment that is not possible to conduct for Venus.

We are faced with the paradox that the relationship between the geoid and the planform of convection appears to be simpler on Venus than on Earth. Yet we are able to say more about interior structure of Earth given our crude understanding of the density anomalies in the Earth's interior. The primary difference between the two planets appears to be the present lack of plate tectonics on Venus [e.g., *Solomon et al.*, 1992]. Based on the observed constancy of sign of the geoid/topography admittances on Venus, we conclude that the tesserae and crustal plateaus are the surface manifestation of processes no longer occuring on the planet. In other words, a period of higher surface mobility once existed on Venus, either in some form of plate tectonic or by a completely different and undetermined process.

It is currently of great interest to hypothesize reasons for the time variation of the surface manifestation of mantle convection on Venus. Included in these hypotheses should be an attempt to understand the difference between present day Venus and the Earth. One such hypothesis is that the presence of water may control the surface expression of convection. Since water is a prime factor in weakening lithospheric scale faults on Earth [e.g., *Hickman*, 1991], the presently anhydrous lithosphere on Venus [e.g., *Grinspoon*, 1993] may prevent the formation of weak plate-boundary faults[*McKenzie*, 1977a], thereby inhibiting the development of Earth-like plate tectonics. The need for weak plate margins is illustrated by numerical models of mantle convection that attempt to mimic plate behavior (i.e., large scale harizontal movement with strain concentrated in narrow regions). Each of these models require either highly non-linear rheologies or *a priori* zones of weakness in the lithosphere [e.g *King et al.*, 1992; *Kiefer*, 1993; *Zhong and Gurnis*, 1995]. One possibility (which is not pursued here), suggests that the observed dramatic changes in tectonic style on Venus may imply a coupling between atmospheric evolution and the surface manifestation of mantle convecton, whereby moister lithosphere on Venus in the past would have low creep strength [e.g., *Mackwell et al.*, 1995] and may have promoted more mobile horizontal tectonics with diffuse boundaries between adjacent tectonic domains.

Appendix A

Computation of Localized Covariances

We begin with equation 2.54,

$$
\begin{aligned}
\sigma^2_{l'm'}(l) \; = \; & (2l+1) \sum_{ml_{1\ldots4}m_{1\ldots4}} (-)^{m_4} a^*_{l_1m_1} b_{l_3m_3} w^{\odot}_{l_20}(l) w^{\odot}_{l_40}(l) \xi_{l_1l_2l_3l_4l'} \\
& \begin{pmatrix} l_1 & l_2 & l \\ 0 & 0 & 0 \end{pmatrix} \begin{pmatrix} l_3 & l_4 & l \\ 0 & 0 & 0 \end{pmatrix} \begin{pmatrix} l_2 & l_4 & l' \\ 0 & 0 & 0 \end{pmatrix} \\
& \begin{pmatrix} l_1 & l_2 & l \\ m_1 & m_2 & m \end{pmatrix} \begin{pmatrix} l_3 & l_4 & l \\ m_3 & m_4 & m \end{pmatrix} \begin{pmatrix} l_2 & l_4 & l' \\ -m_2 & m_4 & m' \end{pmatrix} .
\end{aligned}
\tag{A.1}
$$

From identity 2.18, we have

$$m_1 = -m_2 - m \tag{A.2}$$

$$m_3 = m' - m_2 - m \tag{A.3}$$

$$m_4 = m_2 - m'. \tag{A.4}$$

with which we rewrite and rearrange equation A.1 as

$$\sigma^2_{l'm'}(l) \; = \; (2l+1) \sum_{l_1l_2} w^{\odot}_{l_20}(l) \begin{pmatrix} l_1 & l_2 & l \\ 0 & 0 & 0 \end{pmatrix} \sum_{l_3l_4} w^{\odot}_{l_40}(l) \begin{pmatrix} l_3 & l_4 & l \\ 0 & 0 & 0 \end{pmatrix}$$

$$\begin{aligned}&\forall_{l'} \begin{pmatrix} l_2 & l_4 & l' \\ 0 & 0 & 0 \end{pmatrix} \xi_{l_1 l_2 l_3 l_4 l'} \sum_{m m_2} \frac{(-)^{m_4}}{(1+\delta_{m0})} \begin{pmatrix} l_1 & l_2 & l \\ m_1 & m_2 & m \end{pmatrix} \\ &\forall_{m'} \, a^*_{l_1 m_1} b_{l_3 m_3} \begin{pmatrix} l_3 & l_4 & l \\ m_3 & m_4 & m \end{pmatrix} \begin{pmatrix} l_2 & l_4 & l' \\ -m_2 & m_4 & m' \end{pmatrix}, \end{aligned} \tag{A.5}$$

where $\forall_i$ indicates looping over all i. This rearrangement facilitates elimination of summations which are multiplied by a zero-valued 3-j coefficient. In addition, it isolates summations that depend on l' and m', and thus reduces repetitive calculations. Using identities 2.16 and 2.17, we restrict the limits on summations and loops to

$$l_1 = l - L_{win} \ldots \min(l + L_{win}, L_{obs}) \tag{A.6}$$

$$l_2 = |l - l_1| \ldots \min(l + l_1, L_{win}) \tag{A.7}$$

$$l_3 = l - L_{win} \ldots \min(l + L_{win}, L_{obs}) \tag{A.8}$$

$$l_4 = |l - l_3| \ldots \min(l + l_3, L_{win}) \tag{A.9}$$

$$l' = |l_2 - l_4| \ldots (l_2 + l_4) \tag{A.10}$$

$$m = 0 \ldots l \tag{A.11}$$

$$m_2 = \max(-l_2, -l_1 - m) \ldots \min(l_2, l_1 - m) \tag{A.12}$$

$$m' = \max(0, -l', m + m_2 - l_3, m_2 - l_4) \ldots \min(l', m + m_2 + l_3, l_4 + m_2). \tag{A.13}$$

where L_{obs} is the maximium degree available for the data, and $L_{win} < l$, as discussed before. From identity 2.20, we have the restriction that

$$l_2 + l_1 + l \Rightarrow \text{even} \tag{A.14}$$

$$l_4 + l_3 + l \Rightarrow \text{even} \tag{A.15}$$

$$l' + l_4 + l_2 \Rightarrow \text{even}, \tag{A.16}$$

which imply that the l_2, l_4, and l' loops can be incremented in steps of 2 with appropriate selection of their initial values.

Appendix B

Cylindrical Dynamic Response Kernels

The dynamic response kernels for flow of an incompressible fluid with self-gravitation and radial variations in viscosity has been derived by *Richards and Hager* [1984] and *Hager and Clayton* [1989] for Cartesian and spherical geometries. Here, we derive the the same response kernels for a cylindrical (r, θ) geometry.

We begin by expressing the flow variables in terms of their harmonic decomposition

$$\begin{aligned} v_r(r,\theta) &= \sum_l v_r^l(r)e^{il\theta} & v_\theta(r,\theta) &= \sum_l v_\theta^l(r)ie^{il\theta} & P(r,\theta) &= \sum_l P^l(r)e^{il\theta} \\ \tau_{rr}(r,\theta) &= \sum_l \tau_{rr}^l(r)e^{il\theta} & \tau_{r\theta}(r,\theta) &= \sum_l \tau_{r\theta}^l(r)ie^{il\theta} & \tau_{\theta\theta}(r,\theta) &= \sum_l \tau_{\theta\theta}^l(r)e^{il\theta} \\ \delta U(r,\theta) &= \sum_l \delta U^l(r)e^{il\theta} & \delta g(r,\theta) &= \sum_l \delta g^l(r)e^{il\theta} & \delta\rho(r,\theta) &= \sum_l \delta\rho^l(r)e^{il\theta}, \end{aligned} \tag{B.1}$$

where v is the velocity, P is the pressure, τ is the stress, δU is the anomalous gravitational potential, δg is the radial component of the anomalous gravity field, and $\delta\rho$ is the anomalous density field. From here on, the radial and $l-$dependencies are taken as implicit. The equations of motion and continuity, as well as the constitutive and Poisson's equations, are solved simultaneously by a propagator technique [*Cathles*, 1975; *Hager* *and O'Connell,* 1981].

The equation of continuity is written as

$$
\begin{aligned}
0 &= \nabla \cdot \mathbf{v} && \text{(B.2)} \\
&= \frac{1}{r}\frac{\partial}{\partial r}(r v_r) + \frac{1}{r}\frac{\partial}{\partial \theta}(v_\theta) && \text{(B.3)} \\
&= \frac{1}{r} v_r + D v_r + \frac{-l}{r} v_\theta && \text{(B.4)} \\
\Longrightarrow D v_r &= \frac{l}{r} v_\theta + \frac{-1}{r} v_r \ \otimes && \text{(B.5)}
\end{aligned}
$$

where $D = \partial / \partial r$, and $\otimes$ indicates the form used in the final system of equations.

The constitutive equation can be written as

$$\tau_{ij} = -P\delta_{ij} + 2\eta\varepsilon_{ij}. \qquad \text{(B.6)}$$

Noting that

$$
\begin{aligned}
\varepsilon_{rr} &= D v_r && \text{(B.7)} \\
\varepsilon_{\theta\theta} &= -D v_r && \text{(B.8)} \\
\varepsilon_{r\theta} &= \frac{l}{2r} v_r + \frac{1}{2} D v_\theta + \frac{-1}{2r} v_\theta , && \text{(B.9)}
\end{aligned}
$$

we can rewrite equation B.6 as

$$
\begin{aligned}
\tau_{rr} &= -P + 2\eta D v_r && \text{(B.10)} \\
\tau_{\theta\theta} &= -P - 2\eta D v_r && \text{(B.11)} \\
\Longrightarrow \tau_{rr} - \tau_{\theta\theta} &= 4\eta D v_r && \text{(B.12)} \\
&= \frac{4\eta l}{r} v_\theta + \frac{-4\eta}{r} v_r && \text{(B.13)} \\
\tau_{r\theta} &= \frac{\eta l}{r} v_r + \eta D v_\theta + \frac{-\eta}{r} v_\theta && \text{(B.14)} \\
\Longrightarrow D v_\theta &= \frac{-l}{r} v_r + \frac{1}{r} v_\theta \frac{1}{\eta} \tau_{r\theta} . \ \otimes && \text{(B.15)}
\end{aligned}
$$

Since $U = U_0 + \delta U$ and $g = g_0 + \delta g$, we write the relationship between the gravity field and the gravitational potential as

$$D\delta U = \delta g. \ \otimes \tag{B.16}$$

We write Poisson's equation as

$$\begin{aligned}
-4\pi\gamma\delta\rho &= \nabla^2\delta U \qquad &(\text{B.17})\\
&= \frac{\partial^2\delta U}{\partial r^2} + \frac{1}{r}\frac{\partial\delta U}{\partial r} + \frac{1}{r^2}\frac{\partial^2\delta U}{\partial\theta^2} \qquad &(\text{B.18})\\
&= D\delta g + \frac{1}{r}\delta g + \frac{-l^2}{r^2}\delta U \qquad &(\text{B.19})\\
\Longrightarrow D\delta g &= \frac{l^2}{r^2}\delta U + \frac{-1}{r}\delta g + (\Upsilon\delta\rho). \ \otimes \qquad &(\text{B.20})
\end{aligned}$$

where $\Upsilon = -4\pi\gamma$. Neglecting inertial terms, the equation of motion can be written as

$$\nabla\cdot\tau + \delta\rho\mathbf{g} + \rho\nabla U = 0 \tag{B.21}$$

which we rewrite as

$$\begin{aligned}
0 &= \frac{\partial\tau_{rr}}{\partial r} + \frac{1}{r}\frac{\partial\tau_{r\theta}}{\partial\theta} + \frac{1}{r}(\tau_{rr} - \tau_{\theta\theta}) + \rho\frac{\partial\delta U}{\partial r} - \delta\rho g \qquad &(\text{B.22})\\
&= D\tau_{rr} + \frac{-l}{r}\tau_{r\theta} + \frac{-4\eta}{r^2}v_r + \frac{4\eta l}{r^2}v_\theta + \rho\delta g - \delta\rho g \qquad &(\text{B.23})\\
\Longrightarrow D\tau_{rr} &= \frac{l}{r}\tau_{r\theta} + \frac{4\eta}{r^2}v_r + \frac{-4\eta l}{r^2}v_\theta - \rho\delta g + \delta\rho g \ \otimes \qquad &(\text{B.24})
\end{aligned}$$

and

$$\begin{aligned}
0 &= \frac{\partial\tau_{r\theta}}{\partial r} + \frac{1}{r}\frac{\partial\tau_{\theta\theta}}{\partial\theta} + \frac{1}{r}(\tau_{r\theta} - \tau_{r\theta}) + \frac{\rho}{r}\frac{\partial\delta U}{\partial\theta} \qquad &(\text{B.25})\\
&= D\tau_{r\theta} + \frac{l}{r}\tau_{\theta\theta} + \frac{2}{r}\tau_{r\theta} + \frac{l\rho}{r}\delta U \qquad &(\text{B.26})\\
\Longrightarrow D\tau_{r\theta} &= \frac{-4\eta l}{r^2}v_r + \frac{4\eta l^2}{r^2}v_\theta + \frac{-l}{r}\tau_{rr} + \frac{-2}{r}\tau_{r\theta} + \frac{-l\rho}{r}\delta U, \ \otimes \qquad &(\text{B.27})
\end{aligned}$$

where we have assumed constant viscosity within a given cylindrical shell. From the equations marked with $\otimes$, we construct the following system

$$D\begin{bmatrix} v_r \\ v_\theta \\ \tau_{rr} \\ \tau_{r\theta} \\ \delta U \\ \delta g \end{bmatrix} = \begin{bmatrix} \frac{-1}{r} & \frac{l}{r} & 0 & 0 & 0 & 0 \\ \frac{-l}{r} & \frac{1}{r} & 0 & \frac{1}{\eta} & 0 & 0 \\ \frac{4\eta}{r^2} & \frac{-4\eta l}{r^2} & 0 & \frac{l}{r} & 0 & -\rho \\ \frac{-4\eta l}{r^2} & \frac{4\eta l^2}{r^2} & \frac{-l}{r} & \frac{-2}{r} & \frac{-\rho l}{r} & 0 \\ 0 & 0 & 0 & 0 & 0 & 1 \\ 0 & 0 & 0 & 0 & \frac{l^2}{r^2} & \frac{-1}{r} \end{bmatrix} \begin{bmatrix} v_r \\ v_\theta \\ \tau_{rr} \\ \tau_{r\theta} \\ \delta U \\ \delta g \end{bmatrix} + \begin{bmatrix} 0 \\ 0 \\ \delta\rho g \\ 0 \\ 0 \\ \Upsilon\delta\rho \end{bmatrix} \tag{B.28}$$

We can simplify equation B.28 with the following change of variables

$$\begin{array}{ll} \eta^* = \dfrac{\eta}{\eta_0} & \rho^* = \dfrac{\rho}{\rho_0} \\ \nu = \ln\dfrac{r}{a} & \hat{D} = \dfrac{\partial}{\partial\nu} \\ y_1 = l\eta_o v_r & Dv_r = \dfrac{\hat{D}y_1}{l\eta_0 r} \\ y_2 = l\eta_o v_\theta & Dv_\theta = \dfrac{\hat{D}y_2}{l\eta_0 r} \\ y_3 = r\tau_{rr} + r\rho\delta U & D\tau_{rr} = \dfrac{\hat{D}y_3 - y_3 - \rho^* z_2}{r^2} \\ y_4 = r\tau_{r\theta} & D\tau_{r\theta} = \dfrac{\hat{D}y_4 - y_4}{r^2} \\ z_1 = lr\rho_0\delta U & D\delta U = \dfrac{\hat{D}z_1 - z_1}{lr^2\rho_0} \\ z_2 = r^2\rho_0\delta g & D\delta g = \dfrac{\hat{D}z_2 - z_2}{r^3\rho_0} \end{array} \tag{B.29}$$

where a is the outer radius of the cylindrical domain, η_0 is a reference viscosity, and ρ_0 is a reference density. These variable substitutions permit a partial decoupling of the velocity and stress equations from those related to the potential, leading to the partially decoupled set of equations

$$\begin{aligned} \hat{D}\mathbf{y} &= \mathbf{A}y + \mathbf{S}_A \qquad (B.30) \\ \hat{D}\mathbf{z} &= \mathbf{B}z + \mathbf{S}_B \qquad (B.31) \end{aligned}$$

where

$$\mathbf{A} = \begin{bmatrix} -1 & l & 0 & 0 \\ -l & 1 & 0 & \dfrac{l}{\eta^*} \\ \dfrac{\eta^*}{l} & -4\eta^* & 1 & l \\ -4\eta^* & 4\eta^* l & -l & -1 \end{bmatrix}, \ \mathbf{S}_A = \begin{bmatrix} 0 \\ 0 \\ \delta\rho g r^2 \\ 0 \end{bmatrix}, \qquad (B.32)$$

and

$$\mathbf{B} = \begin{bmatrix} 1 & l \\ l & 1 \end{bmatrix}, \ \mathbf{S}_B = \begin{bmatrix} 0 \\ \Upsilon \rho_0 \delta\rho r^3 \end{bmatrix}. \qquad (B.33)$$

The matrices **A** and **B** have eigenvalues $\lambda^A = (\pm 1 \pm l)$ and $\lambda^B = (1 \pm l)$, respectively.

We discretize the radial distribution of density into a series of J infinitessimally thin density sheets with thickness $2\varepsilon_j$. We write the density of each sheet, σ_j, as

$$\sigma_j = \int_{r_j-\varepsilon_j}^{r_j+\varepsilon_j} \delta\rho(r)\, dr \qquad (B.34)$$

with which we write the general solution to equations B.30 and B.31 as

$$\begin{aligned} y(\nu) &= P_A(\nu,\nu_0)\mathbf{y}(\nu_0) + \sum_{j=1}^{J} P_A(\nu,\nu_j)\mathbf{S}_A^j \qquad (B.35) \\ z(\nu) &= P_B(\nu,\nu_0)\mathbf{z}(\nu_0) + \sum_{j=1}^{J} P_B(\nu,\nu_j)\mathbf{S}_B^j \qquad (B.36) \end{aligned}$$

The solution is propagated from ν_0 to ν with the propagator $\mathbf{P}_x(\nu,\nu_0)$, which can be written as

$$
\begin{aligned}
\mathbf{P}_x(\nu,\nu_0) &= e^{(\nu-\nu_0)\mathbf{X}} && \text{(B.37)}\\
&= \left(\frac{r}{r_0}\right)^{\mathbf{X}} && \text{(B.38)}\\
&= \sum_{i=1}^{n} e^{\lambda_i(\nu-\nu_0)} \prod_{s\neq i} \frac{\lambda_s I - \mathbf{X}}{\lambda_s - \lambda_i}. && \text{(B.39)}
\end{aligned}
$$

Starting and ending vectors are derived from the boundary conditions, which recouple the system of equations. The boundary conditions are defined at surfaces of constant radius and are approximated by first order Taylor series expansions about the deformed boundaries. To first order, only the radial components of the stress and gravity fields need to be considered. At an interface, $r = b$, we have

$$
\begin{aligned}
\tau_{rr}(r)|_{b^-}^{b^+} &= \tau_{rr}(r)|_{b+\delta b^-}^{b+\delta b^+} - D\tau_{rr}(r)\delta b|_{b+\delta b^-}^{b+\delta b^+} && \text{(B.40)}\\
&= 0 - \rho g \delta b|_{b+\delta b^-}^{b+\delta b^+} && \text{(B.41)}\\
&= \rho_b g_b \delta b && \text{(B.42)}
\end{aligned}
$$

where $\rho_b = \rho^- - \rho^+$ and $g_b = g(b)$. This gives the jump condition on $\mathbf{y}$

$$
\begin{aligned}
y_3(r)|_{b^-}^{b^+} &= (r\tau_{rr}(r) + r\rho\delta U)|_{b^-}^{b^+} && \text{(B.43)}\\
&= b\rho_b(g_b\delta b - \delta U) && \text{(B.44)}\\
\Longrightarrow \mathbf{y}(r)|_{b^-}^{b^+} &= [\ 0 \quad 0 \quad b\rho_b(g_b\delta b - \delta U) \quad 0\ ]^T. && \text{(B.45)}
\end{aligned}
$$

For a free surface boundary condition at the top surface, $r = a$, we then have

$$
\begin{aligned}
\mathbf{y}(a^-) &= \mathbf{y}(a^+) - \mathbf{y}(r)|_{a^-}^{a^+} && \text{(B.46)}\\
&= [\ 0 \quad y_2(a) \quad -a\rho_a(g_a\delta a - \delta U_a) \quad 0\ ]^T, && \text{(B.47)}
\end{aligned}
$$

and for a free slip boundary condition at the bottom surface, $r = c$, (e.g., the core-mantle boundary) $\tau_{rr}(c^-) = -\rho_c \delta U_c$, therefore $y_3(c^-) = 0$ and

$$\begin{aligned} \mathbf{y}(c^+) &= \mathbf{y}(c^-) + \mathbf{y}(r)\Big|_{c^-}^{c^+} && \text{(B.48)} \\ &= [\ 0 \quad y_2(c) \quad c\rho_c(g_c\delta c - \delta U_c) \quad 0\ ]^T. && \text{(B.49)} \end{aligned}$$

Geoid and gravity are continuous at an interface, but the radial derivative of gravity is not. Therefore, we find

$$\begin{aligned} \delta g(r)|_{b^-}^{b^+} &= (\delta g(r) - D\delta g(r))|_{b^-}^{b^+} && \text{(B.50)} \\ &= 0 - b\delta b(\Upsilon\rho)|_{b^-}^{b^+} && \text{(B.51)} \\ &= \Upsilon\rho_b\delta b, && \text{(B.52)} \end{aligned}$$

giving the jump condition on $\mathbf{z}$

$$\mathbf{z}(r)|_{b^-}^{b^+} = [\ 0 \quad b^2\rho_0\Upsilon\rho_b\delta b\ ]^T. \tag{B.53}$$

Noting that for a cylindrical mass sheet at $r = b$ the radial dependence of the gravitational potential has the form

$$U^l(r) = \begin{cases} (b/r)^l & \text{if } r \geq b \\ (b/r)^{-l} & \text{if } r \leq b \end{cases}, \tag{B.54}$$

we find $\delta g_{b^+} = D\delta U(r)|_{b^+} = (-l/b)\delta U$ and $\delta g_{b^-} = D\delta U(r)|_{b^-} = (l/b)\delta U$, giving the upper and lower surface boundary conditions

$$\begin{aligned} z_2(a^+) &= a^2\rho_0\delta g_{a^+} && \text{(B.55)} \\ &= -la\rho_0\delta U && \text{(B.56)} \end{aligned}$$

$$
\begin{aligned}
&= -z^1(a^+) && \text{(B.57)}\\
\Longrightarrow \mathbf{z}(a^-) &= \mathbf{z}(a^+) - \mathbf{z}(r)|_{a^-}^{a^+} && \text{(B.58)}\\
&= \begin{bmatrix} z_1(a^+) \\ -z_1(a^+) - a^2\rho_0\Upsilon\rho_a\delta a \end{bmatrix} && \text{(B.59)}
\end{aligned}
$$

and

$$
\begin{aligned}
z_2(c^-) &= c^2\rho_0\delta g_{c^-} && \text{(B.60)}\\
&= -lc\rho_0\delta U && \text{(B.61)}\\
&= z^1(c^-) && \text{(B.62)}\\
\Longrightarrow \mathbf{z}(c^+) &= \mathbf{z}(c^-) - \mathbf{z}(r)|_{c^-}^{c^+} && \text{(B.63)}\\
&= \begin{bmatrix} z_1(c^-) \\ -z_1(c^-) + c^2\rho_0\Upsilon\rho_c\delta c \end{bmatrix}. && \text{(B.64)}
\end{aligned}
$$

For a model with N viscosity layers and a single mass sheet at r_j, we have the following system of equations (dropping superscripts),

$$
\begin{aligned}
\mathbf{y}(c) &= P_A(c,a)\mathbf{y}(a) + P_A(c,\nu_j)\mathbf{S}_A^j && \text{(B.65)}\\
\mathbf{z}(c) &= P_B(c,a)\mathbf{y}(a) + P_B(c,\nu_j)\mathbf{S}_B^j && \text{(B.66)}
\end{aligned}
$$

where

$$
P_A(c,a) = \prod_{n=1}^{N}\left(\frac{r_{n+1}}{r_n}\right)^{A_n} \tag{B.67}
$$

and

$$
P_B(c,a) = \prod_{n=1}^{N}\left(\frac{r_{n+1}}{r_n}\right)^{B_n}. \tag{B.68}
$$

This system can be expanded to

$$\begin{bmatrix} 0 \\ l\eta_o v_\theta(c) \\ c\rho_c(g_c\delta c - \delta U_c) \\ 0 \end{bmatrix} = P_A(c,a)\begin{bmatrix} 0 \\ l\eta_o v_\theta(a) \\ a\rho_a(g_a\delta a - \delta U_a) \\ 0 \end{bmatrix} \tag{B.69}$$

$$+ \quad P_A(c,\nu_j)\begin{bmatrix} 0 \\ 0 \\ \sigma_j g_j r_j \\ 0 \end{bmatrix} \tag{B.70}$$

and

$$\begin{bmatrix} l\delta U_c c\rho_c \\ l\delta U_c c\rho_0 + c^2\rho_o\Upsilon\rho_c\delta_c \end{bmatrix} = P_B(c,a)\begin{bmatrix} l\delta U_a a\rho_a \\ l\delta U_a a\rho_0 + a^2\rho_o\Upsilon\rho_a\delta_a \end{bmatrix} \tag{B.71}$$

$$+ \quad P_B(c,\nu_j)\begin{bmatrix} 0 \\ \Upsilon\rho_0 r_j^2\sigma_j \end{bmatrix}. \tag{B.72}$$

Which in turn can be written as

$$\begin{bmatrix} -\mathbf{P}_A^{12} & 0 & \mathbf{P}_A^{13}g_a & 0 & -\mathbf{P}_A^{13}\rho_a & 0 \\ -\mathbf{P}_A^{22} & 1 & \mathbf{P}_A^{23}g_a & 0 & -\mathbf{P}_A^{23}\rho_a & 0 \\ -\mathbf{P}_A^{32} & 0 & \mathbf{P}_A^{33}g_a & g_c & -\mathbf{P}_A^{33}\rho_a & -\rho_c \\ -\mathbf{P}_A^{42} & 0 & \mathbf{P}_A^{43}g_a & 0 & -\mathbf{P}_A^{43}\rho_a & 0 \\ 0 & 0 & \mathbf{P}_B^{12}\Upsilon a & 0 & l(\mathbf{P}_B^{12} - \mathbf{P}_B^{11}) & l \\ 0 & 0 & \mathbf{P}_B^{22}\Upsilon a & \Upsilon c & l(\mathbf{P}_B^{22} - \mathbf{P}_B^{21}) & l \end{bmatrix} \begin{bmatrix} l\eta_0 v_r(a) \\ l\eta_0 v_\theta(c) \\ a\rho_a\delta a \\ c\rho_c\delta c \\ a\delta U_a \\ c\delta U_c \end{bmatrix} = \begin{bmatrix} \mathbf{P}_{Aj}^{13}\sigma_j r_j g_j \\ \mathbf{P}_{Aj}^{23}\sigma_j r_j g_j \\ \mathbf{P}_{Aj}^{33}\sigma_j r_j g_j \\ \mathbf{P}_{Aj}^{43}\sigma_j r_j g_j \\ \mathbf{P}_{Bj}^{12}\Upsilon\sigma_j r_j^2 \\ \mathbf{P}_{Bj}^{22}\Upsilon\sigma_j r_j^2 \end{bmatrix} \tag{B.73}$$

Since we are not interested in $v_\theta(c)$ we can eliminate the 2nd row and column by inspection, giving

$$\begin{bmatrix} -\mathbf{P}_A^{12} & \mathbf{P}_A^{13} g_a & 0 & -\mathbf{P}_A^{13}\rho_a & 0 \\ -\mathbf{P}_A^{32} & \mathbf{P}_A^{33} g_a & g_c & -\mathbf{P}_A^{33}\rho_a & -\rho_c \\ -\mathbf{P}_A^{42} & \mathbf{P}_A^{43} g_a & 0 & -\mathbf{P}_A^{43}\rho_a & 0 \\ 0 & \mathbf{P}_B^{12}\Upsilon a & 0 & l(\mathbf{P}_B^{12} - \mathbf{P}_B^{11}) & l \\ 0 & \mathbf{P}_B^{22}\Upsilon a & \Upsilon c & l(\mathbf{P}_B^{22} - \mathbf{P}_B^{21}) & l \end{bmatrix} \begin{bmatrix} l\eta_0 v_r(a) \\ a\rho_a\delta a \\ c\rho_c\delta c \\ a\delta U_a \\ c\delta U_c \end{bmatrix} = \begin{bmatrix} \mathbf{P}_{Aj}^{13}\sigma_j r_j g_j \\ \mathbf{P}_{Aj}^{33}\sigma_j r_j g_j \\ \mathbf{P}_{Aj}^{43}\sigma_j r_j g_j \\ \mathbf{P}_{Bj}^{12}\Upsilon\sigma_j r_j^2 \\ \mathbf{P}_{Bj}^{22}\Upsilon\sigma_j r_j^2 \end{bmatrix} \tag{B.74}$$

which we can solve for the deformation and gravitational potential at each boundary.

References

Anderson, D. L., Plate tectonics on Venus., *Geophys. Res. Lett.*, *8*, 309–311, 1981.

Barsukov, V. L., et al., The geology and geopmorphology of the Venus surface as revealed by the radar images obtained by Veneras 15 and 16, *J. Geophys. Res.*, *91*, D378–D398, 1986.

Basaltic Volcanism Study Project, *Basaltic Volcanism on the Terrestrial Planets*, Pergamon, New York, 1981.

Basilevsky, A. T., Structure of central and eastern areas of Ishtar Terra and some problems of venusian tectonics., *Geotectonics*, *20*, 282–288, 1986.

Bindschadler, D. L., and J. W. Head, Tessera terrain, Venus: characterization and models for origin and evolution., *J. Geophys. Res.*, *96*, 5889–5907, 1991.

Bindschadler, D. L., and E. M. Parmentier, Mantle flow tectonics: The influence of a ductile lower crust and implications for the formation of topographic uplands on Venus, *J. Geophys. Res.*, *95*, 21329–21344, 1990.

Bindschadler, D. L., G. Schubert, and W. M. Kaula, Mantle flow tectonics and the origin of Ishtar Terra, Venus, *Geophys. Res. Lett.*, *17*, 1345–1348, 1990.

Bindschadler, D. L., G. Schubert, and W. M. Kaula, Coldspots and hotspots: Global tectonics and mantle dynamics of Venus, *J. Geophys. Res.*, *97*, 13495–13522, 1992a.

Bindschadler, D. L., A. deCharon, K. K. Beratan, S. E. Smrekar, and J. W. Head, Magellan observations of Alpha Regio: Implications for formation of complex ridged terrains on Venus, *J. Geophys. Res.*, *97*, 13563–13578, 1992b.

Bowin, C., The Earth's gravity field and plate tectonics, *Tectonophysics*, *187*, 69–89, 1991.

Bowin, C. O., Topography at the core-mantle boundary, *Geophys. Res. Lett.*, *13*, 1513–1516, 1986.

Burchfiel, B. C., The continental crust, *Sci. Am.*, *249*, 130–142, 1983.

Cathles, L. M., *The Viscosity of the Earth's Mantle*, Princeton University Press, Princeton, N.J., 1975.

Cazenave, A., and C. Thoraval, Mantle dynamics constrained by degree 6 surface topography, seismic tomography and geoid: Inference on the origin of the South Pacific Superswell, *Earth Planet. Sci. Lett.*, *122*, 207–219, 1994.

Cazenave, A., A. Souriau, and K. Dominh, Global coupling of Earth surface topography with hotspots, geoid and mantle heterogeneities, *Nature*, *340*, 54–47, 1989.

Cazenave, A., B. Parsons, and P. Calcagno, Geoid lineations of 1000 km wavelength over the Central Pacific, *Geophys. Res. Lett.*, *22*, 97–100, 1995.

Chase, C. G., and M. K. McNutt, The geoid: Effect of compensated topography and uncompensated oceanic trenches, *Geophys. Res. Lett.*, *9*, 29–32, 1982.

Christensen, N. I., and W. D. Mooney, Sesimic velocity structure and composition of the continental crust: A global view, *J. Geophys. Res.*, *100*, 9761–9788, 1995.

Chui, C., *An Introduction to Wavelets*, Academic Press, San Diego, 1992.

Crough, S. T., and D. M. Jurdy, Subducted lithosphere, hotspots, and the geoid, *Earth Planet. Sci. Lett.*, *48*, 15–22, 1980.

Daubechies, I., *Ten Lectures on Wavelets*, no. 61 in Regional Conference Ser. in Applied Mathematics, *Soc. Indust. Appl. Math.*, Philadelphia, Pa., 1992.

Dorman, L. M., and B. T. R. Lewis, Experimental isostasy, *J. Geophys. Res.*, *75*, 3357–3365, 1970.

Durrheim, R. J., and W. Mooney, Evolution of the Precambrian lithosphere: Seismological and geochemical constraints, *J. Geophys. Res.*, *99*, 15359–15374, 1994.

Dziewonski, A. M., Mapping the lower mantle: Determination of lateral heterogeneity in P velocity up to degree and order 6, *J. Geophys. Res.*, *89*, 5929–5952, 1984.

Edmonds, A. R., *Angular Momentum in Quantum Mechanics*, Princeton University Press, Princeton, N. J., 1957.

Ford, P. G., and G. H. Pettengill, Venus topography and kilometer-scale slopes, *J. Geophys. Res.*, *97*, 13103–13114, 1992.

Forsyth, D. W., Subsurface loading and estimates of the flexural rigidity of continental lithosphere, *J. Geophys. Res.*, *90*, 12,623–13,632, 1985.

Forte, A. M., and W. R. Peltier, Viscous flow models of global geophysical observables 1. forward problems., *J. Geophys. Res.*, *96*, 20,131–20,159, 1991.

Forte, A. M., and W. R. Peltier, The kinematics and dynamics of poloidal–toroidal coupling in mantle flow: The importance of surface plates and lateral viscosity variations, in *Adv. Geophys.*, edited by R. Dmowska and B. Saltzman, 36, pp. 1–117. Academic Press, 1994.

Forte, A. M., R. L. Woodward, and A. M. Dziewonski, Joint inversions of seismic and geodynamic data for models of three-dimensional mantle heterogeneity, *J. Geophys. Res.*, *99*, 21857–21877, 1994.

Fukao, Y., M. Obayashi, H. Inoue, and M. Nenbai, Subducting slabs stagnant in the mantle transition zone, *J. Geophys. Res.*, *97*, 4809–4822, 1992.

Gee, L. S., and T. H. Jordan, Generalized seismological data functionals, *Geophys. J. Int.*, *111*, 363–390, 1992.

Grimm, R. E., The deep structure of venusian plateau highlands, *Icarus*, *112*, 89–103, 1994a.

Grimm, R. E., Recent deformation rates on Venus, *J. Geophys. Res.*, *99*, 23163–23171, 1994b.

Grimm, R. E., and R. J. Phillips, Gravity anomalies, compensation mechanisms, and the geodynamics of western Ishtar Terra, Venus, *J. Geophys. Res.*, *96*, 8305–8324, 1991.

Grimm, R. E., and R. J. Phillips, Anatomy of a venusian hot spot: Geology, gravity, and mantle dynamics of Eistla Regio, *J. Geophys. Res.*, *97*, 16035–16054, 1992.

Grinspoon, D. H., Implications of the high D/H ratio for the source of water in Venus' atmosphere, *Nature*, *363*, 428–431, 1993.

Guest, J. E., M. H. Bulmer, J. Aubele, K. Beratan, R. Greeley, J. W. Head, G. Michaels, C. Weitz, and C. Wiles, Small volcanic edifices and volcanism in the plains of Venus, *J. Geophys. Res.*, *97*, 15949–15966, 1992.

Hager, B. H., Global isostatic geoid anomalies for plate and boundary layer models of the lithosphere, *Earth Planet. Sci. Lett.*, *63*, 97–109, 1983.

Hager, B. H., Subducted slabs and the geoid: Constraints on mantle rheology and flow, *J. Geophys. Res.*, *89*, 6003–6015, 1984.

Hager, B. H., Mantle viscosity: A comparison of models from postglacial rebound and from the geoid, plate driving forces, and advected heat flux, in *Glacial Isostasy, Sea-level and Mantle Rheology*, edited by K. L. R. Sabadini and E. Boschi, 334, *NATO ASI Ser. C*, pp. 493–513. Kluwer Academic, Dordrecht, Netherlands, 1991.

Hager, B. H., and R. W. Clayton, Constraints on the structure of mantle convection using seismic observations, flow models, and the geoid, in *Mantle Convection*, edited by W. R. Peltier, pp. 657–763. Gordon and Breach, New York, 1989.

Hager, B. H., and R. J. O'Connell, A simple global model of plate dynamics and mantle convection, *J. Geophys. Res.*, *86*, 4843–4867, 1981.

Hager, B. H., and M. A. Richards, Long-wavelength variations in Earth's geoid: Physical models and dynamical implications, *Phil. Trans. R. Soc. Lond.*, *328*, 309–327, 1989.

Hager, B. H., R. W. Clayton, M. A. Richards, R. P. Comer, and A. M. Dziewonski, Lower mantle heterogeneity, dynamic topography and the geoid, *Nature*, pp. 541–545, 1985.

Haskell, N. A., The viscosity of the asthenosphere, *Amer. J. Sci.*, *33*, 22–28, 1937.

Haxby, W. F., and D. L. Turcotte, On isostatic geoid anomalies, *J. Geophys. Res.*, *83*, 5473–5478, 1978.

Head, J. W., D. R. Campbell, C. Elachi, J. E. Guest, D. P. McKenzie, R. S. Saunders, G. G. Schaber, and G. Schubert, Venus volcanism: Initial analysis from Magellan data, *Science*, *252*, 276–288, 1991.

Head, J. W., L. S. Crumpler, J. C. Aubele, J. E. Guest, and R. S. Saunders, Venus volcanism: Classification of volcanic features and structures, associations, and global distribution from Magellan data, *J. Geophys. Res.*, *97*, 13153–13198, 1992.

Herrick, R. R., B. G. Bills, and S. A. Hall, Variations in effective compensation depth across Aphrodite Terra, Venus, *Geophys. Res. Lett.*, *16*, 543–546, 1989.

Hickman, S. H., The stress in the lithosphere and the strength of active faults, *Rev. Geophys.*, *29*, 759–775, 1991.

Ivanov, B. A., and A. T. Basilevsky, Density and morphology of impact craters on tessera terrain, Venus, *Geophys. Res. Lett.*, *20*, 2579–2582, 1993.

James, T. S., The Hudson Bay free-air gravity anomaly and glacial rebound, *Geophys. Res. Lett.*, *19*, 861–864, 1992.

Janes, D. M., S. W. Squyres, D. L. Bindschadler, G. Baer, G. Schubert, V. L. Sharpton, and E. R. Stofan, Geophysical models for the formation and evolution of coronae on Venus, *J. Geophys. Res.*, *97*, 16,055–16,068, 1992.

Jarrard, R. D., Relations among subduction parameters, *Rev. Geophys.*, *24*, 217–284, 1986.

Johnson, C. L., and D. T. Sandwell, Lithospheric flexure on Venus, *Geophys. J. Int.*, *119*, 627–647, 1994.

Jordan, T. H., Composition and development of the continental tectosphere, *Nature*, *274*, 544–548, 1978.

Jordan, T. H., The deep structure of the continents, *Sci. Am.*, *240*, 92–107, 1979.

Kaula, W. M., Elastic models of the mantle corresponding to variations in the external gravity field, *J. Geophys. Res.*, *68*, 4967–4978, 1963.

Kaula, W. M., Global harmonic and statistical analysis of gravimetry, in *Geoid Anomalies: Unsurveyed Areas*, edited by H. Orlin, 9, *Geophys. Mon.*, pp. 58–67. Amer. Geophys. Un., Washington, D.C., 1966.

Kaula, W. M., Theory of statistical analysis of data distributed over a sphere, *Rev. Geophys.*, *5*, 83–107, 1967.

Kaula, W. M., *An Introduction to Planetary Physics: The Terrestrial Planets*, John Wiley, New York, 1968.

Kaula, W. M., Venus: A constrast in evolution to Earth, *Science*, *247*, 1191–1196, 1990.

Kaula, W. M., D. L. Bindschadler, R. E. Grimm, V. L. Hansen, K. M. Roberts, and S. E. Smrekar, Styles of deformation in Ishtar Terra and their implications, *J. Geophys. Res.*, *97*, 16085–16120, 1992.

Kiefer, W. S., Mantle viscosity stratification and flow geometry: Implications for surface motions on Earth and Venus, *Geophys. Res. Lett.*, *20*, 265–268, 1993.

Kiefer, W. S., and B. H. Hager, Mantle downwelling and crustal convergence: A model for Ishtar Terra, Venus, *J. Geophys. Res.*, *96*, 20967–20980, 1991a.

Kiefer, W. S., and B. H. Hager, A mantle plume model for the equatorial highlands of Venus, *J. Geophys. Res.*, *96*, 20947–20966, 1991b.

Kiefer, W. S., M. A. Richards, B. H. Hager, and B. G. Bills, A dynamic model of Venus's gravity field, *Geophys. Res. Lett.*, *13*, 14–17, 1986.

King, S. D., A. Raefsky, and B. H. Hager, ConMan: Vectorizing a finite element code for incompressible two-dimensional convection in the Earth's mantle, *Phys. Earth Planet. Inter.*, *59*, 196–208, 1990.

King, S. D., C. W. Gable, and S. A. Weinstein, Models of convection-driven tectonic plates: a comparison of methods and results, *Geophys. J. Int.*, *109*, 481–487, 1992.

Konopliv, A. S., Venus spherical harmonic gravity model to degree and order 90, personal communication, 1995.

Konopliv, A. S., and W. L. Sjogren, Venus spherical harmonic gravity model to degree and order 60, *Icarus*, *112*, 42–54, 1994.

Konopliv, A. S., and W. L. Sjogren, The JPL Mars gravity field, Mars50c, based upon Viking and Mariner 9 doppler tracking data, Tech. Rep. 95-5, Jet Propulsion Lab., Pasadena, Calif., 1995.

Kraus, H., *Thin Elastic Shells: An Introduction to the Theoretical Foundations and the Analysis of Their Static and Dynamic behavior*, John Wiley, New York, 1967.

Kucinskas, A. B., and D. L. Turcotte, Isostatic compensation of equatorial highlands on Venus, *Icarus*, *112*, 104–116, 1994.

Lambeck, K., P. Johnston, and M. Nakada, Glacial rebound and sea-level change in northwestern Europe, *Geophys. J. Int.*, p. in press, 1990.

Le Stunff, Y., and Y. Ricard, Topography and geoid due to lithospheric mass anomalies, *Geophys. J. Int.*, *122*, 982–990, 1995.

Lithgow-Bertelloni, C., M. A. Richards, Y. Ricard, R. J. O'Connell, and D. E. Engebretson, Toroidal-poloidal partitioning of plate motions since 120 MA, *Geophys. Res. Lett.*, *20*, 375–378, 1993.

Mackwell, S. J., M. E. Zimmerman, D. L. Kohlstedt, and S. S. Scherber, Experimental deformation of dry Columbia diabase: Implications for tectonics on Venus, in *Proc. 35th U.S. Symp. Rock Mechanics.* 1995.

Mauk, F. J., A tectonic-based Rayleigh wave group velocity model for prediction of dispersion character through ocean basins, Ph.D. thesis, University of Michigan, Ann Arbor, 1977.

McGill, G. E., S. J. Steenstrup, C. Barton, and P. G. Ford, Continental rifting and the origin of Beta Regio, Venus, *Geophys. Res. Lett.*, *8*, 737–740, 1981.

McGovern, P. J., The structure of volcanoes on the terrestrial planets, Ph.D. thesis, Massachussetts Institute of Technology, Cambridge, Mass., 1995.

McKenzie, D. P., Some remarks on heat flow and gravity anomalies, *J. Geophys. Res.*, *72*, 6261–6273, 1967a.

McKenzie, D. P., Speculations on the consequences and causes of plate motions, *Geophys. J. Roy. Astron. Soc.*, *18*, 1–32, 1967b.

McKenzie, D. P., The initiation of trenches: A finite amplitude instability, in *Island Arcs, Deep Sea Trenches and Back Arc Basins*, edited by M. Talwani and W. C. Pitman III, pp. 57–61. Amer. Geophys. Un., Washington D.C., 1977a.

McKenzie, D. P., Surface deformation, gravity anomalies, and convection, *Geophys. J. Roy. Astron. Soc.*, *48*, 211–238, 1977b.

McKenzie, D. P., The relationship between topography and gravity on Earth and Venus, *Icarus*, *112*, 55–88, 1994.

McNutt, M., Implications of regional gravity for state of stress in the Earth's crust and upper mantle, *J. Geophys. Res.*, *85*, 6377–6396, 1980.

McNutt, M. K., Lithospheric flexure and thermal anomalies, *J. Geophys. Res.*, *89*, 11,180–11,194, 1984.

McNutt, M. K., and A. V. Judge, The superswell and mantle dynamics beneath the South Pacific, *Science*, *248*, 969–975, 1990.

McNutt, M. K., and H. W. Menard, Constraints on yield strength in the oceanic lithosphere derived from observations of flexure, *Geophys. J. Roy. Astron. Soc.*, *71*, 363–394, 1982.

Mitrovica, J. X., and W. R. Peltier, Pleistocene deglaciation and the global gravity field, *J. Geophys. Res.*, *94*, 13651–13671, 1989.

Molnar, P., A review of geophysical constraints on the deep structure of the Tibetan Plateau, the Himalaya and the Karakoram, and their tectonic implications, *Phil. Trans. R. Soc. Lond. A*, *326*, 33–88, 1988.

Molnar, P., P. England, and J. Martinod, Mantle dynamics, uplift of the Tibetan Plateau, and the Indian monsoon, *Rev. Geophys.*, *32*, 357–396, 1993.

Moore, W. B., and G. Schubert, Lithospheric thickness and mantle/lithosphere density contrast beneath Beta Regio, Venus, *Geophys. Res. Lett.*, *22*, 429–432, 1995.

Nakiboglu, S. M., Hydrostatic theory of the Earth and its mechanical implications, *Phys. Earth Planet. Inter.*, *28*, 302–311, 1982.

Nakiboglu, S. M., and K. Lambeck, Deglaciation related features of the Earth's gravity field, *Tectonophysics*, *72*, 289–303, 1981.

Namiki, N., and S. C. Solomon, Impact crater densities on volcanoes and coronae on Venus: Implications for volcanic resurfacing, *Science*, *265*, 929–933, 1994.

Nerem, R. S., et al., Gravity model development for TOPEX/Poseidon: Joint gravity models 1 and 2, *J. Geophys. Res.*, *99*, 24421–24447, 1994.

Nerem, R. S., C. Jekeli, and W. M. Kaula, Gravity field determination and characteristics: Retrospective and prospective, *J. Geophys. Res.*, *100*, 15053–15074, 1995.

Ockendon, J. R., and D. L. Turcotte, On the gravitational potential and field anomalies due to thin mass layers, *J. Geophys. Res.*, *48*, 479–492, 1977.

O'Connell, R. J., Pleistocene glaciation and the viscosity of the mantle, *Geophys. J. Roy. Astron. Soc.*, *23*, 299–327, 1971.

O'Connell, R. J., and B. H. Hager, On the thermal state of the Earth, in *Physics of the Earth's Interior*, edited by A. Dziewonski and E. Boschi, Course 78, *Enrico Fermi Intern. School Physics*, pp. 270–317. Soc. Italiana di Fisica, Bologna, 1980.

Parmentier, E. M., and P. C. Hess, Chemical differentiation of a convecting planetary interior: Consequences for a one-plate planet such as Venus, *Geophys. Res. Lett.*, *19*, 2015–2018, 1992.

Parsons, B., and F. M. Richter, A relation between the driving force and geoid anomaly associated with mid-ocean ridges, *Earth Planet. Sci. Lett.*, *51*, 445–450, 1980.

Parsons, B., and J. G. Sclater, An analysis of the variation of ocean floor bathymetry and heat flow with age, *J. Geophys. Res.*, *82*, 803–827, 1977.

Pavlis, N. K., and R. H. Rapp, The development of an isostatic gravitational model to degree 360 and its use in global gravity modelling, *Geophys. J. Int.*, *100*, 369–378, 1990.

Peltier, W. R., A. M. Forte, J. X. Mitrovica, and A. M. Dziewonski, Earth's gravitational field: Seismic tomography resolves the enigma of the Laurentian anomaly, *Geophys. Res. Lett.*, *19*, 1555–1558, 1992.

Pettengill, G. H., E. Eliason, P. G. Ford, G. B. Loriot, H. Masursky, and G. E. McGill, Pioneer Venus radar results: Altimetry and surface properties, *J. Geophys. Res.*, *85*, 8261–8270, 1980.

Phillips, R. J., Convection-driven tectonics on Venus, *J. Geophys. Res.*, *95*, 1301, 1990.

Phillips, R. J., Estimating lithospheric properties below Atla Regio, Venus, *Icarus*, *112*, 147–170, 1994.

Phillips, R. J., and K. Lambeck, Gravity fields of the terrestrial planets: Long wavelength anomalies and tectonics, *Rev. Geophys. Sp. Phys.*, *18*, 27–76, 1980.

Phillips, R. J., and M. C. Malin, The interior of Venus and tectonic implications, in *Venus*, edited by D. M. Hunten, L. Colin, V. I. Moroz and T. M. Donahue, pp. 158–214. Univ. Arizona Press, Tucson, 1983.

Phillips, R. J., R. E. Grimm, and M. C. Malin, Hot-spot evolution and the global tectonics of Venus, *Science*, *252*, 651–658, 1991a.

Phillips, R. J., R. E. Arvidson, J. M. Boyce, D. B. Campbell, J. E. Guest, G. G. Schaber, and L. A. Soderblom, Impact craters on Venus: Initial analysis from Magellan, *Science*, *252*, 288–297, 1991b.

Phillips, R. J., R. F. Raubertas, R. E. Arvidson, I. C. Sarkar, R. R. Herrick, N. Izenberg, and R. E. Grimm, Impact crater distribution on Venus: Implications for planetary resurfacing history, *J. Geophys. Res.*, *97*, 15923–15948, 1992.

Phipps Morgan, J., W. J. Morgan, Y. Zhang, and W. H. F. Smith, Observational hints for a plume-fed, suboceanic asthenosphere and its role in mantle convection, *J. Geophys. Res.*, *100*, 12753–12767, 1995.

Price, M., and J. Suppe, Constraints on the resurfacing history of Venus from the hypsometry and distribution of tectonism, volcanism, and impact craters, *Earth Moon Planets*, in press, 1995.

Pronin, A. A., The structure of Lakshmi Planum, an indication of horizontal asthenospheric flow on Venus, *Geotectonics*, *20*, 271–281, 1986.

Pronin, A. A., and E. R. Stofan, Coronae on Venus: Morphology, classification, and distribution, *Icarus*, *87*, 452–474, 1990.

Rapp, R. H., Degree variances of the Earth's potential, topography and its isostatic compensation, *Bull. Geod.*, *94*, 84–94, 1982.

Rapp, R. H., Y. M. Wang, and N. K. Pavlis, The Ohio State 1991 geopotential and sea surface topography harmonic coefficient models, Tech. Rep. 410, Dept. Geodetic. Sci. Surv., Ohio State Univ., Columbus, 1991.

Rappaport, N. R., and J. J. Plaut, A 360-degree and -order model of Venus topography, *Icarus*, *112*, 27–33, 1994.

Revenaugh, J. R., and B. P. Parsons, Dynamic topography and gravity anomalies for fluid layers whose viscosity varies exponentially with depth, *Geophys. J. Roy. Astron. Soc.*, *90*, 349–368, 1987.

Ribe, N. M., The dynamics of thin shells with variable viscosity and the origin of toroidal flow in the mantle, *Geophys. J. Int.*, *110*, 537–552, 1992.

Ricard, Y., and C. Vigny, Mantle dynamics with induced plate tectonics, *J. Geophys. Res.*, *94*, 17,543–17,559, 1989.

Ricard, Y., L. Fleitout, and C. Froidevaux, Geoid heights and lithospheric stresses for a dynamic Earth, *Annales Geophysicae*, *2*, 267–286, 1984.

Richards, M. A., and B. H. Hager, Geoid anomalies in a dynamic Earth, *J. Geophys. Res.*, *89*, 5987–6002, 1984.

Richards, M. A., and B. H. Hager, The Earth's geoid and the large-scale structure of mantle convection, in *The Physics of Planets*, edited by S. K. Runcorn, pp. 247–272. John Wiley, New York, 1988.

Richards, M. A., and B. H. Hager, Effects of lateral viscosity variations on long-wavelength geoid anomalies and topography, *J. Geophys. Res.*, *94*, 10299–10313, 1989.

Richards, M. A., B. H. Hager, and N. H. Sleep, Dynamically supported geoid highs over hotspots: Observation and theory, *J. Geophys. Res.*, *93*, 7690–7708, 1988.

Robinson, E. M., and B. Parsons, Effect of a shallow low-viscosity zone on small-scale instabilities under the cooling oceanic plates, *J. Geophys. Res.*, *93*, 3469–3479, 1988a.

Robinson, E. M., and B. Parsons, Effect of a shallow low-viscosity zone on the formation of midplate swells, *J. Geophys. Res.*, *93*, 3144–3156, 1988b.

Russo, R. M., and P. G. Silver, Trench-parallel flow beneath the Nazca plate from seismic anisotropy, *Science*, *263*, 1105–1111, 1994.

Sandwell, D., and K. R. MacKenzie, Geoid height versus topography for oceanic plateaus and swells, *J. Geophys. Res.*, *94*, 7403–7418, 1989.

Sandwell, D. T., and M. L. Renkin, Compensation of swells and plateaus in the North Pacific: No direct evidence for mantle convection, *J. Geophys. Res.*, *93*, 2775–2783, 1988.

Sandwell, D. T., and G. Schubert, Evidence for retrograde lithospheric subduction on Venus, *Science*, *257*, 766–770, 1992a.

Sandwell, D. T., and G. Schubert, Flexural ridges, trenches, and outer rises around coronae on Venus, *J. Geophys. Res.*, *97*, 16,069–16,084, 1992b.

Saunders, R. S., and G. H. Pettengill, Magellan: Mission summary, *Science*, *252*, 247–249, 1991.

Saunders, R. S., G. H. Pettengill, R. E. Arvidson, W. L. Sjogren, W. T. K. Johnson, and L. Pieri, The Magellan Venus radar mapping mission, *J. Geophys. Res.*, *95*, 8339–8355, 1990.

Schaber, G. G., et al., Geology and distribution of impact craters on Venus: What are they telling us?, *J. Geophys. Res.*, *97*, 13257–13302, 1992.

Schubert, G., W. B. Moore, and D. T. Sandwell, Gravity over coronae and chasmata on Venus, *Icarus*, *112*, 130–146, 1994.

Senske, D. A., G. G. Schaber, and E. R. Stofan, Regional topographic rises on Venus: Geology of western Eistla Regio and comparison to Beta Regio and Atla Regio, *J. Geophys. Res.*, *97*, 13395–13420, 1992.

Shapiro, S. S., Structure and dynamics of the continental tectosphere, Ph.D. thesis, Massachussetts Institute of Technology, 1995.

Shapiro, S. S., and B. H. Hager, personal communication, 1995.

Simons, M., B. H. Hager, and S. C. Solomon, Global variations in geoid/topography admittances of Venus, *Science*, *256*, 798–803, 1994.

Sjogren, W. L., B. G. Bills, P. W. Birkeland, P. B. Esposito, A. R. Konopliv, N. A. Mottinger, S. J. Ritke, and R. J. Phillips, Venus gravity anomalies and their correlations with topography, *J. Geophys. Res.*, *88*, 1119–1128, 1983.

Sleep, N. H., Hotspots and mantle plumes: Some phenomenology, *J. Geophys. Res.*, *95*, 6715–6736, 1990.

Sleep, N. H., and R. T. Langan, Thermal evolution of the Earth: Some recent developments, *Advances in Geophysics*, *23*, 1–23, 1981.

Smrekar, S. E., Evidence for active hotspots on Venus from analysis of Magellan gravity data, *Icarus*, *112*, 2–26, 1994.

Smrekar, S. E., and R. J. Phillips, Venusian highlands: Geoid to topography ratios and their implications, *Earth Planet. Sci. Lett.*, *107*, 582–597, 1991.

Solomon, S. C., A tectonic resurfacing model for Venus, *Lun. Plan. Sci. Conf.*, *24*, 1331–1332, 1993.

Solomon, S. C., and J. W. Head, Mechanisms for lithospheric heat transport on Venus: Implications for tectonic style and volcanism, *J. Geophys. Res.*, *87*, 9236–9246, 1982.

Solomon, S. C., and J. W. Head, Lithospheric flexure beneath the Freyja Montes foredeep, Venus: Constraints on lithospheric thermal gradient and heat flow., *Geophys. Res. Lett.*, *17*, 1393–1396, 1990.

Solomon, S. C., and J. W. Head, Fundamental issues in the geology and geophysics of Venus, *Science*, *252*, 252–260, 1991.

Solomon, S. C., J. W. Head, W. M. Kaula, D. McKenzie, B. Parsons, R. J. Phillips, G. Schubert, and M. Talwani, Venus tectonics: Initial analysis from Magellan, *Science*, *252*, 297–311, 1991.

Solomon, S. C., et al., Venus tectonics: An overview of Magellan observations, *J. Geophys. Res.*, *97*, 13199–13256, 1992.

Squyres, S. W., D. M. Janes, G. Baer, D. L. Bindschadler, G. Schubert, E. L. Sharpton, and E. R. Stofan, The morphology and evolution of coronae on Venus, *J. Geophys. Res.*, *97*, 13,611–13,634, 1992a.

Squyres, S. W., D. G. Jankowski, M. Simons, S. C. Solomon, B. H. Hager, and G. E. McGill, Plains tectonism on Venus: The deformation belts of Lavinia Planitia, *J. Geophys. Res.*, *97*, 13579–13600, 1992b.

Stark, M., and D. W. Forsyth, The geoid, small-scale convection, and differential travel time anomalies of shear waves in the central Indian ocean, *J. Geophys. Res.*, *88*, 2273–2288, 1983.

Stockwell, R. G., L. Mansinha, and R. P. Lowe, Localization of the complex spectrum: The S-transform, *IEEE Trans. Sig. Process.*, in press, 1995.

Stofan, E. R., D. L. Bindschadler, J. W. Head, and E. M. Parmentier, Corona structures on Venus: Models of origin, *J. Geophys. Res.*, *96*, 20,933–20,946, 1991.

Strom, R. G., G. G. Schaber, and D. D. Dawson, The global resurfacing of Venus, *J. Geophys. Res.*, *99*, 10899–10926, 1994.

Su, W.-J., R. L. Woodward, and A. M. Dziewonski, Deep origin of mid-ocean-ridge seismic velocity anomalies, *Science*, *359*, 149–152, 1992.

Surkov, Y. A., L. P. Moskalyeva, O. P. Shcheglov, V. P. Kharyukova, O. S. Manvelyan, V. S. Kirichenko, and A. D. Dudin, Determination of the elemental composition of rocks on Venus by Venera 13 and Venera 14, *J. Geophys. Res.*, *88*, A481–A493, 1983.

Surkov, Y. A., V. L. Barsukov, L. P. Moskalyeva, V. P. Kharyukova, and A. L. Kemurdzhian, New data on the composition, structure, and properties of Venus rock obtained by Venera 13 and Venera 14, *J. Geophys. Res.*, *89*, B393–B402, 1984.

Surkov, Y. A., L. P. Moskalyova, V. P. Kharyukova, A. D. Dudin, G. G. Smirnov, and S. Y. Zaitseva, Venus rock composition at the Vega 2 landing site, *J. Geophys. Res.*, *91*, E215–E218, 1986.

Surkov, Y. A., F. F. Kirnozov, V. N. Glazov, A. G. Dunchenko, L. P. Tatsy, and O. P. Sobornov, Uranium, thorium, and potassium in the venusian rocks at the landing sites of Vega 1 and 2, *J. Geophys. Res.*, *92*, E537–E540, 1987.

Turcotte, D. L., An episodic hypothesis for venusian tectonics, *J. Geophys. Res.*, *98*, 17061–17068, 1993.

Tushingham, A. M., and W. R. Peltier, ICE-3G: A new global model of late Pleistocene deglaciation based upon geophysical predictions of post-glacial relative sea-level change, *J. Geophys. Res.*, *96*, 4497–4523, 1991.

Van Bemmelen, R. W., and H. P. Berlage, Versuch einer mathematischen behandlung geotektonischer bewegung unter besonderer berucksichtegung der undationstheorie, *Beitr. Geophys.*, *43*, 19–55, 1935.

van der Hilst, R., Complex morphology of subducted lithosphere in the mantle beneath the Tonga Trench, *Nature*, *374*, 154–157, 1995.

van der Hilst, R., and T. Seno, Effects of relative plate motion on the deep structure and penetration depth of slabs below the Isu-Bonin and Mariana island arcs, *Earth Planet. Sci. Lett.*, *120*, 395–407, 1993.

Varshalovich, D. A., A. N. Moskalev, and V. K. Kjersonskii, *Quantum Theory of Angular Momentum*, World Scientific, Singapore, 1988.

Walcott, R. I., Late Quaternary vertical movements in eastern North America: Quantitative evidence of glacio-isostatic rebound, *Rev. Geophys. and Space Phys.*, *10*, 849–884, 1972.

Walcott, R. I., Structure of the Earth from glacio-isostatic rebound, *Annu. Rev. Earth. Planet. Sci.*, *1*, 15–37, 1973.

Watts, A. B., H. J. Bodine, and M. S. Steckler, Observations of flexure and the state of stress in the oceanic lithosphere, *J. Geophys. Res.*, *85*, 6369–6376, 1980.

Wilson, J. T., A new class of faults and their bearing on continental drift, *Nature*, *207*, 343–347, 1965.

Woodhouse, J. H., and A. M. Dziewonski, Mapping the upper mantle: Three-dimensional modeling of Earth structure by inversion of seismic waveforms, *J. Geophys. Res.*, *89*, 5953, 1984.

Zhang, S., and U. Christensen, Some effects of lateral viscosity variations on geoid and surface velocities induced by density anomalies in the mantle, *Geophys. J. Int.*, *114*, 531–547, 1993.

Zhong, S., and M. Gurnis, Dynamic feedback between a continent-like raft and thermal convection, *J. Geophys. Res.*, *98*, 12219–12232, 1993.

Zhong, S., and M. Gurnis, Towards a realistic simulation of plate margins in mantle convection, *Geophys. Res. Lett.*, *22*, 981–984, 1995.

Zuber, M. T., Constraints on the lithospheric structure of Venus from mechanical models and tectonic surface features, *J. Geophys. Res.*, *92*, E541–551, 1987.

Zuber, M. T., Ridge belts: Evidence for regional and local scale deformation on the surface of Venus, *Geophys. Res. Lett.*, *17*, 1369–1372, 1990.

Zuber, M. T., and E. M. Parmentier, On the relationship between isostatic elevation and the wavelengths of tectonic surface features on Venus, *Icarus*, *85*, 290–308, 1990.